
**Feasibility studies for the measurement
of the time-like electromagnetic proton
form factors at the PANDA experiment.**

Iris Zimmermann

Mainz, Juli 2018

Feasibility studies for the measurement of the time-like electromagnetic proton form factors at the PANDA experiment.

Iris Zimmermann

Dissertation
zur Erlangung des Grades
"Doktor der Naturwissenschaften"

am Fachbereich Physik, Mathematik und Informatik
der Johannes-Gutenberg-Universität
in Mainz

Iris Zimmermann
geb. in Bad Kreuznach

Mainz, Juli 2018

Tag der mündlichen Prüfung: 22. Oktober 2018

Zusammenfassung

Die Erforschung der Eigenschaften des Protons ist ein aktuelles Thema der Hadronenphysik. Dabei stellen die elektromagnetische Formfaktoren des Protons, $G_E(q^2)$ und $G_M(q^2)$, einen Zugang zur Struktur des Protons dar. Wenig erforscht ist dabei der zeitartige Bereich ($q^2 > 0$), welcher durch Reaktionen $\bar{p}p \rightarrow \ell^+\ell^-$ ($\ell = e, \mu, \tau$) untersucht werden kann.

Die vorliegende Arbeit beschäftigt sich mit Machbarkeitsstudien zur Messung der zeitartigen elektromagnetischen Formfaktoren des Protons, $|G_E|$ und $|G_M|$, mittels Prozessen von $\bar{p}p \rightarrow \mu^+\mu^-$ am zukünftigen \bar{P} ANDA-Experiment, welches an dem im Bau befindlichen Beschleunigerkomplex FAIR (Darmstadt) geplant ist. Dazu sollen Kollisionen von Antiprotonen mit einem feststehenden Wasserstofftarget bei Strahlimpulsen von 1.5 GeV/c bis zu 15 GeV/c verwendet werden. Durch die hohe geplante Luminosität bei \bar{P} ANDA wird eine separate Extraktion der elektromagnetischen Formfaktoren aus der Winkelverteilung des nachgewiesenen μ^- (μ^+) möglich.

Diese Arbeit berücksichtigt zunächst die Bedingungen der letzten Datennahmephase (\bar{P} ANDA Phase-3). Die erreichbare Genauigkeit der zu extrahierenden physikalischen Größen wird dabei mit Hilfe von rechnergestützter Monte-Carlo Simulation und anschließender Datenanalyse der rekonstruierten Daten für die Signalreaktion $\bar{p}p \rightarrow \mu^+\mu^-$ bei vier verschiedenen Strahlimpulsen zwischen 1.5 und 3.3 GeV/c ermittelt.

Für die wichtigste Untergrundreaktion $\bar{p}p \rightarrow \pi^+\pi^-$ wurden Datensätze von jeweils 10^8 Ereignissen simuliert und zur Bestimmung des Unterdrückungsfaktors verwendet. Die herausfordernde Signal-Untergrund-Trennung konnte durch eine multivariate Datenklassifizierung (Boosted Decision Trees) optimiert werden. Die Subtraktion der Pionkontamination aus den selektierten Signaldaten wurde in dieser Studie ebenfalls berücksichtigt. Dazu wurden eine Methode entwickelt, um Winkelverteilungen der Pionkontamination mit der erwarteten Statistik und möglichst realistischer Form zu erzeugen. Der Einfluss der Form der Winkelverteilung der Pionkontamination auf die Resultate dieser Arbeit wurde in einer separaten Studie untersucht. Eine Abschätzung von systematischen Unsicherheiten wurde ebenfalls vorgenommen. Es wird darüberhinaus gezeigt, dass eine erfolgreiche Unterdrückung aller anderen relevanten Untergrundkanäle (beispielsweise $\bar{p}p \rightarrow \pi^+\pi^-\pi^0$, $\bar{p}p \rightarrow \pi^0\pi^0$, $\bar{p}p \rightarrow K^+K^-$, etc.) erreicht werden kann.

Im Vergleich zum elektronischen Kanal $\bar{p}p \rightarrow e^+e^-$ werden im Signal $\bar{p}p \rightarrow \mu^+\mu^-$ kleinere Strahlungskorrekturen, hauptsächlich Emission realer Photonen im Endzustand (Final State Radiation), erwartet. Es wurde der Einfluss der Final State Radiation auf die Rekonstruktionseffizienz des Signals mit Hilfe der PHOTOS Software untersucht.

Die Studien zeigen, dass ein empfindlicher Test der Leptonuniversalität bei \bar{P} ANDA möglich sein wird, bedingt durch die hohe Präzision des Verhältnisses der ermittelten Werte des effektiven Formfaktors in beiden Kanälen der Signalreaktion $\bar{p}p \rightarrow \ell^+\ell^-$ ($\ell = e, \mu$).

In einer separaten Studie wurde die erreichbare Präzision der Formfaktoren unter den Bedingungen der ersten Datennahmephase von \bar{P} ANDA (\bar{P} ANDA Phase-1) untersucht.

Abstract

The investigation of the properties of the proton is one of the major topics in modern hadron physics. The inner structure of the proton can be accessed via electromagnetic form factors. Of great interest is the time-like region ($q^2 > 0$), which can be investigated in reactions of $\bar{p}p \rightarrow \ell^+\ell^-$ ($\ell = e, \mu, \tau$).

This work reports on feasibility studies for the measurement of time-like electromagnetic form factors of the proton, $|G_E|$ and $|G_M|$, in reactions of $\bar{p}p \rightarrow \mu^+\mu^-$ at the future \bar{P} ANDA experiment (FAIR, Darmstadt). The studies are performed at four different beam momenta between 1.5 and 3.3 GeV/c. The high luminosity, which will be available at \bar{P} ANDA/FAIR, will allow for the collection of data with high statistics, which is a prerequisite for the separate extraction of the electromagnetic proton form factors from the signal angular distribution of the reconstructed μ^- (μ^+).

At first, the studies were performed for the conditions of the latest data taking phase at \bar{P} ANDA (\bar{P} ANDA Phase-3). The achievable accuracy of the form factors is determined by means of Monte-Carlo simulation and the subsequent data analysis for the signal reaction, assuming $R = |G_E|/|G_M|$ to be equal unity. Data samples for both the signal and for all relevant background channels have been generated and simulated using the PandaRoot software framework together with dedicated event generators.

For the most challenging background channel $\bar{p}p \rightarrow \pi^+\pi^-$, data sets of 10^8 events were generated and used for the determination of the suppression factor. The simulated data samples also allow for the calculation of the expected pion contamination statistics, which will remain in the signal data after the application of all selection criteria. The signal-to-background separation has been optimized through the use of multivariate classification methods (Boosted Decision Trees). A background subtraction will be necessary to remove the pion contamination from the reconstructed data at \bar{P} ANDA. This effect has been taken into account in these feasibility studies. For this purpose, a method was developed in order to construct angular distributions for the pion contamination with both the expected statistics and a mostly realistic shape. The influence of this shape on the extracted precision of the form factors was investigated in a separate study. Systematic uncertainties were estimated as well.

It will be shown, that a sufficient suppression of all other relevant background channels (as for example $\bar{p}p \rightarrow \pi^+\pi^-\pi^0$, $\bar{p}p \rightarrow \pi^0\pi^0$, $\bar{p}p \rightarrow K^+K^-$, etc.) will be achieved at \bar{P} ANDA.

Due to the high rest mass of the muon, QED radiative corrections in the signal $\bar{p}p \rightarrow \mu^+\mu^-$ are expected to be small compared to $\bar{p}p \rightarrow e^+e^-$, mainly caused by final state radiation. The influence of final state radiation on the signal statistics is studied using the PHOTOS software package.

Since \bar{P} ANDA will be able to investigate both channels of $\bar{p}p \rightarrow \ell^+\ell^-$ ($\ell = e, \mu$), it is possible to determine the ratio of the effective form factor obtained with both channels. This allows to perform a sensitive test of lepton universality ($e-\mu$) at \bar{P} ANDA.

A separate study was performed for the conditions of the first data acquisition time period of \bar{P} ANDA (\bar{P} ANDA Phase-1).

Contents

1	Introduction	1
2	The $\bar{\text{P}}\text{ANDA}$ physics program	5
2.1	The $\bar{p}p$ annihilation reaction	5
2.1.1	Total and elastic cross section	6
2.1.2	Light meson production	7
2.2	Hadron spectroscopy	9
2.3	Hypernuclei	12
2.4	Hadrons inside matter	13
2.5	Electromagnetic processes	13
3	Electromagnetic Form Factors of the Proton	17
3.1	Early investigation of the proton structure	17
3.2	Experimental access to the electromagnetic form factors of the proton	19
3.3	Parameterizations of electromagnetic form factors	27
3.3.1	Vector Meson Dominance (VMD)	27
3.3.2	Perturbative QCD parametrization	29
3.3.3	Form factor parameterization based on a modified dipole behavior	30
3.3.4	Comparison	31
3.4	Experimental measurements of electromagnetic proton form factors	32
3.4.1	Space-like electromagnetic form factors data	32
3.4.2	Time-like electromagnetic form factors data	35
3.5	Proton Form Factor Studies for the $\bar{\text{P}}\text{ANDA}$ experiment	37
3.5.1	Measurement of time-like proton form factors with $\bar{p}p \rightarrow e^+e^-$	38
3.5.2	Measurement of time-like proton form factors with $\bar{p}p \rightarrow \mu^+\mu^-$	40
3.5.3	Other Studies	41
4	The $\bar{\text{P}}\text{ANDA}$ Experiment at FAIR	45
4.1	Accelerator Complex FAIR	46
4.1.1	Antiproton production	47
4.1.2	Collector Ring (CR) and Recuperated Experimental Storage Ring (RESR)	47
4.1.3	High-Energy Storage Ring (HESR)	48
4.2	Target systems	49

4.2.1	Frozen Pellet Target	50
4.2.2	Cluster-Jet Target	50
4.2.3	Luminosity	51
4.3	$\overline{\text{P}}\text{ANDA}$ detector	52
4.3.1	Magnets	54
4.3.2	Tracking System	55
4.3.3	Electromagnetic Calorimetry	57
4.3.4	Particle Identification	60
4.3.5	Luminosity Detector	61
4.3.6	Muon Detectors	61
4.4	Muon System at $\overline{\text{P}}\text{ANDA}$	63
4.5	Phases of data taking at $\overline{\text{P}}\text{ANDA}$	70
5	Monte Carlo Simulation with PandaRoot	71
5.1	Experimental measurement and analysis strategy	72
5.2	Feasibility studies: Simulation and analysis strategy	73
5.3	Expected cross sections and statistics at $\overline{\text{P}}\text{ANDA}$ Phase-3	75
5.4	Relevant background channels	76
5.5	Simulation of the signal and background channels	78
5.5.1	The PandaRoot software framework	78
5.5.2	The Muon System in PandaRoot	80
5.5.3	Event generation of $\overline{p}p \rightarrow \mu^+\mu^-$	82
5.5.4	Event generation of $\overline{p}p \rightarrow \pi^+\pi^-$	83
6	Analysis of the Event Samples	89
6.1	Preselection of the pseudo-data	89
6.1.1	Requirements for data preselection	89
6.1.2	Composition of the preselected events for the $\overline{p}p \rightarrow \pi^+\pi^-$ background process	90
6.1.3	Muons from pion decay	93
6.1.4	Kinematical variables and detector observables	96
6.1.5	Particle Identification (PID) with the Muon System	105
6.2	Optimizing the μ/π separation by using Boosted Decision Trees	107
6.2.1	Multivariate Data Analysis	107
6.2.2	Boosted Decision Trees	108
6.2.3	Choosing appropriate input variables	113
6.2.4	Signal efficiency distribution	129
6.3	Background contamination from $\overline{p}p \rightarrow \pi^+\pi^-$	135
6.3.1	Construction of the angular distribution	135
6.4	Analysis strategy	139
6.5	Suppression of other background channels	140

7	Results of the feasibility studies for $\overline{\text{PANDA}}$ Phase-3	147
7.1	Extraction of $ G_E $, $ G_M $ and $R = G_E / G_M $	147
7.1.1	Signal reconstruction efficiency correction	147
7.1.2	Efficiency corrected angular distributions	148
7.1.3	Choice of cuts	148
7.1.4	Direct extraction of $R \pm \Delta R$	150
7.1.5	Simultaneous extraction of $ G_E $ and $ G_M $	150
7.2	Integrated signal cross section and effective form factor of the proton	151
7.3	Systematic uncertainties	154
7.4	Conclusion	155
7.5	Test of lepton universality	156
7.6	Analysis without EMC detector observables	159
7.7	Influence of the angular distribution shape of the pion contamination	161
7.8	Radiative corrections to the $\bar{p}p \rightarrow \mu^- \mu^+$ process using PHOTOS	168
7.8.1	PHOTOS software package	170
7.8.2	Simulation studies using PHOTOS in PandaRoot	170
8	Feasibility studies for $\overline{\text{PANDA}}$ Phase-1	177
8.1	$\overline{\text{PANDA}}$ detector setup during Phase-1	178
8.2	Results of the feasibility study for Phase-1	178
8.2.1	Test of lepton universality	179
8.2.2	Study with EMC detector at $\overline{\text{PANDA}}$ Phase-1	180
8.2.3	Study without EMC detector at $\overline{\text{PANDA}}$ Phase-1	182
8.2.4	Comparison with/without EMC detector	183
9	Conclusions and Outlook	187
A	Multivariate Classification Methods	191
A.1	Fisher discriminants (linear discriminant analysis)	191
A.2	Artificial Neural Networks	191
B	Training of the Boosted Decision Trees at $p_{beam} = 3.3 \text{ GeV}/c$	195
C	Shape extraction of the residual pion distribution after μ-selection	199
D	Angular distributions of μ-selected signal counts and pion contamination	203
E	Influence of the shape of the pion contamination distribution	205
F	Comparison between multivariate data analysis and simple cuts	211
G	Influence of the background fluctuations	217

H Summary tables of the results of these feasibility studies for \bar{P}ANDA Phase-1 and Phase-3	219
--	------------

Chapter 1

Introduction

Matter can be found in different structures and is bound by different forces. While the gravitational force has an influence on the distribution and motion of *macroscopic* matter in the universe, the electromagnetic force is responsible for the stability of atoms on the *microscopic* scale by binding the positively charged nuclei and the electron shells of negative charges together. The nuclei itself are bound systems of smaller particles, the nucleons (neutrons and protons), which are - together with the electrons - the building blocks of matter. Nucleons are systems of quarks, which are bound together by the strong interaction. One of the central issues in modern hadron physics is the characterization of the nucleon structure. The electromagnetic interaction provides a unique tool for the investigation of the inner structure of the nucleon, which can be accessed via electromagnetic form factors [1]. Their measurement in elastic and inelastic scattering experiments, and the measurement of structure functions in deep-inelastic electron scattering constitute a valuable source of information about the nucleon structure.

The first investigations on the spatial charge and magnetic distributions inside the nuclei were performed in the early 1950's, with the historically significant works of R. Hofstadter et al. [2] at the Stanford University High Energy Physics Laboratory. In 1955, the proton form factor was measured for the first time by Hofstadter et al. [3]. Efforts on the development of theoretical models for the nucleus were done simultaneously and the generally accepted model of the proton at that time was provided by M. N. Rosenbluth [4], which described the proton as a neutral baryonic core, which is surrounded by a pion cloud of positive charge.

The proton structure is traditionally studied via elastic electron-proton scattering, for which the reaction amplitude is dominated by the exchange of a single virtual photon between electron and proton, which carries a negative squared four momentum transfer ($q^2 < 0$). The hadronic vertex of this reaction can be parameterized in terms of two form factors: the electric G_E and the magnetic G_M form factor, which are related to the charge and magnetic spatial distribution of the proton.

Over the years, many experiments contributed to the investigation of electromagnetic form

factors of the proton in the *space-like* kinematical region ($q^2 < 0$, with $Q^2 = -q^2$) using elastic electron-proton scattering, while the experimental conditions through technical developments improved steadily. New activities concerning the electromagnetic form factor measurements were stimulated recently by the unexpected results obtained from the GEp Collaboration at JLab using the polarization transfer method for the measurement of the ratio of the proton elastic form factors, $\mu_p G_E/G_M$ [5, 6, 7]. A strong discrepancy between the results obtained using the polarization transfer and the Rosenbluth separation methods was found, starting from $Q^2 = 3$ (GeV/c)² and increasing as a function of Q^2 . While the results obtained with the Rosenbluth separation method are approximately consistent with unity over a large kinematical range of Q^2 , the experiments which use the polarization transfer method suggest a linear decrease of the ratio as a function of Q^2 . A hypothesis to explain this discrepancy is the significant contribution to the elastic electron-proton elastic scattering cross section by hard two-photon exchange, which has been neglected in previous analyses. This contribution would affect the results of the Rosenbluth method significantly, but only slightly the polarization results. Further experimental and theoretical efforts started, such as the OLYMPUS experiment at DESY, which performed a precision measurement of the positron-proton to electron-proton elastic cross section ratio, $R_{2\gamma}$, at low values between $0.6 \leq Q^2 \leq 2.2$ (GeV/c)². The ratio $R_{2\gamma}$ is a direct measure of the contribution of hard two-photon exchange to the elastic cross section [8]. The results of OLYMPUS are smaller than theoretical predictions of the hadronic two-photon exchange, however are in consistency with phenomenological models. Further measurements at higher values of Q^2 are needed, where the discrepancy increases.

Intense activity is related to the determination of the proton charge radius. Recent measurements were performed at PSI (Switzerland) using the Lamb shift in muonic hydrogen and showed results, which are significantly smaller than the values obtained before by investigations on regular hydrogen and elastic electron proton scattering experiments [9]. Future experiments plan to address the proton radius puzzle as e.g. MUon proton Scattering Experiment (MUSE) at PSI [10]. MUSE aims to expand the available comparisons by using muon scattering for the determination of the proton radius, with simultaneous electron scattering measurements.

The kinematical region with positive squared momentum transferred ($q^2 > 0$) is denoted as the *time-like* region and can be accessed via annihilation reactions $\bar{p}p \rightarrow \ell^+\ell^-$ ($\ell = e, \mu$) or the time-reversed electron channel of $e^+e^- \rightarrow \bar{p}p$. In contrast to the space-like region, the situation in the time-like region is different: only very few experiments in the past were able to perform measurements of time-like electromagnetic form factors with very scarce data, mostly measuring the total cross section and connected to that, the effective form factor. Due to the poor statistics of the data in the past, it was never possible to perform a separate determination of the time-like electromagnetic form factors. New experimental and theoretical activities have only recently been started in order to gain more knowledge in the field of time-like nucleon electromagnetic form factors and to understand recently discovered phenomena such as the oscillations in the data of the effective proton form factor in the time-like kinematical do-

main, that was observed first at the BaBar experiment (SLAC, USA) and also later confirmed at BESIII (IHEP, China) [11, 12]. More data of high statistics are expected in the time-like region (as e.g. from BESIII) and also new kinematical regions are planned to be accessed in future experiments in order to understand the nucleon structure and to be able to test the existing theoretical predictions from QCD as e.g. for the asymptotic regime. One of these future experiments will be the $\bar{\text{P}}\text{ANDA}$ experiment, which has a rich physics program including several measurements, which address fundamental questions of Quantum Chromodynamics (QCD), mostly in the non-perturbative regime [13]: high precision hadron spectroscopy, as e.g. the investigation of the nature of the recently found XYZ states [14], hypernuclear physics, hadrons in matter and nucleon structure investigations. The $\bar{\text{P}}\text{ANDA}$ (antiProton ANnihilation at DArmstadt) experiment will be located at the future Facility for Antiproton and Ion Research (FAIR), which is currently under construction at Darmstadt (Germany). The investigation of the nucleon structure at $\bar{\text{P}}\text{ANDA}$ will be performed by measuring structure observables, as e.g. Generalized Distribution Amplitudes (GDA's), which can be studied in the inverted wide angle Compton scattering process $\bar{p}p \rightarrow \gamma\gamma$, nucleon-to-pion TDA's using the $\bar{p}p \rightarrow e^+e^-\pi^0$ process [15], and electromagnetic form factors of the proton in the time-like region. For measuring such electromagnetic processes, antiproton-proton collisions at a fixed hydrogen target with beam momenta between $1.5 \leq p_{beam} \leq 15$ GeV/c will be available at $\bar{\text{P}}\text{ANDA}$. A high luminosity of the order of 10^{31} cm⁻² s⁻¹ will already be present starting from the first year of operation, expected around 2025. This will allow for a separate determination of time-like electromagnetic form factors from the angular distribution of the final state lepton from $\bar{p}p \rightarrow \ell^+\ell^-$ with $\ell = e$ and μ . This work is devoted to feasibility studies for the measurement of the time-like electromagnetic form factors of the proton from the $\bar{p}p \rightarrow \mu^+\mu^-$ process, which will be unique. In contrast to the $\bar{p}p \rightarrow e^+e^-$ process, which will be also used at $\bar{\text{P}}\text{ANDA}$ for the extraction of time-like form factors [16], this channel has the advantage, that radiative corrections due to final state radiations are expected to be smaller. Measuring both channels allows to test the radiative corrections. It will be the first time, that final state muon pairs are used to extract the time-like form factors of the proton. Furthermore, the measurement of both electron and muon channel at $\bar{\text{P}}\text{ANDA}$ will allow for a sensitive test of lepton universality based on the determination of the effective form factor of the proton with both channels.

The outline of this thesis is the following:

- Chapter 2 gives an overview on the planned physics program of the future $\bar{\text{P}}\text{ANDA}$ experiment.
- Chapter 3 is devoted to the topic of electromagnetic form factors of the proton and existing form factor models. An update on the currently existing data on the electromagnetic proton form factors in space-like and time-like region is given.
- Chapter 4 describes the layout of the FAIR facility and the foreseen experimental setup of the $\bar{\text{P}}\text{ANDA}$ experiment including the Muon System of the $\bar{\text{P}}\text{ANDA}$ detector, which is essential for this work.

- Chapter 5 presents the Monte-Carlo simulation studies, which have been performed to test the feasibility of measuring the time-like electromagnetic proton form factors using muon pairs in the final state. The event generators and the PandaRoot software framework, which have been used for the simulation, reconstruction and analysis of the signal $\bar{p}p \rightarrow \mu^+\mu^-$ process and the relevant background channels are described. The main background channel of $\bar{p}p \rightarrow \pi^+\pi^-$ is addressed.
- Chapter 6 gives a detailed explanation of the event analysis used in this work, starting with the preselection procedure of the simulated and reconstructed data samples. The detector response of relevant sub-detectors for this analysis is shown. In particular, the situation of pion decay in the main background channel is investigated and the composition of the preselected events from this channel is shown. The development of an advanced analysis strategy is presented, which is based on multivariate data classification (Boosted Decision Trees) and allows to optimize the signal-background separation. Different cut configurations, in particular varying cut values on the Boosted Decision Tree response are tested and the obtained distributions of the reconstruction efficiency of the signal events are presented. Furthermore, the construction of angular distributions of the pion contamination in the selected signal data is presented.
- Chapter 7 presents the obtained results in these studies on the extracted form factors, their ratio, the determination of the effective proton form factor and the integrated cross section for an assumed time-integrated luminosity of 2 fb^{-1} . A discussion of systematic and total uncertainties is given. An additional study, utilizing the PHOTOS software package, investigates the influence of final state radiation of the signal $\bar{p}p \rightarrow \mu^+\mu^-$ process on the results of these simulation studies.
- Chapter 8 shows the feasibility studies performed under the special conditions of the starting phase of data taking at $\bar{\text{P}}\text{ANDA}$ ($\bar{\text{P}}\text{ANDA}$ Phase-1) with reduced detector setup and reduced luminosity. The expected results for $\bar{\text{P}}\text{ANDA}$ Phase-1 are presented and systematic error contributions are given.

A summary of all results obtained in this work is given, together with a discussion of the future tasks and open questions concerning the measurement of time-electromagnetic form factors of the proton in processes of $\bar{p}p \rightarrow \mu^+\mu^-$ at $\bar{\text{P}}\text{ANDA}$.

Chapter 2

The $\bar{\text{P}}\text{ANDA}$ physics program

The $\bar{\text{P}}\text{ANDA}$ experiment [13] is planned to be one of the major projects at the future accelerating complex FAIR (Facility for Antiproton and Ion Research) at Darmstadt (Germany). $\bar{\text{P}}\text{ANDA}$ aims to gain new knowledge in the field of strong interactions especially in the non-perturbative regime. For this purpose, antiproton proton collisions will be used to produce a broad spectrum of different reaction channels. A precise measurement of e.g. new resonance states like the recently discovered XYZ states will be possible. The $\bar{\text{P}}\text{ANDA}$ physics program covers hadron spectroscopy as charmonium spectroscopy and also the search for gluonic excitations, open charm spectroscopy, the investigation of hadrons in the nuclear medium, hypernuclear physics and electromagnetic processes.

The High Energy Storage Ring (HESR) at FAIR will provide a high intense antiproton beam with momenta between 1.5 and 15 GeV/c. Together with the large acceptance of the $\bar{\text{P}}\text{ANDA}$ detector and its great capability to detect charged and neutral particles, data collection with high statistics will be possible.

2.1 The $\bar{p}p$ annihilation reaction

Using antiproton beams together with proton targets has - in contrast to e^+e^- collisions - the big advantage that all states with allowed quantum numbers can be directly formed and data of high statistics can be collected. This is possible since the (anti-)proton is a composite particle - consisting of three valence (anti-)quarks and sea quarks, which interact via gluon exchange. In case of e^+e^- annihilations (e.g. at the BaBar [17], BELLE [18] and BESIII [19] experiments), the direct formation of charmonium states is limited to states with $J^{PC}=1^{--}$, which are the quantum numbers of the virtual photon being exchanged (as e.g. the J/Ψ , Ψ' and the $\Psi(3770)$ resonances). Precise measurements of their widths and masses can be performed with beams of high quality. Many states of interest can only be produced via decay of intermediate resonances and the corresponding cross sections are much lower in comparison to a direct production, as it will be possible at $\bar{\text{P}}\text{ANDA}$.

The allowed quantum numbers of the $\bar{p}p$ system can be derived from the quantum numbers

	\bar{p}	p	$\bar{p}p$ system
Q	-1	+1	0
$I (I_3)$	(1/2, -1/2)	(1/2, +1/2)	(1,0), (0,0)
s	1/2	1/2	0, 1
J	1/2	1/2	0, 1, 2, ...
P	-1	1	$P = (-1)^{\ell+1}$
B	-1	1	0

Table 2.1: Quantum numbers of the $\bar{p}p$ system and its individual components: electric charge Q , strong isospin I and its 3rd component I_3 , total angular momentum J , parity P , spin s and baryon number B [20, 21].

of the antiproton and the proton. Whereas for the baryon number and the charge of the $\bar{p}p$ system, the quantum numbers of the antiproton and the proton are summed up, the possible parity and C-parity quantum numbers of the $\bar{p}p$ system follow

$$P = (-1)^{\ell+1}, \quad C = (-1)^{\ell+s}, \quad |\ell - s| \leq J \leq \ell + s \quad (2.1)$$

with spin quantum number $s = 0, 1$ and with ℓ as the orbital angular momentum between fermion and antifermion. The flavour quantum numbers are the strong Isospin I , Isospin 3rd component I_3 , Strangeness S , Charm C , Bottomness B and Topness T , while the $\bar{p}p$ system has neither strangeness, nor charmness, bottomness or topness. Possible final states of the annihilation reaction are limited to the allowed quantum numbers of the initial system as e.g. states with the quantum number $J^{PC} = 0^{-+}, 1^{--}, 1^{+-}, 2^{++}$, etc. with J: total angular momentum, P: intrinsic parity and C: charge conjugation parity. Another quantum number is the baryon number, which is an additive quantum number and is conserved in all currently known particle reactions and decays. It can be calculated as

$$B = (n_q - n_{\bar{q}})/3 \quad (2.2)$$

with the number of valence quarks n_q and antiquarks $n_{\bar{q}}$ in the hadron. Quarks (antiquarks) have baryon number $B = 1/3$ ($-1/3$). Therefore mesons have $B = 0$ and baryons (anti-baryons) have $B = 1$ (-1). Particles which do not contain quarks, have a baryon number of zero. Table 2.1 gives an overview of the individual quantum numbers of p , \bar{p} and the quantum numbers of the $\bar{p}p$ system.

2.1.1 Total and elastic cross section

The world data of the measured $\bar{p}p$ annihilation total cross section depending on the antiproton momentum in laboratory frame and given in [GeV/c] is illustrated in Fig. 2.1 [22, 23, 24] together with parameterizations of the total and elastic cross section from Ref. [25]. The total cross section for the $\bar{p}p$ annihilation reaction is in the range of several 10 mb up to 100 mb at the values of beam momentum which will be available at \bar{P} ANDA. The elastic contribution is only $\approx 1/3$ of the total cross section, the difference of the curves for total and elastic cross section is the inelastic contribution, which is also shown (green curve).

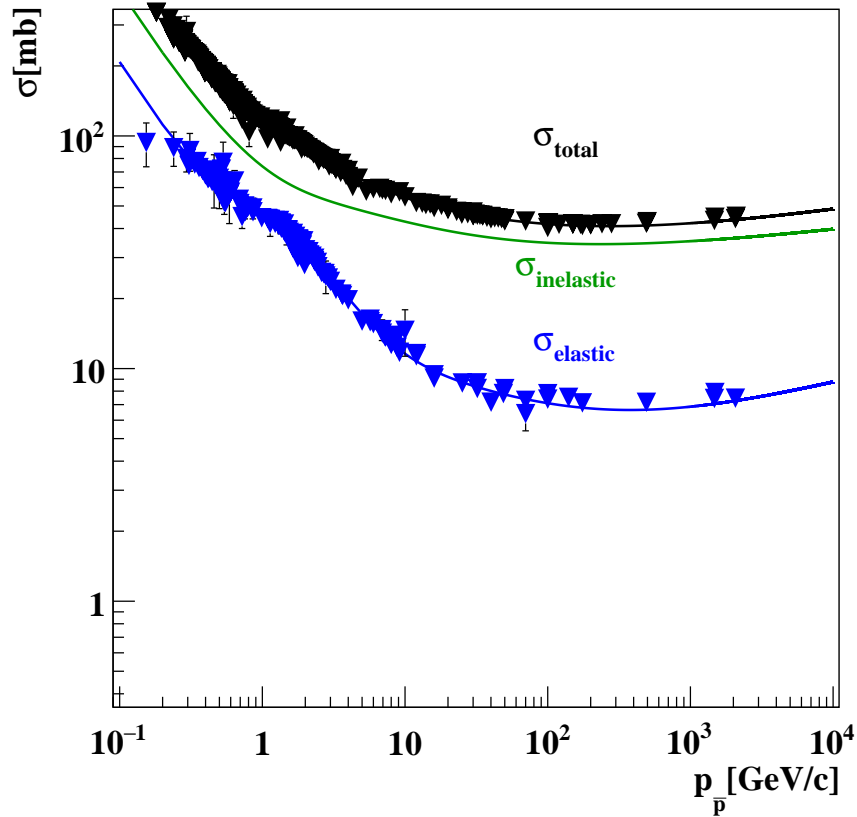


Figure 2.1: Total (black data points) and elastic (blue data points) cross section of the $\bar{p}p$ -interaction. Shown are the data points from the Particle Data Group (2017) [22] together with parametrizations from Ref. [25].

2.1.2 Light meson production

Since the production of light mesons will constitute a strong background for the studies of electromagnetic processes at \bar{P} ANDA, their cross sections are required for an estimation of the contribution of these channels to the total counting rate. This work focuses on feasibility studies concerning the $\bar{p}p \rightarrow \mu^+\mu^-$ reaction, whose cross section is of the order of a few hundred pb at the lowest available antiproton beam momentum at \bar{P} ANDA (see Chapter 5, Tab. 5.1). In order to study the feasibility for a sufficient suppression of the strong hadronic background, Monte-Carlo simulation studies can be performed, which deliver the rejection factors of such background channels. The knowledge of the corresponding cross section value at a certain beam momentum is needed for testing the feasibility for a sufficient suppression, what will be done in this work for several channels with light mesons in the final state.

Figure 2.2 illustrates the existing cross section data of many different hadronic channels [20, 24, 26], from which several channels were studied in this work in order to determine their suppression factors. It can be seen, that in comparison to the $\bar{p}p \rightarrow \mu^+\mu^-$ process, the hadronic

background processes have cross sections, which are in average higher by a factor of 10^5 . Therefore, the signal-background separation is very challenging for this measurement, in particular due to the background from $\bar{p}p \rightarrow \pi^+\pi^-$. Also shown are the parameterizations from Ref. [27], where the cross section was parameterized for the final states of K^+K^- and $\pi^+\pi^-$ as

$$\sigma = a \cdot e^{-b \cdot p_{\bar{p}} + c \cdot p_{\bar{p}}^2 + d} \quad (2.3)$$

and for several other final states shown in Tab. 2.2:

$$\sigma = u \cdot e^{-v \cdot p_{\bar{p}}} + \frac{w}{p_{\bar{p}}}. \quad (2.4)$$

The antiproton beam momentum is given in [GeV/c] and the total cross section in [mb]. The coefficients a , b , c and d for the final states K^+K^- and $\pi^+\pi^-$ are given in Tab. 2.2 and the coefficients u , v and w in Tab. 2.3. More details and parameterizations can be found in [27].

Final state	a [mb]	b [GeV] ⁻¹	c [GeV] ⁻²	d -
$\pi^+\pi^-$	1.339 ± 0.914	0.790 ± 0.058	0.287 ± 0.025	0.491 ± 0.680
K^+K^-	0.812 ± 1.988	0.747 ± 0.104	0.196 ± 0.042	1.228 ± 2.440

Table 2.2: Coefficients used in the parameterization from Ref. [27] for several inelastic channels of antiproton-proton annihilation into charged di-pion and di-kaon pairs.

Final state	u [mb]	v [GeV] ⁻¹	w [mb GeV]
$2\pi^+2\pi^-\pi^0$	24.275 ± 0.805	0.564 ± 0.008	0.007 ± 0.323
$2\pi^+2\pi^-$	6.856 ± 0.179	0.714 ± 0.018	0.254 ± 0.061
$\pi^+\pi^-\pi^0$	8.156 ± 0.487	1.193 ± 0.050	0.334 ± 0.086
$\pi^0\pi^0$	3.879 ± 1.585	4.039 ± 0.360	0.012 ± 0.001

Table 2.3: Coefficients used in the parameterization from Ref. [27] for several inelastic channels of antiproton-proton annihilation with light mesons in the final state.

It will be shown in this work, that the measurement of the $\bar{p}p \rightarrow \pi^+\pi^-$ process at the future $\bar{\text{P}}\text{ANDA}$ Experiment is required in order to perform the subtraction of the remaining pion background contamination from the reconstructed and selected data for $\bar{p}p \rightarrow \mu^+\mu^-$. Another motivation for the measurement of antiproton-proton annihilation into charged light meson pairs at $\bar{\text{P}}\text{ANDA}$, is the test of a recently developed effective meson model with mesonic and baryonic degrees of freedom from [28]. In this model, form factors are added to take into account the composite nature of the interacting hadrons. Details can be found in [28].

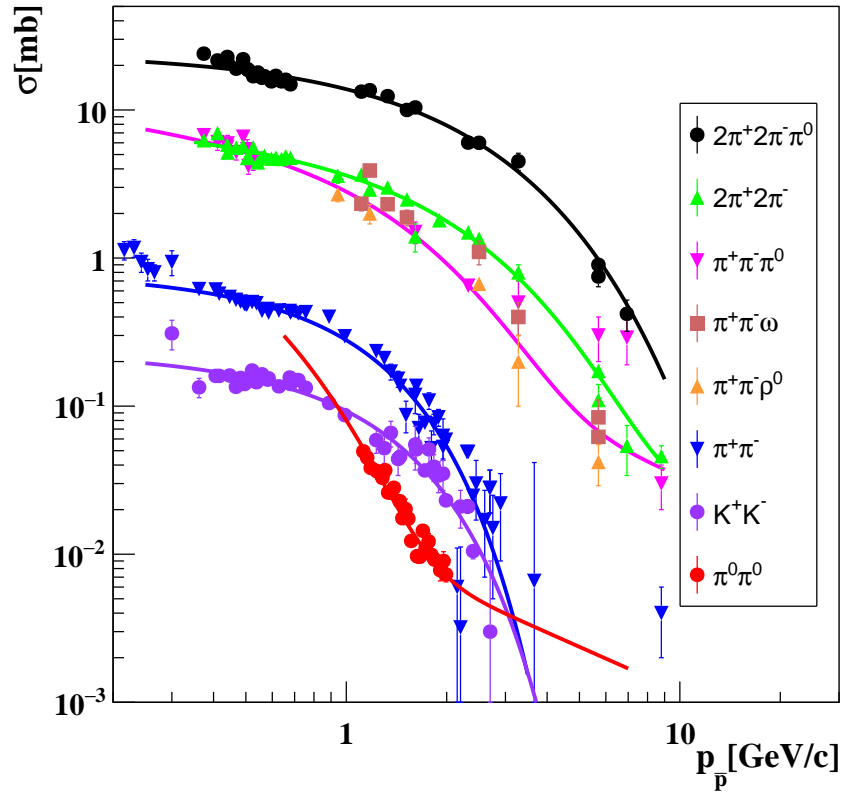


Figure 2.2: Production cross sections of different hadronic states in the $\bar{p}p$ annihilation process depending on the antiproton momentum in the laboratory frame from Ref. [20, 24, 27]. Parameterizations are from Ref. [27]. Hadronic final states, in particular $\pi^+\pi^-$, are of special interest in this work, since they constitute a strong hadronic background in the measurement of time-like electromagnetic form factors of the proton using electromagnetic processes $\bar{p}p \rightarrow \ell^+\ell^-$ ($\ell = e, \mu$).

2.2 Hadron spectroscopy

The QCD hadronic spectrum consists of a variety of stable or long-lived hadrons which can be observed. Studying these QCD bound states allows to gain a better understanding of QCD. Non-relativistic potential models, effective field theories and Lattice QCD are used for the calculation and prediction of these particle spectra. Precision measurements in the fields of charmonium, open charm and baryon spectroscopy are planned to be performed at \bar{P} ANDA, which are necessary for testing these approaches and the determination of their free parameters. In addition, \bar{P} ANDA will search for exotic states as quark-gluon bound states (hybrids), glueballs and multiquark states.

Charmonium and charmed mesons

Charmonium, as a bound system of c and \bar{c} , has been an important tool to investigate the strong interaction since its discovery in 1974 [29, 30]. Due to the high rest mass of the c -quark and, in comparison to that, the small binding energy, a non-relativistic description of the charmonium states is possible. In particular, the description of the dynamical properties of the $c\bar{c}$ -system can be done using non-relativistic (heavy quark) potential models. The choice of the potential function has to fulfill the asymptotic properties of QCD. Thus, the masses and widths can be obtained from the Schrödinger equation. A comparison of experimental data with the model allows to determine its free parameters. Both e^+e^- and $\bar{p}p$ collisions can be used to study the charmonium states, although a direct formation of all charmonium states is only possible in $\bar{p}p$ annihilation processes due the inner (quark) structure of the beam particles. Here, the coherent annihilation of the three quarks and three antiquarks leads to the direct creation of all possible quantum number states. Since this measurement depends only on the beam parameters and their quality, precise masses and widths of the charmonium states can be achieved. A disadvantage is the strong hadronic background, which is produced in $\bar{p}p$ annihilation reactions.

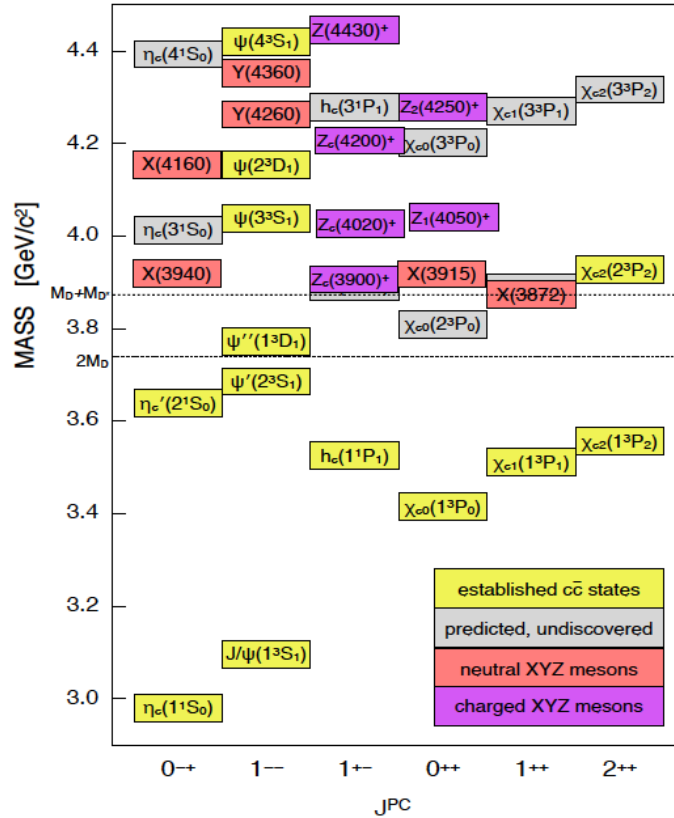


Figure 2.3: The mass spectrum of charmonium and charmonium-like resonances [14], including the recently discovered XYZ states. The nature of the XYZ states is currently unknown. They are possible candidates for tetra-quarks, penta-quarks, hybrid-states or molecule-like states. \bar{P} ANDA will perform precise measurements of widths with an accuracy of $\sim 10\%$ and masses up to 100 keV in the region below and above the open charm threshold [13] in the $\bar{p}p$ center-of-mass range between 2.2 and 5.5 GeV using $\bar{p}p$ annihilations.

Figure 2.3 illustrates the mass spectrum of the predicted, already confirmed charmonium states together with the new resonances with unusual properties [14]. The yellow boxes contain the already predicted and confirmed charmonium states, the grey boxes represent already predicted but not yet discovered states and the red/purple boxes show the recently discovered (unpredicted) charmonium-like states (XYZ). These states possess unusual properties, which can not be explained by a simple quarkonium state. Such states could be realized by hybrids, due to their gluonic content. A possible explanation for that is the vibration of the glue tube (also denoted as the flux-tube), which adds more units of angular momentum to the total momentum of the hybrid [13]. This can be added in terms of quantum numbers to the quantum numbers of a simple quarkonium state. Also tetra-quark, penta-quark or molecule-like states from mesons could be possible candidates for the XYZ states.

The charmonium spectrum shows eight narrow states below the open charm threshold ($=D\bar{D}$ production threshold) at 3.73 GeV, which are all known. However the knowledge of their parameters and decays is by far not complete and precise measurements of their widths and decay modes are required. Measurements with different accuracies could be performed in that case. Whereas the vector states could be measured with small widths in direct formation using e^+e^- collisions, the non-vector states could only be created in decay processes.

Above the heavy flavor threshold of $D\bar{D}$, an unexpected set of states have been recently discovered, denoted as the XYZ states, containing a $c\bar{c}$ pair. The first discovery of the X(3872) was made in 2003 at BELLE, followed by the confirmation of this detected resonance at BaBar. In 2013, BESIII discovered the $Z_c^+(3900)$, a charged resonance which decays as $Z_c^+ \rightarrow J/\Psi + \pi^+$ and therefore could be a possible candidate for a tetra-quark. Although there are several theoretical approaches (as e.g. quarkonium hybrids (gluonic excitations of $q\bar{q}$ states), tetra-quarks and meson molecules) to explain the XYZ states, none of them completely describes the discovered particle states. PANDA will be able to perform high precision measurements in the center-of-mass range between 2.2 and 5.5 GeV using $\bar{p}p$ annihilations. At such energies, a broad spectrum of quark configurations can be studied. This includes also candidates for tetraquarks, glueballs, quarkonium hybrids, etc.

Another interesting field are the open charm mesons, which are composed of a charm and a light quark. This D meson spectrum can be successfully described through the quark model. However, the discovery of the D_s resonances at BELLE, BaBar and CLEO triggered new activity in the theoretical description of such states, since the quark model could not sufficiently explain them. The different model predictions need more high precision data from the experimental side, which provide precise decay widths of the D_s states.

Strange and charmed baryons

The baryon excitation spectrum is one important topic in the research field of non-perturbative QCD. Especially in the nucleon sector, the agreement between observed states and the predictions based on the quark model is poor. While for some of the states of lower mass the predictions show deviations from the measured masses, the predicted states of higher masses could not be observed so far (*missing resonances*).

Deeper knowledge about the dynamics of light quarks in the environment of heavy quarks can be gained through the spectroscopy of charmed and strange baryons. The $\bar{p}p$ annihilations at \bar{P} ANDA allow to study (multi-)strange and also charmed baryons. It will be possible to produce these baryons without the necessity of having additional kaons or D mesons in the final state (in order to conserve the quantum numbers of Strangeness and Charmness).

2.3 Hypernuclei

A hypernucleus can be formed by replacing (at least) one up or down quark with a strange quark in a nucleon, which is bound inside a nucleus. Hence, the nucleus receives a new quantum number, the strangeness. Due to experimental limitations in the past, the available data from hypernuclei studies are poor, although single λ -hypernuclei were discovered in the 1950's.

Due to experimental limitations, only 6 double- λ -hypernuclei are currently known, despite rising experimental efforts in the field of hypernuclei physics. \bar{P} ANDA will be able to produce (double- λ -)hypernuclei of high numbers using $\bar{p}p$ annihilations, which are used for studying hyperon-nucleon interactions. In contrast to nucleons, the hyperons bound in nuclei do not underly the Pauli principle and therefore can populate all possible nuclear states - in contrast to the nucleons, which undergo pairing interactions as well. The hyperon-nucleon interaction strength may be described by using well-known wave functions for single-particle states.

At \bar{P} ANDA, it will be possible, to perform high-precision gamma-spectroscopy of double- λ hypernuclei for the first time and thus, to determine the λ - λ strong interaction strength. The hypernuclear detector setup will include a primary nuclear target for the production of $\Xi^+\Xi^-$ pairs, a secondary target for the formation of the hypernuclei and an germanium array detector for the highly precise γ spectroscopy with an excellent energy precision of a few keV (full-width-half-maximum).

Furthermore, \bar{P} ANDA will be able to study the λ - N weak interaction via decay of $\lambda \rightarrow N\pi$ ($N \equiv$ nucleon), what is suppressed by the Pauli principle since all nucleon states in the nucleus are occupied.

2.4 Hadrons inside matter

It will be possible at $\overline{\text{PANDA}}$, to investigate possible modifications of hadronic properties in nuclear matter in an so far unexplored energy range [13]. While previous experimental efforts concentrated on light quarks, $\overline{\text{PANDA}}$ aims to perform studies on heavier masses in the open and hidden charm sector. Such measurements aim to allow for understanding the origin of mass in context of chiral symmetry breaking in QCD and its partial restoration inside hadronic matter. In particular, $\overline{\text{PANDA}}$ aims to study the J/Ψ - N dissociation cross section ($N \equiv$ nucleon). This cross section serves as an important input for certain high energy heavy ion reactions. Furthermore, antibaryons in nuclei and short-range N - N correlations will be investigated.

2.5 Electromagnetic processes

Different electromagnetic processes at $\overline{\text{PANDA}}$ will allow to study nucleon structure observables. Hard reactions (high energetic probes) are a commonly used tool in this field. An important aspect is the QCD factorization, which allows to divide the amplitude of a hard process into a hard perturbative QCD part and a soft non-perturbative part. The hard part can be described with well-defined operators in terms of quarks and gluons. Together with the matrix element for the process, an extraction of the soft part is possible.

While the charge and magnetic spatial distributions inside the hadron can be investigated using space-like ($q^2 < 0$) electromagnetic form factors, the longitudinal momentum distributions of the hadron constituents are described via *structure functions*. In order to study the hadron structure in three dimensions, the generalized parton distributions (GPD's) have been developed [31, 32]. They provide information on both the spatial distribution of the partons in the transverse plane and their (longitudinal) behavior in momentum space along the direction in which the nucleon is moving.

The framework of GPD's can be used for the description of amplitudes of hard exclusive processes in lepton scattering experiments [33, 34, 35, 36] as e.g. the process of deeply virtual Compton scattering (DVCS) $e^-p \rightarrow e^-p\gamma$. This reaction can be described via a so-called *handbag diagram*, which is illustrated in Fig. 2.4 (a). The reaction amplitude of this process can be factorized into a hard upper part (virtual exchange photon carries a large value of Q^2) which can be described by perturbative QCD and a soft lower part which is parametrized by the GPD's.

Another process which can be described via the handbag approach, is wide angle Compton scattering (WACS). At $\overline{\text{PANDA}}$, the crossed process of WACS can be studied, which is $\bar{p}p \rightarrow \gamma\gamma$. The corresponding Feynman diagram is shown in Fig. 2.4 (b). Here, the two final state photons are emitted at large polar angles in the center-of-mass system. It is believed that only at intermediate energies, which are accessible with $\overline{\text{PANDA}}$, the handbag formalism can be applied [37, 38], however a proof of the QCD factorization theorem at this energy regime was not performed yet. In the case of time-like WACS, the parametrization of the soft part is done via the

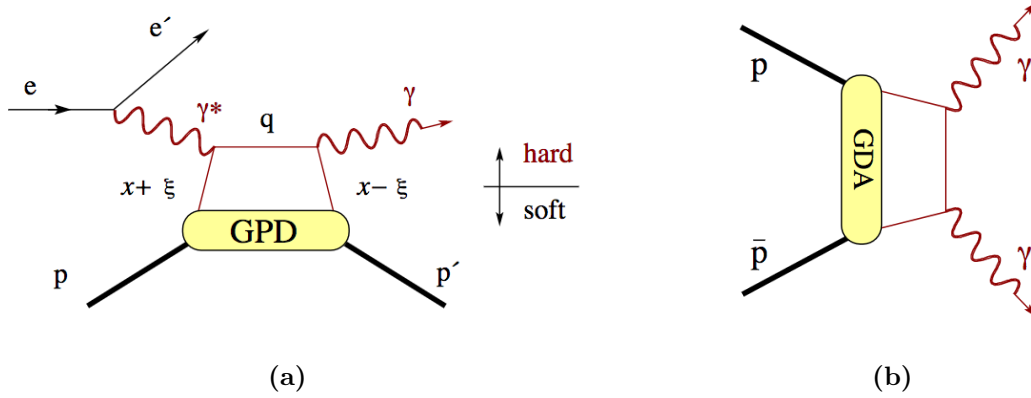


Figure 2.4: (a): Deeply virtual Compton scattering can be described by the handbag diagram, which uses a factorization of the process amplitude into a hard upper part, which can be treated by perturbative QCD and QED and a soft lower part, which can be described by Generalized Parton Distributions (GPD's). (b): Generalized Distribution Amplitudes (GDA's) can be studied in the inverted wide angle Compton scattering process $\bar{p}p \rightarrow \gamma\gamma$ [13].

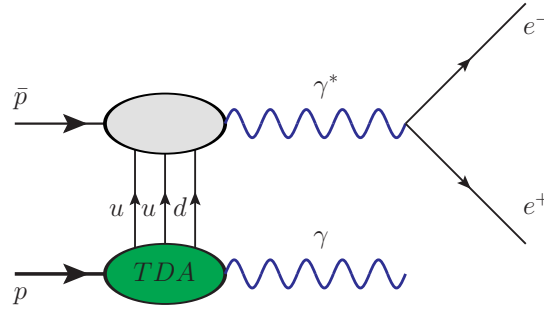


Figure 2.5: The process of $\bar{p}p \rightarrow e^+e^-\gamma$ can be factorized into a hard upper part, where the virtual photon has a large value of q^2 and a soft lower part, where the transition between the proton and the (virtual) photon can be described by a TDA.

Generalized Distribution Amplitudes (GDA's), which constitute the counterparts of the GPD's. The most serious background source is the production of neutral hadrons as $\bar{p}p \rightarrow \pi^0\pi^0$. Since the cross section of $\bar{p}p \rightarrow \gamma\gamma$ is approximately two or three orders of magnitude lower than the background cross section, the measurement at \bar{P} ANDA is a challenge, which will profit from the high luminosity and the almost 4π acceptance of the \bar{P} ANDA detector. If one of the photons is replaced by a pseudo-scalar meson as in $\bar{p}p \rightarrow \pi^0\gamma$, a similar theoretical concept can be applied. This reaction will be also studied with \bar{P} ANDA. Other processes, where QCD factorization can be tested, are $\bar{p}p \rightarrow M\gamma$, with M standing for a neutral meson as for instance the ρ^0 meson.

The quark structure of hadrons can be studied at \bar{P} ANDA with the Drell-Yan $\bar{p}p \rightarrow \mu^+\mu^-X$ process, which allows to gain information on the three-dimensional momentum distributions and the spin structure of the nucleon. A Drell-Yan process is an electromagnetic process in which a quark and an antiquark annihilate into a virtual photon, which produces a lepton pair. A different theoretical approach can be made for the Drell-Yan process $\bar{p}p \rightarrow \gamma^*\gamma$ with the pro-

duction of an electron positron pair $\gamma^* \rightarrow e^+e^-$ by the emitted virtual photon. The Feynman diagram for this reaction is illustrated in Fig. 2.5. The reaction amplitude for this process can be factorized into a hard part for a large virtuality of the photon γ^* and a soft part, containing Transition Distribution Amplitudes (TDA's) [39, 40], which parameterize the transition between the proton and a photon.

A similar description based on TDA's can be applied also when the photon is replaced by a neutral meson as in $\bar{p}p \rightarrow e^+e^-\pi^0$ or $\bar{p}p \rightarrow e^+e^-\rho^0$.

Feasibility studies have been performed for the possibility of accessing nucleon-to-pion TDA's with the $\bar{p}p \rightarrow e^+e^-\pi^0$ process at the \bar{P} ANDA experiment [15], what is possible at high center-of-mass energy and high invariant mass squared of the lepton pair q^2 and under the kinematical constraint that the neutral pion is emitted either under small (forward) or under large (backward) angles. The feasibility for a sufficient suppression of relevant background channels i.e. $\bar{p}p \rightarrow \pi^+\pi^-\pi^0$ was investigated in detailed simulation studies for center-of-mass energy squared $s = 5 \text{ GeV}^2$ ($s = 10 \text{ GeV}^2$) in the kinematic regions $3.0 < q^2 < 4.3 \text{ GeV}^2$ ($5 < q^2$), while the π^0 must be scattered in the forward or backward cone of $|\cos(\theta_{\pi^0})| > 0.5$ in the $\bar{p}p$ center-of-mass frame. The studies show, that high signal efficiencies around 40% can be kept, while background suppression factors of 5×10^7 (1×10^7) at low (high) q^2 for $s = 5 \text{ GeV}^2$ and of 1×10^8 (6×10^6) at low (high) q^2 for $s = 10 \text{ GeV}^2$ will be achieved. The calculation of the expected signal statistics was done under the assumption of a time-integrated luminosity of 2 fb^{-1} and the studies showed that a lepton signal of high purity can be reconstructed.

In addition, the $\bar{p}p$ annihilations at \bar{P} ANDA allow to access the structure of the proton via measuring electromagnetic form factors (FF's) of the proton in the time-like region. For that purpose, reactions of the type $\bar{p}p \rightarrow \ell^+\ell^-$ ($\ell = e, \mu, \tau$) can be studied. Although the $\bar{p}p$ annihilation reaction also allows the creation of tau leptons of opposite charge in the final state, this channel will not be used at \bar{P} ANDA due to the very low cross section and its high production threshold (due to the heavy rest mass of the tau lepton). Figure Fig. 2.6 shows the lowest order (tree-level) contribution to the reaction amplitude of this process, in which a single, virtual photon carries the squared four-momentum transfer $q^2 > 0$.

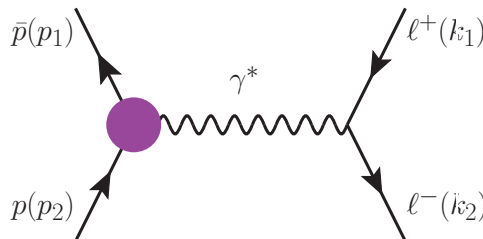


Figure 2.6: Tree-level contribution to the reaction amplitude of the $\bar{p}p \rightarrow \ell^+\ell^-$ process ($\ell = e, \mu$). \bar{P} ANDA will be able to investigate time-like electromagnetic form factors through this reaction over a wide kinematical range of q^2 .

This reaction allows to study the FF's of the proton in the time-like region over a large kinematical range. A challenge of using $\bar{p}p$ annihilations is the rejection of the strong hadronic background while the signal channels have rather small cross sections.

Feasibility studies have been performed on the di-electron channel $\bar{p}p \rightarrow e^+e^-$ demonstrating that the moduli of the time-like FF's of the proton, $|G_E|$ and $|G_M|$, can be measured with high precisions up to a few percent at $\overline{\text{PANDA}}$ [16]. The most important background channel is expected to be $\bar{p}p \rightarrow \pi^+\pi^-$. The ratio of the total cross sections for the main background channel is about five to six orders of magnitude larger than that of the signal. These studies show that a pion background rejection factor of 10^{-8} can be achieved, corresponding to a signal pollution of less than 1%. At the same time, total signal efficiencies between 40% and 50% are kept, depending on the value of q^2 .

$\overline{\text{PANDA}}$ is the first experiment, that considers the $\bar{p}p \rightarrow \mu^+\mu^-$ process (which will be denoted in the following as the *muon channel*), for the simultaneous determination of the time-like FF's of the proton. Measuring the muon channel does not only serve as a cross check of the extracted FF values obtained in the measurement of $\bar{p}p \rightarrow e^+e^-$ (*electron channel*). It constitutes also an excellent opportunity for the test of lepton universality. In particular, $\overline{\text{PANDA}}$ will be able to compare the FF values obtained by both muon and electron channels in the time-like regime of q^2 based on the same data set, which serves as an additional cross check. Radiative corrections due to final state radiation are expected to be smaller for the muon channel in comparison to the electron channel. Measuring both channels also serves as a valuable test of the radiative corrections.

The signal-background separation for the case of the muon channel is much more challenging in comparison to the electron channel, due to the very similar rest masses of muon and pion. This work aims to demonstrate the feasibility of using the muon channel in order to extract the time-like electromagnetic proton FF's simultaneously from the angular distribution of the reconstructed final state μ^- (also the μ^+ could be considered for that purpose).

Furthermore, $\overline{\text{PANDA}}$ aims to measure the $\bar{p}p \rightarrow e^+e^-\pi^0$ process, which allows to access the kinematical region below the proton production threshold ($q^2 = 4 M_p^2$). This region is denoted as *unphysical region* and is accessible due to the neutral pion in the final state, which reduces the q^2 of the produced virtual photon.

Another measurement, which could be performed at $\overline{\text{PANDA}}$, is the determination of the relative phase between G_E and G_M by measuring single spin polarization observables. For that purpose, a transversely polarized target is under development for the $\overline{\text{PANDA}}$ experiment [41].

Chapter 3

Electromagnetic Form Factors of the Proton

A quantitative understanding of the inner structure of the nucleon is one of the open questions in modern hadronic physics. The key observables for a characterization of the nucleon structure are nucleon form factors (FF's), which can be accessed using electromagnetic probes.

In the following, a short overview on the historical efforts on the investigation of the FF's of the proton will be given [1], which had its starting point in the field of investigations of the structure of nuclei in the first half of the 20th century. The first review paper, which included the measurement of the proton FF, was written by Hofstadter in 1956 [42].

3.1 Early investigation of the proton structure

The first indication that the proton is a particle with inner structure, was found in the year 1933 by O. Stern. He performed the first measurements of the proton's magnetic moment [43] and found the proton's anomalous moment to be approximately 2.81 times larger than the expected value for a point-like Dirac particle (with spin 1/2). This leads to the conclusion, that the proton can not simply possess a point-like charge and magnetic moment.

In 1950, Rosenbluth [4] discussed a model of the proton, which considers the proton as a neutron core surrounded by a meson cloud of positive charge. This model was denoted as the weak meson coupling model. When a high energy electron enters the meson cloud, it would notice a reduced charge (e') and magnetic moment ($\kappa'e'$, with the effective proton magnetic moment κ').

In 1956, R. Hofstadter [42] connected the results of Ref. [44] for the elastic electron-proton scattering cross section at a fixed angle and energy, to the Mott cross section for the scattering of an electron (carrying spin 1/2) by a spin-less proton, σ_{Mott} , with the internal charge density distribution $\rho(\vec{r})$, as:

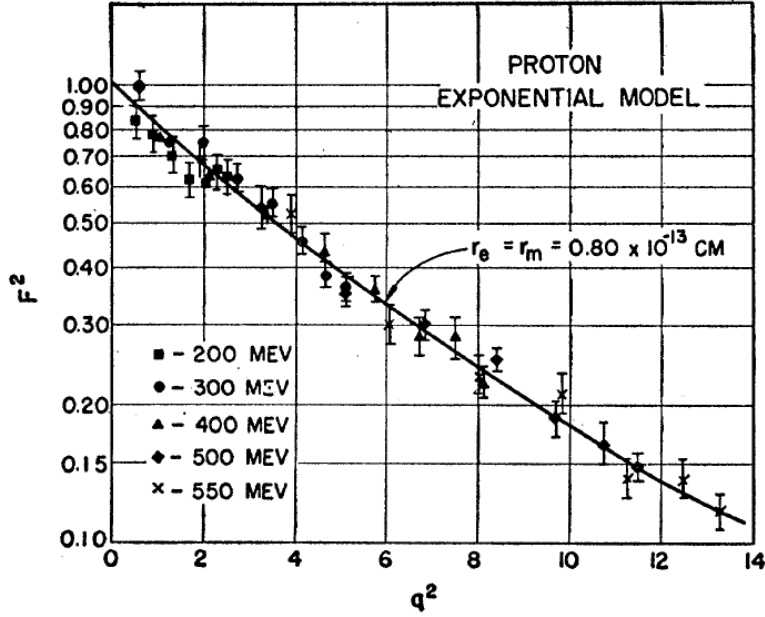


Figure 3.1: Original results from the paper of R. Hofstadter in 1956 [42]: "The square of the FF plotted against q^2 . q^2 is given in units of 10^{26}cm^{-2} . The solid line is calculated for the exponential model with rms radii = $0.80 \times 10^{-13} \text{cm}$."

$$\sigma(\theta_e) = \sigma_{Mott} \left| \int_{\text{volume}} \rho(\vec{r}) e^{i\vec{q}\cdot\vec{r}} d^3\vec{r} \right|^2 = \sigma_{Mott} |F(|\vec{q}|)|^2 \quad (3.1)$$

with

$$\sigma_{Mott} = \left(\frac{e^2}{2E_e} \right) \cdot \frac{\cos^2 \frac{\theta_e}{2}}{\sin^4 \frac{\theta_e}{2}}. \quad (3.2)$$

Here, E_e stands for the incident energy of the electron beam and θ_e is the scattering angle of the electron in laboratory frame. The target mass is assumed to be infinite. Hence, a phenomenological FF squared could be obtained from the absolute differential cross section measurements [42, 1] by

$$|F(|\vec{q}|)|^2 = \frac{\sigma(|\vec{q}|)}{\sigma_{Mott}} \quad (3.3)$$

where $\vec{q} = \vec{p}_{beam} - \vec{p}_e$ and \vec{q} stands for the momentum transferred by the exchanged virtual photon. His historical results, which were obtained from these measurements, are shown in Fig. 3.1 in his paper [42]. Later, the charged and the static magnetic FF's were defined by Clementel and Villi as $F_1(|\vec{q}|) = \frac{e'}{e}$ and as $F_2(|\vec{q}|) = \frac{\kappa' e'}{\kappa_0 e}$ [45] (where κ_0 stands for the anomalous magnetic moment).

R. Hofstadter et al. introduced the Dirac and Pauli FF's, $F_1(|\vec{q}|)$ and $F_2(|\vec{q}|)$ [44, 42, 46], where the Pauli FF, $F_2(|\vec{q}|)$, represents the deviation of the effective magnetic moment from a point-like anomalous magnetic moment, and the Dirac FF, $F_1(|\vec{q}|)$ describes the deviation of the effective charge from a point-like charged Dirac particle.

In the following, the process of elastic lepton-proton scattering and its crossed channel, the

$\bar{p}p$ annihilation into a lepton pair (with $q^2 > 0$, corresponding to the time-like (TL) kinematical region) are considered for unpolarized beam and target. The cross sections will be presented.

3.2 Experimental access to the electromagnetic form factors of the proton

The traditional way to access the electromagnetic proton FF is the measurement of observables in the elastic electron-proton scattering, giving access to the FF in the space-like (SL) q^2 region ($q^2 < 0$). At tree-level, this process occurs under the exchange of a single virtual photon between electron and proton, which carries the four-momentum squared transfer Q^2 (with $Q^2 = -q^2$). The elastic electron-proton scattering for an unpolarized target and beam is described usually within the formalism of A. M. Rosenbluth [47]. Since also heavier leptons (μ and τ) shall be described with this formula, the rest mass of the lepton will not be neglected in the following. The process occurs as

$$\ell^-(k_1) + p(p_1) \rightarrow \ell^-(k_2) + p(p_2) \quad (3.4)$$

with the lepton (ℓ) and the proton (p). The four momenta of the involved particles are written in parenthesis and are denoted as

$$p_{1,2} = (E_{1,2}, \vec{p}_{1,2}), \quad k_{1,2} = (\epsilon_{1,2}, \vec{k}_{1,2}). \quad (3.5)$$

Figure 3.2 shows the lowest order contribution to the reaction amplitude of the elastic lepton-proton scattering. Here, the virtual photon carries the four-momentum squared transfer $q^2 = \nu^2 - \vec{q}^2$ with transferred energy ν and transferred three momentum squared $\vec{q}^2 = (\vec{p}_2 - \vec{p}_1)^2$. For elastic electron scattering on a proton of the rest mass M_p and in the laboratory frame, q^2 can be calculated as

$$q^2 = t = (p_2 - p_1)^2 = p_2^2 + p_1^2 - 2M_p E_2 = 2M_p^2 - 2M_p E_2 < 0, \quad (3.6)$$

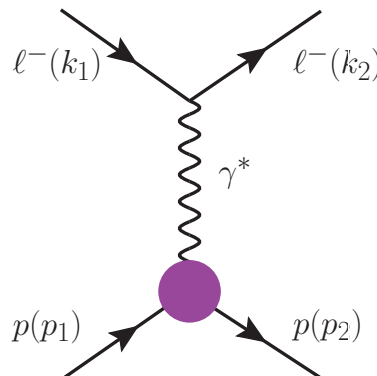


Figure 3.2: Feynman diagram of the lowest order contribution to the reaction amplitude of the elastic electron proton scattering process.

since $\vec{p}_1 = 0$ and $E_2 > M_p$ with E_2 as the energy of the recoil proton. $p_{1(2)}$ stands for the four momenta of the initial (final) state proton and $k_{1(2)}$ are the four momenta of the incident (scattered) lepton in the laboratory frame. The reaction amplitude (\mathcal{M}) is a complex scalar and can be obtained from the involved currents and the photon propagator as

$$-i\mathcal{M} = \frac{i}{q^2} j_\mu \mathcal{J}^\mu \quad (3.7)$$

with the leptonic current j_μ containing the four component Dirac spinors $u(k_i)$, ($i=1,2$) of the leptons:

$$j_\mu = j_\mu^{leptonic} = -ie\bar{u}(k_2)\gamma_\mu u(k_1). \quad (3.8)$$

The lepton-photon interaction vertex is described using Dirac gamma matrices $\gamma^\nu = \{\gamma^0, \gamma^1, \gamma^2, \gamma^3\}$, since the leptons are considered to be point-like particles without inner structure. The nucleon electromagnetic current is denoted as \mathcal{J}_μ and contains the hadronic vertex Γ^μ , which describes the interaction between the virtual photon and the proton. L. L. Foldy and G. Salzman [48, 49] came to the short expression of

$$\mathcal{J}^\mu = \mathcal{J}_{hadronic}^\mu = -ie\bar{N}(p_2)\Gamma^\mu(p_1, p_2)N(p_1), \quad (3.9)$$

where $N(p_1)$ ($N(p_2)$) is the Dirac spinor of the proton in the initial (final) state. The hadronic current transforms as a Lorentz four-vector and satisfies current conservation. Also, the Dirac equation must be fulfilled and the nucleons are on-shell (the relativistic energy-momentum relation is fulfilled). The hadronic vertex is written in terms of the Dirac and Pauli FF's, $F_1(Q^2)$ and $F_2(Q^2)$, as

$$\Gamma^\mu(p_1, p_2) = \left[\gamma^\mu F_1(Q^2) + \frac{i\sigma^{\mu\nu}q^\nu}{2M_p} F_2(Q^2) \right], \quad \sigma^{\mu\nu} = \frac{1}{2}[\gamma^\mu, \gamma^\nu]. \quad (3.10)$$

Due to the hermiticity of the hadronic current operator, it is implied that the SL FF's $F_1(Q^2)$ and $F_2(Q^2)$ are real functions of the four-momentum squared transfer q^2 . M_p stands for the proton mass. Using the given expressions for the leptonic and hadronic current, the amplitude of the process 3.4 can be written as

$$-i\mathcal{M} = \frac{-ig^{\mu\nu}}{q^2} [ie\bar{u}(k_2)\gamma^\nu u(k_1)] [-ie\bar{N}(p_2)\Gamma^\mu(p_2, p_1)N(p_1)], \quad (3.11)$$

where $g^{\mu\nu}$ is the metric tensor. The cross section for reaction 3.7 is proportional to the absolute square of the amplitude

$$d\sigma \sim |\mathcal{M}|^2 \quad (3.12)$$

The cross section is obtained (see Ref. [50]) as

$$d\sigma = \frac{\overline{|\mathcal{M}|^2}}{\mathcal{I}} (2\pi)^4 \delta^4(k_1 + p_1 - k_2 - p_2) d\Phi, \quad d\Phi = \frac{d^3\mathbf{k}_2}{(2\pi)^3 2\epsilon_2} \frac{d^3\mathbf{p}_2}{(2\pi)^3 2E_2} \quad (3.13)$$

where the bar denotes an averaging and summation over the polarizations of the initial respectively final state particles. Here, $d\Phi$ stands for the phase-space element for the final state particles and the flux of the colliding particles

$$\mathcal{I} = 4\sqrt{(k_1 p_1)^2 - m_e^2 M_p^2}. \quad (3.14)$$

The Dirac delta, $\delta^4(k_1 + p_1 - k_2 - p_2)$, insures four momentum conservation for each component. For elastic electron-proton scattering, the differential cross section in the laboratory frame [1] follows as

$$\left(\frac{d\sigma}{d\Omega}\right)_{lab} = \frac{\alpha^2}{4\epsilon_1^2} \cdot \frac{\cos^2 \frac{\theta_e}{2}}{\sin^4 \frac{\theta_e}{2}} \frac{\epsilon_1}{\epsilon_2} \times \left\{ F_1^2(Q^2) + \tau \left[F_2^2(Q^2) + 2 \left(F_1(Q^2) + F_2(Q^2) \right)^2 \tan^2 \frac{\theta_e}{2} \right] \right\}, \quad (3.15)$$

where $\alpha \approx 1/137$ is the fine structure constant, $\tau = Q^2/4M_p^2$ and $\theta_e \angle(\vec{k}_1, \vec{k}_2)$ is the scattering angle of the electron in laboratory system.

The Sachs form factors

By building linear combinations of the Dirac and Pauli form factors, the so-called *Sachs form factors*, $G_E(Q^2)$ and $G_M(Q^2)$, are obtained:

$$\begin{aligned} G_E(Q^2) &= F_1(Q^2) - \tau F_2(Q^2) \\ G_M(Q^2) &= F_1(Q^2) + F_2(Q^2) \end{aligned} \quad (3.16)$$

with $\tau = \frac{Q^2}{4M_p^2}$ and M_p as the proton's rest mass. The Sachs FF's are the commonly used since the electron-proton elastic cross section has a simple form when it is expressed through G_E and G_M . In the Breit frame, where the transferred energy of the virtual photon is zero, and in non-relativistic approach (for small values of q^2), an interpretation of the FF's can be made. Under these assumptions, the Sachs FF's are the Fourier transforms of the charge and magnetization spatial distributions inside the proton. In the non-relativistic limit ($Q^2 \rightarrow 0$), the rms mean radii of the charge and magnetization distributions can be extracted via

$$\begin{aligned} \langle r_E^2 \rangle &= -6\hbar^2 \left. \frac{dG_E(Q^2)}{dQ^2} \right|_{Q^2=0} \\ \langle r_M^2 \rangle &= -6\hbar^2 \left. \frac{dG_M(Q^2)}{dQ^2} \right|_{Q^2=0} \end{aligned} \quad (3.17)$$

The *Rosenbluth formula* takes a compact form when parameterized in terms of the Sachs form factors and takes into account both the spins of electron and the proton [1] :

$$\frac{d\sigma}{d\Omega} = \left(\frac{d\sigma}{d\Omega}\right)_{Mott} \times \left[\frac{G_E^2(Q^2) + \tau G_M^2(Q^2)}{1 + \tau} + 2\tau G_E^2(Q^2) \tan^2 \frac{\theta}{2} \right] \quad (3.18)$$

In the TL region, where the four-momentum squared transfer of the exchanged virtual photon is $q^2 > 0$, electromagnetic form factors can be studied via annihilation reactions of

$$\bar{p}p \rightarrow \ell^+ \ell^-, (\ell = e, \mu) \quad (3.19)$$

or via the time-reversed electron channel

$$e^+ e^- \rightarrow \bar{p}p. \quad (3.20)$$

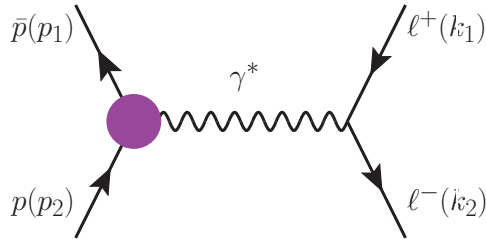


Figure 3.3: Lowest order contributing diagram to the reaction amplitude of the antiproton-proton annihilation into final states of $\ell^+\ell^-$.

In particular, muon pairs can be produced through the $\bar{p}p \rightarrow \mu^+\mu^-$ process. This process, which involves final state particles which are approximately 200 times heavier than the electrons, carries the same information on the FF's as the electron channel and constitutes the channel of interest in this work.

The lowest order contribution to the reaction amplitude is shown in Figure 3.3. The four momenta of the involved particles are written in parenthesis. Four-momentum conservation at the hadronic vertex implies that q^2 is equal to the $\bar{p}p$ center-of-mass energy squared s :

$$q^2 = (p_1 + p_2)^2 = s \quad (3.21)$$

and is positive, what can be shown as

$$s = (p_1 + p_2)^2 = 2M_p^2 + 2p_1p_2 = 2M_p(M_p + E_{beam}) > 4M_p^2. \quad (3.22)$$

The last two terms are obtained in the laboratory frame, where the target proton is at rest (see Figure 3.4 (a)), so that $\vec{p}_2 = \vec{0}$ and the $\bar{p}p$ production threshold is given as $4M_p^2$. In the TL region, the FF's possess a non-zero imaginary part, starting from the threshold $q^2 = 4m_\pi^2$. Below that threshold, they are also real [51].

In the Born approximation, assuming one photon exchange, the differential cross section of the annihilation of antiproton proton into a lepton pair can be written as a function of the Sachs FF's [52, 53] in the $\bar{p}p$ center-of mass system as

$$\frac{d\sigma}{d\cos\theta_{CM}} = \frac{\pi\alpha^2}{2s} \frac{\beta_\ell}{\beta_p} \left[\frac{1}{\tau} \left(1 - \beta_\ell^2 \cos^2\theta_{CM} \right) |G_E|^2 + \left(2 - \beta_\ell^2 + \beta_\ell^2 \cos^2\theta_{CM} \right) |G_M|^2 \right]. \quad (3.23)$$

Here, θ_{CM} stands for the polar angle of the negative charged lepton (with $\ell \equiv \ell^-$) measured with respect to the antiproton direction in the $\bar{p}p$ center of mass frame, which points into the positive z -direction (see Fig. 3.4 (b)), $\alpha \approx 1/137$ is the fine structure constant and the kinematic

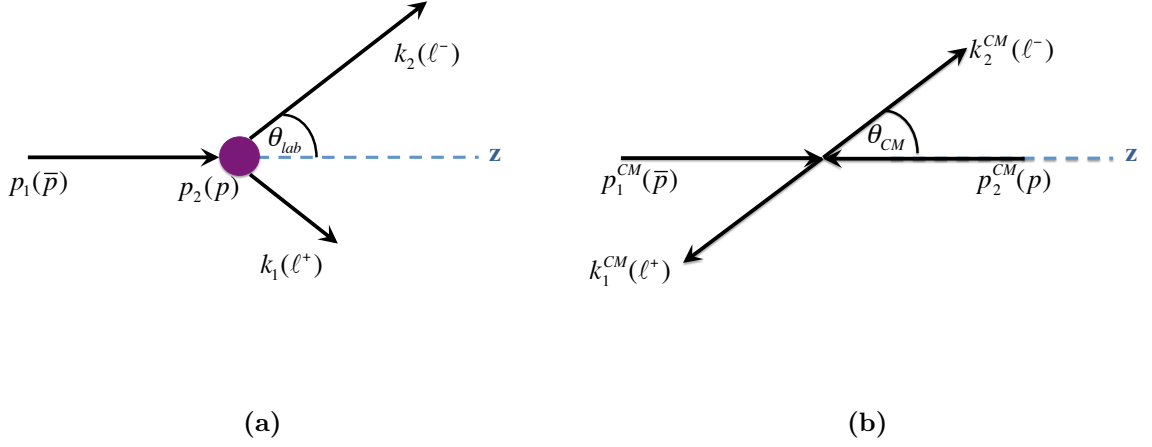


Figure 3.4: Kinematics of the annihilation reaction in (a) laboratory frame and (b) in the $\bar{p}p$ center-of-mass frame.

factors are

$$\beta_{\ell,p} = \sqrt{1 - 4M_{\ell,p}^2/s}$$

$$\tau = \frac{q^2}{4M_p^2},$$

where $\beta_{\ell,p}$ is the velocity of the lepton or the proton. Figure 3.5 shows the differential cross section of $\bar{p}p \rightarrow \mu^+\mu^-$ (in Born approximation) as a function of $\cos(\theta_{CM})$ for (a) $p_{beam} = 1.5$ GeV/c ($q^2 = 5.1$ (GeV/c)²) and (b) $p_{beam} = 3.3$ GeV/c ($q^2 = 8.2$ (GeV/c)²). These momenta are the minimal and maximal values of p_{beam} considered in this work.

Eq. 3.23 can be also written as [54]

$$\frac{d\sigma}{d\cos\theta_{CM}} = N_0 [1 + A_0 \cdot \cos^2\theta_{CM}], \quad (3.24)$$

with

$$N_0 = \frac{\pi\alpha^2}{2s} \frac{\beta_\ell}{\beta_p} \left[(2 - \beta_\ell^2) |G_M|^2 + \frac{1}{\tau} |G_E|^2 \right],$$

$$A_0 = \beta_\ell^2 \frac{1 - \frac{1}{\tau} R^2}{2 - \beta_\ell^2 + \frac{1}{\tau} R^2}, \quad R = \frac{|G_E|}{|G_M|}.$$

Integration of Eq. 3.24 over the solid angle in the range of $|\cos(\theta_{CM})| \leq \bar{a}$ leads to the integrated cross-section formula

$$\sigma_{int} = \int_{-\bar{a}}^{\bar{a}} \frac{d\sigma}{d\cos(\theta_{CM})} d\cos(\theta_{CM}) \quad (3.25)$$

$$= N_0 [2\bar{a} + A_0 \frac{2}{3} \bar{a}^3], \quad (3.26)$$

which q^2 -dependence for the case of $\bar{a} = 1.0$ is depicted in Fig. 3.6 for each lepton type. Here \bar{a} is the upper limit of the angular acceptance.

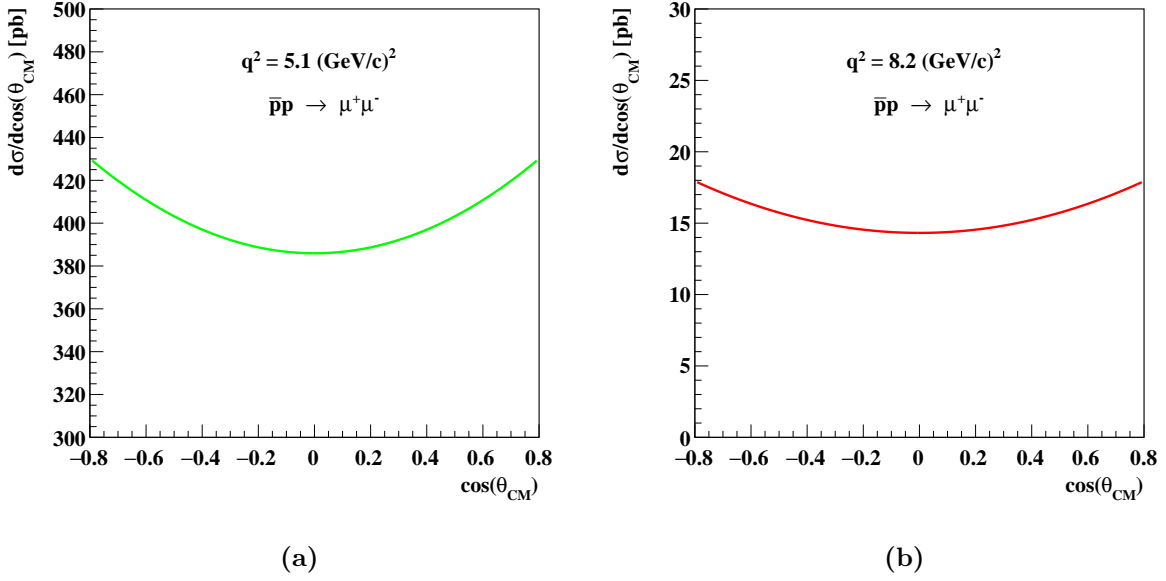


Figure 3.5: Differential cross section of the reaction $\bar{p}p \rightarrow \mu^+\mu^-$ (in Born approximation) as a function of $\cos(\theta_{CM})$ for (a) $p_{beam} = 1.5$ GeV/c ($q^2 = 5.1$ (GeV/c) 2) and (b) $p_{beam} = 3.3$ GeV/c ($q^2 = 8.2$ (GeV/c) 2). These momenta are the minimal and maximal values of p_{beam} considered in this work.

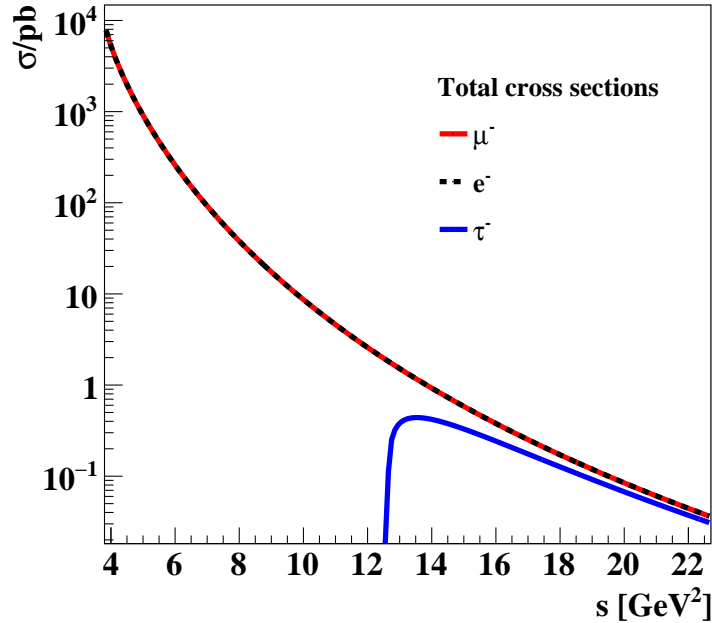


Figure 3.6: Integrated cross-section of the reaction $\bar{p}p \rightarrow \ell^+\ell^-$ (in Born approximation) as a function of the $\bar{p}p$ center-of-mass energy squared, s . It was integrated over the full angular range for the produced final states e^+e^- (black dashed line), $\mu^+\mu^-$ (red solid line) and $\tau^+\tau^-$ (blue solid line). The cross section curves of the $\bar{p}p \rightarrow e^+e^-$ and $\bar{p}p \rightarrow \mu^+\mu^-$ processes coincide within the solid line.

The measurement of the corresponding angular distribution of the negatively (positively) charged lepton at a fixed energy requires a high luminosity to collect enough statistics over the whole angular range. With the precise knowledge of the luminosity, an individual extraction of the time-like electromagnetic proton FF's, $|G_E|$ and $|G_M|$, is possible. Integration of Eq. 3.23 over the full angular range of $\cos\theta_{CM}$ (Eq. 3.26 with $\bar{a} = 1$) leads to the total cross section

$$\sigma(q^2) = \frac{2\pi\alpha^2}{q^2} \left(1 - \frac{\beta_\ell^2}{3}\right) \frac{\beta_\ell}{\beta_p} \left[|G_M|^2 + \frac{1}{2\tau}|G_E|^2\right], \quad (3.27)$$

depending on the four-momentum transfer squared q^2 . The effective proton FF, denoted as $|F_p|$, is a quantity, which can be determined also at low statistics experiments. It is a linear combination of the FF's, $|G_E|$ and $|G_M|$, and can be obtained by the measurement of the cross section of the annihilation reaction 3.19 via

$$\sigma(q^2) = \frac{4\pi\alpha^2}{q^2} \left(1 - \frac{\beta_\ell^2}{3}\right) \frac{\beta_\ell}{\beta_p} \left(1 + \frac{1}{2\tau}\right) |F_p|^2 \quad (3.28)$$

with the definition of the effective proton FF

$$|F_p| = \sqrt{\frac{2\tau|G_M|^2 + |G_E|^2}{2\tau + 1}} \quad (3.29)$$

Its dependence on the cross section is

$$|F_p| = \sqrt{\frac{\sigma(q^2)}{\frac{4\pi\alpha^2}{q^2} \left(1 - \frac{\beta_\ell^2}{3}\right) \frac{\beta_\ell}{\beta_p} \left(1 + \frac{1}{2\tau}\right)}} \quad (3.30)$$

The effective proton FF describes in particular the size of deviation from a point-like cross section

$$\sigma(q^2) = \sigma_{point}(q^2) |F_p|^2 \quad (3.31)$$

where $\sigma_{point}(q^2)$ is given by

$$\sigma_{point}(q^2) = \frac{4\pi\alpha^2}{q^2} \left(1 - \frac{\beta_\ell^2}{3}\right) \frac{\beta_\ell}{\beta_p} \left(1 + \frac{1}{2\tau}\right) \quad (3.32)$$

Under the assumption, that $|G_E| = |G_M|$ (which means $R = 1$), several experiments in the past could extract the effective proton FF based on rather scarce data. More details about the currently available experimental data on the proton effective FF will be given in section 3.4.

Asymptotic and boundary behavior

By using the Phragmen-Lindelöf theorem [55], which applies to analytical functions of complex variables, the asymptotic behavior of the proton FF's can be predicted as

$$\lim_{q^2 \rightarrow -\infty} F_i^{SL}(q^2) = \lim_{q^2 \rightarrow \infty} F_i^{TL}(q^2), \quad (i = 1, 2). \quad (3.33)$$

From that, it can be concluded, that the imaginary part of the TL form factor needs to vanish for increasing values of q^2 and the relative phase between the FF's therefore must be equal to zero or π .

Perturbative QCD predicts a strong decrease of the form factors for high values of Q^2 in the space-like region:

$$F_1(Q^2) \sim \frac{\alpha_s^2(Q^2)}{Q^4} \quad F_2(Q^2) \sim \frac{\alpha_s^2(Q^2)}{Q^6} \quad (3.34)$$

$$G_E^{SL}(Q^2) \sim G_M^{SL}(Q^2) \sim \frac{\alpha_s^2(Q^2)}{Q^4} \sim \frac{1}{Q^4 \ln^2(Q^2/\lambda^2)} \quad (3.35)$$

and in the time-like region

$$G_E^{TL}(q^2) \sim G_M^{TL}(q^2) \sim \frac{\alpha_s^2(q^2)}{q^4} \sim \frac{1}{q^4 \ln^2(q^2/\lambda^2)}, \quad (3.36)$$

where $\alpha_s(q^2)$ is the strong coupling constant and λ denotes the only free parameter in QCD. Its value is determined by the comparison of QCD predictions with experimental data.

The Dirac and Pauli FF's are normalized at $Q^2 = 0$ in terms of the charge respectively the magnetic moment (μ_p) of the proton:

$$F_1(0) = 1, \quad F_2(0) = \mu_p - 1, \quad (3.37)$$

where $\mu_p = 2.79284734462$ (normalized to the nuclear magneton μ_N). For $Q^2 \rightarrow 0$, the Sachs form factors of the nucleons converge to

$$\begin{aligned} G_E^p(0) &= 1 & G_E^n(0) &= 0 \\ G_M^p(0) &= 2.79 & G_M^n(0) &= -1.91 \end{aligned} \quad (3.38)$$

where the index p stands for proton and n stands for the neutron. In this limit, the form factors are equal to the charge and the magnetic moment of the target nucleon (normalized to the nuclear magneton μ_N).

At the proton mass threshold $q^2=4M_p^2$, the Sachs form factors take the same value $G_E(4M_p^2) = G_M(4M_p^2)$, which can be seen directly at Eq. 3.16 for $\tau = -1$.

The unphysical region

The region below the proton mass threshold $0 < q^2 < 4M_p^2$, which is denoted as the *unphysical region*, can not be directly accessed via the annihilation reactions given in Eq. 3.19. A possibility to access the unphysical region, is to study the annihilation process of $\bar{p}p \rightarrow \pi^0 e^+ e^-$, which is illustrated in Fig. 3.7. In this process, the neutral pion, which is emitted in addition to the virtual photon, lowers the q^2 , which therefore can take values below the threshold [56].

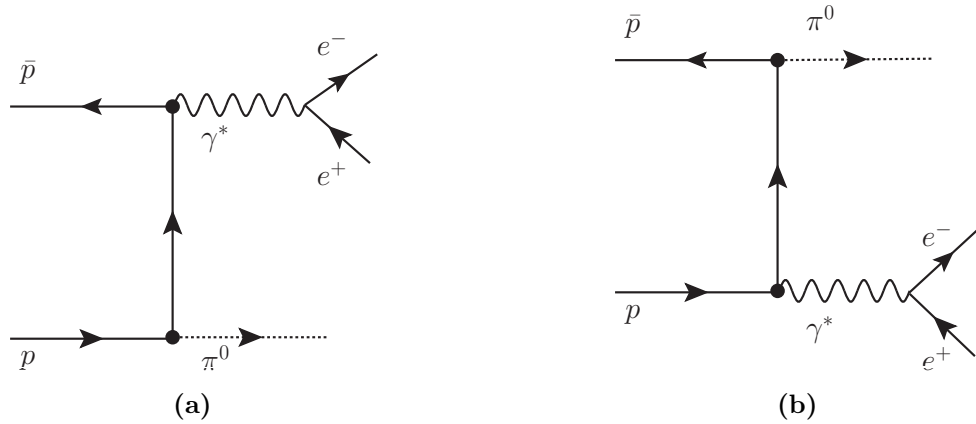


Figure 3.7: Feynman diagrams for the $\bar{p}p \rightarrow e^+e^-\pi^0$ process with the production of an e^+e^- pair from the antiproton (left) respectively from the proton (right).

3.3 Parameterizations of electromagnetic form factors

There are different theoretical approaches in QCD, aiming to describe electromagnetic form factors. Especially at low values of four-momentum squared transfer, only non-perturbative methods can be used for the calculations. Many of these models have been developed for the interpretation of data in the SL region. In the following, two models will be presented, which could be extended to the TL region.

3.3.1 Vector Meson Dominance (VMD)

In the VMD models, the interaction of the virtual photon with a hadronic system occurs through the exchange of intermediate vector mesons as $\omega(782)$, $\rho(770)$ and $\phi(1020)$. These vector mesons carry the same quantum numbers as the virtual photon ($J^{PC}=1^{--}$). They are the lightest hadrons with vector numbers and occur as resonances at the corresponding values of the four-momentum transfer squared q^2 in the cross section of the annihilation process $e^+e^- \rightarrow hadrons$.

In the crossed reaction, which is the elastic electron-nucleon scattering process of $e^-N \rightarrow e^-N$, the nucleon FF's are expected to be dominated by the lowest lying resonances from the TL region at low values of SL four-momentum squared transfer ($q^2 < 0$) [1]. A large number of VMD models for the description of F_1 and F_2 exist, which provide a parameterization of the nucleon FF's with only a few numbers of parameters as masses or coupling constants [51].

Iachello, Jackson and Landé [57] already developed a "semi-phenomenological" VMD-based model for the SL FF's in 1973, that predicted a linear decrease of the ratio $R = |G_E|/|G_M|$ for protons. This prediction is in agreement with modern measurements in 2010 based on the method of polarization transfer [58] (see section 3.4.1). In this model, the nucleon FF's are composed of an intrinsic FF, $g(Q^2)$, and a term, describing the interaction of the virtual photon with the nucleon cloud.

The Dirac and Pauli FF's for the nucleon are split into two terms, which take account of the isoscalar (with Isospin $I = 0, I_3=0$) as ω, ϕ, \dots) and the isovector (with Isospin ($I = 1, I_3 = (-1, 0, 1)$)) as ρ^-, ρ^0 and ρ^+ vector mesons ($J^P = 1^-$) separately:

$$F_i(Q^2) = F_i^S(Q^2) + F_i^V(Q^2), \quad (i = 1, 2). \quad (3.39)$$

The connection to the Sachs FF of the nucleons is

$$\begin{aligned} G_M^p &= (F_1^S + F_1^V) + (F_2^S + F_2^V), \\ G_E^p &= (F_1^S + F_1^V) - \tau(F_2^S + F_2^V), \\ G_M^n &= (F_1^S - F_1^V) + (F_2^S + F_2^V), \\ G_E^n &= (F_1^S - F_1^V) - \tau(F_2^S + F_2^V), \end{aligned} \quad (3.40)$$

with $\tau = Q^2/4M_p^2$. Here, $F_i^S(Q^2)$ denotes the isoscalar FF's and $F_i^V(Q^2)$ stands for the isovector FF's. They are parameterized as

$$F_1^S(Q^2) = \frac{1}{2}g(Q^2) \left[(1 - \beta_\omega - \beta_\phi) + \beta_\omega \frac{M_\omega^2}{M_\omega^2 + Q^2} + \beta_\phi \frac{M_\phi^2}{M_\phi^2 + Q^2} \right], \quad (3.41)$$

$$F_1^V(Q^2) = \frac{1}{2}g(Q^2) \left[(1 - \beta_\rho) + \beta_\rho \frac{M_\rho^2}{M_\rho^2 + Q^2} \right], \quad (3.42)$$

$$F_2^S(Q^2) = \frac{1}{2}g(Q^2) \left[(-0.120 - \alpha_\phi) \frac{M_\omega^2}{M_\omega^2 + Q^2} + \alpha_\phi \frac{M_\phi^2}{M_\phi^2 + Q^2} \right], \quad (3.43)$$

$$F_2^V(Q^2) = \frac{1}{2}g(Q^2) \left[3.706 \frac{M_\rho^2}{M_\rho^2 + Q^2} \right], \quad (3.44)$$

with the intrinsic form factor $g(Q^2) = 1/(1+\gamma Q^2)^2$, where the factor $\gamma = 0.25 \text{ GeV}^{-2}$ was obtained by fitting SL data [57]. In the same way, the coupling constants were determined to $\beta_\omega = 1.102$, $\beta_\phi = 0.112$, $\beta_\rho = 0.672$ and $\alpha_\phi = -0.052$. For the meson masses, the standard values were used: $M_\rho = 0.765 \text{ GeV}$, $M_\omega = 0.783 \text{ GeV}$, $M_\phi = 1.019 \text{ GeV}$. The width of the ρ was included by replacing the ρ meson term [59, 60] as

$$\left[\frac{M_\rho^2}{M_\rho^2 + Q^2} \right] \rightarrow \left[\frac{M_\rho^2 + 8\Gamma_\rho m_\pi / \pi}{M_\rho^2 + Q^2 + (4m_\pi^2 + Q^2)\Gamma_\rho \alpha(Q^2)/m_\pi} \right] \quad (3.45)$$

with the parameterization of [51]

$$\alpha(Q^2) = \frac{2}{\pi} \left[\frac{Q^2 + 4M_\pi^2}{Q^2} \right]^{1/2} \ln \left[\frac{\sqrt{Q^2 + 4M_\pi^2} + \sqrt{Q^2}}{2M_\pi} \right] \quad (3.46)$$

For the width of the ρ , $\Gamma_\rho = 0.112 \text{ GeV}$ was used whereas the widths of the ω and ϕ were neglected.

By replacing $Q^2 \rightarrow -q^2$, introducing a complex phase in the intrinsic FF $g(Q^2)$ and $\left[\frac{M_\rho^2}{M_\rho^2 + Q^2} \right]$, the VMD model was extended to the TL region by [61] as

$$g(q^2) = 1/(1 - \gamma e^{i\theta} q^2)^2 \quad (3.47)$$

and the ρ meson term, which also becomes complex as

$$\left[\frac{M_\rho^2}{M_\rho^2 - q^2} \right] \rightarrow \left[\frac{M_\rho^2 + 8\Gamma_\rho m_\pi / \pi}{M_\rho^2 - q^2 + (4M_\pi^2 - q^2)\Gamma_\rho \alpha(q^2)/m_\pi + i\Gamma_\rho 4m_\pi \beta(q^2)} \right] \quad (3.48)$$

$$\alpha(q^2) = \frac{2}{\pi} \left[\frac{q^2 - 4M_\pi^2}{q^2} \right]^{1/2} \ln \left[\frac{\sqrt{q^2 - 4M_\pi^2} + \sqrt{q^2}}{2M_\pi} \right], \quad (3.49)$$

with $\beta(q^2) = \left[\frac{\left[\frac{q^2}{4M_\pi^2} - 1 \right]^3}{\frac{q^2}{4M_\pi^2}} \right]^{1/2}$ for $q^2 \geq 4M_\pi^2$ and $\beta(q^2) = 0$ for $q^2 < 4M_\pi^2$. For the latter case, the phase vanishes since there are no hadronic channels existing below the pion production threshold.

Here, $\gamma = 0.25$ (GeV/c) $^{-2}$ as before, and the phase angle $\theta = 53^\circ$. Based on that extension to the TL domain, the parametrizations of the FF are given as

$$\begin{aligned} F_1^S(q^2) &= \frac{1}{2}g(q^2) \left[(1 - \beta_\omega - \beta_\phi) + \beta_\omega \frac{M_\omega^2}{M_\omega^2 + q^2} + \beta_\phi \frac{M_\phi^2}{M_\phi^2 + q^2} \right], \\ F_1^V(q^2) &= \frac{1}{2}g(q^2) \left[(1 - \beta_\rho) + \frac{\beta_\rho}{D_\rho(q^2)} \right], \\ F_2^S(q^2) &= \frac{1}{2}g(q^2) \left[(-0.120 - \alpha_\phi) \frac{M_\omega^2}{M_\omega^2 + q^2} + \alpha_\phi \frac{M_\phi^2}{M_\phi^2 + q^2} \right], \\ F_2^V(q^2) &= \frac{1}{2}g(q^2) \left[\frac{3.706}{D_\rho(q^2)} \right], \end{aligned} \quad (3.50)$$

where $D_\rho(q^2)$ stands for the propagator, taking into account the finite width of the ρ meson resonance

$$D_\rho(q^2) = \frac{M_\rho^2 - q^2 + (4M_\pi^2 - q^2)\Gamma_\rho \alpha(q^2)/M_\pi}{M_\rho^2 + 8\Gamma_\rho / \pi} \quad (3.51)$$

for $q^2 \geq 4M_\pi^2$ where $D_\rho(q^2)$ is normalized as $D_\rho(q^2 = 0) = 1$ [51, 61]. The list of equations 3.50 contain the contributions from the ω and ϕ vector mesons in the form of real poles.

3.3.2 Perturbative QCD parametrization

For high values of Q^2 in the SL regime, perturbative QCD (pQCD) predicts the asymptotic behavior of the FF's (see subsection 3.2). Due to the high Q^2 value carried by the virtual photon, the lowest order diagram for the photon-proton interaction in the electron-proton scattering process can be described as it is shown in Fig. 3.8 [62, 63, 51]. In this model, the virtual photon sees the proton made of three collinear constituent quarks. The transferred momentum is shared equally between them, which requires at least two gluons for the momentum exchange. Each gluon line is associated with a gluon propagator, which contributes with $1/Q^2$. Therefore in total 4 gluon vertices contribute to the reaction amplitude with a factor $(\alpha_s)^{1/2}$. The proton FF's, $G_E(Q^2)$ and $G_M(Q^2)$, are then proportional to α_s^2 :

$$G_E(Q^2) = G_M(Q^2) \sim \frac{\alpha_s^2(Q^2)}{Q^4} \quad (3.52)$$

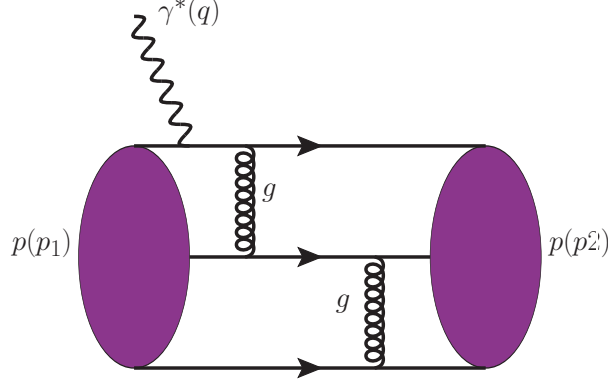


Figure 3.8: Lowest order diagram in pQCD for the photon-proton interaction vertex in electron-proton scattering.

where $\alpha_s(Q^2)$ was obtained for the SL regime as

$$\alpha_s^2(Q^2) = \frac{g_s^2(Q^2)}{4\pi} \sim \frac{1}{\beta_0 \ln(Q^2/\lambda_{QCD}^2)}, \quad \beta_0 = 11 - \frac{2}{3}n_f, \quad Q^2 > \lambda^2, \quad (3.53)$$

with the QCD scale parameter λ_{QCD} and the number of quark flavors $n_f = 3$. The analytical extension of the pQCD parameterization to the TL regime is done by the following replacement

$$Q^2 \rightarrow -q^2, \quad \ln(Q^2/\lambda^2) \rightarrow \ln(q^2/\lambda_{QCD}^2) - i\pi, \quad q^2 > \lambda^2. \quad (3.54)$$

The modulus of the proton FF's can be written as

$$|G_{E,M}| = \frac{C}{q^4 (\ln^2(q^2/\lambda_{QCD}^2) + \pi^2)} \quad (3.55)$$

with the coefficient C and the QCD scale parameter λ_{QCD} , which can be determined by fitting experimental data in the TL regime for $|G_E| = |G_M|$. The values were suggested by [64] to be $C = 89.45 \text{ (GeV/c)}^4$ and $\lambda_{QCD} = 0.3 \text{ GeV/c}$. The pQCD parameterization assumes a relative phase between the proton FF's to be zero. This assumption can be tested by experiments measuring polarization observables as it is planned at the future $\bar{\text{P}}\text{ANDA}$ Experiment using a transversely polarized hydrogen target.

3.3.3 Form factor parameterization based on a modified dipole behavior

The existing data on $G_M(Q^2)$ in the SL region show a dipole behavior up to a value of $Q^2 \simeq 31 \text{ (GeV/c)}^2$ and can be well described by

$$\frac{G_M(Q^2)}{\mu_p} = \frac{1}{[1 + (Q^2/m_d^2)]^2}, \quad m_d^2 = 0.71 \text{ (GeV/c)}^2, \quad Q^2 = -q^2. \quad (3.56)$$

In the TL region, the $|G_M|$ can be parameterized in terms of q^2 in a similar way. Ref. [54] suggests a modified dipole behavior of $|G_M|$, which was obtained by fitting existing TL data:

$$|G_M| = \mathcal{A} \left[1 + q^2 / \left(0.71 \text{ [GeV/c}^2] \right) \right]^{-2} \left[1 + q^2/m_a^2 \right]^{-1} \quad (3.57)$$

with q^2 expressed in $(\text{GeV}/c)^2$. Here, the numerator $\mathcal{A} = 22.5$ is a constant extracted by fitting time-like data. The parameter $m_a^2 = (3.6 \pm 0.9) (\text{GeV}/c)^2$ characterizes the deviation from the dipole q^2 -dependence.

This parameterization is used for the evaluation of the cross section and of the number of expected counts in this work (see section 5.3) at different values between $5.1 (\text{GeV}/c)^2 \leq q^2 \leq 8.2 (\text{GeV}/c)^2$, together with the assumption, that the ratio of the FF's, $R = |G_E|/|G_M|$ is equal to 1. This assumption is strictly valid only at the $\bar{p}p$ threshold, but can be also assumed for any other value of q^2 since there is no theoretical argument existing against it. More details can be found in Ref. [54].

3.3.4 Comparison

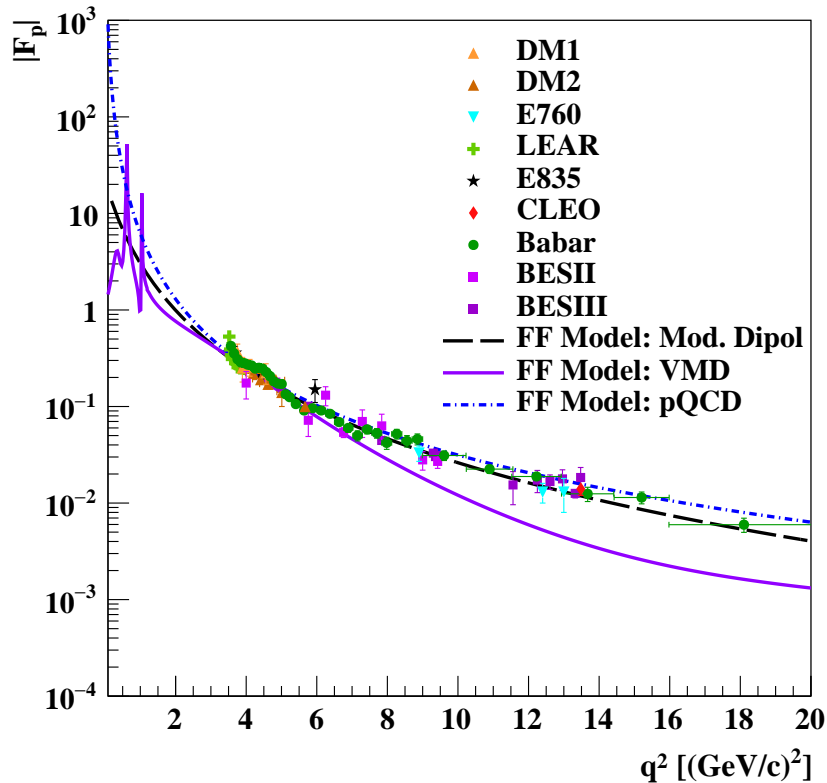


Figure 3.9: The effective form factor of the proton in the time-like region, $|F_p|$, as a function of q^2 determined for different form factor parameterizations. Shown are the curves based on the VMD model (violet plain line), which shows structures at the meson poles in the unphysical region, the pQCD inspired model (blue dashdotted line) and the modified dipole parameterization based on Eq. 3.57 (black dashed line). The last one is used in these feasibility studies. Also shown are experimental data, that were taken under the assumption that $|G_E|=|G_M|$ at E835 [65, 66], FENICE [67], PS170 [68], E760 [69], DM1 [70], DM2 [71, 72], BES [73], BESIII [74], CLEO [75] and BABAR [76, 77].

Figure 3.9 illustrates the q^2 -dependence of the effective form factor determined for the differ-

ent form factor parametrizations, which were presented in this section: the VMD model (violet plain line), the pQCD inspired model (blue dashdotted line) and the modified dipole parameterization based on Eq. 3.57 (black dashed line). The latter one is used in this work. Experimental data from E835 [65, 66], FENICE [67], PS170 [68], E760 [69], DM1 [70], DM2 [71, 72], BES [73], BESIII [74], CLEO [75] and BABAR [76, 77] are shown as well.

A comparison between the parametrizations and the data shows, that the data are in good agreement with the "pQCD-inspired" parameterization and the modified dipole parameterization, which is used in this work. Above $q^2 \approx 8 \text{ (GeV}/c)^2$, a discrepancy appears between the data and the VMD parameterization. The VMD parameterization shows a different trend to lower values of $|F_p|$, what is caused by the structures at the meson poles.

Detailed information on the available experimental data of the space-like and time-like electromagnetic form factors will be given in the following section.

3.4 Experimental measurements of electromagnetic proton form factors

3.4.1 Space-like electromagnetic form factors data

In the space-like domain, two methods can be used to extract the space-like proton FF's: the Rosenbluth and the polarization transfer method. Both methods are based on the assumption that the elastic electron-proton scattering reaction takes place under the exchange of a single virtual photon.

Rosenbluth separation method

The original and unique method for the separate extraction of the values for G_E^2 and G_M^2 until the 1990's was the Rosenbluth separation method. The idea behind this technique is the measurement of the elastic electron-nucleon scattering cross section at a fixed Q^2 at different angles of the scattered electron. This is can be done by changing both the beam energy and the scattering angle of the electron over the whole accessible range in the experiment. A newer expression of Eq. 3.18 is

$$\frac{d\sigma}{d\Omega} = \left(\frac{d\sigma}{d\Omega} \right)_{Mott} \times \left[\frac{G_E^2(Q^2) + \frac{\tau}{\epsilon} G_M^2(Q^2)}{1 + \tau} \right] \quad (3.58)$$

with the virtual photon polarization $\epsilon = \left[1 + 2(1 + \tau) \tan^2 \frac{\theta_e}{2} \right]^{-1}$ and $\tau = Q^2/(4M_p^2)$. For the individual extraction of the FF's, the reduced cross section

$$\left(\frac{d\sigma}{d\Omega} \right)_{reduced} = \frac{\epsilon(1 + \tau)}{\tau} \left(\frac{d\sigma}{d\Omega} \right)_{exp} / \left(\frac{d\sigma}{d\Omega} \right)_{Mott} = G_M^2 + \frac{\epsilon}{\tau} G_E^2 \quad (3.59)$$

is used, where $\left(\frac{d\sigma}{d\Omega} \right)_{exp}$ stands for the experimentally measured cross section and $\left(\frac{d\sigma}{d\Omega} \right)_{Mott}$ as it was defined in Eq. 3.2. The reduced cross section depends linearly on ϵ .

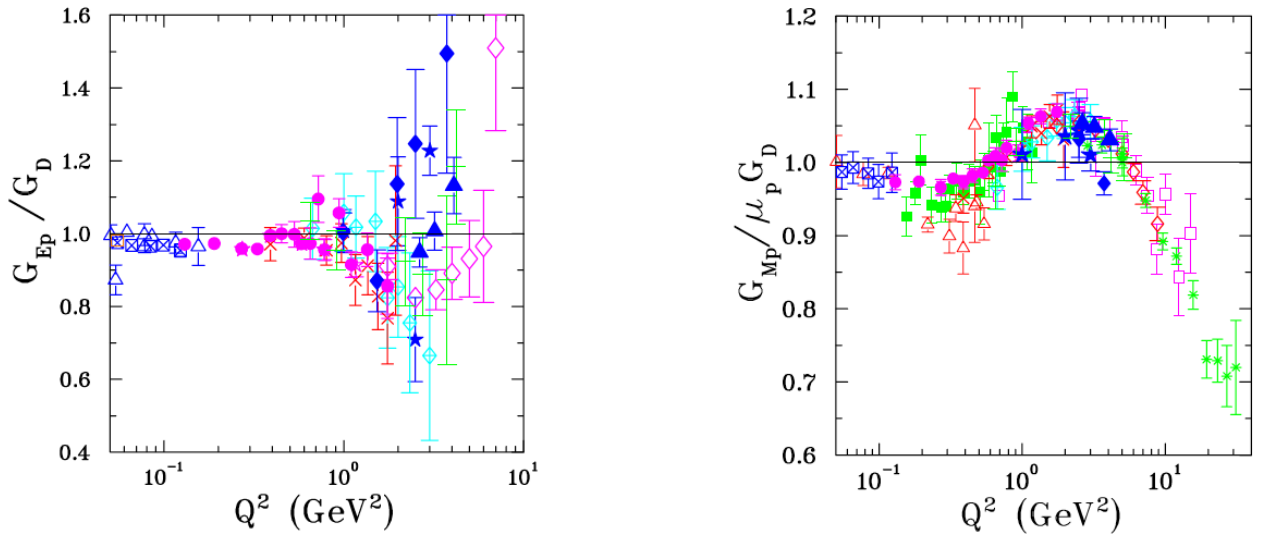


Figure 3.10: The SL electric (left) and magnetic (right) FF of the proton depending on Q^2 [GeV/c]², being normalized to the dipole function $G_d(Q^2)$ (see Ref. [1] and references therein). The data shown were obtained with the Rosenbluth method.

The measurement is performed at different values of ϵ at a fixed value of Q^2 , which makes it possible to extract the slope $(1/\tau) \cdot G_E^2$ and the intercept G_M^2 independently. Figure 3.10 illustrates the extracted values of the FF's based on this technique with data [78, 79]. The Rosenbluth method leads to larger uncertainties on the extracted value of G_E for higher values of Q^2 due to the factor τ^{-1} in the term of the electric contribution in Eq. 3.59. The FF's $G_{M,E}(Q^2)$ can be described according to the dipole behavior for values up to $\simeq 8$ (GeV/c)² [1]:

$$G_M(Q^2) = \mu_p G_E(Q^2) = \mu_p G_d(Q^2), \quad G_d(Q^2) = \left(1 + \frac{Q^2}{0.71}\right)^{-2} \quad (3.60)$$

Polarization Transfer Method

At the beginning of the 21th century, the technical possibilities for the production of polarized electron beams of high intensity allowed the application of a new method for the extraction of proton FF's. This method, denoted as *polarization method*, was originally suggested by Akhiezer and Rekalov in 1968 [80]. The experimental measurement was performed by the GEp collaboration [5, 6, 7, 58], using a longitudinally polarized electron beam together with an unpolarized proton target. By measuring the longitudinal (P_l) and the transverse (P_t) polarization components of the final state proton (in one-photon-exchange approximation), the FF's ratio could be determined by

$$R = \frac{G_E}{G_M} = -\frac{P_t}{P_l} \cdot \frac{E_e + E'_e}{2M_p} \cdot \tan \frac{\theta'_e}{2} \quad (3.61)$$

with the energy E_e (E'_e) of the initial (final) state electron in laboratory frame and θ'_e as the angle in lab frame between the electron beam direction and the scattered electron momentum. In contrast to the Rosenbluth separation method, the polarization transfer method only needs a single measurement at a fixed value of Q^2 for the extraction of R , if the polarimeter is able to

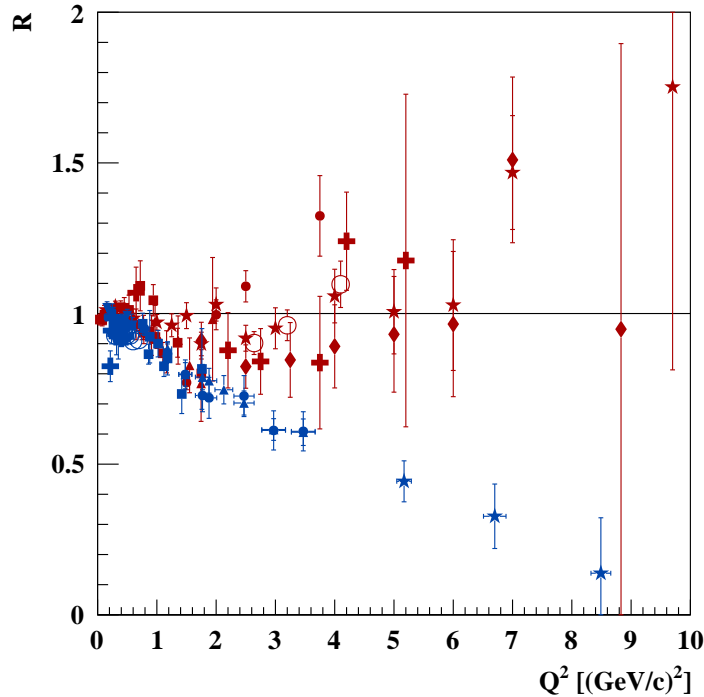


Figure 3.11: Available experimental data on the proton FF's ratio $R = \mu_p G_E / G_M$ obtained with the Rosenbluth [82, 78, 83, 84] (red data points) and polarization method [5, 6, 7, 58, 81] (blue data points) at different values of Q^2 . The data obtained with both methods show clearly a different trend.

measure both polarization components at the same time. This means a reduction of systematic errors in terms of changes of the angle and the beam energy. Also the measurement of the beam polarization and the analyzing power of the polarimeter is not needed for the extraction of R .

Figure 3.11 shows the obtained results from both the polarization [5, 6, 7, 58, 81] and the Rosenbluth method [82, 78, 83, 84]. A strong discrepancy between the results obtained using the polarization transfer and the Rosenbluth separation methods was found, starting from $Q^2 = 3 \text{ (GeV/c)}^2$ and increasing as a function of Q^2 . While the results obtained with the Rosenbluth separation method are approximately consistent with unity over a large kinematical range of Q^2 , the experiments which use the polarization transfer method suggest a linear decrease of the ratio as a function of Q^2 . A widely accepted hypothesis for a possible explanation is the contribution of hard two-photon exchange, which is neglected in the standard radiative corrections applied to the Rosenbluth separation data [85, 86, 87].

Further experimental and theoretical efforts were triggered by this surprising result. In 2011, Ref. [88] determined the two-photon exchange amplitudes at a value around $Q^2 = 2.5 \text{ (GeV/c)}^2$ based on the available cross section and polarization data for elastic electron-proton scattering reactions. A precision measurement of the positron-proton to electron-proton elastic cross section ratio $R_{2\gamma}$ at low values between $0.6 \leq Q^2 \leq 2.2 \text{ (GeV/c)}^2$ was performed in 2012 by the

OLYMPUS experiment at DESY/Hamburg. The ratio $R_{2\gamma}$ is a direct measure of the contribution of hard two-photon exchange to the elastic cross section [8]. One further advantage of this method is that systematic uncertainties are cancelled in the cross section ratio. The results of OLYMPUS are smaller than theoretical predictions of the hadronic two-photon exchange, however are in consistency with phenomenological models. Further measurements at higher values of Q^2 are needed, where the discrepancy increases.

3.4.2 Time-like electromagnetic form factors data

Due to the low luminosity available at collider experiments in the past, only scarce data could be collected in the time-like region, allowing the determination of the FF ratio $R = |G_E|/|G_M|$, the integrated cross section of the signal reaction and the effective FF of the proton. Table 3.1 shows a summary of the existing data sets from $\bar{p}p$ annihilation experiments for the extraction of time-like nucleon FF's. Also the crossed channel $e^+e^- \rightarrow \bar{p}p$ reaction was studied by several

Exp.	Reaction	Year	Scan points	Range [GeV]	Events	Ref.
M.S.T. Coll.	$\bar{p}p \rightarrow e^+e^-$	1976/77	2	near threshold	34	[89]
PS170	$\bar{p}p \rightarrow e^+e^-$	1991	4	near threshold	~ 2000	[90]
PS170	$\bar{p}p \rightarrow e^+e^-$	1991	4	1.94 - 2.05	~ 1300	[91]
PS170	$\bar{p}p \rightarrow e^+e^-$	1994	9	threshold - 2.05	~ 2000	[68]
E760	$\bar{p}p \rightarrow e^+e^-$	1993	3	3.0 - 3.6	29	[69]
E835	$\bar{p}p \rightarrow e^+e^-$	1999	4	3.0 - 3.8	144	[66]
E835	$\bar{p}p \rightarrow e^+e^-$	2003	2	3.4 - 3.5	66	[65]

Table 3.1: Overview of experimental results from $\bar{p}p$ annihilation experiments for extraction of the time-like nucleon FF's [92].

experiments, which are summarized in Table 3.2. In the following, a brief overview will be given of the four experiments, which extracted the FF ratio R :

- The PS170 experiment at the Low Energy Anti-Proton Ring (LEAR) [68] used reactions of $\bar{p}p \rightarrow e^+e^-$ for the determination of R .
- Furthermore, the BABAR experiment (SLAC) collected data of low statistics using initial state radiation (ISR) processes of $e^+e^- \rightarrow \bar{p}p\gamma$ over a wide kinematic range [97, 76, 77]. BABAR collected a total luminosity of 469 pb^{-1} at the center-of-mass energy of $\sqrt{s} = 10.58 \text{ GeV}/c$. Under the requirement, that the ISR photon was detected, in total 7876 events of $e^+e^- \rightarrow \bar{p}p$ were found up to $\sqrt{s} = 4.5 \text{ GeV}/c$, while the ratio R could be extracted up to $\sqrt{s} = 3.0 \text{ GeV}/c$. A comparison of the extracted values on R by BABAR and PS170 shows that the results follow different trends in the lower q^2 range. While the data of the PS170 experiment are compatible with the assumption of $R = 1$, the BABAR data show a relatively large deviation from $R = 1$ at intermediate energies.
- More recently, the BESIII experiment [74] performed measurements at different center-of-mass energies between 2.2324 GeV and 3.6710 GeV in reactions of $e^+e^- \rightarrow \bar{p}p$. The results

Exp.	Reaction	Year	Scan points	Range [GeV]	\mathcal{L} [pb ⁻¹]	Events	Ref.
Adone73	$e^+e^- \rightarrow \bar{p}p$	1973	1	2.1	0.2	25	[93]
FENICE	$e^+e^- \rightarrow \bar{p}p$	1993	1	2.1	0.1	28	[94]
FENICE	$e^+e^- \rightarrow \bar{p}p$	1994	4	1.9 - 2.4	0.3	70	[95]
FENICE	$e^+e^- \rightarrow \bar{p}p$	1998	1	2.1	< 0.1	7	[67]
DM1	$e^+e^- \rightarrow \bar{p}p$	1979	4	1.925 - 2.180	0.4	~ 70	[70]
DM2	$e^+e^- \rightarrow \bar{p}p$	1983	6	1.975 - 2.25	0.5	~ 100	[71]
DM2	$e^+e^- \rightarrow \bar{p}p$	1990	1	2.4	0.2	7	[72]
CLEO	$e^+e^- \rightarrow \bar{p}p$	2005	1	3.671	21	16	[75]
BESII	$e^+e^- \rightarrow \bar{p}p$	2005	10	2.0 - 3.07	5	80	[73]
BESIII	$e^+e^- \rightarrow \bar{p}p$	2015	12	2.2324 - 3.6710	159.6	1368	[74]
CMD-3	$e^+e^- \rightarrow \bar{p}p$	2015	12	1.89 - 2.00	6.976	2862	[96]

Table 3.2: Overview of experimental results from e^+e^- annihilation experiments for extraction of the time-like nucleon FF's [92].

taken at BESIII, are consistent with the BABAR results with large uncertainties.

- The CMD-3 detector, which is located at the electron-positron collider VEPP-2000 collected a large luminosity for \sqrt{s} below 2.0 GeV/ c . While the total cross section was measured close to the threshold, the combined data from the interval between 1.92 GeV and 2.00 GeV allowed an extraction of R with a relative statistical uncertainty of 15%.

The time-like data taken by the E835 experiment [98] at Fermi Lab ($\bar{p}p \rightarrow e^+e^-$), the data taken at FENICE and the DM1 experiment were used by R. Baldini et al. for the determination of the upper and lower limits of R [99]. The currently available world data on R are summarized in Figure 3.12.

The first measurement of the integrated cross section of the reaction $e^+e^- \rightarrow \bar{p}p$ and the extraction of the effective FF of the proton, denoted as $|F_p|$, was performed in 1973 at the Adone Storage Ring (Frascati). Since then, data have been collected at several experiments and extracted $|F_p|$, as for example:

- the DM1 and DM2 detectors (Orsay) within the range of 1.925 GeV to 2.400 GeV from 1979 to 1990. With a time-integrated luminosity of $\mathcal{L} = 1.1$ pb⁻¹, $|F_p|$ could be measured based on 170 events of $\bar{p}p$ [100, 71, 101].
- FENICE at Adone measured $|F_p|$ from $\sqrt{s} = 1.9$ GeV up to 2.4 GeV [67]
- CLEO at the Cornell Electron Storage Ring measured the cross section at 3.672 GeV and extracted $|F_p|$ based on a time-integrated luminosity of $\mathcal{L} = 21$ pb⁻¹.
- the BESII detector at the BEPC collider gathered $\mathcal{L} = 5$ pb⁻¹ for the $e^+e^- \rightarrow \bar{p}p$ process from $\sqrt{s} = 2.00$ GeV up to 3.07 GeV and measured the cross section and $|F_p|$ [73].

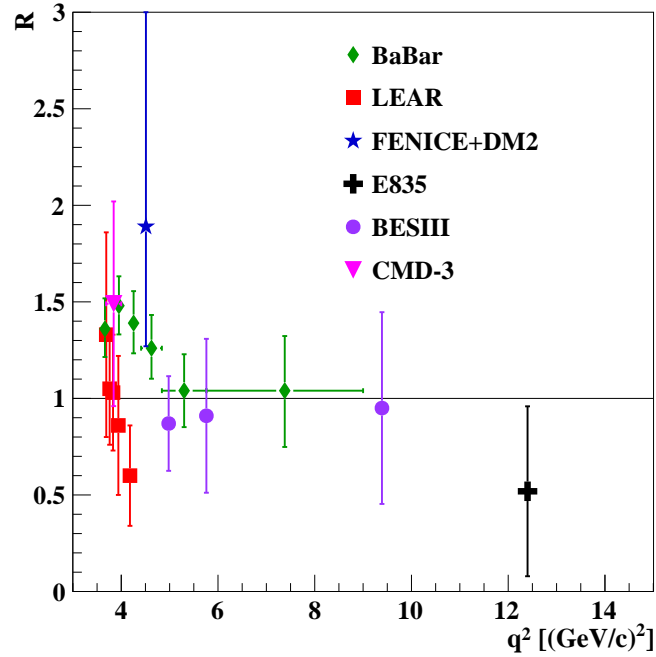


Figure 3.12: Available data on the proton FF's ratio $R = |G_E|/|G_M|$ depending on q^2 , from Ref. [77] (diamonds), from Ref. [68] (squares), from Ref. [99] (massive cross) and (star), from Ref. [74] (dots) and from Ref. [96] (down triangle). The data taken at BABAR and LEAR show clearly different trends.

- BESIII (after upgrading both BESII and the BEPC) collected data between 2.2324 GeV and 3.6710 GeV with $\mathcal{L} = 160 \text{ pb}^{-1}$ for the extraction of R , $|F_p|$ and the cross section of $e^+e^- \rightarrow \bar{p}p$ [74].

The currently available world data on the effective proton FF, $|F_p|$, are summarized in Fig. 3.13. Recently, periodic interference structures in the time-like proton form factor were discovered based on precise data taken by the BaBar experiment [11]. If the time-like form factor data are plotted against the three-momentum of this relative motion of the final state antiproton-proton, a periodic oscillation pattern occurs in the near-threshold region in form of a sinusoidal modulation. A possible explanation for this behavior are rescattering processes at a relative distance of 0.7 - 1.5 fm between the centers of the formed hadrons, which could cause a non-zero imaginary part in the time-like proton form factor. More details can be found in Ref. [11, 12]. Recently, this phenomenon could be confirmed by data taken at BESIII using initial state radiation processes of $e^+e^- \rightarrow \bar{p}p\gamma$. By determining the effective form factor, this phenomenon could be confirmed in 2018 at BESIII and was presented for the first time at the 668. WE-Heraeus-Seminar on Baryon Form Factors (Bad Honnef/Germany) [102].

3.5 Proton Form Factor Studies for the PANDA experiment

The moduli of the time-like electromagnetic proton FF's, $|G_E|$ and $|G_M|$, can be accessed experimentally in $\bar{p}p \rightarrow \ell^+\ell^-$ ($\ell = e, \mu$) processes with unpolarized beam and target. The

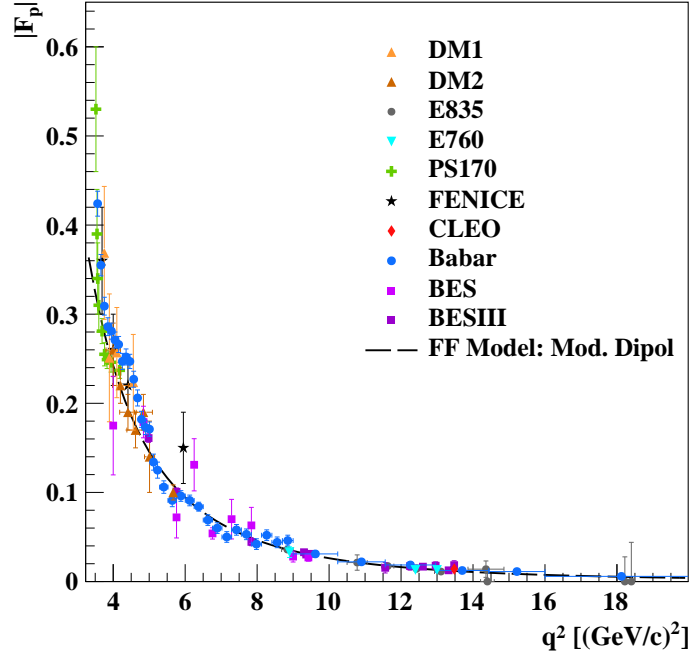


Figure 3.13: The effective time-like FF of the proton, $|F_p|$, at different values of q^2 , determined by using cross sections of reactions of $e^+e^- \rightarrow \bar{p}p$ respectively $\bar{p}p \rightarrow e^+e^-$. The data were taken under the assumption that $|G_E|=|G_M|$ at E835 [65, 66], FENICE [67], PS170 [68], E760 [69], DM1 [70], DM2 [71, 72], BES [73], BESIII [74], CLEO [75] and BABAR [76, 77]. Also shown is the parameterization based on Eq. 3.57 (black dashed line), which is used in this feasibility study.

expected statistical precision for the measurement of time-like electromagnetic proton form factors with \bar{P} ANDA was investigated in the framework of the PandaRoot software for detector simulation and event reconstruction for both muon and electron channels. The possibility to achieve an optimal signal-background separation and sufficient background suppression of all relevant background channels was investigated. At the same time, the studies aim to keep the highest possible signal reconstruction efficiency. Different methods have been used to generate and analyze the processes of interest. In the following, a brief summary of the feasibility studies on the two different channels will be given.

3.5.1 Measurement of time-like proton form factors with $\bar{p}p \rightarrow e^+e^-$

The feasibility to measure the time-like FF of the proton with the $\bar{p}p \rightarrow e^+e^-$ process at the future \bar{P} ANDA experiment was investigated in two independent simulation studies [16], which are based on the PandaRoot software framework. Dedicated event generators have been used for the full simulation of the $\bar{p}p \rightarrow e^+e^-$ reaction at different center-of-mass energies within the range of $(5.4 \leq q^2 \leq 13.9)$ $(\text{GeV}/c)^2$.

The most challenging background source is the $\bar{p}p \rightarrow \pi^+\pi^-$ process, with an average cross section ratio of $\sigma(\bar{p}p \rightarrow \pi^+\pi^-)/\sigma(\bar{p}p \rightarrow e^+e^-) \approx 10^5 - 10^6$ depending on q^2 . For this background

process, 10^8 background events were generated at each considered value of q^2 in order to estimate the achievable background suppression factors. Different detector observables and particle identification algorithms for several subdetectors as the $\overline{\text{PANDA}}$ Electromagnetic Calorimeter, the Straw Tube Tracker, the Micro Vertex Detector and Cherenkov Detectors have been utilized to achieve a sufficient signal-background separation.

Ref. [16] presents two independent simulation studies, which are denoted as Method I and Method II. The difference between those methods are a) the number of generated events, b) the selection criteria, c) the angular distribution model, which were used as input for the event generator of the signal and d) the fit functions, which were used for the separate extraction of $|G_E|$ and $|G_M|$ from the reconstructed and signal efficiency corrected angular distribution of the final state electron (positron). In both studies, $R = |G_E|/|G_M| = 1$ and a time-integrated luminosity of 2 fb^{-1} for each considered value of beam momentum were assumed. Total signal efficiencies range between 40% and 50% and - at the same time - background suppression factors of the order of 10^{-8} were achieved in these studies. The expected signal pollution could be reduced to values of a few percent, depending on q^2 .

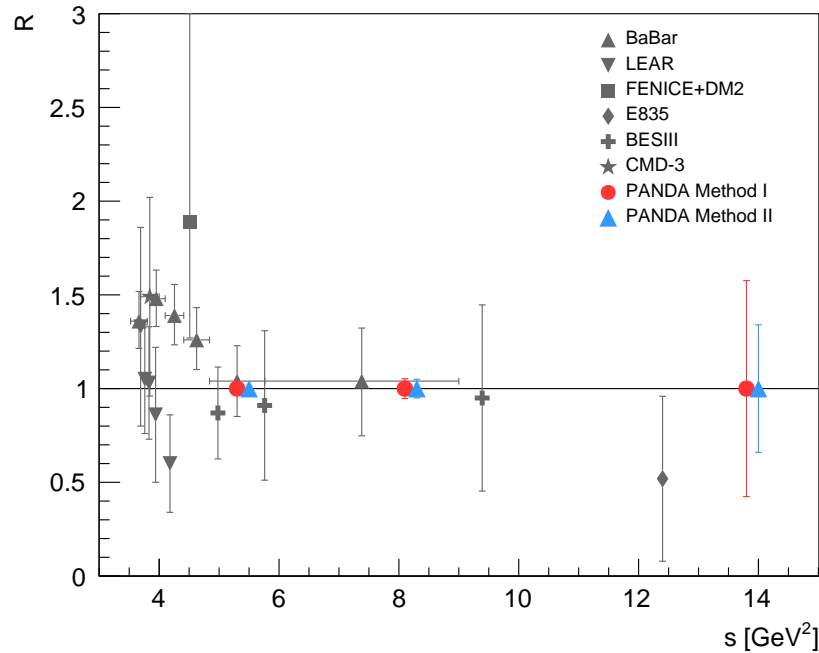


Figure 3.14: Expected precisions of the determination of the proton form factor ratio from the feasibility studies for $\overline{\text{PANDA}}$ obtained by method I (red circles) and method II (blue up triangles) for the $\bar{p}p \rightarrow e^+e^-$ process at different values of q^2 [16]. The existing world data on the time-like ratio $R = |G_E|/|G_M|$ are also shown, from Ref. [68] (triangles down), from Ref. [77] (up triangles), from Ref. [99] (diamond) and (square), from Ref. [96] (star) and from Ref. [74] (massive crosses). The expected precision of R at PANDA is much better than the currently available data, in particular when going to lower values of q^2 , where the cross section for the signal process increases.

Figure 3.14 shows the obtained results of the studies from Ref. [16] together with the currently existing world data. More data are soon expected to be published by BESIII.

Additionally, possible systematical uncertainties have been investigated, showing that the background misidentification and luminosity uncertainty dominate the total uncertainty at lower beam momenta. At higher values of beam momenta, the total uncertainty is dominated by the statistical fluctuations due to the smaller cross section of the $\bar{p}p \rightarrow e^+e^-$ process. The total (statistical and systematic) relative uncertainty is expected to range between 3.3% and 57.0% for the ratio R of the TL proton FF's. The extraction of the individual values of $|G_E|$ and $|G_M|$ is expected to be feasible for values of q^2 up to 13.9 (GeV/c)^2 with a very high total precision between 2.2% up to 48.0% and 3.5% up to 9.7%, respectively. In comparison to the available world data on R , the expected precision at PANDA is much better, in particular going to lower values of q^2 , where the signal cross section increases. More details can be found in Ref. [16].

3.5.2 Measurement of time-like proton form factors with $\bar{p}p \rightarrow \mu^+\mu^-$

This work aims to determine the expected precision, with which the moduli of the time-like electromagnetic proton form factors (FF's), $|G_E|$ and $|G_M|$, and their ratio $R = |G_E|/|G_M|$ can be extracted at the future $\bar{\text{P}}\text{ANDA}$ experiment [13] with reactions of the type

$$\bar{p}p \rightarrow \mu^+\mu^-. \quad (3.62)$$

Due to the high luminosity at $\bar{\text{P}}\text{ANDA}$, the simultaneous extraction of the TL FF's from the measured angular distribution of the produced μ^- (μ^+) will be possible. A time-integrated luminosity $\mathcal{L} = 2 \text{ fb}^{-1}$ is assumed in this work. This value of \mathcal{L} corresponds to 4 months of pure data taking time at the design peak luminosity of $2 \cdot 10^{32} \text{ cm}^{-2} \text{ s}^{-1}$ (at ideal conditions of 100% efficiency and full detector acceptance).

The same information on the TL proton FF's, which will be received by measuring the $\bar{p}p \rightarrow e^+e^-$ channel (electron channel), is contained in the muon channel (and also the tau channel). Therefore, they are independent signal channels and can serve as a consistency check for the FF data obtained from the electron channel and - in addition - gives the opportunity, to test lepton universality in the time-like region. Due to the heavy tau lepton rest mass ($\approx 1.776 \text{ GeV}/c^2$), the total cross section of this channel is much smaller than in the case of the two much lighter leptons, electron and muon. Therefore the tau channel is not considered as a possible signal channel at $\bar{\text{P}}\text{ANDA}$.

It will be the first time that muons in the final state will be used to measure the time-like proton FF's. One advantage of measuring $\bar{p}p \rightarrow \mu^+\mu^-$ is that radiative corrections due to final state radiation are expected to be smaller in comparison to the electron channel due to the heavy muon mass. Therefore, the comparison of the results from both signal channels using electron and muon, allows to study the radiative corrections, which will be taken into account later during the analysis of the measured data.

A great challenge is the μ/π (signal/background) separation, due to the very similar rest masses of muon and pion. It is aimed to achieve an optimal S/B separation, keeping at the same time the highest possible reconstruction efficiency for the signal. To achieve that, a multivariate analysis is performed, using different classification methods from the field of machine learning.

3.5.3 Other Studies

Accessing the unphysical region via $\bar{p}p \rightarrow \pi^0 e^+ e^-$

The reaction of $\bar{p}p \rightarrow \ell^+ \ell^- \pi^0$ allows to study time-like proton FF's in the unphysical region below the $4M_p^2$ production threshold.

The feasibility to measure the FF's in the unphysical region at $\overline{\text{PANDA}}$ has been studied by Ref. [103]. The simulation studies, which are presented in this work, were performed based on a vector dominance parameterization of the proton FF's at two different values of q^2 ($q^2 = 0.605 \pm 0.005$ (GeV/c)² close to the ω resonance and at $q^2 = 2.0 \pm 0.125$ (GeV/c)²) in combination with different ranges of the production angle of the neutral pion in laboratory frame.

A first order model was developed for the event generation of the most challenging background process, which is the $\bar{p}p \rightarrow \pi^+ \pi^- \pi^0$ process. The signal pollution could be reduced to the percent level or even less, based on particle identification information from different detectors and kinematic fits. Total signal efficiencies between a few % and 30% were achieved.

The signal-to-background cross section ratio could be estimated to be of the order of 10^4 at $q^2 = 0.605 \pm 0.005$ (GeV/c)² respectively 10^7 at $q^2 = 2.0 \pm 0.125$ (GeV/c)². The studies show, that a precision at the percent level for the measurement of R at the lower q^2 and a few percent at the higher q^2 can be expected at $\overline{\text{PANDA}}$.

Later, this process was studied by Ref. [104] within a Regge framework. The angular distributions of the $e^+ e^-$ pair in the final state and the differential cross sections for the kinematics at $\overline{\text{PANDA}}$ are provided. A test of the developed model was performed using an approach on the process of real photon production $\bar{p}p \rightarrow \gamma \pi^0$, for which data are available in the energy range of $2.911 \text{ GeV} \leq \sqrt{s} \leq 3.686 \text{ GeV}$. The model was extended afterwards to a virtual (time-like) photon in the final state. More details can be found in Ref. [104].

Further studies for this channel, using the PandaRoot software package, are needed and will be performed in the future. The development of a dedicated event generator, which is based on the cross section of the $\bar{p}p \rightarrow \ell^+ \ell^- \pi^0$ signal process, is currently in progress at the $\overline{\text{PANDA}}$ Mainz EMP group.

Determination of the relative phase between the FF's

Also foreseen at $\overline{\text{PANDA}}$ is the measurement of the relative phase between the FF's. This measurement can be performed in single- or double polarization experiments. The antiproton proton annihilation into pairs of charged leptons, using a polarized antiproton beam or/and polarized proton target, carries information on the phase difference between the FF's, $\Phi = \Phi_M - \Phi_E$ with $G_{E,M} = |G_{E,M}|e^{i\Phi_{E,M}}$. For the case of a polarized beam, the differential cross section can be written as

$$\frac{d\sigma}{d\Omega} = \frac{d\sigma_0}{d\Omega} (1 + A_y^C \chi_{1y}) \quad (3.63)$$

where A_y^C stands for the single spin asymmetry in center-of-mass system due to the antiproton polarization and is determined by the component of the polarization vector along the y-axis, which stands perpendicular to the reaction plane. $\vec{\chi}_1$ is the antiproton polarization in its rest frame. In the center-of-mass system, A_y^C is proportional to the relative phase between the proton FF's:

$$A_y^C \sim \frac{\beta_\ell^2 \sin 2\theta}{\sqrt{\eta_p}} \text{Im}(G_M G_E^*). \quad (3.64)$$

The development of a transversely polarized target for $\overline{\text{PANDA}}$ is currently in progress [41].

Test of lepton universality

The principle of lepton universality states that, according to the Standard Model, the couplings of the gauge bosons to the leptons must be independent on the lepton flavor. Since the lepton universality is an integral part of the Standard Model, a violation of this universality would be a sign for new physics beyond the Standard Model. Only hints for the violation of lepton universality exist so far from experiments as e.g. BaBar, Belle and recently the LHCb (CERN) [105]. As an example, the LHCb experiment measured the ratio of the branching fractions of the $B^+ \rightarrow K^+ \mu^+ \mu^-$ and $B^+ \rightarrow K^+ e^+ e^-$ decays using proton-proton collision data. The ratio of the branching fractions, denoted as R_K , within a fixed range of the di-lepton mass squared from q_{min}^2 to q_{max}^2 is given by

$$R_K[q_{min}^2, q_{max}^2] = \frac{\int_{q_{min}^2}^{q_{max}^2} dq^2 \frac{d\Sigma(B^+ \rightarrow K^+ \mu^+ \mu^-)}{dq^2}}{\int_{q_{min}^2}^{q_{max}^2} dq^2 \frac{d\Sigma(B^+ \rightarrow K^+ e^+ e^-)}{dq^2}} \quad (3.65)$$

where Σ stands for the q^2 -dependent partial width of the B meson decay. Details of the measurement can be found at Ref. [105].

A calculation of the Standard Model prediction for R_K was obtained to be equal unity within an uncertainty of $\mathcal{O}(10^{-3})$ by Ref. [106, 107]. More recent calculations, which have been performed by [108], showed, that the largest theoretical uncertainty of R_K is due to QED corrections and result in a relative uncertainty of $\approx 1\text{-}2\%$.

In the measurement at LHCb, a time-integrated luminosity of 3 fb^{-1} was achieved at center

of mass energies between 7 and 8 TeV. The measurement was performed in the range of $1 < q^2 < 6$ (GeV/c)², where q^2 is the di-lepton invariant mass squared. The ratio of branching fractions was measured with a value of

$$R_K = 0.745_{-0.074}^{+0.09}(\text{stat.}) \pm 0.036(\text{syst.}). \quad (3.66)$$

which is compatible with the value predicted by the Standard Model within 2.6 standard deviations and is the most precise measurement of the ratio of branching fractions to date. Further data from an upgrade of the LHCb and from Belle-II are expected within the next years.

$\overline{\text{PANDA}}$ could be able to contribute to the field of lepton universality tests, in a sensitive measurement of the ratio of the effective proton FF,

$$\mathcal{R}_{e\mu} = \frac{|F_p(\bar{p}p \rightarrow \mu^+\mu^-)|}{|F_p(\bar{p}p \rightarrow e^+e^-)|}, \quad (3.67)$$

under the assumption, that the QED radiative corrections are well-known for both channels. The effective proton FF can be determined from the integrated cross sections of the $\bar{p}p \rightarrow \ell^+\ell^-$ process (with $\ell = e, \mu$). A theoretical prediction of the ratio $\mathcal{R}_{e\mu}$ will only be possible when all radiative corrections have been calculated for both channels.

Chapter 4

The $\bar{\text{P}}\text{ANDA}$ Experiment at FAIR

The $\bar{\text{P}}\text{ANDA}$ experiment [13] is planned to be one of the major projects at the future accelerator complex FAIR (Facility for Antiproton and Ion Research) at Darmstadt (Germany). $\bar{\text{P}}\text{ANDA}$ aims to gain new knowledge in the field of strong interactions in the non-perturbative regime. For this purpose, antiproton-proton collisions will be used to study the physics of strong interactions including charmonium spectroscopy, charmed hybrids and glueballs. A precise measurement of e.g. new resonance states like the recently discovered XYZ states will be possible.

The antiproton beam will be provided by the High Energy Storage Ring (HESR) with beam momenta ranging between 1.5 and 15 GeV/ c . In the following, a short overview of the accelerator complex FAIR and HESR will be given, followed by a detailed description of the $\bar{\text{P}}\text{ANDA}$ detector and its components. In particular, the most important sub-detector for this work will be introduced: the Muon System at $\bar{\text{P}}\text{ANDA}$.

4.1 Accelerator Complex FAIR

On the grounds of the GSI Helmholtzzentrum für Schwerionenforschung at Darmstadt, the accelerator complex FAIR is currently under construction. FAIR will host numerous experiments for research reaching from the fields of structure of matter, physics directly after the big bang until the development of the current state of matter.

FAIR will provide antiproton and ion beams with properties of both high quality and intensity. The setup of FAIR is shown in Figure 4.1. The already existing devices of the GSI research facility, the UNILAC and the SIS18 synchrotron, will serve as pre-accelerating devices for heavy ion beams with high intensities.

The experiments can be divided into four main topics. The APPA Physics (Atomic, Plasma Physics and Applications), CBM (Compressed Baryonic Matter), Nustar (Nuclear Structure, Astrophysics and Reactions) and $\bar{\text{P}}\text{ANDA}$ (Antiproton Annihilation at Darmstadt).

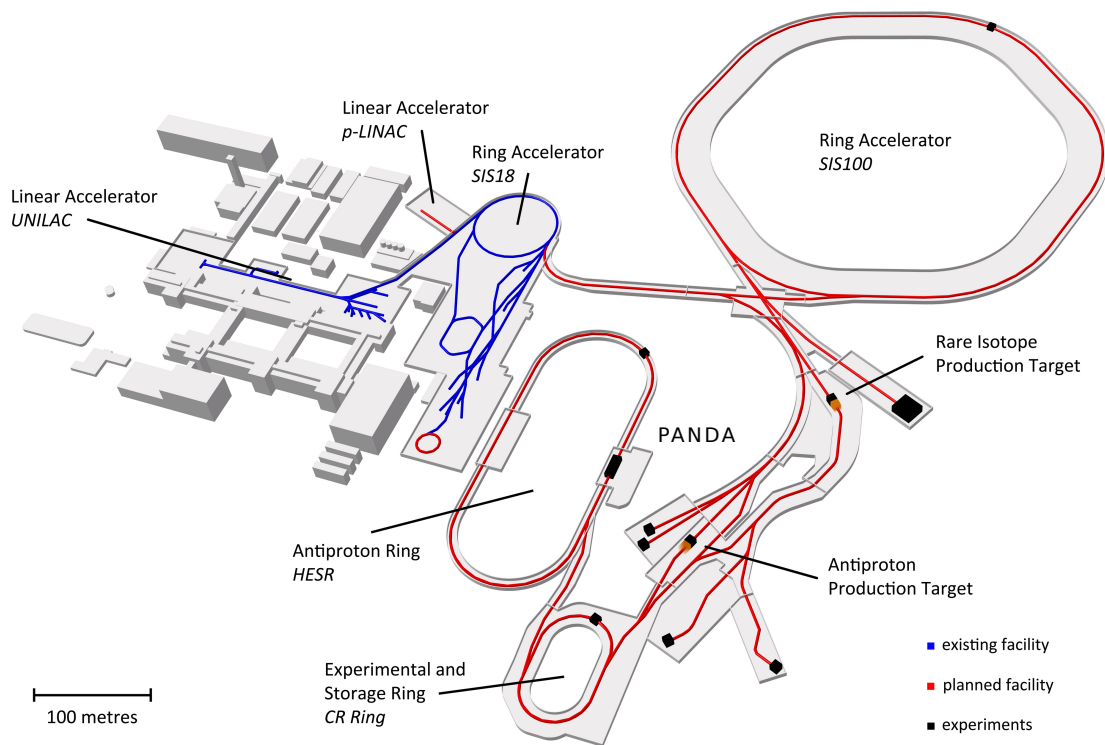


Figure 4.1: Future accelerator complex FAIR with the antiproton ring HESR, where $\bar{\text{P}}\text{ANDA}$ will be located as an internal target experiment [109].

4.1.1 Antiproton production

For the antiproton production, a new proton injector (p-LINAC) [110] will be constructed, which produces and accelerates protons to a kinetic energy of 70 MeV. The produced protons are accelerated by the SIS 18 (SchwerIonen Synchrotron) to a kinetic energy of 4 GeV. Afterwards, the protons enter the SIS100 synchrotron (a normal conducting magnetic synchrotron). After several injections from the SIS 18, roughly $2.5 \cdot 10^{13}$ protons are accumulated per bunch and then are accelerated to an energy of 29 GeV. The protons leave the SIS 100 in bunches compressed to 50 ns.

In the next step, the proton beam collides with a metal target causing reactions of the type $p + A \rightarrow \bar{p} + X$. Here, A is the mass number of the target material, X stands for the final state particles which can be scattered primary protons, secondary particles (leptons or hadrons) and the residue of the target nucleus after interaction. The production threshold for antiproton production can be calculated to an kinetic energy in the laboratory system of $6 m_p c^2 = 5.6$ GeV for the initial proton. The target properties have to be optimized to maximize the antiproton production yield. Since the yield increases with the target thickness, the target length plays an important role to find an optimal target design. However, the target length is limited by the fact, that after reaching a certain length, the absorption of protons and antiprotons inside the target starts to dominate.

Additionally, a high density of the target material increases the collection efficiency. A disadvantage of using such materials is their low heat capacity. In order to avoid a possible target melting, large beam diameters are necessary. Studies in Ref. [110] show, that the highest productions yield can be achieved using copper or nickel. Directly after the target, a pulsed magnetic horn will collect the produced antiprotons within a cone of 80 mrad at particle energies around 3 GeV. A separation from primary protons and secondary particles follows, before the beam is transported to the Collector Ring (CR).

4.1.2 Collector Ring (CR) and Recuperated Experimental Storage Ring (RESR)

The separated antiprotons are injected in the CR at a momentum of 3.8 GeV/c. They are collected and a cooling of the large phase-space is performed [111]. The momentum bite of the beam, $\delta p/p$, is reduced from 3% at injection down to 0.1% at extraction. At the same time, the transverse emittance is decreased from 240 mm mrad down to 5 mm mrad. In the start version of FAIR, the pre-cooled beam will be directly injected into the High Energy Storage Ring (HESR). A realization of a later upgrade would include the Recuperated Experimental Storage Ring (RESR), which would be located in the same hall as the CR and would accumulate antiprotons coming from the CR within 3 hours to bunches containing 10^{11} particles at 3.8 GeV/c.

	"Modularised Start Version"	"High Resolution Mode"	"High Luminosity Mode"
Momentum range	1.5 - 15 GeV/c	1.5 - 8.9 GeV/c	1.5 - 15 GeV/c
Number of \bar{p}	10^{10}	10^{10}	10^{11}
Peak luminosity	$\sim 10^{31} \text{cm}^{-2} \text{s}^{-1}$	$2 \cdot 10^{31} \text{cm}^{-2} \text{s}^{-1}$	$2 \cdot 10^{32} \text{cm}^{-2} \text{s}^{-1}$
Average luminosity	$\sim 10^{31} \text{cm}^{-2} \text{s}^{-1}$	$1 \cdot 10^{31} \text{cm}^{-2} \text{s}^{-1}$	$1 \cdot 10^{32} \text{cm}^{-2} \text{s}^{-1}$
Momentum resolution (rms)	$\Delta p/p < 5 \cdot 10^{-5}$	$\Delta p/p \leq 4 \cdot 10^{-5}$	$\Delta p/p = 1 \cdot 10^{-4}$
Beam cooling	Stochastic cooling	Electron cooling	Stochastic cooling

Table 4.1: Operation modes of the High Energy Storage Ring (HESR) for the Modularized Start Version in the beginning phase of FAIR and the original design version, with high resolution and high luminosity mode [13].

4.1.3 High-Energy Storage Ring (HESR)

The HESR will serve both as a storage ring and as an accelerator for the beam [112]. Entering the HESR with a momentum of 3.8 GeV/c, the beam can be ac-/decelerated to final antiproton momenta in the range of 1.5 GeV/c and 15 GeV/c. Two different operation modes will be possible at the HESR: the *High Resolution Mode* and the *High Luminosity Mode*. As an example, a high momentum resolution is necessary for charmonium spectroscopy while investigations in the field of nucleon structure require data sets of high statistics, which will be provided by the *High Luminosity Mode* of HESR. Table 4.1 summarizes the key properties of the operation modes of the HESR during the starting phase of FAIR (Modularised Start Version) and the original design version with high resolution and high luminosity mode.

Figure 4.2 shows the layout of the HESR, which is designed as a racetrack geometry with a total length of 574 m and straight sections of 132 m. Normally conducting magnets will be located at different positions at the HESR for the beam deflection. In operation, the HESR will first accumulate the number of required antiprotons, followed by beam cooling, which corresponds to a reduction of the beam phase-space volume and shrinks the beam size, divergence and energy spread. The cooling system needs to provide high cooling rates for the injected antiprotons in HESR. All heating processes need to be compensated to keep the quality of the beam at a high and constant level.

The HESR was designed with two beam cooling strategies: *stochastic cooling* in the high luminosity mode and *electron cooling* in the high resolution mode (for beam momenta up to 8.9 GeV/c). For the *stochastic cooling*, a pick-up sensor is used to measure the phase-space position of the beam and to send a correction signal to a kicker, which corrects the beam to the setpoint. More detailed, the particle bunches are kicked continuously to reduce the number of particles with deviating momenta from the average value. Due to the high time resolution a precise correction of the phase-space position individually for transverse and longitudinal direction is possible. Simulation studies predict that a momentum spread of $\delta p/p \leq 8 \cdot 10^{-5}$ will be achieved by the stochastic cooling after ~ 300 s [113].

For the *electron cooling*, a cold dense electron beam is accelerated to the mean velocity of

the beam. Both beams are superimposed and in case of velocity deviations, the antiprotons undergo Coulomb scattering with the electron. This cooling process stops as soon as the thermal equilibrium between electron and antiproton beam is reached. After passing the interaction section of the electron cooler, electrons and antiprotons with a narrow momentum distribution are separated again. The application of electron cooling will guarantee high cooling rates at HESR. Feasibility studies on the application of electron cooling at the foreseen beam energies of several MeV exist and show positive results [114].

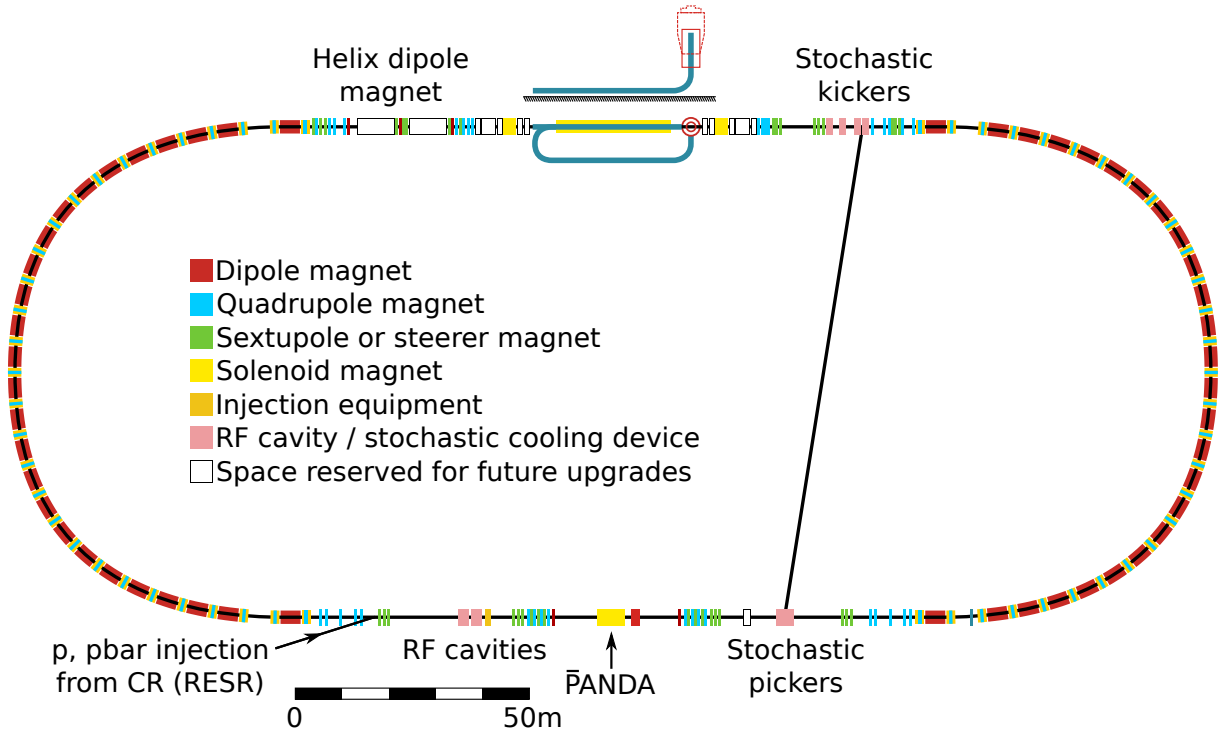


Figure 4.2: The High Energy Storage Ring (HESR), where the PANDA Experiment will be located as an internal target experiment [13]. During the start version of FAIR, the antiproton bunches will be injected directly by the Collector Ring and the HESR will perform both the antiproton accumulation and the beam cooling.

4.2 Target systems

Different target systems are planned to fulfill the requirements of the wide experimental program at $\bar{\text{P}}\text{ANDA}$ (see [115]). Inside the ultra-high vacuum of the storage ring, the target has to fulfill several requirements. For the strongly localized IP, a very small size and thickness of the target material will be realized by using a monolayer of atoms. Gaseous and non-gaseous targets are foreseen to cover the needs of the whole physics program at $\bar{\text{P}}\text{ANDA}$. In case of gaseous target materials, even target windows of very small thickness are not acceptable. Instead of using a target cell, a jet of condensed particles (like clusters or pellets), being shot perpendicular through the antiproton beam, will be used at $\bar{\text{P}}\text{ANDA}$. In order to achieve the original design peak luminosity of $2 \cdot 10^{32} \text{cm}^{-2} \text{s}^{-1}$, a target thickness of $4 \cdot 10^{15} \text{atoms/cm}^2$ has to be realized. A frozen pellet target and a cluster-jet target are the two basic options for the

studies with gaseous targets. Both of them will provide the required target densities at the interaction point although having different influence on the beam quality as well as an accurate definition of an IP.

4.2.1 Frozen Pellet Target

For the pellet target, a stream of frozen molecule droplets will be injected into the evacuated interaction area by a fine nozzle. Their spatial positions can be reconstructed by a pellet tracking system using optical detection devices, implying individual detectable pellets in the beam area. In order to achieve high luminosities, several small pellets have to interact simultaneously at the interaction point [115].

4.2.2 Cluster-Jet Target

An advantage of the Cluster-Jet Target is the homogeneous flux of hydrogen atoms through the antiproton beam. The jet is formed by the expansion of pressurized, pre-cooled gas into vacuum through a Laval-type nozzle. Condensation of the atoms leads to the formation of hydrogen clusters inside the narrow supersonic jet. Each of the clusters may contain 10^3 up to 10^6 atoms, depending on the inlet pressure and the initial gas temperature before it enters the nozzle. Due to the high mass of the clusters in comparison to the residual gas, the jet keeps its shape and direction over large distances of several meters inside vacuum.

The target installation for both solutions foresees the connection of the source, sitting above the $\bar{\text{P}}\text{ANDA}$ detector, with the interaction point by a thin pipe going through the whole vertical detector volume. At interaction point it shows a x-cross shape which is attached to the beam pipe, the beam dump sitting below the detector. Alternative target gases are deuterium, nitrogen or argon. Especially the Hyperon spectroscopy will make use of a primary and secondary target which are currently under development [13]. Table 4.2 presents the frozen pellet and cluster-jet target properties at $\bar{\text{P}}\text{ANDA}$.

	<i>Cluster Jet Target</i>	<i>Pellet Target</i>
effective target thickness	$1 \cdot 10^{15} \text{ atoms/cm}^2$	$5 \cdot 10^{15} \text{ atoms/cm}^2$
target thickness adjustable	yes (0 up to max)	yes (by reduction of pellet rate)
volume density distribution	homogeneous	granular
size transversal to \bar{p} beam	2-3 mm	$\leq 3\text{mm}$
size longitudinal to \bar{p} beam	15 mm	$\leq 3\text{mm}$
target particle size	nm scale	$20 \mu\text{m}$
mean vertical particle distance	$\leq 10\mu\text{m}$	2-20 mm
target material	H_2, D_2	H_2, D_2

Table 4.2: Overview of the $\bar{\text{P}}\text{ANDA}$ target solutions, Cluster-Jet and Pellet Target, and their properties [115]. The Pellet target will be only available at a later stage of the experiment.

4.2.3 Luminosity

The Luminosity (L) is a quantity characterizing the performance in colliders concerning event rates. It depends on the properties of target and beam and is connected to the cross section σ of a signal reaction by

$$L = \frac{1}{\sigma} \frac{dN}{dt}. \quad (4.1)$$

The luminosity is given in $[\text{cm}^{-2} \text{s}^{-1}]$. The signal event rate is $\frac{dN}{dt}$. L is a global characteristic of a collider experiment depending on the number of target particles N_T and the incoming flux of beam projectiles ϕ_P . Assuming a beam crossing the target area at the interaction point, it is defined as

$$L = N_T \cdot \phi_P \quad (4.2)$$

with

$$\phi_P = n_P \cdot v_P \quad (4.3)$$

Here, the projectile density is n_P and their velocity is v_P . After injection into the HESR, the antiprotons are pre-cooled to an equilibrium at 3.8 GeV/c with target being switched-off. The next step consists of ac-/deceleration to the final beam momentum. Afterwards the beam is focused in the areas of cooling systems and the target. In total this takes about 120 seconds for the beam preparation for the lowest beam momentum of 1.5 GeV/c up to 290 seconds for 15.0 GeV/c.

Figure 4.3 shows the time-dependence of the Luminosity during one operation cycle at HESR [115].

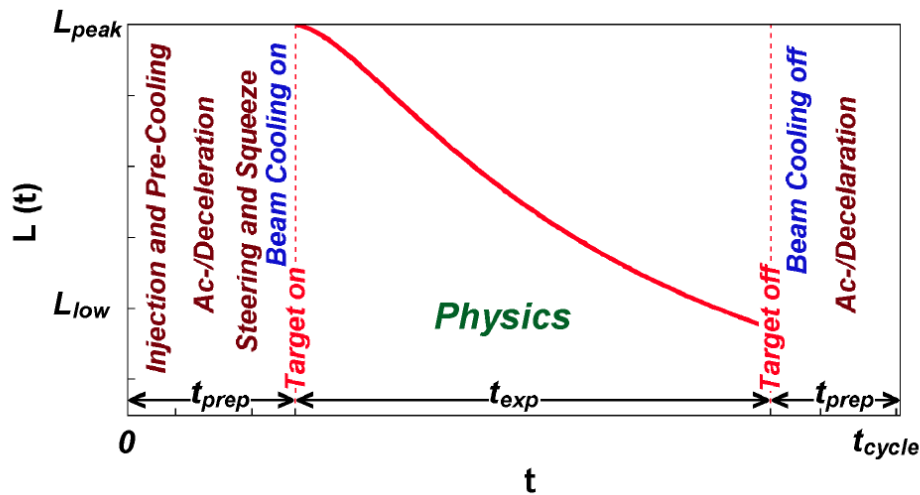


Figure 4.3: Time dependence of the luminosity during an operation cycle $L(t)$ at HESR including the RESR [115]. The red line corresponds to a fixed target density and therefore decreases during the time measurement (Target ON).

Due to the interactions between the beam and the target, the beam intensity will decrease exponentially during one operation cycle at HESR. These interactions are mainly of hadronic nature, single Coulomb scattering processes and energy straggling. In comparison to that, energy losses due to intra-beam interactions can be neglected.

The effect of decreasing beam intensity on the sinking luminosity $L(t)$ (see Figure 4.3) can be compensated by increasing the cluster/pellet target density during one accelerator cycle. This allows to stabilize the luminosity, provides constant event rates and maximizes the average luminosity. For that, the remaining antiprotons at the end of one operating cycle will be kept in the storage ring and new bunches of antiprotons will be injected to specially reserved empty space. Alternatively, the beam/target overlap can be increased at constant target beam density depending on the antiproton consumption.

The average luminosity can be denoted as

$$\bar{L} = L_0 \cdot \frac{\tau \left[1 - \exp^{-t_{exp}/\tau} \right]}{t_{exp} + t_{prep}} \quad (4.4)$$

with L_0 as the peak luminosity after switching the target to "ON". τ is the 1/e beam lifetime, t_{exp} is the experimental data taking time (which is the time of beam being shot at the target). The total time t_{cycle} is the sum of preparation and experimental time. With an original $\bar{\text{P}}\text{ANDA}$ design peak luminosity of $2 \cdot 10^{32} \text{cm}^{-2} \text{s}^{-1}$, the average luminosity is twice as low and amounts $1 \cdot 10^{31} \text{cm}^{-2} \text{s}^{-1}$. The antiproton beam will lead to an event rate up to 20 MHz at $\bar{\text{P}}\text{ANDA}$. In the following, the full setup of the $\bar{\text{P}}\text{ANDA}$ detector will be described. Not all detectors will be available in the beginning of the data taking phase. Details about the data taking phases will be given later, in Section 4.5.

4.3 $\bar{\text{P}}\text{ANDA}$ detector

The design of the $\bar{\text{P}}\text{ANDA}$ detector was developed for reaching almost full 4π acceptance, high detection efficiency and rate capabilities, high resolution electromagnetic calorimetry, particle tracking and identification [13]. As a fixed target experiment, the produced final states undergo a Lorentz boost in the forward direction. Therefore the detector will consist of two main components ensuring a good momentum resolution.

First, the target spectrometer, which surrounds the interaction point, is based on a superconducting solenoid magnet and will be used for the detection of the produced particles at higher angles. Second, the forward spectrometer will be used for the particle detection under forward angles, and is based on a dipole magnet.

For the precise interaction vertex reconstruction and as a part of the tracking system, a silicon tracker (Micro Vertex Detector) will surround the interaction point. This device is important especially for the detection of decay vertices of short-lived particles like D mesons.

Both the target spectrometer and the forward spectrometer are designed with several sub-detectors showing high tracking capabilities (MVD, STT, GEM stations), precise charged particle identification (Barrel DIRC, Disc DIRC, FRICH), a time of flight system (ToF) and electromagnetic calorimetry (EMC) at high event rates in order to allow precise detection of the broad spectrum of different final states relevant for the $\bar{\text{P}}\text{ANDA}$ physics program. Detectors for muon identification will be placed at the outer areas of both target spectrometer and forward spectrometer. The following section gives an overview of the different detector systems and their properties.

For charged particle tracking a superconducting solenoid magnet will be placed around the interaction point inside the target spectrometer. Depending on the beam momentum, field strengths up to 2 Tesla will be provided with high precision (better than $\pm 2\%$). For antiproton momenta lower than 3 GeV/c, the magnetic field will be reduced to 1 Tesla. The forward spectrometer will contain a dipole magnet for the deflection of small angle tracks.

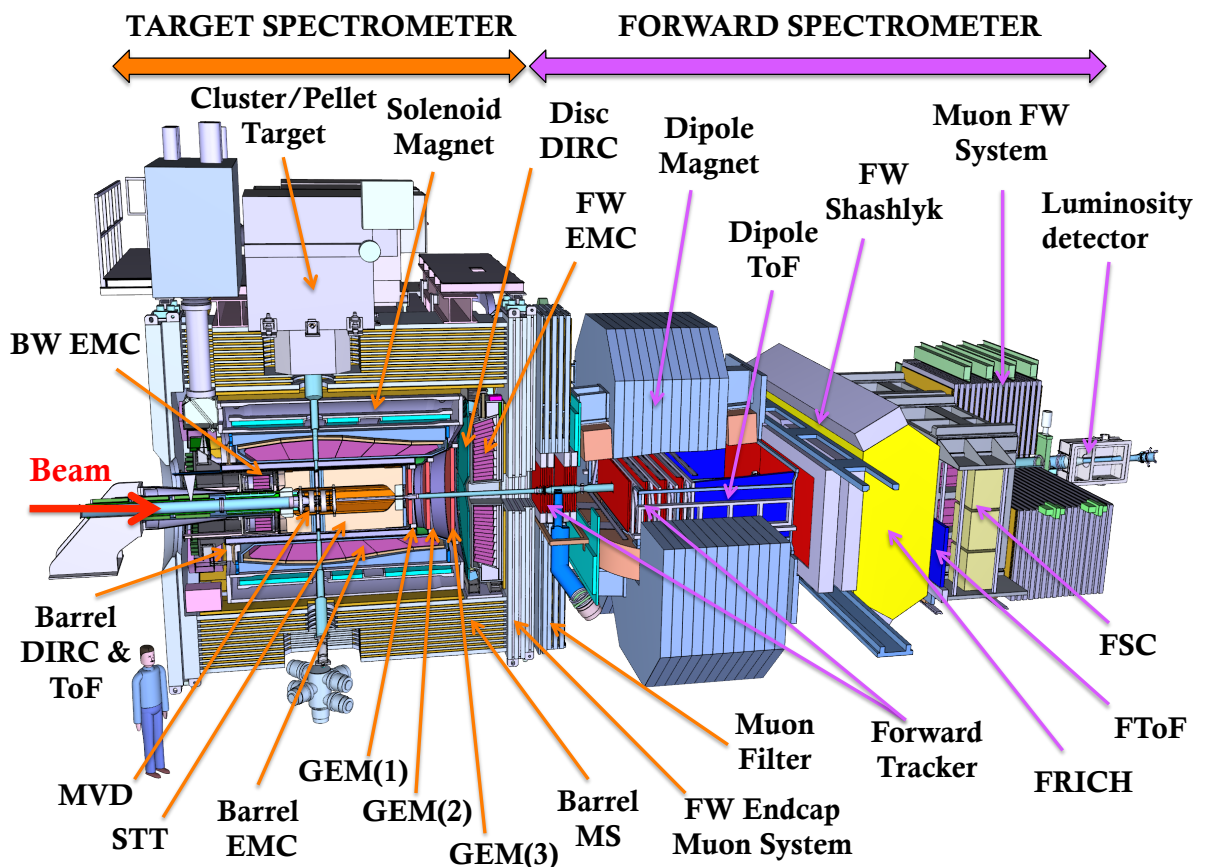


Figure 4.4: Full experimental setup of the $\bar{\text{P}}\text{ANDA}$ Experiment. The detector consists of two major parts, providing almost full 4π coverage: the Target Spectrometer and the Forward Spectrometer, which will be both equipped with sub-detectors ensuring high tracking capabilities, precise particle identification and electromagnetic calorimetry at high event rates.

The design of the target spectrometer follows an onion like structure surrounding the interaction point, which is similar to the experimental setups at many current collider experiments. In order to reach a high angular coverage, the target spectrometer has 3 major components: the Barrel part, which covers polar angles in the laboratory system between 22° and 140° , completed by the Forward Endcap for angles down to 5° (vertical) respectively 10° (horizontal) as well as the Backward Endcap for detection at angles between 145° and 170° .

For the momentum reconstruction and identification of charged particles, large magnetic fields will be used in combination with the tracking facilities at both spectrometers. Inside the target spectrometer, a solenoidal field with a maximum field strength of 2 Tesla will surround the target point and in the forward spectrometer a dipole field with field strength up to 1 Tm will be available for angles below $5^\circ/10^\circ$. For the insertion of target installations, cut outs are placed in both parts of the detector and the magnets.

4.3.1 Magnets

Solenoid magnet

The target spectrometer will be equipped with a superconducting solenoid coil [116] providing a magnetic field with maximum strength of 2 Tesla and having an inner radius of 1.05 m and a length of 2.8 m. Two warm bores of 100 mm diameter inside the cryostat for the solenoid coils will be placed above and below the interaction point. This enables the insertion of the target pipe for different internal targets. Liquid helium will be used for the coil cooling. The coil is designed to achieve a field homogeneity better than 2% over the volume occupied by MVD and STT. For the material of the $\bar{\text{P}}\text{ANDA}$ solenoid, Niobium-titanium (NbTi) fibers inside a copper matrix was chosen.

The tracking system inside the solenoid will be able to provide momentum reconstruction of the charged particle tracks with angles down to $5^\circ/10^\circ$. A return yoke made of iron will provide a backflow of the magnetic flux of the solenoid magnet field. Additionally, the yoke serves as absorber material for the muon detection system of $\bar{\text{P}}\text{ANDA}$ inside the target spectrometer. In order to avoid dead material in the front, the coils of the magnet will be placed outside the Electromagnetic Calorimeter.

Dipole magnet

Due to the fact, that $\bar{\text{P}}\text{ANDA}$ is a fixed target experiment, the forward system is of great importance for $\bar{\text{P}}\text{ANDA}$. Due to momentum conservation, most particles will be emitted under forward angles and will enter the forward system. The magnetic field inside the forward system will be provided by a dipole magnet with a maximal bending power of 2 Tm. The dipole magnet covers angles between 10° in horizontal and 5° in vertical direction. The antiproton beam will be deflected by the dipole magnet by 2.2° at the maximal antiproton momentum of 15 GeV/c. For a compensation of this effect, further correction dipole magnets will be placed before and

after the $\bar{\text{P}}\text{ANDA}$ experiment in the beam line of HESR.

4.3.2 Tracking System

The tracking system at $\bar{\text{P}}\text{ANDA}$ aims to reconstruct charged particle tracks with large acceptance and high momentum resolution up to $\approx 1\%$. Three sub-detectors will be combined to achieve an optimal track reconstruction in the target spectrometer: the Mirco Vertex Detector (MVD) enclosing the interaction point, followed by the Straw Tube Tracker (STT) and three Gas Electron Multiplier stations (GEM's) in forward direction. The tracking in combination with the magnetic field inside the target spectrometer will provide high resolution tracking and momentum reconstruction.

The central task of the Micro Vertex Detector (MVD) [117] is the precise reconstruction of both the primary beam-target interaction vertex as well as secondary decay vertices of short lived particles like D-Mesons or hyperons. Since the MVD will be the innermost sub-detector of the tracking system, it delivers the closest tracking point to the interaction point. In addition, it will perform charged particle identification for low energy particles by measuring the energy loss per unit path length dE/dx .

The MVD will be exposed to high particle fluxes and therefore is built of materials with high radiation resistance and needs to deal with high event rates. It is divided into a barrel and a forward part and contains silicon pixel detectors with fast read-out electronics and silicon strip detectors. The central part consists of four barrel shaped layers with an inner (outer) radius of 2.5 cm (13.0 cm).

In the up-stream part, six disc-shaped silicon pixel detectors will be placed perpendicular to the beam pipe. Silicon pixel detectors have been chosen for the two inner barrel layers and the two forward wheels, while the two outermost barrel layers and the six forward disks will be realized with double-sided silicon strip sensors. The vertex resolution is expected to be below $35 \mu\text{m}$ in a plane perpendicular to the beam and smaller than $100 \mu\text{m}$ along the beam axis.

Straw Tube Tracker

The Straw Tube Tracker (STT) will be the main part of the tracking system in the $\bar{\text{P}}\text{ANDA}$ target spectrometer [118]. It will possess a cylindrical geometry and contain an ensemble of 4636 straw tubes of 150 cm length filled with an Argon/ CO_2 gas mixture (90/10). The tube walls will be made of aluminized Mylar. The main task of the STT is the precise momentum measurement from the reconstructed trajectories. Charged particles with momenta between a few hundreds MeV/c and $8 \text{ GeV}/c$ can be detected with expected spatial resolution about ~ 1 mm along the beam axis and $\sim 150 \mu\text{m}$ in the plane perpendicular to the beam. The magnetic field allows a precise reconstruction of the charged particles three-momenta. Another task of the STT is the energy loss dE/dx measurement for particle identification especially for proton, kaon

and pion separation at particle momenta below 1 GeV/ c . In forward direction, it is followed by a set of Gas Electron Multiplier Stations.

Gas Electron Multiplier Stations

As a first tracking station in forward direction, the Gas Electron Multiplier (GEM) stations [119] will complete the target spectrometer tracking system. Particles will be tracked at small forward angles up to 22° by three planar GEM stations with gaseous micro-pattern detectors based on GEM foils. They will be located at 1.1 m, 1.4 m and 1.9 m behind the target (in beam direction) and have to show high rate capabilities due to the relativistic Lorentz boost of the final state particles to forward angles. Each station is equipped with double planar read-out pads and accomplishes 2 projections per plane. The spatial resolution will be better than 100 μm .

Forward Tracker Stations

The Forward Tracker stations inside the forward spectrometer will be used for the track reconstruction of charged particles inside the magnetic dipole field at small forward angles. It consists of three pairs of tracking drift detectors, where one pair will be located in the front, the second pair within and the third pair behind the dipole magnet. Each pair will consist of two individual detectors. Hence, in total 6 independent detectors will form the Forward Tracker. Each detector will be composed of four double-layers of straw tubes, two with vertical wires and two with wires, which will be tilted by a few degrees for the reconstruction of the vertical coordinate. This configuration of double-layers will allow to reconstruct charged particle tracks in each pair of tracking detectors individually.

4.3.3 Electromagnetic Calorimetry

The energy measurement of photons, electrons and positrons will be performed at $\bar{\text{P}}\text{ANDA}$ with the Electromagnetic Calorimeter (EMC), which has a geometric coverage of $\approx 96\%$. Charged particles and higher energetic photons cause electromagnetic showers while crossing material. For charged particles this is the case when their energy exceeds the critical energy of the material and they emit Bremsstrahlung. The critical energy E_c is defined as the energy, at which a particles' energy loss due to ionization and excitation is equal to the energy loss due to bremsstrahlung. For electrons, E_c can be approximated by [120]

$$E_c \approx 800/(Z + 1.2) \text{ MeV}, \quad (4.5)$$

with Z as the atomic charge of the material. For the scintillation material of the EMC, lead tungstate (PbWO_4) is foreseen, which has a value of $E_c \approx 9 \text{ MeV}$. The relative energy resolution $\sigma(E)/E$ of the EMC can be written as

$$\sigma(E)/E = \frac{a}{\sqrt{E}} \oplus \frac{b}{E} \oplus c, \quad (4.6)$$

where the first term stands for the contribution caused by the statistical fluctuations of the shower (intrinsic resolution), the second term is mainly due to electronic noise and pile-up at very high rates. The third term is a constant, caused by e.g. calibration errors, longitudinal leakage or dead channels in the read-out. $\bar{\text{P}}\text{ANDA}$ aims to achieve a high relative energy resolution on the %-level for electrons and photons for energies between 0.01 GeV up to 14.6 GeV. High spatial and energy resolution together with low energy thresholds are mandatory for high signal yield and a good background suppression. Especially the decay of neutral pions into two gammas will be present in numerous channels: to avoid a possible misidentification of the event both gammas need to be detected. The energy threshold for an electron- or photon induced cluster of crystals is chosen to be 10 MeV, for a single crystal it is 3 MeV.

Figure 4.5 shows the layout of the EMC at $\bar{\text{P}}\text{ANDA}$. Three parts for the EMC will be installed inside the target spectrometer (the Barrel EMC, the Backward End-cap EMC and the Forward End-cap EMC) and one additional part will be installed in the forward region inside the forward spectrometer (the Forward "Shashlyk" EMC).

All parts will be equipped with PbWO_4 (shortly denoted as *PWO*) crystals. A special developed material of the second generation will be used, which is denoted as *PWO-II*. The *PWO-II* scintillating material is doped by a few parts per million of Lanthanium or Yttrium leading to a high light yield increase of about 80% in comparison to the standard *PWO* crystals used at the CMS experiment at CERN. Table 4.3 summarizes the most important properties of the crystals. The *PWO-II* crystals have a short radiation length of 0.89 cm and a Molière radius of 2.2 cm. This material is used at several high energy physics experiments (e.g. ALICE and CMS at CERN) and has proved itself to be radiation hard and not hygroscopic. Furthermore, lead tungstate shows fast response with a decay time of 6 ns, which is needed for the high event

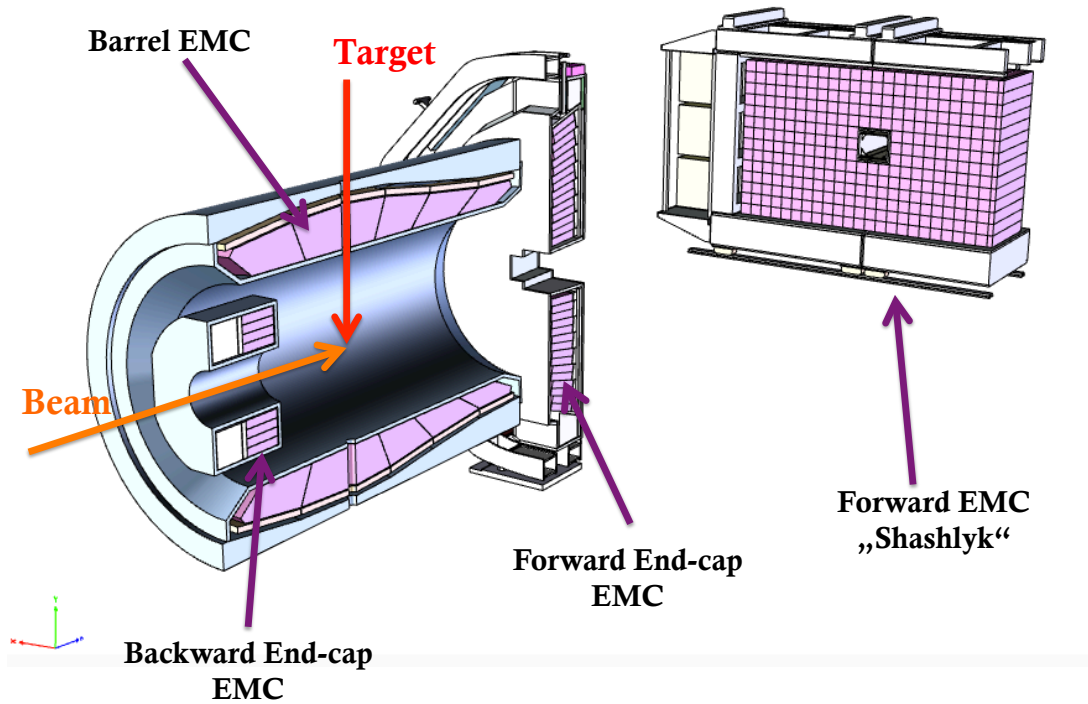


Figure 4.5: The Electromagnetic Calorimeter (EMC) inside the Target Spectrometer, consisting of the Barrel EMC, the Backward End-cap EMC and the Forward End-cap EMC. In the Forward Spectrometer, the *Shashlyk*-type Forward EMC will be located for electromagnetic calorimetry [121]. A challenging task in this work is an efficient μ/π separation, which is done mostly with variables provided by the Muon System. Variables from the EMC improve the μ/π separation and are also used for the data classification.

rates expected at $\bar{\text{PANDA}}$ ($\sim 10^7$ events/s). Its high material density allows the construction of compact detectors [121]. Very important, e.g. for the measurement of lepton pairs with final states e^+e^- , is the ability to distinguish between electrons and pions. This requirement is fulfilled for momenta over 0.5 GeV/c. A disadvantage of lead tungstate is the low light yield at room temperature. Although it can be improved drastically by decreasing the temperature: the yield increases by factor of four, if the crystals are operated at $T = -25^\circ\text{C}$.

For the $\bar{\text{PANDA}}$ EMC, Crystals of 20 cm length will be used, which corresponds to $\approx 22 X_0$ and allows to absorb mostly the full electromagnetic shower energy. Here, X_0 is the radiation length of the material, which is a specific constant of the material and is connected to the energy loss due to the Bremsstrahlung process for electrons of energy E via

$$-dE/dx = E/X_0. \quad (4.7)$$

The shape of the crystals inside the different parts of the EMC varies strongly. For the Backward End-cap EMC, rectangular crystals are a good choice which are also easy to manufacture. At the Barrel EMC, the crystal geometry and their alignment are more complex. The crystals are

<i>Properties</i>	<i>PbWO₄</i>
Density (ρ)	8.28 g cm ⁻³
Radiation length (X_0)	0.89 cm
Energy loss (dE/dx) for MIP	10.2 MeV cm ⁻¹
Decay time (τ_{decay})	6 ns and 30 ns
Light yield (LY)	fast component: 0.6% of NaI slow component: 0.1% of NaI
d(ln(LY))/dT	-3%/°C

Table 4.3: Main properties of PWO-II.

not pointing towards the target position, but are tilted by 4° to avoid losing particles due to the dead zone effect. This has the consequence that the trajectories starting at interaction point never pass through gaps between the crystals and therefore are getting lost. At the Forward End-cap EMC, a single crystal will possess a front face of $24 \times 24 \text{ mm}^2$. All crystals will be oriented "off-point" with respect to the interaction point in order to guarantee that no particles are able to pass the EMC through a gap between two neighbor crystals without being detected.

EMC inside the Target Spectrometer

The target spectrometer EMC is composed of three major parts (see Figure 4.5). The Barrel EMC (which contains 11360 crystals) covers angles between 22° up to 140° , the Forward End-cap EMC (which contains 3600 crystals) covers angles between 5° up to 10° and the Backward End-cap EMC (which contains 524 crystals) covers angles between 149° and 167° . For the thermal insulation of the Backward End-cap EMC, vacuum panels (VIP) are currently planned to ensure a high local and global temperature stability for homogeneous light yields.

The readout of the produced scintillation light will be realized by vacuum photo-triodes at the Forward End-cap. Since the Barrel and Backward End-cap of the EMC are placed inside the magnetic field of the target spectrometer, the choice of photomultipliers or vacuum triodes for readout are not an option. Instead, large area avalanche photo diodes (LAAPDs) have been chosen which show fast readout and good radiation hardness and are insensitive to the magnetic field. The APD is a high sensitivity photodiode, which can be operated at high event rates and achieve a high gain by applying a reverse voltage. In contrast to a p-i-n diode, the APD has an additional very thin layer of highly doped p-layer. Therefore high electric field strengths are produced in this area of the p-n layers. When a charged particle crosses the depleted zone, it can create free electron-hole pairs. The electron is accelerated towards the plus pole and due to the high field strength causing an intern charge amplification: a charge avalanche is formed.

The energy resolution it is expected to be high with $\sigma(E)/E = 1.54\%/\sqrt{E} \oplus 0.3\%$ [GeV] in an energy range between a few MeV up to 10 GeV.

EMC inside the Forward Spectrometer

The forward spectrometer EMC (Forward EMC "Shashlyk") [122] will be a sampling calorimeter of the shashlik type for the detection of electromagnetic particle showers and energy deposition measurement. Alternating active (scintillators) and passive layers (lead) build the basic structure of the Forward EMC. Readout will be performed by photomultipliers from the back side, while the produced scintillator light is transported by optical fibers through the detector structure. The Forward EMC consists of 378 smaller modules, each with an overall detector length of 1150 mm (z -direction) and covers an angular range up to 5° .

Energies up to 15 GeV will be detected. For the energy resolution it is aimed to achieve $\sigma_E/E \approx 4\%/\sqrt{E/\text{GeV}}$, which has already been achieved with similar modules [121].

4.3.4 Particle Identification

To achieve a highly efficient particle identification at $\overline{\text{PANDA}}$, an advanced system of detectors will be available at both target spectrometer and forward spectrometer [123]. A detector ensemble for a pion-kaon and proton separation for momenta up to 3.5 GeV/ c based on Cherenkov imaging will be present in the target spectrometer. Surrounded by the Barrel EMC, the Detector of Internally Reflected Cherenkov Light (DIRC) will cover additionally backward angles with a similar compact design like the DIRC which has been successfully deployed in the BaBar experiment at SLAC [124]. For pion-kaon separation in the forward region up to momenta of 4 GeV/ c , a focussing disc DIRC will be installed in the Forward Endcap of the target spectrometer. For slow particles, which are not generating signals in the DIRC, a Time of Flight System (TOF) will complete the system inside the target spectrometer.

Detector of Internally Reflected Cherenkov Light (DIRC)

The first of three detectors for particle identification (PID) in the target spectrometer is the Barrel DIRC, which has an angular coverage of 22° up to 140° . It will consist of an ensemble of fused silica panels, each with 1.7 cm thickness which will be arranged cylindrical in a distance of about 50 cm around the beam axis. For the read-out Micro-channel plate photomultiplier tubes (MCP-PMT), insensitive to the magnetic field, will be positioned at the downstream end of the Barrel DIRC. The light produced inside the quartz panels will be focused by lenses into an expansion volume filled with mineral oil. The MCP-PMTs will be attached to this volume for the read-out of two spatial coordinates. A similar detection concept will be realized for the forward region for polar angles in the range of 5° to 22° . A disk shaped, planar DIRC (disc DIRC) will be positioned directly before the Forward End-cap of the EMC (in beam direction). The panels will be constructed utilizing the same material of 2 cm thickness and a 110 cm radius. The arrangement of four independent parts will be centered around the beam line. A focusing device will be placed at the end of each panel for Cherenkov light measurement. Three dimensional patterns can be constructed in combination with a time measurement of the detected photon. Such patterns serve as input for PID likelihoods, which can be calculated for different particle

hypothesis.

Time of Flight System (TOF)

The third detector for particle identification is a time-of-flight system (TOF) between the Barrel DIRC and the EMC. In total 5760 scintillator panels will form the TOF enclosing the DIRC barrel. It is planned to use plastic scintillator panels with a fast signal production. Two silicon photomultipliers will be attached to each panel end for a fast readout. A time resolution of 100 ps is planned to be achieved. In the forward spectrometer a TOF wall at a distance of 7 m from the interaction point is planned for the TOF stopping counter. As material also plastic scintillators in combination with fast phototubes at each end will provide good π/K (K/p) separation up to 2.8 GeV/ c (4.7 GeV/ c) with a time resolution in the order of 50 ps. This will be complemented by a similar device placed inside the dipole magnet openings for the detection of low energy particles stopping inside the dipole [118].

Ring Imaging Cherenkov Detector (RICH)

For an efficient π/K and K/p separation under polar angles of $5^\circ - 22^\circ$ in the forward spectrometer, a Ring Imaging Cherenkov Detector (RICH) will be installed. A dual radiator design was chosen, based on two radiator materials with different refraction indices: silica aerogel ($n=1.0304$) and freon (C_4F_{10}) gas ($n=1.00137$). A $\pi/\text{K}/\text{p}$ separation will be possible for particle momenta between 2 GeV/ c up to 15 GeV/ c .

4.3.5 Luminosity Detector

A dedicated and independent detector for the precise luminosity determination will be placed downstream at the very end of the $\bar{\text{P}}\text{ANDA}$ detector, the Luminosity Detector. It reconstructs the tracks of elastically scattered antiprotons at target protons at small polar angles. The Luminosity Detector will be located in a distance of 10.5 m downstream from the interaction point and is designed with a polar angular acceptance of $3 \text{ mrad} < \theta < 9 \text{ mrad}$. It consists of 4 disk-shaped tracking planes with a diameter of $\approx 30 \text{ cm}$. The antiproton tracking will be performed by 400 high voltage monolithic active pixel sensors (HV-MAPS) inside an evacuated volume. Track back propagation to the interaction point delivers the scattering angles at the interaction vertex and therefore can be used to measure the angular dependence of the scattering cross section. Fitting the angular distribution with the expected cross section leads to the time-integrated luminosity value with an accuracy better than 5% at lower antiproton beam momenta.

4.3.6 Muon Detectors

For the muon detection, the Muon System (MS) [125] will be installed at $\bar{\text{P}}\text{ANDA}$. Since muons are able to transverse most of detectors while interacting only via multiple scattering with the materials, the Muon detectors are positioned as the outermost detectors. The range system technique is used, which is based on a sampling structure of active and passive layers in all subsystems of the MS. Three parts will be positioned inside the target spectrometer: the

Barrel MS, the Forward End-cap and the Muon Filter. The fourth part of the $\bar{\text{P}}\text{ANDA}$ Muon System will be placed inside the forward spectrometer: the Forward Range System.

The active layers of the $\bar{\text{P}}\text{ANDA}$ Muon System will be based on Mini Drift Tubes (MDT's), which are rectangular drift tubes with a central anodic wire for the measurement of one of two coordinates along the detector planes. MDT's have already proven their successful performance at experiments as D0 (FNAL) [126, 127, 128] and COMPASS (CERN) [129]. The second coordinate will be reconstructed by strip boards, placed on top of the MDT's, in which a signal is induced by a particle while traversing the MDT's. The innermost layer has a double detection layer structure (denoted as the *zero bi-layer*) and will be placed in front of the first detection layer. The zero bi-layer allows to perform a precise measurement of the starting point coordinate of each particle track in front of the Muon System and helps the track back propagation to the interaction point.

The passive layers will be realized by an iron absorber layers. The absorber acts as stopping material for especially the pions, which constitute an important background source at the measurements, where the signal reaction contains muons.

The laminated iron yoke of the solenoid magnet (denoted as the Barrel MS) inside the Target Spectrometer has a second function. It acts as a range system for muon detection with a total of 13 detection layers. Each detection layer is 3 cm thick. The passive layers will have 3 cm thickness, with the inner- and outermost layers of 6 cm thickness. Since the produced particles have higher momenta at small angles in the forward region, the Forward End-cap of the Muon System inside the target spectrometer will have thicker iron absorber layers with 6 cm each. The removable Muon Filter, which is placed between the solenoid and the Dipole magnet, will add another 4 absorber layers of the same thickness.

The Forward Range System has the same basic structure and materials as the Muon System parts in the target spectrometer with a total of 16 detection and absorption layers. It also may serve as a hadron calorimeter in the forward spectrometer with moderate resolution.

In total 3751 MDT's will be used, with 2133 MDT's for the Barrel part, 1042 for End-cap and the Muon Filter and 576 inside the Forward Range System. Since the Muon System at $\bar{\text{P}}\text{ANDA}$ is the most important detector used in this feasibility study, a more detailed description will be given in the following section.

4.4 Muon System at $\overline{\text{PANDA}}$

Many reactions at $\overline{\text{PANDA}}$ will contain muons in their final state e.g. from the process of $\overline{p}p \rightarrow \mu^+\mu^-$, which is the considered reaction in this work, or also the production of the J/Ψ resonance in $\overline{p}p \rightarrow J/\Psi + X \rightarrow \mu^+\mu^- + X$, the production in Drell-Yan processes $\overline{p}p \rightarrow \gamma^* + X \rightarrow \mu^+\mu^- + X$ [125] and from the decay of other charmonium states. Since most of the signal processes, which contain final state muons, have smaller cross sections than the corresponding background reactions, the information provided by the Muon System must enable a very good signal-background separation. The following section gives a detailed description of the Muon System at $\overline{\text{PANDA}}$.

Description of the Muon System

The main task of the Muon System at $\overline{\text{PANDA}}$ is the identification of final state muons via pattern recognition and matching of the tracks inside the Muon System to the tracks inside the magnetic field.

For the separation of muons from other particle species the Range System technique is used. The main concept of this technique is the sequential energy loss and particle tracking of charged particles inside a system of alternating active and passive layers. The different behavior of muons and pions inside the sandwich structure of the Muon System is used later during the data analysis for μ/π separation. Observables from the Muon System, as e.g. path length inside the iron absorber and the number of fired detection layers, have the highest separation power of all detection observables at the $\overline{\text{PANDA}}$ detector concerning μ/π separation. Therefore the Muon System provides the most important information for the feasibility studies in this work.

The absorber layers are usually realized by using a very dense absorber medium for stopping most of the slow particles. For that purpose, iron will be used in the Muon System at $\overline{\text{PANDA}}$. While passing through a material, muons are only slightly interacting with the material and loose energy primarily due to atomic ionization and excitation, while e.g. pions undergo also hadronic interactions with the material. Therefore, the patterns of muons and pions are significantly different in the Muon System, in particular at lower particle momenta around 1 GeV/c, where most of the pions can be stopped inside the first absorber layers.

In comparison to the electron, the muon rest mass is higher by a factor of ≈ 200 , so that the energy loss of muons due to Bremsstrahlung is much smaller in comparison to electrons (the probability of this process is $\propto 1/M^2$, M: particle rest mass). For muons, the interaction mechanism becomes important at few hundred GeV, what is far from the particle energies at $\overline{\text{PANDA}}$. Since the cross sections for interactions with the nuclei of the absorber material are extremely small in comparison to the atomic electron cloud, muon-nucleus interactions are negligible.

For the detector layers, all parts of the Muon System will be instrumented with Mini Drift Tubes (MDT's) (see Fig. 4.10), which are rectangular aluminum drift tubes with a central an-

odic wire, filled with a 70% Argon/30% CO_2 mixture and are operated in proportional mode. They will provide one coordinate only and will perform a Yes/No readout of the wires (no drift time measurement). The second coordinate will be reconstructed by copper-laminated strip boards attached to the MDTs, obtained also with a Yes/No readout of the stripes. The strip board consists of a fiberglass plate, which has a copper film on the surface oriented towards the MDT. Inside the copper film, strips are scratched, in which a signal is influenced when a charged particle traverses the MDT. More details about the regular detector layers of the Muon System will be given in the next section. The innermost layer has a special setup (denoted as the *zero bi-layer*). It will allow for a very precise measurement of the starting point coordinates of each particle track in front of the Muon System and provides three spatial coordinates, with maximal possible detection efficiency for reconstruction of the starting point of the tracklet in the Muon System also for multi-particle events recognition.

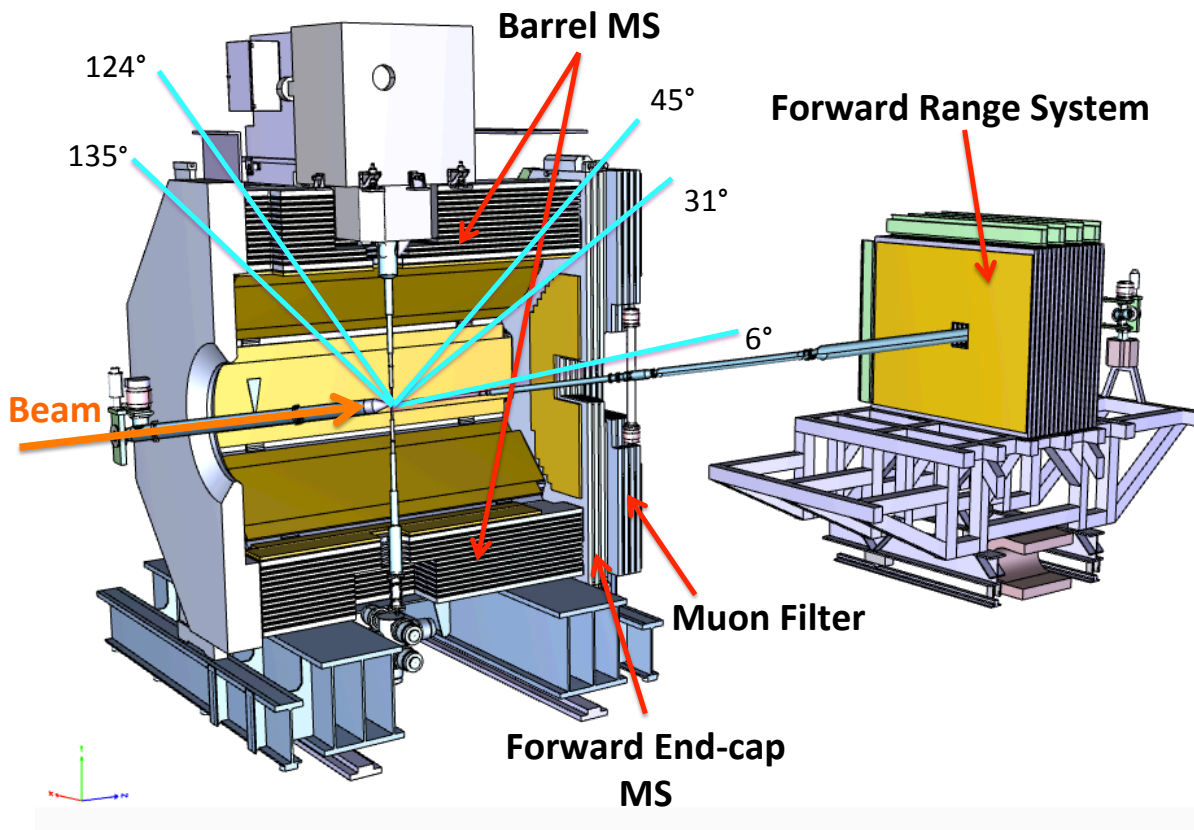


Figure 4.6: Layout of the Muon System of the $\bar{\text{PANDA}}$ experiment. The four parts are distributed over the whole detector, with a geometrical coverage of polar angles between 1° and 135° degrees: the Barrel MS, the Forward End-cap (EC), the Muon Filter (MF) and the Forward Range System (FRS). The Muon System is based on the range system technique for muon detection in a laminated iron absorber. For the detection, Mini Drift Tubes (MDT's) attached to strip boards are used. The iron absorber of the Barrel Muon System serves also as a return yoke for the solenoid magnet. The Forward Range System serves additionally as a hadron calorimeter.

Figure 4.6 shows the MS, which is divided into four main parts. Inside the target spectrometer, the Barrel (B) will geometrically cover polar angles between 31° and 135° degrees, what is complemented by the Forward End-cap (EC), which geometrically covers polar angles down to 6° degrees. The removable Muon Filter (MF) will be positioned directly behind the End-cap (in beam direction) and will possess a very similar structure and size. It fulfills two main tasks: first, it increases the total absorber depth of the EC and second, it serves as an additional magnetic screen between the solenoid and the dipole magnet. The fourth part of the $\overline{\text{PANDA}}$ Muon System will be located at the forward spectrometer: the Forward Range System (FRS), which will be positioned in a distance of ≈ 9 m downstream from the interaction point with geometrical coverage of polar angles between 1° and 7° degrees.

In the Barrel part, the laminated yoke of the solenoid magnet will host in total 13 detector layers, each of them with a thickness of 3 cm. Due to mechanical reasons, the first and the last iron absorber layers will have a thickness of 6 cm. Figure 4.7 shows a typical module for the Barrel MS with alternating detector and absorber layers, which will consist of MDT's and strip boards attached to each other. The alignment of the MDT's in a regular detector layer is shown in Figure 4.8. The strip board will be realized by a fiberglass laminate board with copper metallization on one side being oriented to the MDT's. Inside the copper film, the straight strips of 10 mm width will be scratched. The design of the Barrel was chosen for the need to detect minimal ionizing muons with small initial momenta ≈ 1 GeV. The coordinate accuracy (given by the wire pitch and the stripes) of $1 \times 1 \text{ cm}^2$ is regarded as an optimal choice, since a better coordinate accuracy is not needed due to the typical multiple scattering of minimal ionizing particles inside the iron absorber. Higher pitches would reduce the precision of track reconstruction and therefore the energy reconstruction for stopped particles in the Muon System. Figure 4.10 shows a cross section view of a regular detector layer consisting of MDT plus strip board attached to it. The anode wires are oriented perpendicular to the image plane.

For the detection of muons under forward angles, bigger depths of the Muon System parts are needed. The End-cap and the Muon Filter will be equipped with absorber layers of 6 cm thickness each. Together, they will provide 11 (6+5) detection layers and 9 (5+4) iron layers. The structure of the Forward Range System will be very similar to that of the other parts of the Muon System although the size and shape is optimized for a measurement of particles with higher momenta. Therefore a large depth is needed which will be realized by a total number of 16 detection layers and, additionally, iron absorber layers of 6 cm thickness will be used.

For the zero bi-layer, the future setup has not been chosen yet. A possible realization of the zero bi-layer is a "sandwich" of two MDT's with a common strip board placed between them. The MDT's are shifted by 5 mm (= half the wire pitch of 10 mm). The longitudinal wires provide the first coordinate, while the common strip board gives the second and third coordinate. For the common strip board, a double-sided "chess board" is a possible option. The chess board is copper-laminated from both sides and pads of the size $20 \times 20 \text{ mm}^2$, are being scratched into

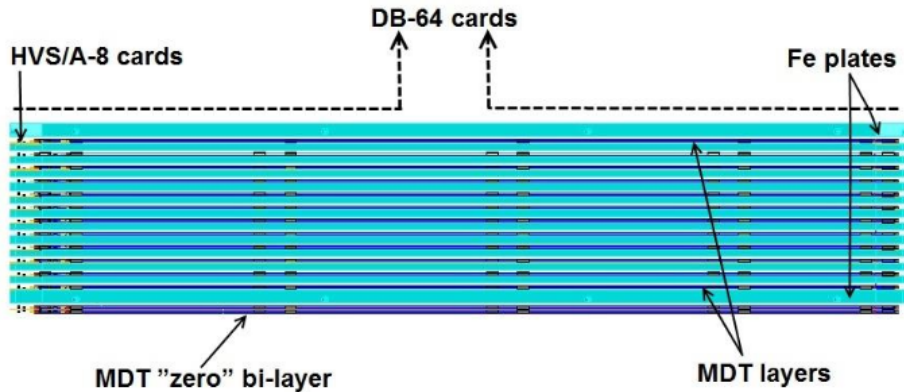


Figure 4.7: Cross section of a typical Barrel module of the $\bar{\text{P}}\text{ANDA}$ Muon System [125]. A sandwich structure of alternating absorber (Fe plates) and regular detector layers (Mini-Drift Tubes arranged in layers) is used for the detection of muons. The path length of a charged particle track inside the sandwich structure serves as one of the most powerful variables for μ/π separation, which is challenging due to the similar rest mass of muon and pion. The innermost detection layer ("zero" bi-layer) consists of two MDT layers with a common strip board in between and provides a precise starting point coordinate of each particle track.

the copper film. Those squares will be connected diagonally, so that they provide two diagonal coordinates. This realization for the zero bi-layer, consisting of the two MDT's and the "chess board", is tested during prototype tests, which are currently in progress.

For the readout system of the detector layers (MDT's plus strip boards), electronics cards with amplifiers are considered. Afterwards, the amplified signals will be fed into discriminator boards. For instance at the barrel part, the amplified signals from the wires and strips will be fed into 64-channel discriminator boards (DB-64). For the read-out of the wires, HVSA-8 cards will be used and the strips will be read-out by ASICs amplifiers Ampl-8.3 [130]. More detailed information can be found in [125].

Currently, further prototype tests are in progress at CERN and performed by the $\bar{\text{P}}\text{ANDA}$ group of JINR Dubna. One important aspect of those test measurements will be the cross check of the digitization procedure and the ability to tune the digitization algorithm in the PandaRoot software framework. Also, the abilities to separate μ/π will be tested with the prototype. Based on the results of the prototype tests, an advanced particle identification algorithm will be developed for the PandaRoot software (the software for event reconstruction and data analysis at $\bar{\text{P}}\text{ANDA}$).

Table 4.4 gives an overview of the Muon System instrumentation. The angular coverage of each subsystem in terms of polar particle production angles is illustrated in Figure 4.9 at different center-of-mass energies, which are relevant for this work.

The following section gives a more detailed description of the regular detector layers used

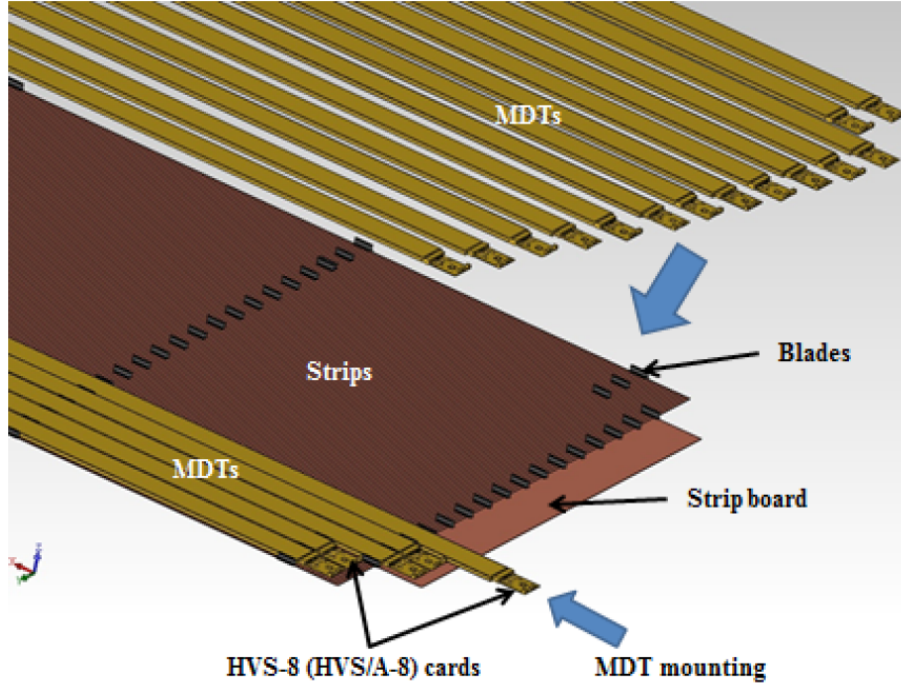


Figure 4.8: Regular detector layer of the Muon System: MDT's are attached via support "blades" onto the strip board [125]. The MDT's are typically of 4 m length, while the strips have 1.5 m length, being oriented perpendicular to the anode wires of the MDT's.

	MDT's	Wires	Strips	% of resources
Barrel	2133	17064	49916	61.2
End Cap	618	4944	8911	14.9
Muon Filter	424	3392	6876	10.7
Forward Range System	576	4608	7128	13.2
Total	3751	30008	72831	100

Table 4.4: The instrumentation of the Muon System at $\bar{\text{P}}\text{ANDA}$ [125].

for the $\bar{\text{P}}\text{ANDA}$ MS.

Regular detector layers

The detection layers of the $\bar{\text{P}}\text{ANDA}$ Muon System will be made of MDT's attached to strip boards [125]. One spatial coordinate will be provided by the MDT's (according to a Yes/No readout of the wire in the individual MDT), while the second spatial coordinate will be provided by the strip boards. A coordinate accuracy of $10 \times 10 \text{ mm}^2$ will be achieved. Muons or any other charged particle pass through the gas-filled volume and ionizes the atoms of the gas. The electrons, which were knocked off the atoms, drift along the electric field lines and end up at the positively charged anode wire.

The geometry of a single MDT is sketched in 4.10. It is of the type of a so-called *Iarocci*

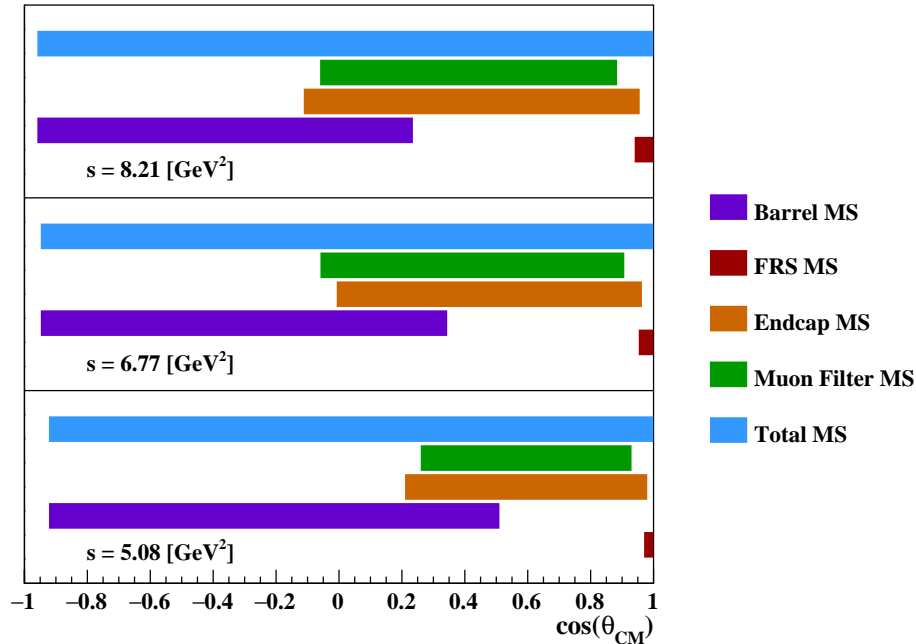


Figure 4.9: Angular coverage of the Muon System subsystems in the $\bar{p}p$ center-of-mass frame for low center-of-mass energies $s = 5.08, 6.77$ and 8.20 GeV², which are relevant for this work.

tube (streamer tube) instrumented with a metallic cathode and being operated in proportional mode for almost no aging in a high rate environment. The detection volume will be filled with a gas mixture of 70 % Argon (to avoid the absorption of free electrons) and 30 % CO₂ at atmospheric pressure. The MDT has a special "open cathode" geometry as it is shown in Figure 4.10, where a gas-tight plastic box (polyphenylene oxide, also denoted as Noryl) will surround the "comb-like" cathode. Primary particles crossing the gas filled tube will ionize the gaseous atoms. Being operated in proportional mode, the high electric field strength between anode and cathode lead to an acceleration of the ions and electrons, causing a localized avalanche of ionization reactions in the gas. Since the avalanches are highly localized, they can be used to reconstruct the hit positions and therefore the particle trajectory. The electrons drifting through the detector will be collected by the anode wire. A gas gain of $\sim 10^5$ can be realized in the proportional mode.

The external electrodes will be realized by double-sided copper-laminated fiberglass strip boards of 2 mm thickness. These strip boards will be directly placed on top of the plastic surface of the MDT's. The 1 cm wide strips are oriented perpendicular to the anode wires of the MDT's. When the charge avalanche is formed close to the anode wire of a MDT, a small signal is induced inside the strips of the external electrode which is proportional to the produced charge through ionization of the gas atoms. Since the plastic box is a dielectric medium, it is transparent to the electric pulses on the anode wires allowing the influence of small signals in the strips.

Former R&D work at JINR/LNP has demonstrated the feasibility for the two-coordinate read-

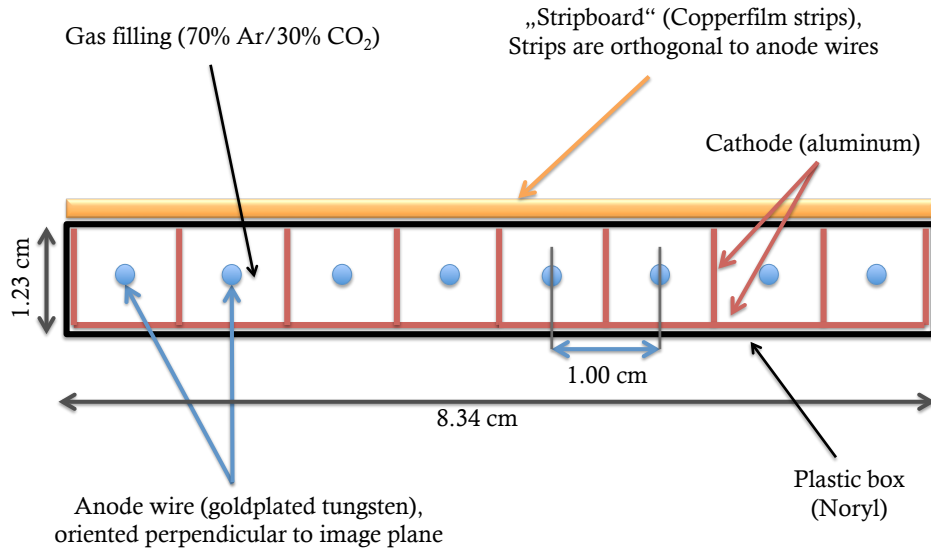


Figure 4.10: Cross section view of a Mini-Drift Tube with strip board attached to the air-tight plastic box on the open side of the aluminum cathode (red). The anode wires (blue) are oriented perpendicular to the image plane. An Argon/CO₂ mixture (70%/30%) is used as gas filling. A Yes/No readout at each anode wire for the hit reconstruction in the MDT will be done, leading to a coordinate accuracy of $1 \times 1 \text{ cm}^2$, which is given by the anode wires and the copper strips. A better accuracy is not needed due to the typical multi-scattering behavior of slow muons.

out with the detection layers consisting of MDT's plus strip boards using a prototype for the Muon System [125]. The R&D works showed, that the avalanche coordinate along the wire can be reconstructed by the perpendicularly oriented strips with high accuracy. A coordinate accuracy for the strip readout of 0.4 mm (rms) was achieved with the prototype, using a drift time measurement for the coordinate reconstruction. Such values for the coordinate accuracy is more than it is required at the \bar{P} ANDA Muon System.

In the next section, a short overview of the planned data taking phases and the corresponding conditions at \bar{P} ANDA will be given.

4.5 Phases of data taking at $\bar{\text{P}}\text{ANDA}$

- Phase-0: this phase is not part of the $\bar{\text{P}}\text{ANDA}$ Experiment. A few detector components of the future $\bar{\text{P}}\text{ANDA}$ detector will already be tested at other facilities, as e.g. the Backward End-cap of the EMC will be used for measurements at the Mainzer Mikrotron (MAMI). This phase is planned to start from 2018 until the first data taking phase of $\bar{\text{P}}\text{ANDA}$ starts.
- Phase-1: the first data taking phase of $\bar{\text{P}}\text{ANDA}$ is planned to start in 2025, when the antiprotons are available at FAIR. Since the RESR will not be present in that phase, the average luminosity will be lower in comparison to the original planned design luminosity. For the Phase-1, the average luminosity is estimated to be of the order of $10^{31} \text{ cm}^{-2}\text{s}^{-1}$. In this phase, the HESR will be used itself for the accumulation of the antiprotons. There are two consequences: a) the extra accumulation time will increase the duty cycle time (t_{exp}) and b) limits the maximum number of antiprotons per bunch to $N_{max} = 10^{10}$ due to technical limitations of the HESR. Furthermore, the $\bar{\text{P}}\text{ANDA}$ detector setup will be a reduced setup, where a few sub-detectors and the Pellet target will not be present. The corresponding sub-detectors are: Disc DIRC, the second and third GEM station, the Dipole Time-of-Flight and the Forward RICH detector.
- Phase-2: in this phase, the full detector setup of $\bar{\text{P}}\text{ANDA}$ will be present, as it is shown in Fig. 4.4. Since the RESR will not be present also in this phase, the average luminosity will be the same as in Phase-1.
- Phase-3: this phase would start, as soon as the RESR could be realized. Using the RESR, the accumulation up to 10^{11} antiprotons per bunch would be possible before they are injected into the HESR. Therefore, an average luminosity of the order of $10^{32} \text{ cm}^{-2}\text{s}^{-1}$ would be available, as it was originally planned for the operation of $\bar{\text{P}}\text{ANDA}$.

Chapter 5

Monte Carlo Simulation with PandaRoot

In this work, Monte Carlo (MC) simulation studies are used to investigate the feasibility of measuring time-like electromagnetic proton form factors (FF's) at two different $\bar{\text{P}}\text{ANDA}$ phases of data taking (Phase-1 and Phase-3, for details see Section 4.5 in the previous Chapter). In the following, the feasibility studies for the conditions of Phase-3 will be presented, where the full detector setup of the $\bar{\text{P}}\text{ANDA}$ detector will be present and luminosity will be of the order of $10^{32} \text{ cm}^{-2}\text{s}^{-1}$. A time-integrated luminosity of 2 fb^{-1} is assumed, corresponding to a pure data taking time of approximately 4 months under ideal conditions at the original design peak luminosity.

The simulation studies are based on the PandaRoot software framework [131] in combination with dedicated event generators for the signal reaction $\bar{p}p \rightarrow \mu^+\mu^-$ and the main background channel $\bar{p}p \rightarrow \pi^+\pi^-$ [132]. Also other possible background channels are studied and rejection factors are estimated based on MC simulation studies.

The PandaRoot software contains the complete $\bar{\text{P}}\text{ANDA}$ detector geometry together with a realistic magnetic field map, which was calculated with the TOSCA software [133]. Different methods have been developed for the selection and analysis of the signal process and the main background process.

The goal of this feasibility study is the estimation of the statistical and total relative uncertainty of the measurement of $|G_E|$ and $|G_M|$, their ratio R and the effective proton FF, $|F_p|$, using the $\bar{p}p \rightarrow \mu^+\mu^-$ channel.

5.1 Experimental measurement and analysis strategy

A possible strategy for the experimental measurement of the time-like electromagnetic proton FF's from the $\bar{p}p \rightarrow \mu^+\mu^-$ channel and the subsequent data analysis shall be proposed in this Section and is illustrated in Fig. 5.1.

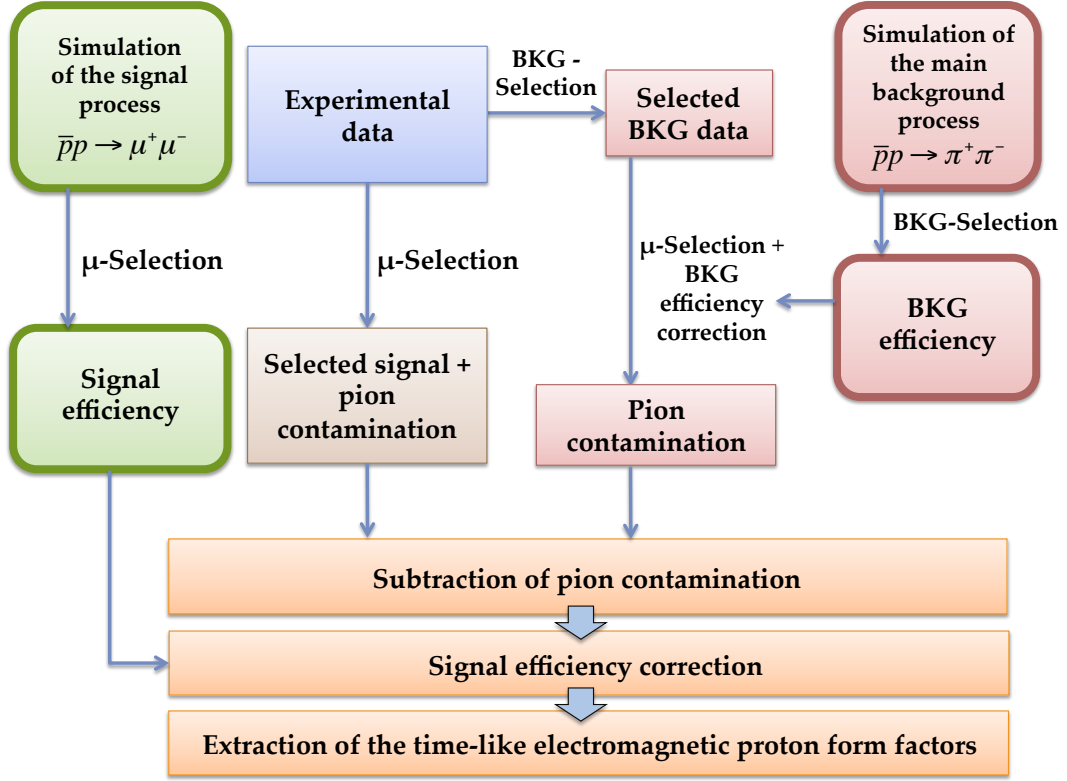


Figure 5.1: Analysis strategy for measuring time-like electromagnetic proton FF's in reactions $\bar{p}p \rightarrow \mu^+\mu^-$ at PANDA.

Two major analyses are required to extract the time-like electromagnetic proton form factors from the selected and efficiency corrected signal data. The first analysis will select the signal data and is denoted as " μ -selection" (see Figure 5.1). The second analysis aims to reconstruct the pion contamination, stemming from $\bar{p}p \rightarrow \pi^+\pi^-$ and is denoted as BKG-selection (BKG stands for *background*). Final states with subsequent pion decays will also be included in the second selection.

In the following, the strategy presented in Fig. 5.1 is described. First, the μ -selection will be applied to the measured *experimental data*, which leads to the μ -selected signal data mixed with the *pion contamination*. A background subtraction will be used in order to remove the *pion contamination* from the μ -selected data.

In order to obtain the angular distribution of the pion contamination, a separate selection for the pion background, denoted as *BKG-selection* will be applied on the *experimental data*.

The angular distribution of the reconstruction efficiency related to the BKG-selection (*BKG efficiency*) needs to be determined in a separate MC simulation and analysis study. The angular distribution of the BKG efficiency can be used afterwards for the efficiency correction of the BKG-selected data. In this way, the *pion contamination* can be subtracted.

After subtraction, the signal distribution needs to be efficiency corrected with the *signal efficiency*. The signal efficiency distribution is obtained with an independent MC simulation of high statistics for the $\bar{p}p \rightarrow \mu^+\mu^-$ process utilizing the μ -selection. The μ -selection was developed within this work based on a multivariate data analysis.

A fit function based on the formula of the differential cross section of the signal reaction will be used to fit the efficiency corrected signal distribution and to extract the time-like electromagnetic proton form factors.

The measurement of the differential cross section of the $\bar{p}p \rightarrow \pi^+\pi^-$ process should ideally be done at the data taking period for the measurement of the final states of the $\bar{p}p \rightarrow \mu^+\mu^-$ signal reaction. Therefore it is not possible to reduce the data amount e.g. by using an online trigger to reject parts of the hadronic background during this time period of data taking.

It is expected, that the pion differential cross section will be determined from the experimental data with high purity. This has two reasons: charged final states from $\bar{p}p \rightarrow \pi^+\pi^-$ can be identified at \bar{P} ANDA with a high reconstruction efficiency due to good tracking and particle identification capabilities and moreover, the cross section of the pion background process is larger by a factor of 10^5 in comparison to the signal cross section, what allows to fully suppress final states from the $\bar{p}p \rightarrow \mu^+\mu^-$ process.

5.2 Feasibility studies: Simulation and analysis strategy

In order to investigate the possibility to measure the time-like electromagnetic proton FF's with signal reactions of $\bar{p}p \rightarrow \mu^+\mu^-$ at \bar{P} ANDA, feasibility studies have been performed. They are based on the MC simulation of the signal process and of all relevant background processes at the considered values of beam momentum. The most challenging background source is the $\bar{p}p \rightarrow \pi^+\pi^-$ process. This channel is thoroughly investigated in this work.

The full simulation and analysis strategy is illustrated in Fig. 5.2 and will be described in the following. An event sample for the signal process with high statistics after application of the μ -selection (S1) is used for the determination of the signal reconstruction efficiency. A second, statistically independent sample contains the physically expected number of signal events and undergoes the μ -selection (S2).

Typical numbers of expected events for the most challenging background process of $\bar{p}p \rightarrow \pi^+\pi^-$ are of the order of 10^{11} - 10^9 at the considered values of beam momentum, assuming a time-

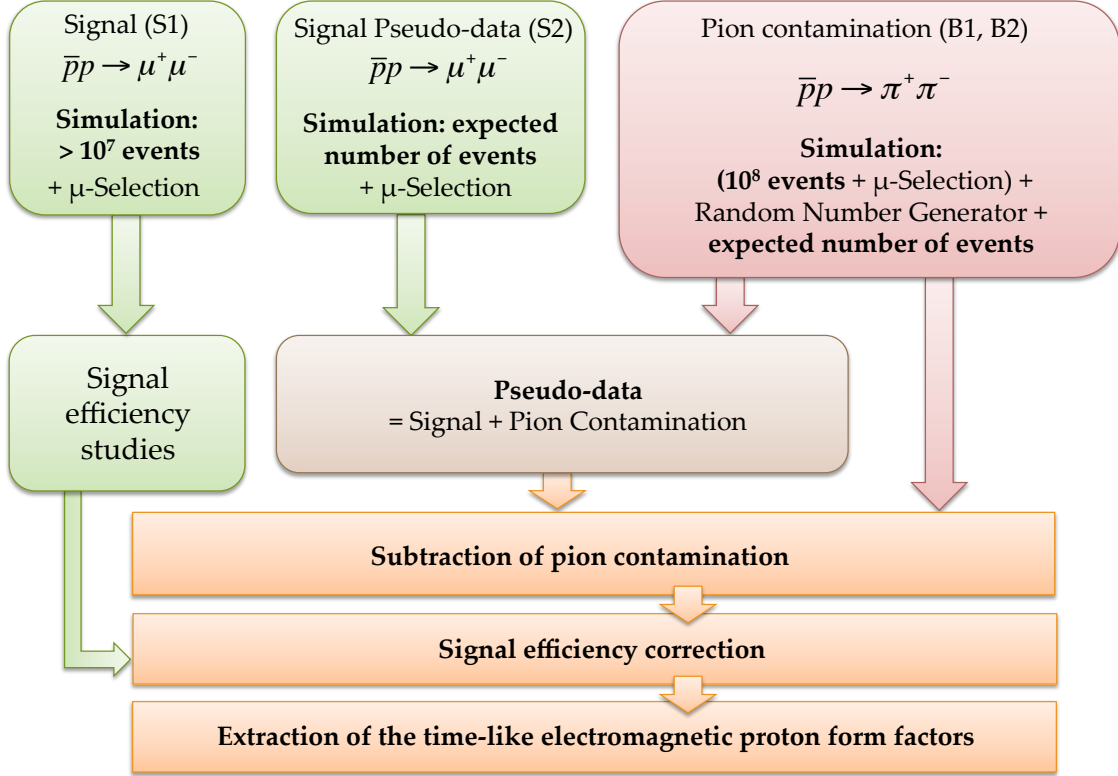


Figure 5.2: Simulation and analysis strategy used in this work. The reconstruction efficiency of the signal is studied using an event sample of high statistics (S1). The signal pseudo-data (S2) is based on the physical signal sample, which contains the number of expected signal events at the considered beam momentum. The pion contamination (B1, B2) is obtained by using a background sample of 10^8 events in combination with a Random Number Generator.

integrated luminosity of 2 fb^{-1} at $\bar{\text{P}}\text{ANDA}$ Phase-3. This value corresponds to 4 months of pure data taking time at the original $\bar{\text{P}}\text{ANDA}$ design peak luminosity ($\sim 10^{32} \text{ cm}^{-2} \text{ s}^{-1}$). The computational simulation of the expected amount of pion background data from the $\bar{p}p \rightarrow \pi^+\pi^-$ process (for detailed numbers see Tab. 5.1) is not possible within a reasonable time period. In these studies, samples of 10^8 events are generated for the individual pion background sample. This number is sufficient to determine the background rejection factor and also to include a background subtraction into this study. With the pion background rejection factor, the number of expected events for the pion contamination are calculated.

Since the expected signal-to-background (S/B) ratios after application of all cut criteria are ranging between 1:5 and 1:13, a background subtraction will be used for removing the pion contamination from the μ -selected experimental data in the future measurement at $\bar{\text{P}}\text{ANDA}$. After the background subtraction, the statistical fluctuations of the pion contamination will remain in the signal data and therefore will have an influence on the extracted values of the FF's. In

order to include this effect in this work, a background subtraction is performed. For that purpose, two statistically independent angular distributions of the expected pion contamination are needed, which contain typically between 10^5 - 10^6 events at the lowest value of beam momentum.

Since the simulation of the very large amount of physically expected background events is not possible within a reasonable time period, a method was developed in this work in order to obtain the reconstructed angular distributions of the pion contamination. Reconstructed angular distributions of the pion contamination with both the expected statistics and a more realistic shape are obtained. This is achieved by fitting the μ -selected and reconstructed background data with a 7th degree polynomial in order to extract the shape of this distribution. The obtained fit function with its parameters is used as an input for a random number generator, which fills two statistically independent histograms according to the function, until the expected statistics is reached. The new histograms contain the angular distributions of the reconstructed pion contamination (B1, B2) and are used for the further analysis.

A second method for the construction of the reconstructed pion contamination was developed to study the influence of the π^- angular distribution shape on the extracted statistical relative uncertainty of FF's and R.

The μ -selected pseudo-data are generated by adding the histograms of the reconstructed and μ -selected physical sample to the histogram of pion contamination (S2+B1). From these pseudo-data, the histogram of the second statistically independent pion contamination is subtracted (S2+B1-B2).

After that, the so obtained histogram is corrected using the signal reconstruction efficiency and finally, the proton FF's are determined.

5.3 Expected cross sections and statistics at $\overline{\text{PANDA}}$ Phase-3

Table 5.1 gives an overview of the expected number of events at PANDA Phase-3 and values of the integrated cross section for the signal and the main background process at four different beam momenta. For this calculation, a time-integrated luminosity of $\mathcal{L} = 2 \text{ fb}^{-1}$ is assumed.

For the calculation of the integrated signal cross section, Eq. 3.26 is used (with $\bar{a} = 0.8$), and the input of the FF's is required. In this work, the parameterization of $|G_M|$ given in Eq. 3.57 from Ref. [54] is used together with the assumption that $|G_E| = |G_M|$.

It can be directly seen from Tab. 5.1, that for both signal and the background process, the number of expected events decreases with increasing values of q^2 . Therefore, the highest signal data statistics will be expected in the measurements at the lowest value of beam momentum at $\overline{\text{PANDA}}$, at $p_{beam} = 1.5 \text{ GeV}/c$. Due to the $\overline{\text{PANDA}}$ detector acceptance, the signal efficiency drops fast for angles $|\cos(\theta_{CM})|$ larger than 0.8. Therefore all studies are performed for the reduced angular range of $|\cos(\theta_{CM})| < 0.8$.

p_{beam} [GeV/c]	q^2 [(GeV/c) ²]	$\sigma_{int}(\bar{p}p \rightarrow \mu^+\mu^-)$ [pb]	$N_{int}(\bar{p}p \rightarrow \mu^+\mu^-)$	$\sigma_{int}(\bar{p}p \rightarrow \pi^+\pi^-)$ [μ b]	$N_{int}(\bar{p}p \rightarrow \pi^+\pi^-)$	$\frac{\sigma(\bar{p}p \rightarrow \pi^+\pi^-)}{\sigma(\bar{p}p \rightarrow \mu^+\mu^-)}$
1.5	5.08	641	128×10^4	133	265×10^9	0.21×10^6
1.7	5.40	415	830×10^3	101	202×10^9	0.24×10^6
2.5	6.77	89.2	178×10^3	22.6	452×10^8	0.25×10^6
3.3	8.20	24.8	497×10^2	2.96	593×10^7	0.12×10^6

Table 5.1: Number of physically expected events N_{int} and integrated cross-sections σ_{int} for an angular range, which is limited to $|\cos(\theta_{CM})| < 0.8$. For the calculations, a time-integrated luminosity of $\mathcal{L} = 2 \text{ fb}^{-1}$ was assumed, corresponding to the conditions of $\bar{\text{P}}\text{ANDA}$ Phase-3. For $|G_M|$, the parameterization from Ref. [54], which is given in Eq. 3.57, is used together with the assumption that $|G_E| = |G_M|$.

From the ratio of the total cross sections, $\sigma(\bar{p}p \rightarrow \pi^+\pi^-)/\sigma(\bar{p}p \rightarrow \mu^+\mu^-)$, it can be seen that the smallest value is obtained at the beam momentum of 3.3 GeV/c, while the highest value corresponds to $p_{beam} = 2.5 \text{ GeV}/c$. Higher values of beam momentum are not considered since the corresponding cross section values are low and therefore the expected signal statistics would be poor, leading to large statistical fluctuations in the angular distribution of the signal.

5.4 Relevant background channels

The suppression of the strong hadronic background is one of the main experimental challenges measuring time-like proton FF's with the $\bar{p}p \rightarrow \mu^+\mu^-$ process. Possible background channels are

- $\bar{p}p \rightarrow n\pi^+n\pi^-m\pi^0$ with $n \geq 2$ and $m \geq 0$
- $\bar{p}p \rightarrow K^+K^-\pi^0$
- $\bar{p}p \rightarrow \pi^+\pi^-\pi^0$
- $\bar{p}p \rightarrow \pi^+\pi^-\omega$
- $\bar{p}p \rightarrow \pi^+\pi^-\rho^0$
- $\bar{p}p \rightarrow \pi^+\pi^-$
- $\bar{p}p \rightarrow K^+K^-$
- $\bar{p}p \rightarrow \pi^0\pi^0$

with cross sections, which are of the order of 0.01 up to 10 mb, depending on the channel (see Fig. 2.2 in Chapter 2). Such cross sections are in average higher by a factor of 10^4 up to 10^7 in comparison to the $\bar{p}p \rightarrow \mu^+\mu^-$ process (see Tab. 5.1).

Due to the high momentum and spatial resolution as well as the nearly 4π acceptance of the $\bar{\text{P}}\text{ANDA}$ detector, it will be possible to suppress reactions of the type $\bar{p}p \rightarrow n\pi^+n\pi^-m\pi^0$ with $n \geq 2$ and $m \geq 0$ very efficiently at $\bar{\text{P}}\text{ANDA}$. This can be done by counting the detected

charged particles in the final states and utilizing kinematical cuts as e.g. on the sum of the polar production angles in the $\bar{p}p$ center-of-mass system $(\theta^+ + \theta^-)_{CM}$, on the invariant mass $M_{inv} = \sqrt{(p_{l^+} + p_{l^-})^2}$ and on the modulus of the difference of the azimuthal angles in lab frame $|\phi^+ - \phi^-|_{lab}$. Also it is required, that both reconstructed tracks must hit the Muon System, which helps to reject events containing neutral pions which decay before they enter the Muon System. Processes, which contain ω and ρ^0 mesons, can be identified and removed by this technique since these mesons decay into pions to 100%.

The cross section of $\bar{p}p \rightarrow \pi^+\pi^-\pi^0$ is seven orders of magnitude larger than the signal cross section. Also here, the kinematical cuts are a very powerful tool to suppress this channel. In order to estimate the achievable background rejection factor for this channel, a Monte-Carlo simulation study was performed in this work. Details on the rejection factors for all relevant channels can be found in Section 6.5. The rejection factor ϵ_B is defined in this study as

$$\epsilon_B = \frac{N_{reco}}{N_{MC}} \quad (5.1)$$

with N_{reco} stands for the total number of reconstructed events after application of the μ -selection. N_{MC} stands for the number of generated MC events for the considered background process. A rejection factor of the order of 10^{-9} is achieved in a dedicated simulation study, which will be presented in Section 6.5. The signal pollution from this channel is expected to be lower than 1% at \bar{P} ANDA and thus is negligible.

The cross sections of final states with two charged (neutral) mesons are six (five) orders of magnitude larger than the signal cross section. The neutral pions from $\pi^0\pi^0$ decay electromagnetically (with a lifetime smaller than 10^{-16} s) as $\pi^0 \rightarrow 2\gamma \rightarrow 2(e^+e^-)$ even before they enter the tracking system. This process has a high probability ($> 98.82\%$). Also possible, but with a much lower probability ($< 1.18\%$), is Dalitz decay into three body final states of $e^+e^-\gamma$. Also for this channel, Monte-Carlo simulation studies have been performed and show, that it is feasible to achieve a rejection factor of this channel better than 10^{-7} .

Reactions with two charged hadrons in the final state (π or K) have cross sections, which are about six orders of magnitude larger than the signal cross section. Final states of K^+K^- can be identified much better than the states with two charged pions $\pi^+\pi^-$ due to the higher rest mass of the kaon. A Monte-Carlo simulation study for the K^+K^- channel is part of this feasibility study and shows that a suppression factor for this channel of the order of 10^{-8} can be achieved.

In comparison to the estimated value of ϵ_B for the channel of $\bar{p}p \rightarrow K^+K^-$, a better suppression factor is expected for the channel $\bar{p}p \rightarrow K^+K^-\pi^0$, where the kinematical cuts and the Muon System information are even more powerful due to the additional neutral pion in the final state. This channel has a cross section, which is roughly five orders of magnitude larger than the signal cross section.

The most important background source in this study is the production of two charged pions ($\bar{p}p \rightarrow \pi^+\pi^-$). The integrated cross-section of the $\bar{p}p \rightarrow \pi^+\pi^-$ reaction is estimated to be larger than that of the signal by a factor of 10^5 - 10^6 depending on the beam energy [134, 135]. The very similar rest masses of μ and π make it difficult to distinguish between muons and pions especially at higher particle momenta, where they show a quite similar behavior inside the \bar{P} ANDA Muon System.

In the following, the feasibility studies focus on the $\bar{p}p \rightarrow \mu^+\mu^-$ signal process and the main background process of $\bar{p}p \rightarrow \pi^+\pi^-$ under the conditions at \bar{P} ANDA Phase-3.

5.5 Simulation of the signal and background channels

5.5.1 The PandaRoot software framework

PandaRoot is the offline software for the event simulation, reconstruction and data analysis at \bar{P} ANDA, which is currently under development within the common FairRoot framework for the future FAIR experiments [136]. PandaRoot is based on the data analysis software ROOT [137] and comprises different software packages and tools for studying experimental setups and the simulation of physical processes. It possesses a modular structure with interchangeable algorithms and allows to connect all modules via interfaces and input/output of the considered data.

The common structure of the software packages used at the FAIR experiments comprises the following components:

- External packages containing the ROOT package (for data plotting, fitting, etc.), Geant3 / Geant4 [138] [139] (based on C++ and Fortran for the particle propagation through matter), Virtual Monte Carlo (VMC) [140], Pythia [141] and more.
- FairRoot taking care of the framework for data input/output, the interfaces between the modules and the infrastructure. The data are processed until the final stage of event analysis is reached and are stored in ROOT file format (several TObjects are available to store the data in trees, chains and branches).
- ExperimentRoot, which is the specific software for the individual experiment. In the case of \bar{P} ANDA, it is denoted as PandaRoot.

The standard simulation chain contains the following steps:

- Event generation. For each physical event, a set of primary particles are produced fulfilling the required kinematical properties and - if available - following the physical cross section of the process. Each produced particle has a certain particle species, a defined four-momentum and spatial production vertex and a time information. Different event generators are available, as e.g. the EvtGen [142], which allows to study a single event channel, the "Box" Generator, which creates uniform variable distributions and the EMFF

generators, which allow the creation of different electromagnetic processes and their corresponding background channels. The EMFF generators are of great importance for this work since they are used for the generation of the processes of interest.

- Transport Code - VMC. Geant is used for the simulation of the particle propagation through matter. The version can be chosen at the Monte-Carlo interface (VMC). The individual detector parts are defined with their materials and geometry and defined as active or passive materials. Particle interactions as e.g. Cherenkov radiation emission, ionization and excitation of the materials, charge transfer reactions and the production of electromagnetic or hadronic showers. The "MCHits" data includes all interaction information like spatial hit information and energy loss for each event.
- Digitization. In this step the detector response is modeled using electronic thresholds, amplification and efficiency. Those values need to be gained in real measurements with the detector components or prototypes. The data are denoted as "DigiHits" and possess the same format as the real data.
- Reconstruction. The tracking inside the individual sub-detectors is done by the local reconstruction. In this step, the DigiHits are translated into physical information about 3-dimensional hit patterns or total energy losses. Track searching and fitting is performed in the tracking subsystems. This is followed by a global reconstruction, where the local reconstructed information is combined to provide information for the event analysis. This includes combining information of neighbor sub-systems to a common information.
- The particle identification (PID) is based on the detector information from a complete sub-detector and can be combined to a global PID based on the information of different sub-detectors.
- Event analysis. At the final step the PandaRoot software provides a broad spectrum of detector information, PID probabilities and kinematical information. The reconstructed 4-momenta (event vertices) can be fitted with 4-Constraint (vertex fits) utilizing the RhoFit class, which helps to identify particle decays. Also methods for the calculation of invariant masses, the transformation of angular information from lab to the center-of-mass system of the $\bar{p}p$ system is available.

The passage of particles through the \bar{P} ANDA detector material includes the decay of unstable particles (as e.g. π , μ , K ,...). The simulation with PandaRoot is based on the same algorithms for the particle track reconstruction and analysis as they will be used later for the real data. The particle transportation can be performed either through the Geant3 or Geant4 models using the same software codes and detector geometries [136].

The basic scheme of the simulation process used in this work is shown in Fig. 5.3. After event generation, the produced final states are propagated through the material of the \bar{P} ANDA detector. For particle propagation, the GEANT4 software package [139] is used in this work.

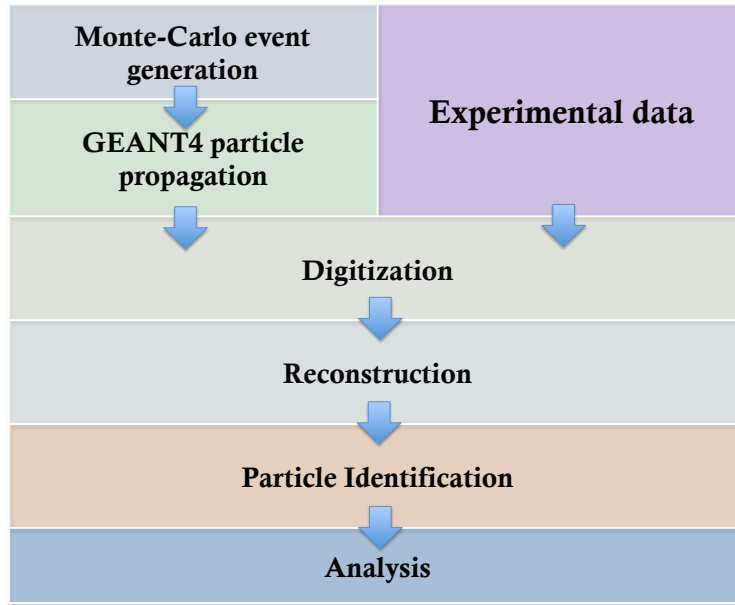


Figure 5.3: Procedure of the standard simulation and analysis chain in PandaRoot.

Afterwards, the digitization is performed, which is followed by the event reconstruction (details can be found in the following subsection). At this step, the reconstruction of the trajectories inside the sub detectors is performed by fitting the charged particle tracks. Finally, the particle identification and the analysis of the reconstructed data are conducted. For the development of powerful strategies for the rejection of events from the background channels, Monte Carlo event generators are needed to study the behaviors of muons and pions inside the $\bar{\text{P}}\text{ANDA}$ detector. A realistic detector geometry as well as reliable event generators form an important part of the used simulation and reconstruction software in this study. Two dedicated event generators ("twoLep-Gen" and "twoPionGen") are used (details are given in section 5.5.4). They are implemented into the PandaRoot software. The differences in the detector responses between the signal and all relevant background processes are studied and used for signal-background separation.

5.5.2 The Muon System in PandaRoot

Muon System Geometry

The Muon System in the PandaRoot software has been implemented with a detailed and full geometry in accordance with the technical drawings of the iron yoke in the Target Spectrometer, the Muon Filter and the Forward Range System [125]. Also different materials, which will be used, are included in the software implementation. The GEANT4 detector model is optimized for smallest possible memory consumption in Monte-Carlo Simulations.

Figure 5.4 shows the layout of the Mini Drift Tube (MDT's) detectors in the Muon System, consisting of four parts: Barrel, End cap, Muon Filter and Forward Range System. A detailed description of the Muon System of $\bar{\text{P}}\text{ANDA}$ can be found in Section 4.4. The barrel part is

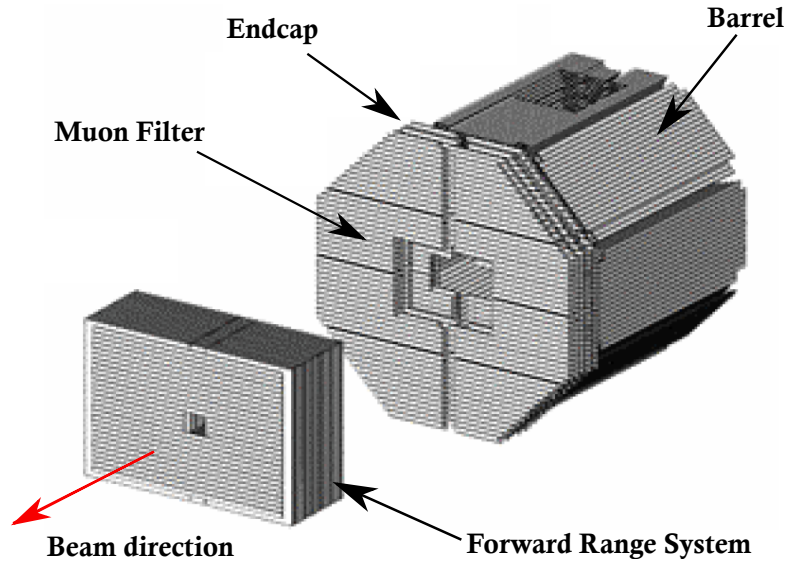


Figure 5.4: Layout of the Mini Drift Tubes (MDT's) of the \bar{P} ANDA Muon System as it is seen by the PandaRoot software.

divided into 13 absorber layers (iron) and hosts 12 detection layers (consisting of MDT's plus silicon strip boards) and the additional zero bi-layer as the innermost detection layer without iron material in front of it. The zero bi-layer helps to match tracks from the inner tracking sub-detectors (Straw Tube Tracker and Micro Vertex Detector) and the reconstructed tracklets in the MDT's with high accuracy. The geometrical description of the strip boards was performed for the whole Muon System Model in PandaRoot.

The End cap is segmented into five layers of steel plates and contains in total five detection layers with the last layer mounted outside on the fifth steel plate. A similar structure is used for the design of the Muon Filter, which consists of four steel plates alternating with detector layers.

For the Forward Range System, 16 steel plates of rectangular shape are used. The concept of the detection layers in the Forward Range System is the same as in the Barrel and the End cap, consisting of MDT's together with a zero bi-layer in the front.

Digitization

The conversion of the simulated information into digital signals (*digitization*) is currently in a preliminary stage [125]. It is implemented in a simplified way by position smearing of each MDT hit in PandaRoot. Currently ongoing Prototype tests for the Muon System will serve as input for the development of a more enhanced digitization implementation in the PandaRoot software. The magnetic field was implemented according to the TOSCA calculations with a sufficient grid size for a description inside the iron yoke segments. The influence signal on the strips of the strip boards and the their digitization is also implemented into the PandaRoot software.

Reconstruction and Particle Identification

The track reconstruction inside the Muon System is done via associating hits inside different MDT planes into tracklets. These tracklets allow to distinguish between the tracks of different particles and correlate them to tracks coming from the inner tracking system, obtaining also the corresponding PID information and vertex momenta. This is necessary for an efficient separation of muons from the large hadronic background, which is one of the main challenges of this work.

Two tracking algorithms are available for the Muon System. The first algorithm uses a global tracking what means that it extrapolates the reconstructed charged tracks from the inner tracking system to the different muon layers. MDT hits which are close to the extrapolated points are associated then within a certain correlation window. A disadvantage of this algorithm is its slowness, which makes it hard to use it for a fast *online* hardware trigger.

The second algorithm is based on a standalone track following and is used for this work. The fast track reconstruction sets the starting point at the first detection layer (zero bi-layer) and the track is followed to the outer layers. This allows also to reconstruct tracklets, where no track from the inner tracking system was reconstructed (e.g. cosmic muons crossing the $\bar{\text{P}}\text{ANDA}$ detector). When the starting point is set, hits are searched inside the next following layer inside a search cone. If multiple hits are present, the closest hit to the previous hit will be chosen. This procedure is repeated until either the following layer does not contain any hits or the last detection layer is reached. The Muon Filter and the End cap form one system and the tracklets are reconstructed over the whole system. For polar angles between 30° and 40° in laboratory frame, the Barrel and End cap overlap. In that region, the algorithm starts first with the reconstruction of a tracklet inside the Barrel part until the last hit position is known, followed by searching for close hits inside the End cap, which could be associated with the Barrel tracklet (the so-called *hybrid tracking*). By reconstructing the charged tracklets inside the search cones, the searching algorithm is able to provide detector observables like e.g. *number of hits per layer*, the *number of fired detection layers* or the *path length inside the iron absorber* material. Especially the path length inside the iron absorber in combination with the momentum reconstructed at the zero bi-layer serve as input variables for the particle identification algorithm (PID) of the Muon System. The current calculation of the PID probability from the Muon System is based on simple cuts, taking into account different cases of incoming particle momenta and thresholds. Details about the calculation can be found in Section 6.1.5.

5.5.3 Event generation of $\bar{p}p \rightarrow \mu^+\mu^-$

The event generation for the signal process $\bar{p}p \rightarrow \mu^+\mu^-$ is based on the differential cross-section given by Eq. 3.23 under the assumption that $|G_E| = |G_M|$. The "acceptance/rejection" method is used for the event generation [132], using the non-normalized probability density

function

$$f(\cos \theta_{CM}) = 1 + A \cos^2 \theta_{CM}, \quad (5.2)$$

where θ_{CM} is the polar production angle of the negative lepton with respect to the antiproton beam momentum in the $\bar{p}p$ center-of-mass system.

An upper bound $C = 1 + |A|$ is determined for the density function with $f < C$. To obtain an event, a value of $\cos\theta_{CM}$ is generated using a Random Number Generator in a user specified range. At this step, a flat probability density is used for the generation of $\cos\theta_{CM}$. After that, the corresponding value of the cross section is calculated. A second random variable y between 0 and C is generated uniformly and y is compared to the calculated value of the cross section. The event is accepted, if y does not exceed the cross section value, otherwise the event is rejected. For accepted events, also the azimuthal angle ϕ_{CM} is uniformly generated in the range of $[0, 2\pi]$. Here, ϕ_{CM} is the production angle of the lepton with negative charge in the azimuthal plane, which is perpendicular to the beam direction. Finally the final state four-momenta of the particles are calculated from the values of $\cos\theta_{CM}$ and ϕ_{CM} . This procedure is repeated until a user-specified number of accepted events is reached.

Currently, this event generator does not include radiative corrections, which are expected to be small in case of the muon channel. In particular, the largest contribution is expected from final state radiation, which should be much smaller for the muon channel in comparison to the electron channel due to the large mass of the muon in comparison to the electron. An event generator, which also takes into account first order radiative corrections for the electron channel is currently under development by the Mainz EMP group, and will be extended to the case of muons in the future. In this work, the influence of final state radiation in the muon channel was investigated and will be presented in Sec. 7.8, Chapter 7.

For the reconstruction efficiency study of the signal process, a data sample with high statistics is generated at each value of beam momentum (see Table 5.2). A statistically independent data sample for the expected signal data contains the number of expected events (as listed in Table 5.2) depending on the antiproton beam momentum. The event generation was limited to the angular range of $|\cos\theta_{CM}| < 0.8$ due to two reasons. The first reason is the PANDA detector acceptance, which leads to quickly dropping signal reconstruction efficiencies for values of $|\cos\theta_{CM}| \geq 0.8$. The second reason is the generation of a sufficient number of background events, since at higher values of beam momentum, the differential cross section diverges for values of $|\cos\theta_{CM}| \rightarrow 1$ (see Fig. 5.5).

5.5.4 Event generation of $\bar{p}p \rightarrow \pi^+\pi^-$

For the simulation of the main background channel $\bar{p}p \rightarrow \pi^+\pi^-$, a dedicated event generator ("twoPionGen") has been developed by Ref. [132] using phenomenological parameterizations from [54] based on different reaction mechanisms of the $\bar{p}p \rightarrow \pi^+\pi^-$ reaction. In this work, both the proton target and the antiproton beam are unpolarized as well as final state pions, which

p_{beam} [GeV/c]	q^2 [(GeV/c) ²]	$N_{gen}^{(1)}(\mu^+\mu^-)$ x 10 ⁷	$N_{gen}^{(2)}(\mu^+\mu^-)$
1.5	5.08	4.98	1281441
1.7	5.40	4.27	829762
2.5	6.77	4.38	178369
3.3	8.20	4.33	49658

Table 5.2: Number of generated Monte-Carlo events (N_{gen}) for each value of the considered beam momenta. The reconstruction efficiency of the signal is determined with samples of high statistics ($N_{gen}^{(1)}$). For the data analysis, real data samples with the expected signal statistics are generated ($N_{gen}^{(2)}$), each containing the expected number of signal events under the assumption of a time-integrated luminosity of $\mathcal{L}= 2 \text{ fb}^{-1}$ (corresponding to $\bar{\text{P}}\text{ANDA}$ Phase-3).

are generated. Antiproton momenta from 0.79 GeV/c up to 12.0 GeV/c in laboratory frame are covered. Since there is no single description for the whole kinematic range available, the cross section parameterization is performed independently at different kinematic regimes, depending on the fact, if there are data or theoretical predictions available. The full kinematical range is divided into three subregions, denoted as the "low energy region", "high energy region" and the "transition energy region".

In the following, a brief description of this parameterization is given.

The low energy region

For antiproton beam momenta p_{beam} (in lab frame) in the range of $0.79 \leq p_{beam} \leq 2.43 \text{ GeV}/c$ (denoted as the "low energy region"), data taken at the CERN 28 GeV proton synchrotron [134] were used for the cross section parameterization. The differential cross section $d\sigma/d\Omega$ (with $d\Omega = d\cos\theta_{CM} d\phi$) was measured as a function of $\cos\theta_{CM}$ at 20 different values of beam momentum. An angular range of $|\cos\theta_{CM}| < 0.94$ was covered in these measurements. For each value of beam momentum the data were fitted with a Legendre polynomial series

$$\frac{d\sigma}{d\Omega} = \sum_{n=0}^{n_{max}} a_n P_n(\cos\theta_{CM}), \quad (5.3)$$

where a_n are the free fit parameters and P_n stands for the Legendre polynomial of the order n . The number of orders were varied in order to achieve an optimal value of χ^2 per degree of freedom (denoted as *reduced* χ^2) close to unity. This was achieved by adding sequentially the next higher order a_{n+1} to the previously used polynomial series of the order n and comparing both reduced χ^2 from the current and the previous fit, until the reduced χ^2 did not improve significantly. At the highest value of beam momentum in the low energy region, several orders n for the fit function were considered. The same number of orders, up to a_{10} were then used for the whole low energy range [132].

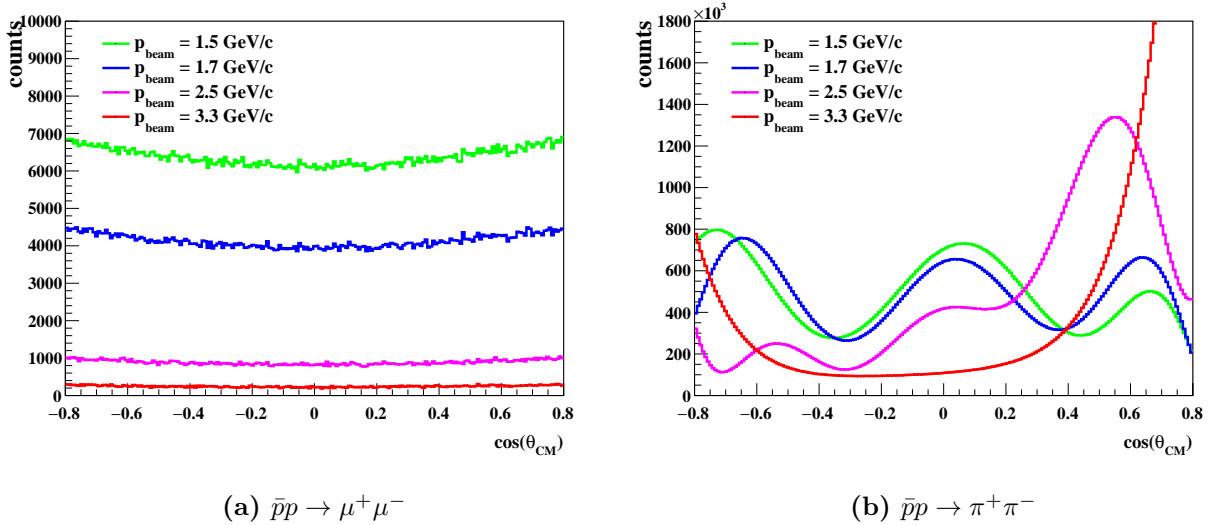


Figure 5.5: Angular distributions of the Monte-Carlo generated negatively charged final state particles before reconstruction at $p_{beam} = 1.5$ GeV/c (green), 1.7 GeV/c (blue), 2.5 GeV/c (magenta) and 3.3 GeV/c (red) for (a) the signal process $\bar{p}p \rightarrow \mu^+\mu^-$ and (b) the main background process $\bar{p}p \rightarrow \pi^+\pi^-$. Due to the limited \bar{P} ANDA detector acceptance, the events have been generated in the angular range $|\cos(\theta_{CM})| < 0.8$.

The high energy region

For beam momenta in the range of $5.0 \leq p_{beam} \leq 12.0$ GeV/c (the so-called “high energy regime“), predictions by J. van de Wiele and S. Ong have been made recently using a Regge theory approach [135]. The model is expected to be valid for large values of the center-of-mass energy squared s . Details be found in Ref. [135]. For obtaining the cross section parameterization, the model is compared to the available data from [143, 144, 145, 146] in order to determine the values of the few model parameters.

The transition energy region

For momenta in the intermediate region $2.43 < p_{beam} < 5.0$ GeV/c, an interpolation is used since there are no available data or valid models existing. The Regge-inspired parameterization, which is used in the high energy region, was extrapolated from the lowest value of 5.0 GeV/c down to 3.0 GeV/c, with 4 numerical values of the differential cross section are available at different antiproton momenta. In range of 2.43 GeV/c up to 3.0 GeV/c, where no predictions from theory or data are existent, the values of the cross section at the borders were used for interpolation.

The event generator covers all values of beam momentum and angle $\cos\theta_{CM}$ over the full kinematical range at \bar{P} ANDA. This was reached by a linear nearest neighbor interpolation between points $(p_{beam}, \cos\theta_{CM})$ with a given value of the differential cross section.

Figure 5.6 shows the differential cross section for the process of $\bar{p}p \rightarrow \pi^+\pi^-$ at different values of beam momenta, p_{beam} , (in lab frame). The functions, which are used for the event generation, are also shown.

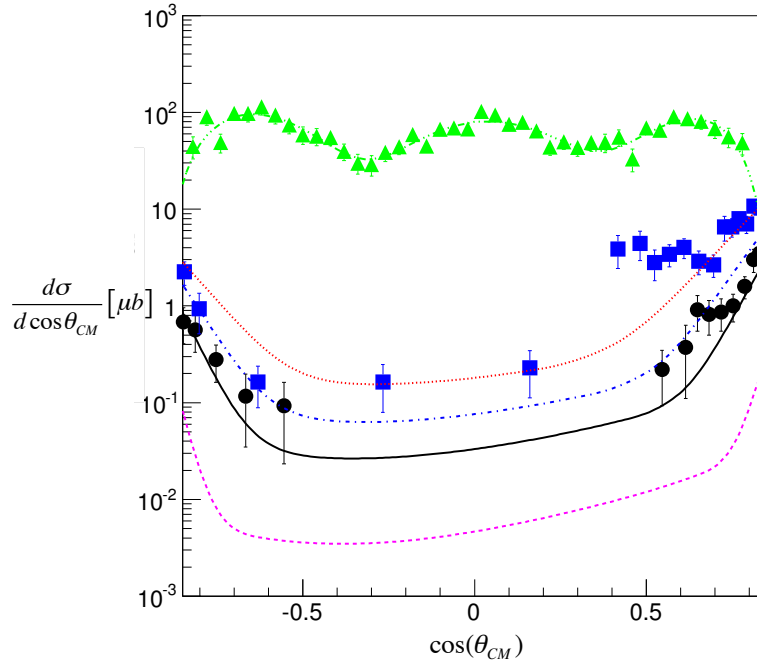


Figure 5.6: Angular distributions of data and model calculations for the π^- angular distribution from the main background reaction $\bar{p}p \rightarrow \pi^+\pi^-$ as a function of $\cos(\theta_{CM})$ [16] at the following values of beam momentum: p_{beam} at 1.7 GeV/c (green triangles and dash-triple dotted line) from Ref. [134], 5 GeV/c [143] (blue full squares and dash-dotted line) and 6.21 GeV/c [144] (black full circles and solid line). For $p_{beam} = 3$ GeV/c (red dotted line) and $p_{beam} = 10$ GeV/c (magenta dashed line) the results of the event generator are given additionally.

Both event generators ("twoLepGen" respectively "twoPionGen") follow the same generation procedure which was described in Section 5.5.3. The starting point is the differential cross section at a fixed point of $(p_{beam}, \cos\theta_{CM})$ obtained by the description for the background channel given above. From that point, the procedure of event generation is the same as described for the signal in Section 5.5.3.

For the main background $\bar{p}p \rightarrow \pi^+\pi^-$ reaction, an event sample containing 10^8 events was generated at four different beam momenta ($p_{beam} = 1.5, 1.7, 2.5$ and 3.3 GeV/c) in the range of $|\cos(\theta_{CM})| < 0.8$. The angular distribution of the generated π^- is depicted in Fig. 5.5 b) at $p_{beam} = 1.5$ GeV/c (green), 1.7 GeV/c (blue) and 3.3 GeV/c (magenta).

Since the expected number of pion background events is of the order of $10^{11} - 10^9$ for beam momenta between 1.5 and 3.3 GeV/c, the generation of event samples with realistic statistics

is not feasible in this work. However, the number of 10^8 events is sufficient for the estimation of the pion background rejection factor and for the construction of the angular distribution of the expected pion contamination in the μ -selected signal. Since the pion contamination will typically be larger by a factor of 4 up to 9 in comparison to the signal, a subtraction of this background is foreseen as a part of the data analysis of the real data at $\overline{\text{PANDA}}$. The subtraction requires the measurement of the differential cross section of the $\bar{p}p \rightarrow \pi^+\pi^-$ process in a separate analysis. From that, the angular distribution of the pion contamination can be obtained. Since this angular distribution will be obtained by a different analysis than the signal events, the statistical fluctuations will not be the same as in the pion contamination which will be hidden inside the μ -selected signal data. Therefore, two statistically independent pion contamination distributions for the $\bar{p}p \rightarrow \pi^+\pi^-$ process were constructed in this work and are used in the analysis. A detailed description of a possible analysis strategy of the experimental data later was given in Sec. 5.1.

After the event generation, the simulation follows the standard chain, as it is illustrated in 5.3. The next step after the reconstruction of the events, is the data preselection, which will be presented in the following section.

Chapter 6

Analysis of the Event Samples

In the last section, the simulation tools and the procedure for MC simulation of both the signal and the main background process were described. In this chapter, the first step of the analysis is presented: the preselection, which in particular allows to reduce the amount of background data by e.g. suppressing secondary particles.

6.1 Preselection of the pseudo-data

In this work, the "raw events", on which no cut has been applied yet, are denoted as *reconstructed events*. The reconstructed events contain the reconstructed momenta, production vertices, production angles, PID information etc. of the simulated particles and are available after the reconstruction and the particle identification steps of the Standard Chain for Simulation and Analysis with Panda Root (Fig. 5.3, Chapter 5). Such events contain not only primary, but also secondary particles. A first event filtering is performed, which is denoted in the following *data preselection*.

6.1.1 Requirements for data preselection

Before the signal background separation can be performed, the preselection criteria are applied to the data. Since the muon pairs will consist of two particles of opposite charge, the preselection criteria for each individual event are chosen as described the following:

- Each event must contain one positive and one negative track after the preselection.
- If more than one positive-negative track pair can be combined, the pair with the value of $(\theta^+ + \theta^-)_{CM}$ which is the closest to 180° is selected.
- The identification of muons require the information of the Muon System. Therefore it is essential for the preselection, that both tracks enter the Muon System. Events without information from the Muon System are discarded.

Since the decay of unstable particles is included in these simulations, pion decay into a muon (and the corresponding (anti-)neutrino) is considered as well. The amount of such muons from pion decay and possible rejection factors will be investigated in this work.

Another source of secondary particles is the interaction of pions with the detector material which can produce heavier hadrons like kaons and protons. The composition of the preselected events is presented in the following section.

6.1.2 Composition of the preselected events for the $\bar{p}p \rightarrow \pi^+\pi^-$ background process

First, the composition in terms of particle species shall be investigated. After preselection of the reconstructed events, MC information can provide information about the different particle species which can be found in the data. As an example, we consider the case of the lowest beam momentum, 1.5 GeV/c. About 7.27×10^6 ($\approx 7.27\%$) of the MC generated events (10^8) for the $\bar{p}p \rightarrow \pi^+\pi^-$ process are accepted by the preselection after event reconstruction.

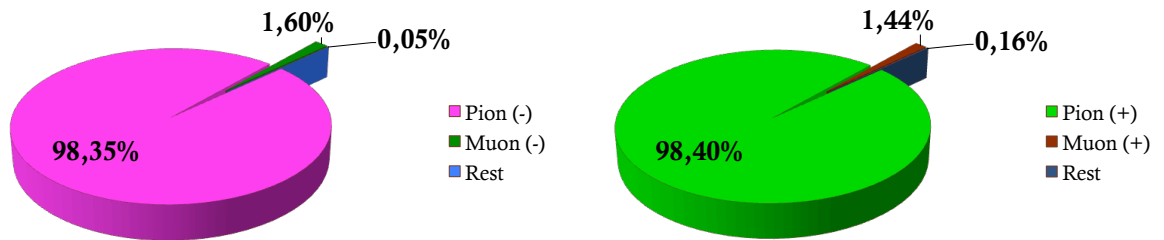
Table 6.1 shows the composition of the preselected data in terms of particle species. An illustration of the percentages of different species of particles from the selected data is shown in Fig. 6.1 for the case of $p_{beam} = 1.5$ GeV/c. From the preselected events (7.27×10^6 events), around 1.56% of the events contain at least one μ^- (1.44% in the case of μ^+) produced by a pion decay. Also electrons (positrons) can be found, but with a very low contribution to the preselected events ($< 0.01\%$), which are caused by interaction of the primary pions with the detector material.

Heavier particles, like K mesons, protons or neutrons can be produced in hadronic interactions (e.g. quasi-elastic charge transfer reactions or pion induced nucleon knock-out processes). The EMC has a thickness of about 20 radiation lengths X_0 , which corresponds to slightly more than one hadronic interaction length λ_0 . Therefore more than 30% of the pions are expected to undergo nuclear interactions before they reach the Muon System. Charge exchange reactions, as for instance, the conversion of a π^+ to a π^0 , result in a subsequent decay of the π^0 into two photons, which are detected by the EMC. In this case, the requirement that both tracks show hits in the Muon System, will lead to a sufficient rejection of such events. The Monte Carlo information of the reconstructed and preselected events from the background sample shows a percentage of π^- (π^+) larger than 98% (see Fig. 6.1). The amount of secondary muons is smaller than 2% for all positively (negatively) charged tracks. Other particle species ($K^{+/-}$, proton, neutron, $e^{+/-}$) contribute with less than 0.2% to the total amount of preselected events. It can be seen that for $\approx 0.03\%$ of the generated π^- (π^+), the tracks are misclassified after the preselection as a positively charged track (and vice versa). Also for the case of $p_{beam} = 1.7$ GeV/c, the composition of the reconstructed and preselected data in terms of the particle species is shown in Tab. 6.2 and illustrated in Fig. 6.2. The percentage of misclassified tracks is similar to the case of $p_{beam} = 1.5$ GeV/c.

For the signal process of $\bar{p}p \rightarrow \mu^+\mu^-$, the composition of the reconstructed and preselected signal sample of high statistics was investigated. More than 99,99% of the generated and preselected μ^- (μ^+) are correctly identified as μ^- (μ^+). In less than 0.01% of the cases, the positive

Table 6.1: Composition of the reconstructed and preselected background event sample for the $\bar{p}p \rightarrow \pi^+\pi^-$ process. The preselection of the reconstructed data requires one positively (+) and one negatively (-) charged track per event. In total 7.27×10^6 events from the generated background sample were accepted by the preselection at $p_{beam} = 1.5 \text{ GeV}/c$. 10^8 events were originally generated.

1.5 GeV/c	MC Particle code	Tracks with negative charge (-)	Tracks with positive charge (+)
π^-	-211	7152340 (98.35%)	2202 (0.03%)
π^+	211	2193 (0.03%)	7155600 (98.40%)
μ^-	13	116280 (1.56%)	35 (< 0.01%)
μ^+	-13	51 (< 0.01%)	105035 (1.44%)
e^-	11	120 (< 0.01%)	239 (< 0.01%)
e^+	-11	15 (< 0.01%)	21 (< 0.01%)
p	2212	1138 (0.02%)	8648 (0.12%)
K^+	321	15 (< 0.01%)	371 (< 0.01%)
K^-	-321	2 (< 0.01%)	0 (0.00%)
n	2112	1 (< 0.01%)	0 (0.00%)
not identified	-	2 (< 0.01%)	6 (< 0.01%)
Σ total		7272157 (100%)	7272157 (100%)



(a) Tracks with negative charge

(b) Tracks with positive charge

Figure 6.1: Particle species and their contribution to the reconstructed and preselected data for the $\bar{p}p \rightarrow \pi^+\pi^-$ process at $p_{beam} = 1.5 \text{ GeV}/c$. The percentages of the different particle species (MC particle code) inside the reconstructed and preselected tracks with (a) negative charge and (b) positive charge are illustrated.

Table 6.2: Composition of the reconstructed event sample for $\bar{p}p \rightarrow \pi^+\pi^-$ after preselection. In total 7.82×10^6 events from the generated sample (1×10^8 events were originally generated for the $\bar{p}p \rightarrow \pi^+\pi^-$ process) were accepted by the preselection at $p_{beam} = 1.7 \text{ GeV}/c$. The preselection of the reconstructed data requires one positively (+) and one negatively (-) charged track per event. Different particle species can be found in the preselected data, the percentage and absolute numbers are given.

1.7 GeV/c	MC Particle code	Tracks with negative charge (-)	Tracks with positive charge (+)
π^-	-211	7699246 (98.44%)	2961 (0.04%)
π^+	211	2612 (0.03%)	7701031 (98.46%)
μ^-	13	117953 (1.51%)	45 (< 0.01%)
μ^+	-13	47 (< 0.01%)	106989 (1.37%)
e^-	11	140 (< 0.01%)	250 (< 0.01%)
e^+	-11	16 (< 0.01%)	28 (< 0.01%)
p	2212	1588 (0.02%)	9851 (0.13%)
K^+	321	9 (< 0.01%)	457 (< 0.01%)
K^-	-321	4 (< 0.01%)	0 (0.00%)
n	2112	0 (0.00%)	0 (0.00%)
not identified	-	3 (< 0.01%)	6 (< 0.01%)
Σ total		7821618 (100%)	7821618 (100%)

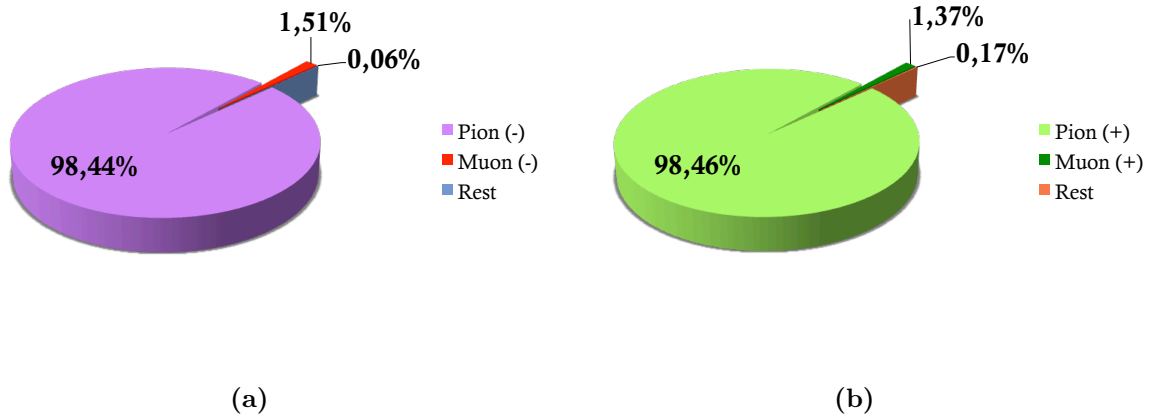


Figure 6.2: Particle species and their contribution to the reconstructed and preselected event sample (based on the generated sample for the $\bar{p}p \rightarrow \pi^+\pi^-$ process) at $p_{beam} = 1.7 \text{ GeV}/c$ for (a) tracks with negative charge and (b) positive charge.

(negative) track was misclassified as opposite charge (and vice versa). The only species except from muons, are secondary electrons ($< 0.005\%$).

In the following, the decay of pions on the example of the reconstructed and preselected data based on the pion background event sample will be discussed.

6.1.3 Muons from pion decay

In this feasibility study, the pion and the muon are treated as unstable particles, which can undergo a decay on their way through the detector. Since the charged pion has a mean lifetime of $\tau_0 = 2.6 \cdot 10^{-8}$ s, it is possible that the pion decays before reaching the muon system. A rough estimation of the decay rate can be made, based on the law of decay as a function of the distance x [m] between the target interaction point and the zero layer of the Muon System:

$$\frac{N(x)}{N_0} = e^{-\frac{x}{\beta\gamma c\tau_0}} \quad (6.1)$$

Here, β is the velocity of the π and $\gamma = E_\pi/m_\pi c^2$. For this very rough estimation, the influence of the magnetic field on the particle's trajectory is neglected, as well as interactions with the detector material. Pions, which are produced at a beam momentum of 1.5 GeV/c, have particle energies between $E_{min,lab} \approx 0.64$ GeV ($E_{max,lab} \approx 2.09$ GeV), which corresponds to the maximum (minimum) polar production angle, θ_{lab} , in the lab frame. With a corresponding distance of 2.65 m (1.68 m) between interaction point and the zero-bi layer of the Muon System, a fraction of 2.2% (4.7%) of the produced π is expected to decay before they reach the Muon System.

The Monte-Carlo simulation shows, that indeed a small percentage of pions decay on their way to the Muon System. Table 6.3 summarizes the percentage of generated Monte-Carlo events, which suffer a decay of one or both pions at the considered values of beam momentum. At $p_{beam} = 1.5$ GeV/c, 2.2% (2.5%) of the 10^8 MC generated π^- (π^+) undergo a decay, while the corresponding partner pion of opposite charge survives. Both pions decay only with a probability of 0.07% as $\pi^+\pi^- \rightarrow \mu^+\mu^-\bar{\nu}_\mu\nu_\mu$, which makes a sufficient suppression of such events possible at \bar{P} ANDA. This will be discussed in section 6.5. However, also such events will be removed by the background subtraction.

Table 6.3: Percentage of MC events without/with pion decay (one respectively both of the final state pions) in 10^8 generated events at the considered values of beam momentum.

p_{beam}	1.5 GeV/c	1.7 GeV/c	2.5 GeV/c	3.3 GeV/c
no decay	95.22%	95.15%	94.92%	94.65%
$\mu^-\mu^+$	0.07%	0.07%	0.08%	0.11%
$\pi^-\mu^+$	2.47%	2.49%	2.55%	2.71%
$\mu^-\pi^+$	2.24%	2.29%	2.45%	2.53%

Figure 6.3 and Fig. 6.4 show the spatial distribution of the pion decay vertices from $\pi^- \rightarrow \mu^-\bar{\nu}_\mu$ from Geant4 (MC truth information from the MCHits data) in the x-y respectively x-z

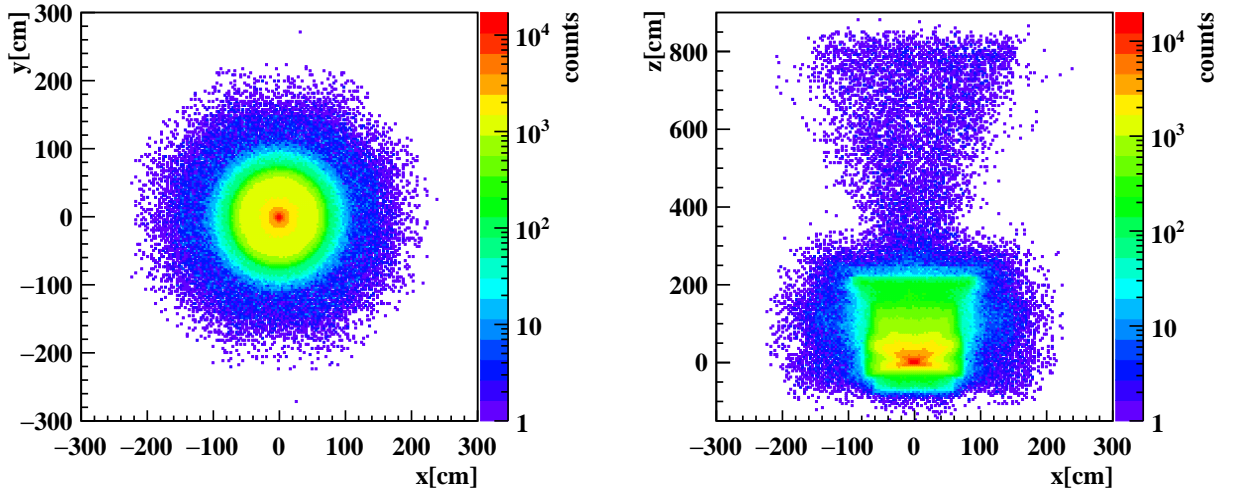


Figure 6.3: Spatial production vertices of the μ^- from the decay process $\pi^- \rightarrow \mu^- \bar{\nu}_\mu$ from Geant4 in (left) the x-y plane and (right) the x-z plane (lab frame) at $p_{beam} = 1.5$ GeV/c. The antiproton beam points along the the z-axis, the x-y plane is oriented perpendicular to the beam direction, where the y-axis is oriented antiparallel to the hydrogen injection from above by the Cluster-Jet target. The x-z plane shows a cross section view through the \bar{P} ANDA detector. Most of the pion decays occur close to the origin of the $\pi^- \pi^+$ production.

plane around the $\bar{p}p$ interaction vertex at $p_{beam} = 1.5$ GeV/c and 3.3 GeV/c, respectively. It can be seen that most of the pion decays occur very close to the interaction vertex.

Figure 6.5 shows the residual of the production angles $|\theta_\pi - \theta_\mu|$ (in laboratory frame, [DEG]) between the original pion (with negative charge) and its decay muon from the MC truth information (MCHits data) for (a) $p_{beam} = 1.5$ GeV/c and (b) $p_{beam} = 3.3$ GeV/c.

At 1.5 GeV/c it can be seen that, if the pion was emitted under forward angles, most of the secondary muons are produced within a cone with an opening angle (*kink angle*) $|\theta_\pi - \theta_\mu|$ up to 1° [DEG] around the original flight direction of the π^- (see Fig. 6.5). In particular at 3.3 GeV/c, where the differential cross section for the $\bar{p}p \rightarrow \pi^+ \pi^-$ process diverges for values of $\cos(\theta_{CM}) > 0.8$ (see Fig. 5.5 (b)), the produced pions possess high momenta in the laboratory frame when produced under forward angles. If then a decay occurs very close to the interaction point, what means so far only little or no interaction happened with the detector material, the kink angles between the pion and its decay muon (in laboratory frame) are small. In such events, the decay muon behaves like the original pion. Such high energetic secondary muons can most probably not be distinguished from a signal muon in the μ -selection. Simulation studies allow to estimate the achievable rejection factors for the different final states from the $\bar{p}p \rightarrow \pi^+ \pi^-$ reaction, which can contain also decay muons. The rejection factors will be given in Sec. 6.5. Events, which suffer from a decay of a single or both final state pions, will also be removed later by the background subtraction.

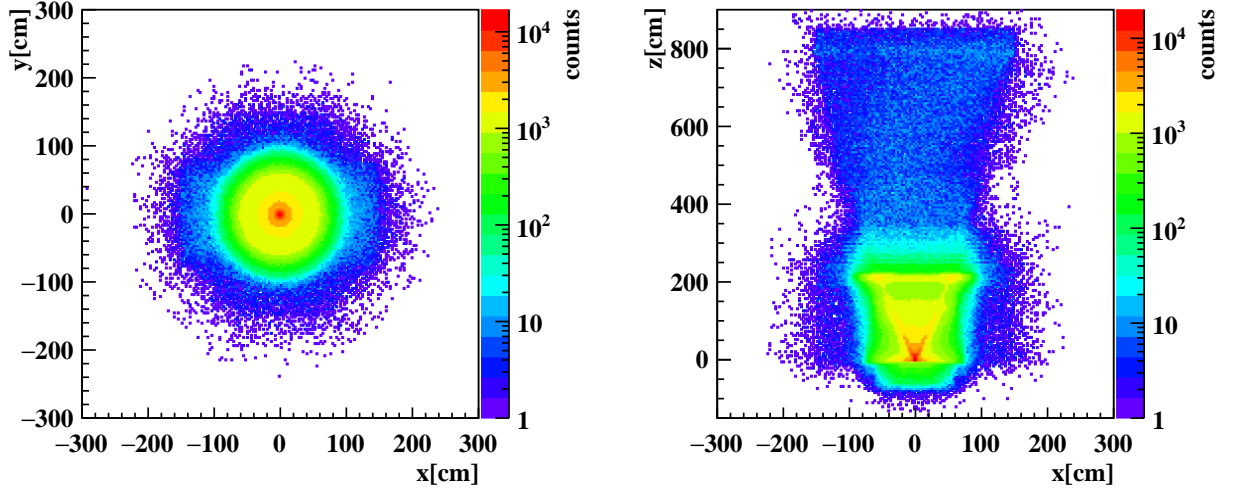


Figure 6.4: Spatial production vertices of the μ^- from the decay process $\pi^- \rightarrow \mu^- \bar{\nu}_\mu$ from Geant4 at $p_{beam} = 3.3$ GeV/ c in (left) the x-y plane and (right) the x-z plane (lab frame). The antiproton beam points along the the z-axis, the x-y plane is oriented perpendicular to the beam direction, where the y-axis is oriented antiparallel to the hydrogen injection from above by the Cluster-Jet target. The x-z plane shows a cross section view through the \bar{P} ANDA detector.

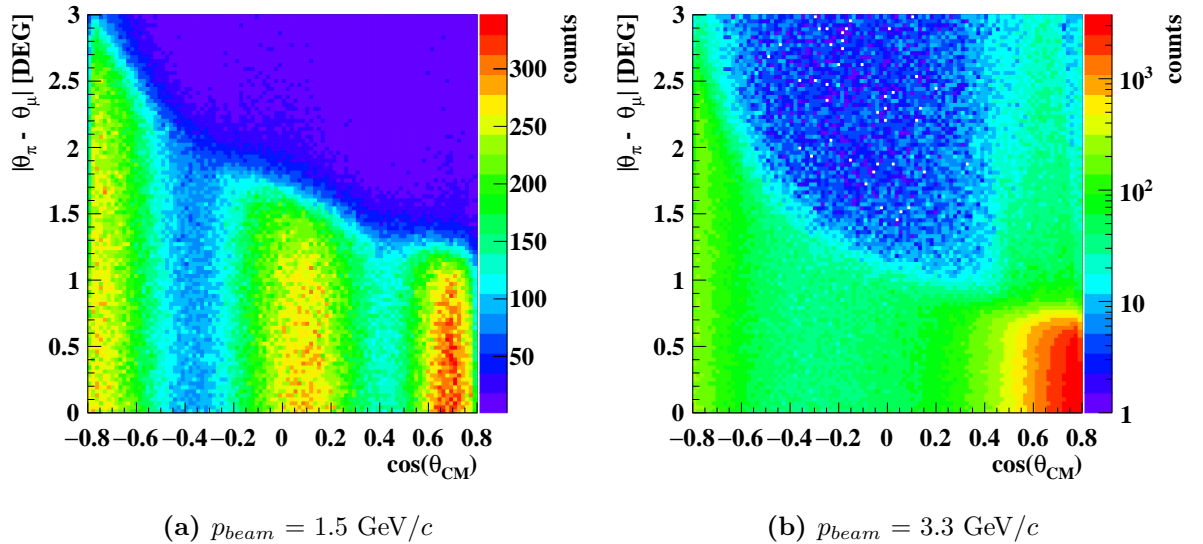


Figure 6.5: Residual of production angles (in laboratory frame) of the primary pion and the secondary muon from the decay $\pi^- \rightarrow \mu^- \bar{\nu}_\mu$ depending on $\cos(\theta_{CM})$ at $p_{beam} = 1.5$ GeV/ c (left) and $p_{beam} = 3.3$ GeV/ c (right). Most of the pions possess high momenta in laboratory frame. For such pions, the decay muon is emitted under a small angle $|\theta_\pi - \theta_\mu|$ (in laboratory frame, [DEG]) with respect to the flight direction of the original pion.

6.1.4 Kinematical variables and detector observables

Both the signal $\bar{p}p \rightarrow \mu^+\mu^-$ and the main background $\bar{p}p \rightarrow \pi^+\pi^-$ process have two-body final states with particles of equal mass. In the CM system, the muon (pion) pairs are emitted back-to-back, carry the whole energy of the initial state and can be both measured due to the high detection capabilities at PANDA. For the track reconstruction, the STT and MVD provide the most important information of the charged particles. Several observables can be used to separate the signal from the background. In the following, we present the properties of different variables after the data have been preselected.

Kinematical variables

Kinematical variables are used to suppress secondary particles and thus, ensure a high quality of the data. One of the kinematical variables is $(\theta^+ + \theta^-)_{CM}$, which is the sum of the polar production angles of both charged tracks in the center-of-mass frame. The polar production angle of a particle in laboratory frame is obtained from the reconstructed three-momentum. The determination of the three-momentum at vertex is based on the trajectory reconstruction using information from both STT and MVD. From the three-momentum, the particle's energy at production vertex is calculated assuming muon mass hypothesis. After Lorentz-Transformation into the center-of-mass system, the sum of the polar production angles $(\theta^+ + \theta^-)_{CM}$ is ideally peaked around 180° , since the final state particles are produced back-to-back in the $\bar{p}p$ -center-of-mass frame. The corresponding distribution of $(\theta^+ + \theta^-)_{CM}$ is depicted in Fig. (6.6 (a) at $p_{beam} = 1.5$ GeV/c, (c) at $p_{beam} = 1.7$ GeV/c and in Fig. 6.7 (a) at $p_{beam} = 2.5$ GeV/c, (c) at $p_{beam} = 3.3$ GeV/c.

For all cases, one can see that the peak of the background distribution is shifted to smaller angles in comparison to the signal peak, due to the assumed muon mass hypothesis, which does not hold for the pions. Thus, the $(\theta^+ + \theta^-)_{CM}$ variable will contribute to the signal-background separation later.

From the determined four-momenta, the invariant mass M_{inv} is calculated as

$$M_{inv} = \sqrt{(p_1 + p_2)^2}, \quad (6.2)$$

where $p_{1,2}$ are the four-momenta of the produced final state particles. Cuts are applied during the analysis on this variable in order to suppress events, which contain secondary particles. The distributions of M_{inv} after data preselection at the considered values of beam momentum are shown in Fig. 6.6 (b) at $p_{beam} = 1.5$ GeV/c, (d) at $p_{beam} = 1.7$ GeV/c and in Fig. 6.7 (b) at $p_{beam} = 2.5$ GeV/c, (d) at $p_{beam} = 3.3$ GeV/c.

The invariant mass spectrum shows a hump at the region around 1.8 GeV/c² at $p_{beam} = 1.5$ GeV/c and 1.7 GeV/c, which is caused by the decay of a single pion ($\pi \rightarrow \mu\nu$). For $p_{beam} = 2.5$ GeV/c and 3.3 GeV/c, this hump begins around 2.0 GeV/c² respectively 2.2 GeV/c² due to the higher value of beam momentum.

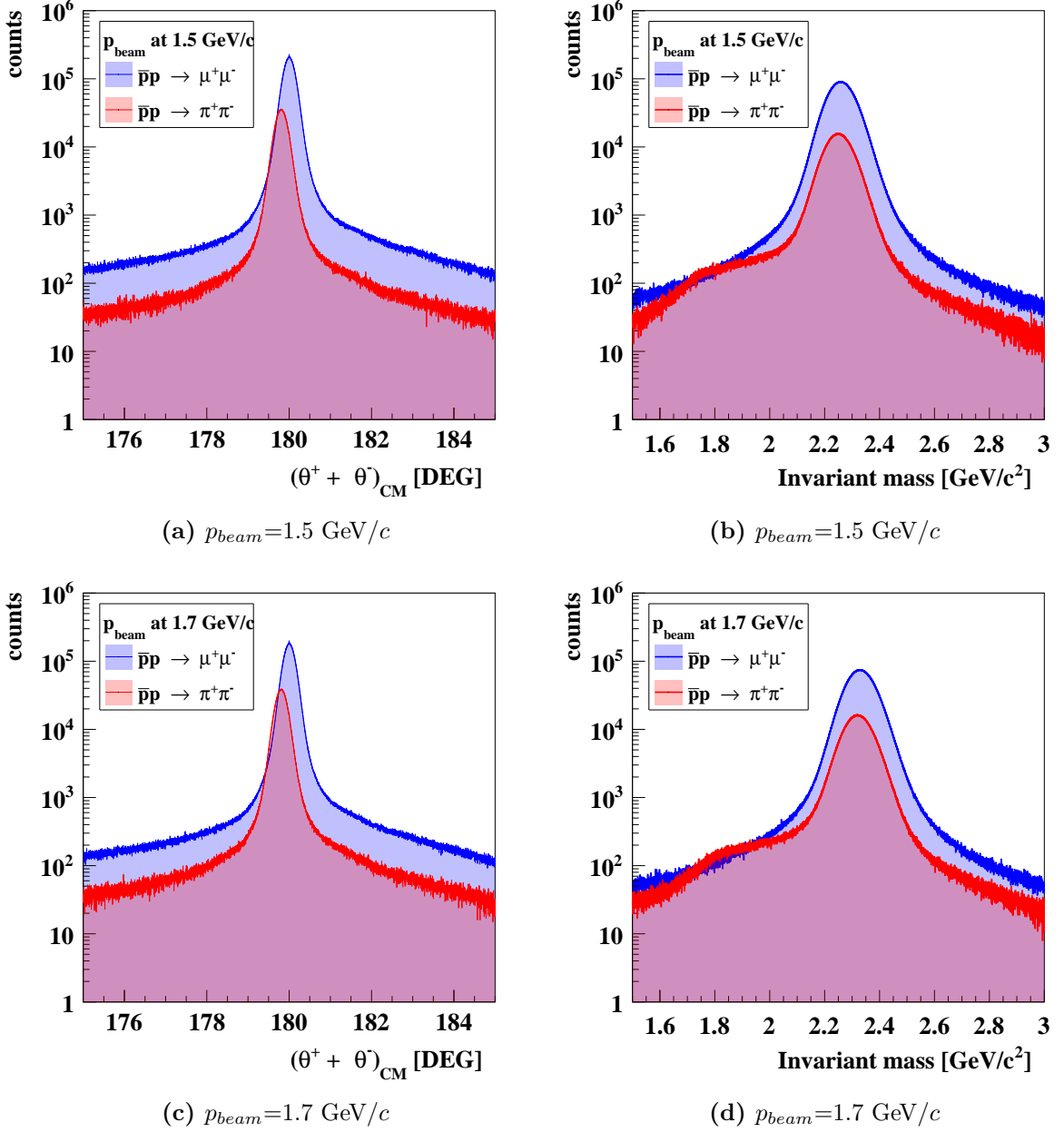


Figure 6.6: The left column shows the distribution of the reconstructed kinematic variable $(\theta^+ + \theta^-)_{CM}$ after preselection for the signal (blue) and the background (red). The plots are based on the preselected samples of the high statistics for the signal and the main background at (a) $p_{beam} = 1.5 \text{ GeV}/c$ and (c) $p_{beam} = 1.7 \text{ GeV}/c$. The right column shows the distribution of the reconstructed invariant mass M_{inv} of the final state after preselection for the signal (blue) and the background events (red) at (b) $p_{beam} = 1.5 \text{ GeV}/c$ and (d) $p_{beam} = 1.7 \text{ GeV}/c$.

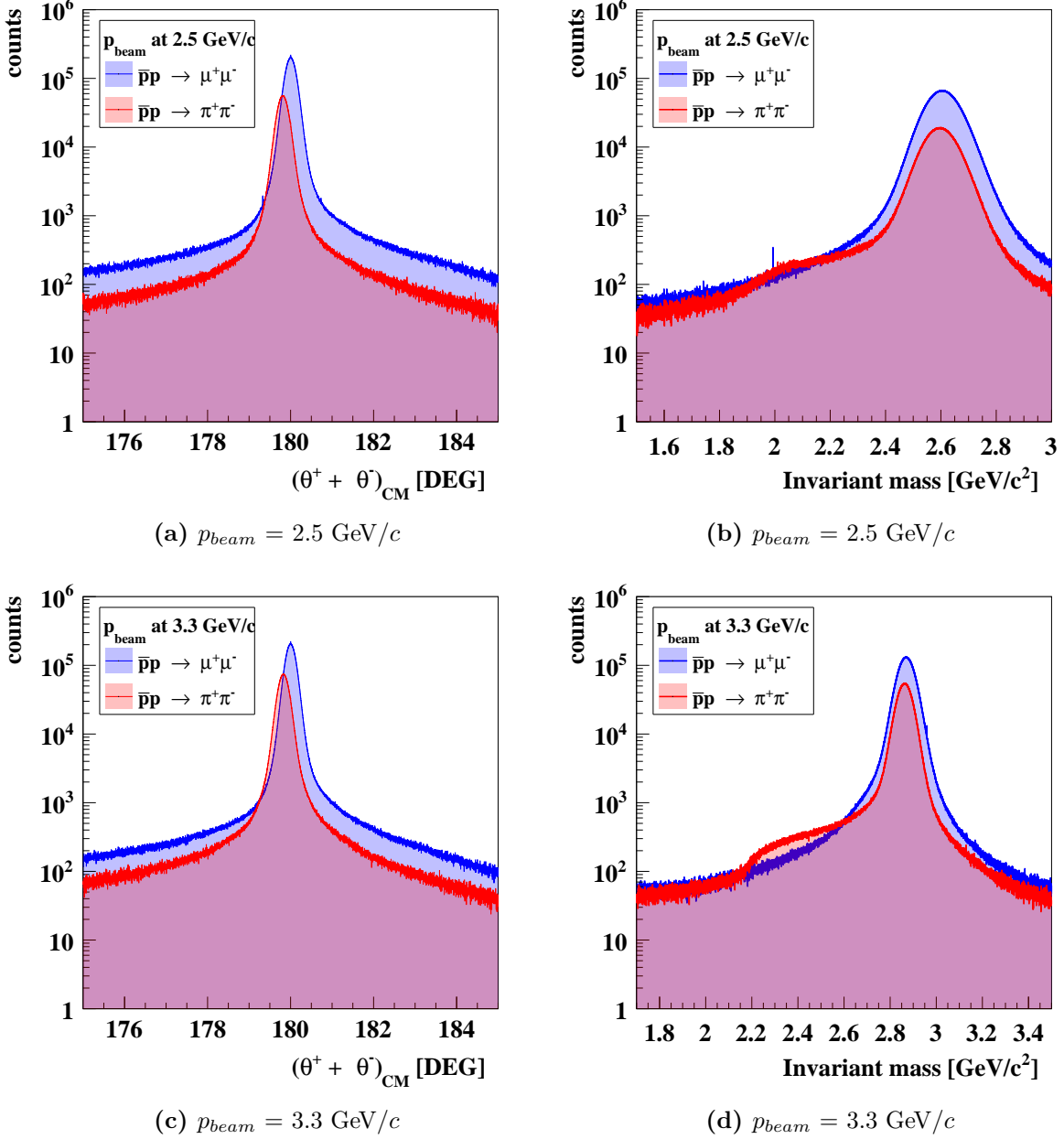


Figure 6.7: The left column shows the distribution of the reconstructed kinematic variable $(\theta^+ + \theta^-)_{CM}$ after preselection for the signal (blue) and the background (red). The plots are based on the preselected samples of the high statistics for the signal and the main background at (a) $p_{beam} = 2.5 \text{ GeV}/c$ and (c) $p_{beam} = 3.3 \text{ GeV}/c$. The right column shows the distribution of the reconstructed invariant mass M_{inv} of the final state after preselection for the signal (blue) and the background events (red) at (b) $p_{beam} = 2.5 \text{ GeV}/c$ and (d) $p_{beam} = 3.3 \text{ GeV}/c$.

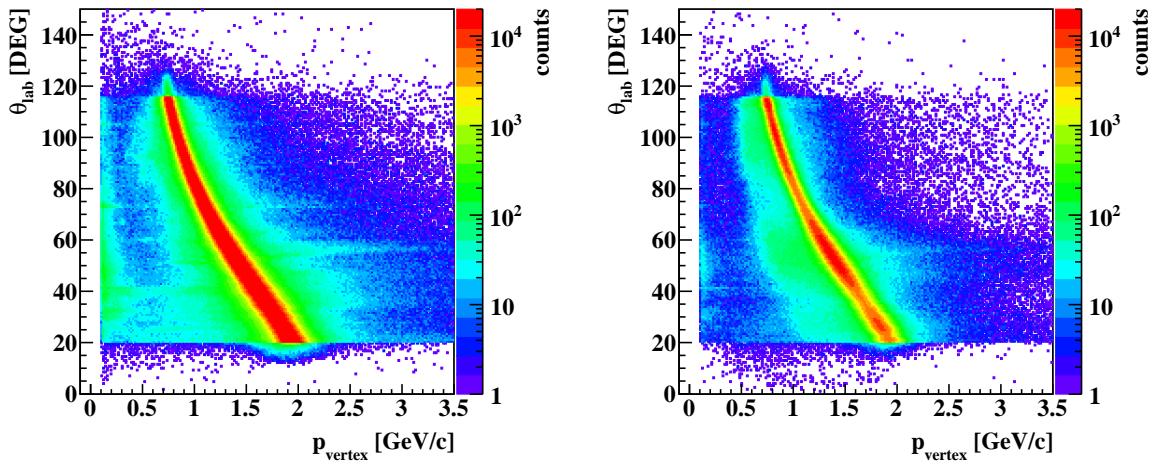


Figure 6.8: Momentum dependence of the polar production angle in lab frame, θ_{lab} (reconstructed at vertex) [DEG], for reconstructed and preselected negatively charged particles from (left) $\bar{p}p \rightarrow \mu^+\mu^-$ and from (right) $\bar{p}p \rightarrow \pi^+\pi^-$.

Observables from the Muon System

The most important sub detector related to the μ/π separation is the Muon System of the \bar{P} ANDA detector. Its sandwich structure consists of alternating active and passive layers, which enable to observe the different behavior of μ and π inside the detector. The pions interact with the detector material via ionization processes of the atomic electron clouds (electromagnetic interactions), excitation or also via the strong force. In contrast to the muons, which only interact via ionization energy losses inside the material, pions interact via both ionization energy loss and hadronic showering.

A high energetic pion could behave like a muon when a) it undergoes only ionization processes inside the Muon System material and b) it decays into a muon and a corresponding (anti-)neutrino. Heavy secondary particles, e.g. protons, neutrons and kaons, can be produced in nuclear interactions. For example, during the interaction of π^- with a nucleus (as e.g. tungsten from the EMC crystals), a K^+ meson can be produced together with a Σ^+ hyperon (baryon with strangeness) conserving strangeness.

After the μ -selection, which will be presented in the next section, the only particle species, contributing to the pion contamination, are pions and muons from pion decay.

Particles, which are scattered backwards (in lab frame), are partly absorbed by the Muon System due to their lower momenta at backward angles. The momentum dependence on the polar production angle is depicted in Figure 6.8. Particles, which are produced under small forward angles, possess higher momenta than particles emitted under backward angles.

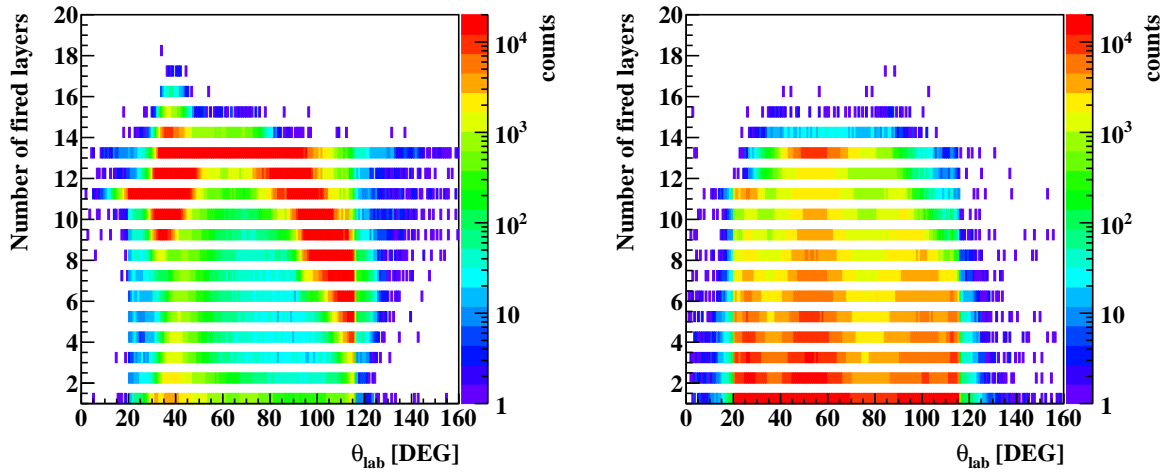
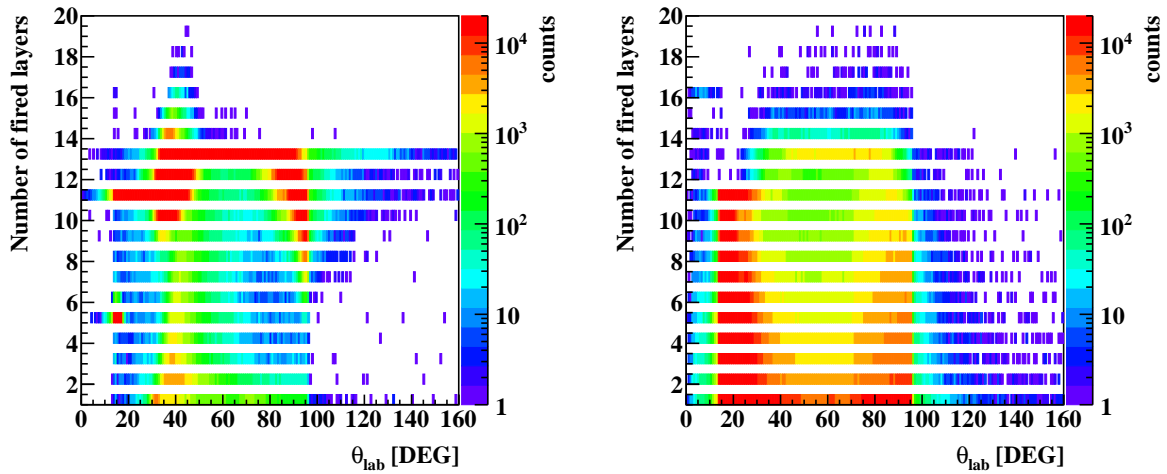
(a) $p_{beam} = 1.5 \text{ GeV}/c$ (b) $p_{beam} = 3.3 \text{ GeV}/c$.

Figure 6.9: Angular dependence of the number of fired detection layers in laboratory frame for negatively charged particles from the signal (left column) and the background (right column) after reconstruction and preselection at (a) $p_{beam} = 1.5 \text{ GeV}/c$ and (b) $p_{beam} = 3.3 \text{ GeV}/c$. The different behavior of muons and pions in the Muon System is the key ingredient for an efficient μ/π separation. From these differences in the detector response from muon and pion, one can deduce, that the number of fired detection layers is a variable of strong separation power.

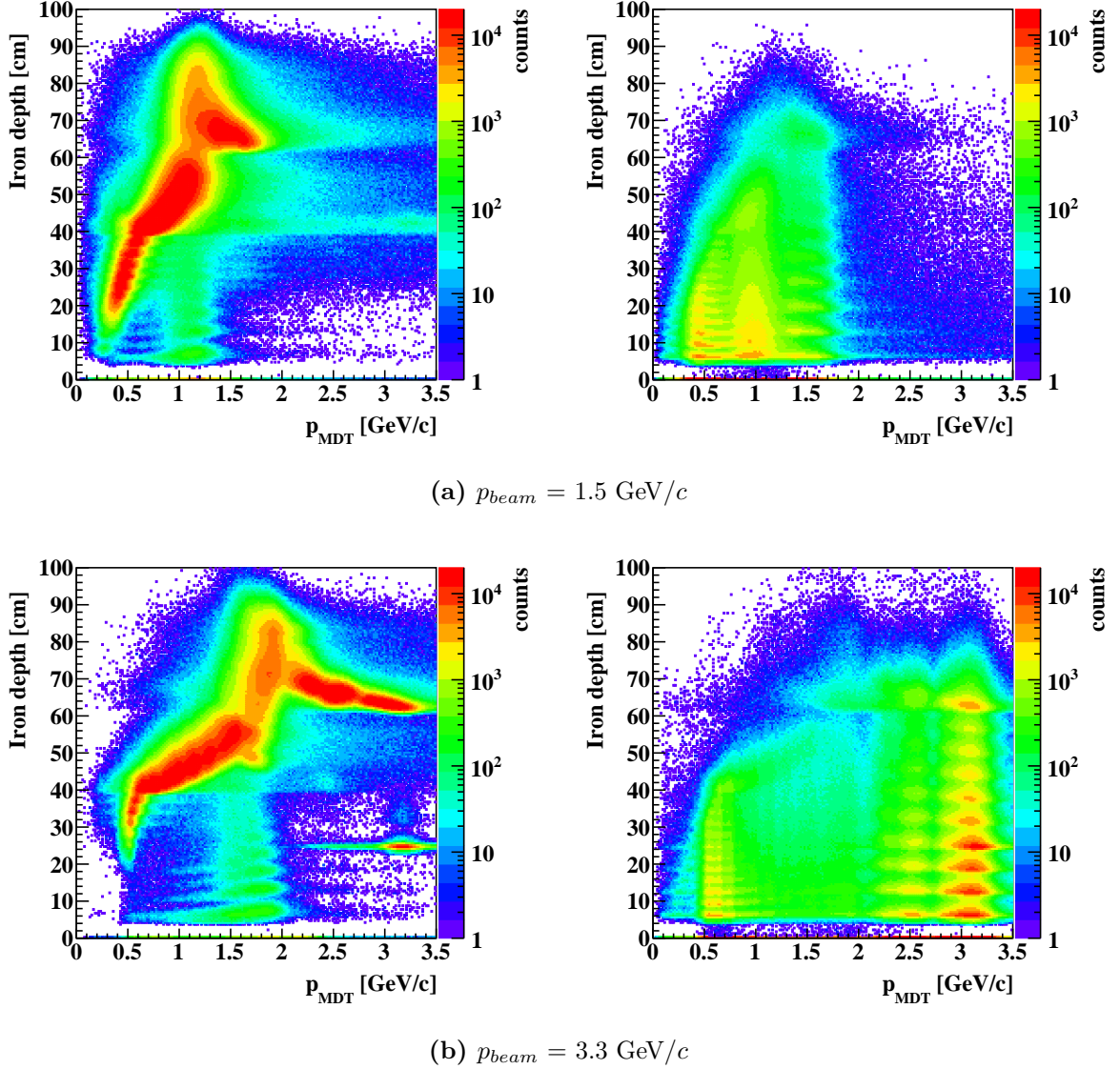


Figure 6.10: Dependence of the iron depth inside the iron absorber on the initial momentum at the zero bi-layer from the Muon System, for negatively charged particles for the reconstructed and preselected signal (left column) and the background (right column) at $p_{beam} = 1.5 \text{ GeV}/c$ (a) and $p_{beam} = 3.3 \text{ GeV}/c$ (b). This variable has a strong separation power and is used, in combination with p_{MDT} , for the determination of the PID probability from the Muon System.

The Figures 6.9 (a) and (b) show the number of fired detection layers versus reconstructed polar production angle in laboratory frame for negatively charged tracks. It can be seen, that the π^- from the pion background sample for the background process $\bar{p}p \rightarrow \pi^+\pi^-$ are absorbed within the first layers of the Muon System at $p_{beam} = 1.5 \text{ GeV}/c$ and $p_{beam} = 3.3 \text{ GeV}/c$. As an example, at $p_{beam} = 1.5 \text{ GeV}/c$, about 7.10% of all the tracks pass 11 detection layers or more. From that fraction, the MC information shows that about 9.37% are decay muons (μ^-) and 90.59% of the particles are π^- . A very small percentage of 0.04% consists of misidentified

particles of opposite charge (μ^+ and π^+).

Another important variable for the signal-background separation provided by the Muon System is the path length of the trajectories inside the Muon System (denoted as *iron depth*). This observable considers the angles of incidence of each individual track, which are reconstructed by trigonometric calculations using the spatial hit information of the detection layers. The dependence of the iron depth on the initial momentum at the Muon System zero bi-layer (p_{MDT}) for reconstructed and preselected negatively charged particles in the signal sample with high statistics (left) and background sample (right) can be seen in Fig. 6.10.

Observables from the EMC and STT

The deposited energy inside the electromagnetic calorimeter (E_{EMC}/p , with p as the magnitude of the reconstructed particle 3-momentum at the interaction vertex) or the mean energy loss per unit of length in the Straw Tube Tracker (dE/dx *STT*) are observables with less separation power than the observables from the Muon System, since here muons and pions show a quite similar behavior inside the detector materials as shown in Figures 6.11 and 6.12. Although they are weak variables, they can help to improve the signal-background separation when multivariate data classification is used to optimize the μ/π separation. Figure 6.11 shows the momentum dependence of the variable dE/dx *STT* for negatively charged particle candidates at a) $p_{beam}=1.5$ GeV/ c and b) $p_{beam}=3.3$ GeV/ c . The strong peak around dE/dx *STT* [a.u.] = 5 shows the oscillating cross section behavior of the pion pair production depending on $\cos\theta_{CM}$. This pattern is caused by pions, which lose energy mostly in electromagnetic processes (ionization and excitation) inside the detector material.

A set of shower shape variables from the EMC are available, which can be powerful tools for an efficient e/π separation. In the case of μ/π separation, they are also rather weak variables, however they help to slightly improve the performance of multivariate classifiers. Hadronic showers show a typical small lateral shower width in combination with a deep shower depth in longitudinal direction. Therefore the lateral moment (LAT) is smaller in case of hadronic showers in comparison to electromagnetic cascades.

Most of the energy deposition in a electromagnetic shower occurs in only a few crystals surrounding the central crystal of the cluster (which is defined as the crystal with the highest energy deposition, surrounded by a certain number of crystals (3x3 or 5x5) forming the cluster). In contrast to that, hadronic showers show a broader transversal profile and have - depending on the initial momentum of the primary particle and the absorber material - a shorter length in longitudinal direction.

The ratio of the deposited shower energy inside the EMC and the particle momentum at vertex, E_{EMC}/p , is another rather weak variable for μ/π separation. As it is shown in Figure 6.12, the momentum dependence of the energy loss ratio E_{EMC}/p of muon (left plot) and pion (right

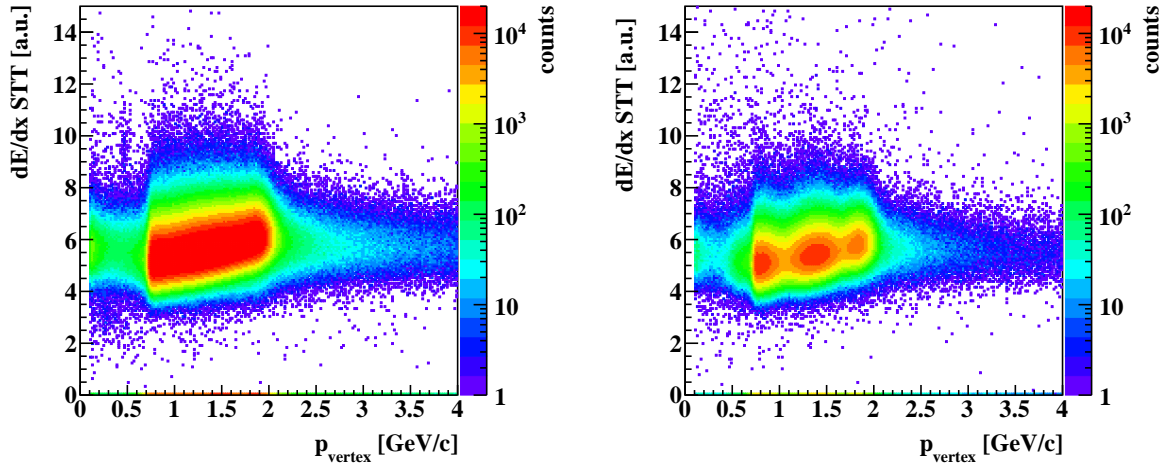
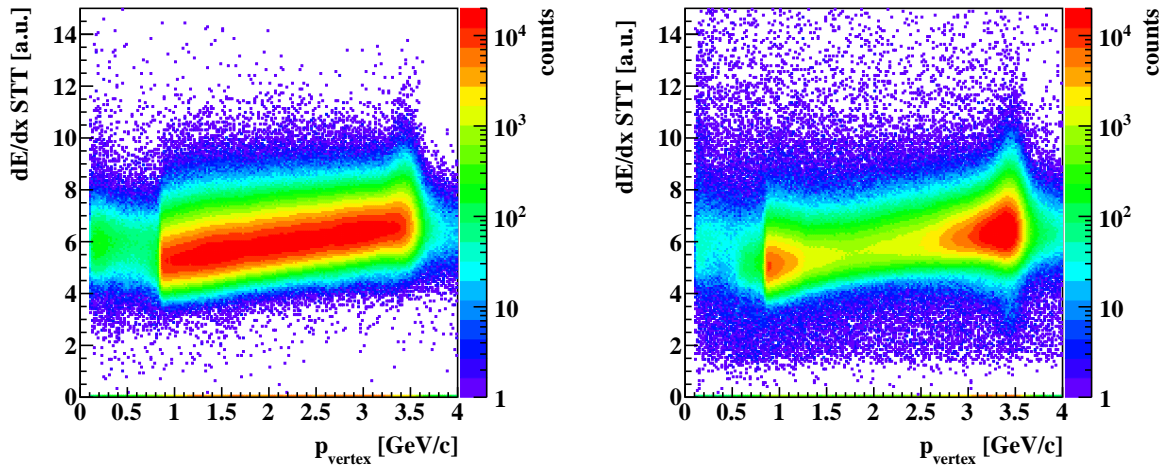
(a) $p_{beam} = 1.5 \text{ GeV}/c$ (b) $p_{beam} = 3.3 \text{ GeV}/c$

Figure 6.11: Mean energy loss per unit of length in the STT depending on the reconstructed momentum at vertex for negatively charged particles for the reconstructed and preselected signal (left column) and the background (right column) at $p_{beam} = 1.5 \text{ GeV}/c$ (a) and $p_{beam} = 3.3 \text{ GeV}/c$ (b).

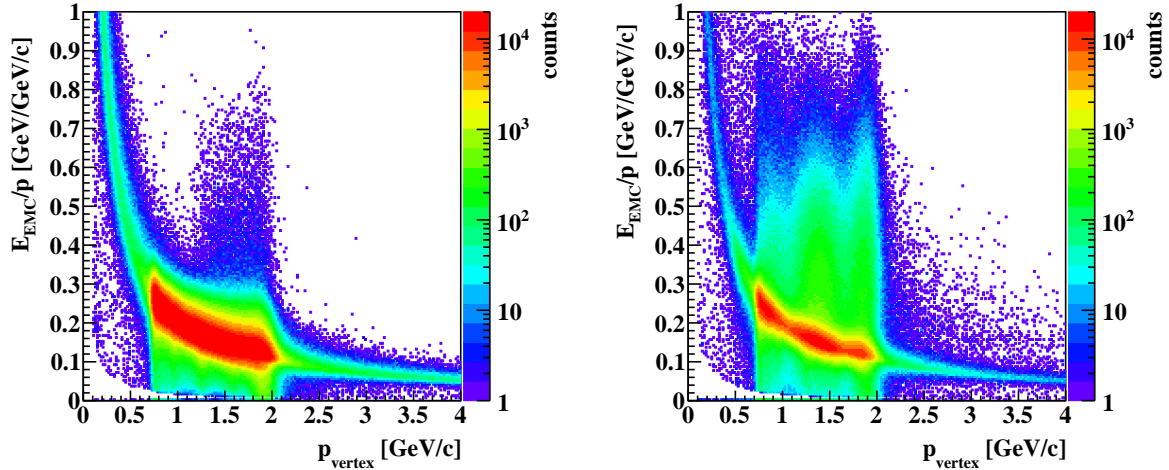
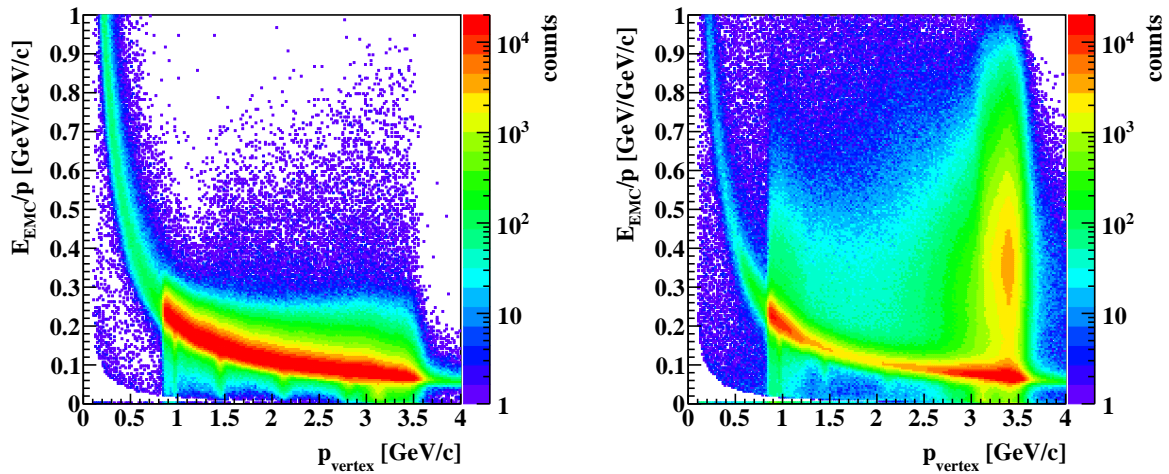
(a) $p_{beam} = 1.5 \text{ GeV}/c$ (b) $p_{beam} = 3.3 \text{ GeV}/c$

Figure 6.12: Deposited energy inside the EMC divided by reconstructed momentum at vertex versus reconstructed momentum at vertex ($p_{vertex} \equiv p$ [GeV/c]). The detector response for negatively charged particles after reconstruction and preselection are shown at (a) $p_{beam} = 1.5 \text{ GeV}/c$ and (b) $p_{beam} = 3.3 \text{ GeV}/c$. The left column (right column) shows the reconstructed and preselected signal (background). Since this detector response is very similar for muons and pions, it is obvious, that this variable has a much lower separation power than variables from the Muon System.

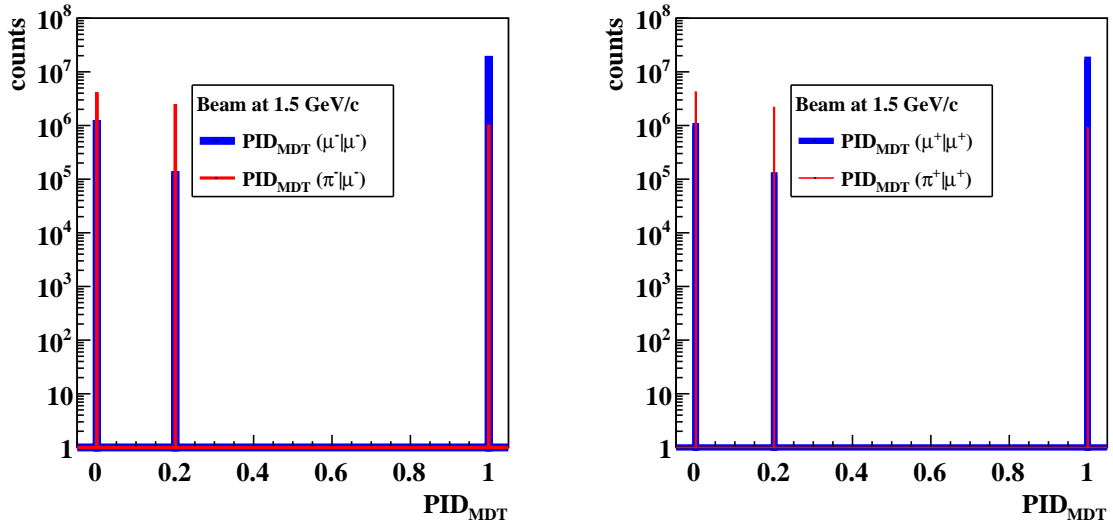


Figure 6.13: The PID probability for being a muon, PID_{MDT} , is calculated based on simple cuts on variables from the Muon System for μ^- (left) and μ^+ (right). The iron depth and the initial particle momentum measured at the zero bi-layer of the Muon System are used for the determination of the PID probability. $\text{PID}_{MDT}(\mu^-|\mu^-)$ is the probability to identify a μ^- correctly, while $\text{PID}_{MDT}(\pi^-|\mu^-)$ is the probability misidentify a π^- as μ^- .

plot) differs only slightly concerning their patterns. The background shows a strong and narrow curve at small values around $E_{EMC}/p \approx 0.2$, caused by ionization and excitation of the detector material. The much more extended structure between momenta of 0.7 and 2.0 GeV/c is due to the kinematic of the reaction. The oscillating behavior of the pion differential cross section (at $p_{beam} = 1.5$ GeV/c) can be seen clearly in this pattern, whereas at $p_{beam} = 3.3$ GeV/c the asymmetric shape of the differential cross section is visible.

6.1.5 Particle Identification (PID) with the Muon System

Since an efficient μ/π separation depends strongly on the performance and design of the Muon System, this detector provides the most important PID probability for this analysis. Different identification probabilities using information from other detectors (for instance from the electromagnetic calorimeter (EMC), the Straw Tube Tracker (STT) or the Micro Vertex Detector (MVD)), are also available, but provide weak variables in this work, and are not used in the analysis. The probability for being muon, denoted as PID_{MDT} , is based on a selection, using simple cuts. Figure 6.13 shows the discrete distributions of the Muon System identification probability PID_{MDT} , for being (left) μ^- or (right) μ^+ . This PID probability is calculated based on two variables from the Muon System: the path length inside the iron absorber (iron depth) and initial particle momentum p_{MDT} measured at the zero bi-layer. Threshold values are defined for both of them, which depend on the considered module of the Muon System. There are three Muon System modules available in PandaRoot:

Muon System Module	Iron threshold	p_{min}	p_{max}
1	40 cm	0.2 GeV/c	0.8 GeV/c
-1	60 cm	0.4 GeV/c	1.1 GeV/c
2	60 cm	0.4 GeV/c	1.1 GeV/c

- a) Muon System Module 1: MS Barrel
- b) Muon System Module 2: MS Forward Endcap plus Muon Filter
- c) Muon System Module -1: Hybrid Tracking (End cap plus Barrel for common track reconstruction)

The lower threshold for the Barrel MS is due to the lower particle momenta at higher values of the polar production angle in lab frame θ_{lab} . A minimal and maximal initial particle momentum (p_{min} and p_{max}) is additionally set.

The following five cases can be distinguished:

1. ($p_{MDT} < p_{min}$) \rightarrow $PID_{MDT}(\mu) = 0.0$
2. ($p_{MDT} > p_{min}$) **and** (iron thickness $>$ iron threshold) \rightarrow $PID_{MDT}(\mu) = 1.0$
3. ($p_{MDT} > p_{max}$) **but** (iron thickness $<$ iron threshold) \rightarrow $PID_{MDT}(\mu) = 0.0$
4. ($p_{min} < p_{MDT} < p_{max}$) and (iron thickness $>$ iron threshold $\cdot (\frac{p_{MDT}-p_{min}}{p_{max}-p_{min}})$) \rightarrow $PID_{MDT}(\mu) = 1.0$
5. ($p_{min} < p_{MDT} < p_{max}$) but (iron thickness $<$ iron threshold $\cdot (\frac{p_{MDT}-p_{min}}{p_{max}-p_{min}})$) \rightarrow $PID_{MDT}(\mu) = 0.0$

The default value of the $PID_{MDT}(\mu)$ variable is 0.2, since 5 kind of particles are available: ($k = \mu, \pi, K, p, e$). If a certain event does not match any of the five cases, it keeps the default value. The remaining background after preselection needs to be suppressed keeping as much signal efficiency as possible.

In case of the signal channel $\bar{p}p \rightarrow e^+e^-$ [16], a background rejection factor of the order of 10^{-8} was achieved, keeping at the same time a large signal reconstruction efficiency between 40% and 50% for beam momenta between 1.7 GeV/c and 6.4 GeV/c. Taking into account the cross section ratio $\sigma(\bar{p}p \rightarrow e^+e^-)/\sigma(\bar{p}p \rightarrow \pi^+\pi^-) \approx 10^{-6}$, the background rejection factor of the order of 10^{-8} is necessary to reduce the signal pollution to values of a few percent. Due to the big difference in their rest masses and interaction mechanisms with matter, electrons and charged pions can be separated very successfully at \bar{P} ANDA. However, an efficient μ/π separation is much more difficult to achieve, since the difference of the rest masses of μ and π is only ≈ 34 MeV/c². In order to find the optimal analysis strategy for this study, the most powerful variables have to be identified and tested. The optimized strategy for signal-background separation based on multivariate data analysis will be presented in the following section.

6.2 Optimizing the μ/π separation by using Boosted Decision Trees

The biggest challenge of measuring time-like FF's from $\bar{p}p \rightarrow \mu^+\mu^-$ is the efficient suppression of pions produced in reactions of $\bar{p}p \rightarrow \pi^+\pi^-$. The detector response of muons and pions are very similar due to their very similar rest masses. It will be shown that an analysis based on simple cuts on a set of variables is not sufficient in the case of the μ/π separation. Therefore, a new analysis strategy based on Boosted Decision Trees is developed and will be presented in this chapter.

6.2.1 Multivariate Data Analysis

Multivariate Data Analysis (MVA) encompasses the simultaneous observation and analysis of more than one statistical variable. The goal is to optimize the background rejection while keeping as much signal efficiency as possible. The following studies make use of the Toolkit for Multivariate Data Analysis (TMVA) from ROOT [137, 147]. It is a machine learning environment for the parallel testing and evaluation of different multivariate classification methods. For each individual purpose the user can choose between the following techniques:

- Rectangular cut optimisation
- Projective likelihood estimation (PDE approach)
- Multidimensional probability density estimation
- Multidimensional k-nearest neighbour method
- Linear discriminant analysis (H-Matrix, Fisher, ...)
- Function discriminant analysis (FDA)
- Artificial neural networks (three different feed-forward multilayer perceptrons (MLP))
- Boosted/Bagged decision trees
- Predictive learning via rule ensembles
- Support Vector Machine (SVM)

The TMVA package [147] includes C++-based algorithms for the training, testing and evaluation of different multivariate classification methods. For the training, well-known data sets for signal and background are given to each of the TMVA classifiers. The multivariate classification consists of two major steps in general: the *training phase*, where individual weights are assigned to each event, and the *application phase*, where the trained classifiers are used for the classification of (unknown) data samples of interest. An additional preselection in form of cuts can be applied before the training. The basic working scheme for the multivariate data classification is described in Fig. 6.14. All TMVA classifiers are trained based on the same training data

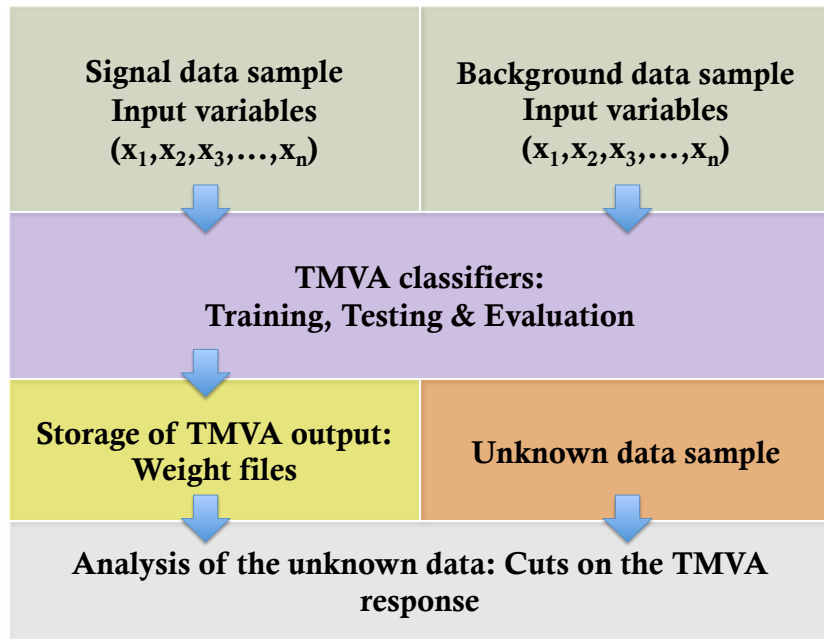


Figure 6.14: Basic working principle of the data classification with MVA. The working flow consists of two major steps: The training phase, where the training, testing and evaluation of the classifiers are performed, followed by the application phase (= analysis of the unknown data sample).

(for signal respectively background), the trained methods are applied on the test data and the last step is the evaluation of the classification. Linear correlations between the input variables are calculated and can be used later for an optimization of the input variable set. The training results for each classifier are stored in a Root-file together with the correlation information. During the training, a variable ranking (depending on the separation power) is performed for each method. This variable ranking helps to choose a set of powerful input variables. Additionally, the package provides information about the performance of each classification method. In Subsection 6.2.3, it will be shown that the classification methods with the best performance concerning the μ/π separation, are Boosted Decision Trees. In the following, their corresponding classification algorithms are described.

6.2.2 Boosted Decision Trees

A simple *decision tree*, as shown in Fig. 6.15, is a sequential application of cuts on a sample of events to separate signal from background events. The training of a decision tree can be seen as the definition of the optimal cut criterium and most powerful variable for each node: a single discriminating variable (the most powerful one concerning signal background separation) is used to classify each event as either signal-like (following the right path) or background-like (following the left path). The training data sample is split into two subsamples (S- and B-like subsample) before the next nodes are defined. Following this technique, a tree is grown until a

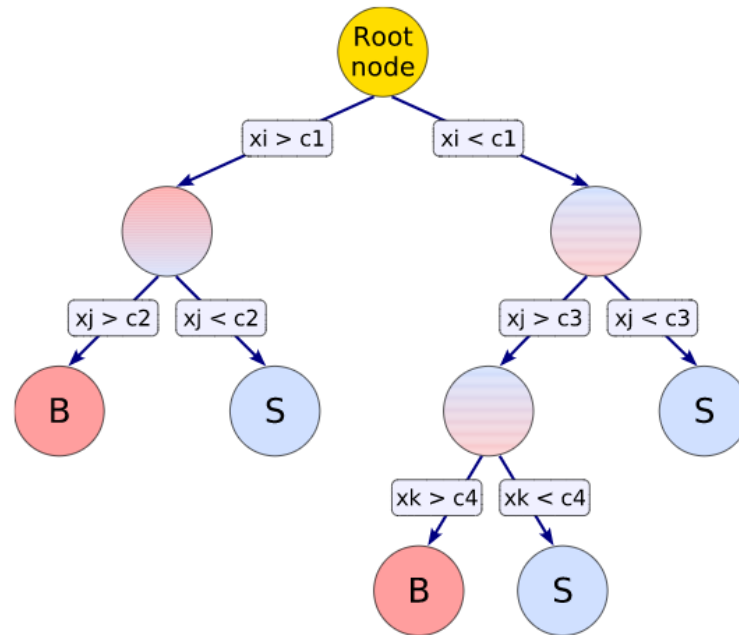


Figure 6.15: Typical structure of a decision tree [147]. The uppermost node are the root nodes, from which the tree is developed during the training phase. The most powerful variable is chosen to achieve the best signal-background separation at this node. A cut is applied on this variable which splits the data sample into two sub-samples. The growing process of the tree stops as soon as a certain criterium is fulfilled. The leaf nodes define the end of the tree and are labeled as "S" (Signal) or "B" (Background) depending on the majority of the events ending up in the individual node.

certain criterium is fulfilled (e.g. minimum number of events or a certain signal purity (minimum or maximum) was reached). The final nodes (leaf nodes) are assigned to be either signal (S) or background (B) depending on the majority of events ending up in this leaf node. In this way, the n -dimensional variable space (n is the number of variables) is divided into regions, which are classified as signal or background. After this training process, an unknown data sample of interest is given to the tree. Each event will be classified either as signal or background depending in which leaf node is ends up. The visualization of decision trees can be done in a two-dimensional scheme (see Figure 6.15), which makes them a very transparent tool.

A disadvantage of using decision trees is their high sensitivity to statistical fluctuations in the training data sample. In this case, the selection of the variable on a certain node can be affected by fluctuations, so that the tree structure is influenced strongly by the individual statistical fluctuations in the training sample. For example, if two variables have similar separation power at a certain node, one variable is picked as the more powerful one, due to a fluctuation while the other variable could have been more powerful without fluctuation. In that case, the decision tree has learned not only the characteristics of signal and background, but also the statistical fluctuations. This results in an incorrectly trained decision tree whose output can

not be trusted. To cure the weaknesses of decision trees, the so-called *boosting technique* is used [148]. In this technique, the event classification is performed by a sequential application of classification algorithms on a reweighted set of training data. This results in a strongly improved classification performance. The final classification is given by a weighted majority vote by the set of algorithms (a so-called *random forest*). Hence, the boosting technique allows to combine a set of weak classifiers into an enhanced, much more powerful classification algorithm.

Different boosting techniques are available. The most popular boosting algorithm is adaptive boost (AdaBoost) [149]. For event classification, the overall classification performance is enhanced by giving a higher event weight to a misclassified event in the next tree to be grown. Another boosting technique, which is tested here, is the *gradient boosting (BDTG)*, which shows a very similar performance compared to the BDT, but is even more robust in the case of noisy data (outliers or mislabelled data). Apart from that, also the BDTG shows a very good out-of-the-box performance just as the BDT.

The training of the Boosted Decision Trees works as follows [147]: The first step is to set the event weights, with equal weights are set at the beginning. During the training of the classifier based on AdaBoost, here denoted as *BDT*, the forest is grown sequentially, tree after tree. The first tree uses the original event weights. After growing each individual tree, misclassified events are given higher event weights, which are used at the following tree. Hence, this tree is grown using a modified sample, where the weights of previously misidentified events are multiplied with a common boost weight

$$\alpha = \frac{1 - err}{err}. \quad (6.3)$$

Here *err* stands for the misclassification rate of the previous tree. The response of a weak classifier (a single tree) is denoted as $h(x)$, with x as the tuple of input variables. For a signal (background) event, it is $h(x) = +1$ (-1). The boosted event classification can be written as

$$y_{Boost}(x) = \frac{1}{N_{collection}} \cdot \sum_{i=1}^N \ln(\alpha_i) \cdot h_i(x) \quad (6.4)$$

where the sum runs over all existing weak classifiers (decision trees). A normalization of the weights is applied after each step to keep their sum constant. Depending on the value of $h(x)$, an event is classified as signal-like (background-like) when $y_{Boost}(x)$ has a high (low) value.

In order to find the optimal configuration of the weights, a so-called loss function $L(F, y)$ is minimized. For the AdaBoost algorithm, the exponential loss function

$$L(F, y) = e^{-F(x)y} \quad (6.5)$$

is used. For the BDTG, the loss function is based on a binomial log-likelihood loss

$$L(F, y) = \ln(1 + e^{-2F(x)y}) \quad (6.6)$$

It contains the true value y (which can be either signal ($+1$) or background (-1)), which is directly known due to the well-known training event sample. The model response function $F(x)$ contains

the parameterized base functions ("weak learners", corresponding to single decision trees) $f(x)$ and a set of parameters $P \in \{\alpha_m\}_0^M$, where α_m is the weight for the m -th weak learner. It is defined as

$$F(x; P) = \sum_{m=0}^M \alpha_m \cdot f_m(x), \quad (6.7)$$

where the sum runs over the base functions. The boosting is performed step-wise, where in each step the weight for the current weak learner is optimized using its misclassification rate. The loss function is minimized after every step of the step-wise growing of the forest, running over all events. The parameters P are adjusted in a way such that the deviation between $F(x)$ and the true value y is minimized. The final response function contains all weak learners and the optimized set of parameters which provide the best classifier performance. Typically, the boosting is applied several hundred up to several thousand times which leads to large random forests.

While for the BDT, the algorithm can be obtained by an analytical minimization of the loss function, this is not possible for the more complex loss function of the BDTG. In this case, the so-called *steepest-descent approach* is used to minimize the loss function and hence, to find the optimal set of event weights. (This is realized by the calculation of the current gradient of the loss function with respect to the weak learners and proceed in an iterative way until its loss function is minimized.)

All trees of the BDT are grown sequentially using the same data samples during the *training phase*. The weights, which have been assigned to the events are stored as output for the application phase later on. The trained BDT are tested and their performance is evaluated. For that purpose, the training event sample is split into two independent parts before the training. The first part is used for the training, the second part for testing.

Boosted Decision Trees using short individual trees (low tree depth of only 2 or 3), have the advantage that they are robust against overtraining, show also good performance even with weak variables and have short evaluation times. In case of poorly discriminating input variables, they are ignored by the learning algorithm.

After the training and testing phase, the *application phase* follows. During that phase, an unknown data sample is fed to the trained BDT. The individual event passes through the whole forest and a likelihood estimator is constructed from the fact, how often this event is classified as signal or background. This estimator delivers the classifiers response, which can be used to separate the signal from background by applying a cut on the BDT response. Quantities like signal efficiency, background suppression and the signal purity are defined by this cut on the BDT response. The BDT classifier can be customized for a certain classification problem. Different configuration options are available for the BDT classifier, like the number of trees in the random forest, the maximum depth of a single decision tree and the separation criterion for

Table 6.4: Used configuration options for BDT classification. The purity of a node (p) is defined as the ratio of the signal events to all events in the node.

Option	Value	Description
NTrees	1000	Total number of trees
MaxDepth	3	Maximum depth of decision tree
nEventsMin	50	Minimum number of events in leaf node
BoostType	Ada Boost	Boosting type for the trees in the forest
AdaBoostBeta	0.5	Learning rate for AdaBoost
SeparationType	Gini-Index : = $p(1-p)$	Separation criterium for node splitting
nCuts	20	Number of used grid points in the variable range for finding optimal cut in node splitting
PruneMethod	NoPruning	Method used for pruning (= removal of insignificant branches)

the node splitting.

Table 6.4 summarizes the options used in this work. The number of trees are chosen to achieve a stable performance (small NTrees lead to a poor performance) and avoid overtraining¹ (what happens at very large forests). BDT methods can be easily overtrained due to their high number of model parameters.

Different values of NTrees were tested, starting from NTrees=300 up to NTrees = 5000. For NTrees > 1000, no significant improvement could be seen concerning the performance of the BDT, so that NTrees = 1000 was chosen in this work. Another option is the *maximum depth* of the individual decision trees, which should be small (2 or 3) for a good BDT performance. As a separation criterion at each node, the *Gini-Index* is used. It is given by $p \cdot (1-p)$, where p stands for the purity at the certain node (the ratio of signal events to the total number of events at the node). The optimal variable and cut value achieves the highest gain of purity. The cut values are scanned over the variable range. The stepping value of the variable scan can be adjusted by the option *nCuts*. Here, the default value of 20 allows a good performance at small computing times, while higher values do not improve the performance. When a specified minimum number of events is reached in the leaf nodes (*nEventsMin*), the node splitting stops. The learning rate β of the AdaBoost algorithm is given as an exponent to the boost weight, α^β .

In the following, the full procedure of the MVA is described on the example of the lowest beam momentum 1.5 GeV/ c .

¹Overtraining occurs, when a (more complex) classifier has many model parameters of the algorithm (e.g. many nodes) and the training data sample contains only a few data points. As a consequence, the classifier becomes sensitive to statistical fluctuations in the training data set and its general applicability to statistical independent data is lost.

6.2.3 Choosing appropriate input variables

First, the input variables for the MVA need to be chosen. The best variables are those with the strongest separation power. The following variables are considered:

- Path length inside iron absorber of the Muon System, denoted as *iron depth*. The length of the reconstructed trajectories is calculated inside the absorber and detection layers based on the spatial hit information.
- Iron depth divided by initial momentum at layer zero of the Muon System, denoted as *Iron depth/p_{MDT}*.
- Number of hits inside the Muon System. The total number of hits over all detection layers for the individual event: *MDT Hits*.
- Number of fired detection layers inside the Muon System. The total number of hits over all detection layers for the individual event: *MDT Number of fired layers*.
- Initial momentum of charged particle track at zero bi-layer of the Muon System: *p_{MDT}*.
- *Track quality* from the Muon System.
- *Identification probability* for being a muon based on Muon System observables: $PID_{MDT}(\mu)$.
- Ratio of the deposited energy inside the EMC to the reconstructed momentum at interaction vertex (p) for the associated track: E_{EMC}/p .
- EMC Lateral moment (*LAT*). Electromagnetic showers usually show a much smaller lateral shower width in comparison to hadronic showers due to the difference in the interaction mechanisms of leptons and hadrons in matter. The lateral moment is defined as:

$$LAT = \frac{\sum_{i=3}^N E_i r_i^2}{\sum_{i=3}^N E_i r_i^2 + E_1 r_0^2 + E_2 r_0^2} \quad (6.8)$$

where N is the number of crystals affected by the shower, E_i is the deposited energy in the i -th crystal with $E_1 > E_2 > \dots > E_N$. The lateral distance between the central and the i -th crystal is given by r_i . Here r_o stands for the average distance between two crystals. Since the numerator does not contain the three highest energy depositions, the ratio will show smaller values for electromagnetic showers in comparison to the hadronic one.

- Deposited energy inside crystal clusters of 3x3, the central cluster is defined by the crystal of maximal energy deposition.
- Zernike moments $Z20$ and $Z53$, which are also shower shape variables.
- Mean energy loss per unit of length inside the STT, $(dE/dx)_{STT}$.
- Number of hits inside STT, *STT Hits*.

- Invariant mass of the final state particles: M_{inv} .
- Sum of the polar production angles of the two produced charged tracks in the $\bar{p}p$ -center-of-mass system: $(\theta^+ + \theta^-)_{CM}$. This quantity is ideally peaked around 180° for the signal.

These variables are given as an input to the training of the classifiers. Figure 6.16 illustrates the distributions of different kinematical variables and Muon System observables from the input variable set for the MVA training phase. It is essential for an optimal performance of the BDT, that the signal and background represent the real signal and background as closely as possible. Therefore, cuts, which will be applied on real data (e.g. for suppressing secondary particles) need to be used also for the training samples. As an example, at $p_{beam} = 1.5 \text{ GeV}/c$ only events are selected for the training, which fulfill the condition of $2.1 < M_{inv} < 2.4$ and $(\theta^+ + \theta^-)_{CM} > 178.0^\circ$. The cuts are applied to the training samples before the training starts. An amount of $2 * 10^5$ training events, given to the TMVA training, provide sufficient statistics, since half of the training events are used for the training itself, the other half for testing the trained classifiers. Overtraining can be avoided by using event samples of such large statistics.

As expected, the Muon System offers the best variables for the μ/π separation: The distributions of muons and pions have the smallest overlap, as it can be seen in case of the iron depth and the number of fired detection layers of the Muon System shown in Fig. 6.16. Most of the pions are absorbed within the first layers, however pions with higher momenta are able to cross the Muon System. Also the iron depth shows a small overlap in the distributions of muon and pion.

Variables from the EMC and the STT are less powerful than the observables from the Muon System and show distributions with a much bigger overlap area. The deposited energy in the EMC shows similar distributions (see Figure 6.17).

In order to list the variables according to their separation power, TMVA provides a variable ranking. This measure of the variable importance can be used for a single decision tree as well as for a forest. The variable ranking by the BDT is based on how often a certain variable is chosen to split tree nodes, weighted by the corresponding squared separation gain and by the number of events passing the node [150]. For the BDT classification, also variables of little separation power can be included and help to improve the performance.

Table 6.5 shows the variable ranking for the BDT method in this study. The separation power (denoted in Tab. 6.5 as *Separation*) shows, that the most powerful variables are the identification probability from Muon System and the number of fired detection layers. Extremely weak variables are ignored by the BDT and therefore are not chosen for the final set of input variables in this study. As an example, the zernike moments are not used due to that reason. For the case of highly correlated variables, only one of these variables is used since they both provide nearly the same information. An example is the number of hits inside the Muon System (*MS Hits*) and the number of fired layers (*Mdtilayers*), where the first variable has less separation power and is

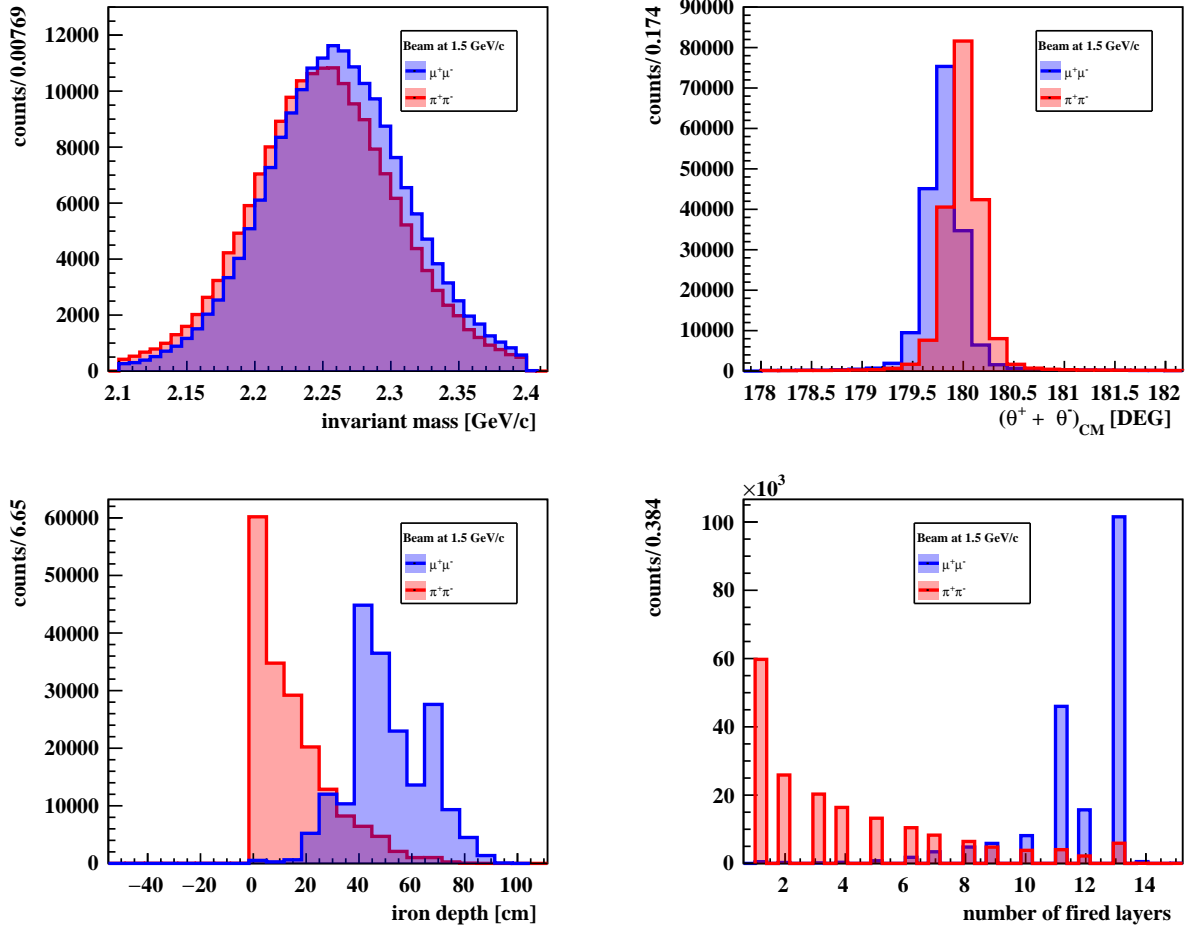


Figure 6.16: Kinematical variables and Muon System observables at $p_{beam} = 1.5$ GeV/ c , after event reconstruction and preselection, which are used for the MVA. Shown are the distributions of the invariant mass (upper left plot) and the sum of the polar production angles of both tracks in the $\bar{p}p$ center-of-mass system (upper right plot). The iron depth and the number of fired layers for negatively charged particles show different patterns, which makes them very useful for the μ/π separation. The signal distributions are shown in blue, while the background distributions are shown in red.

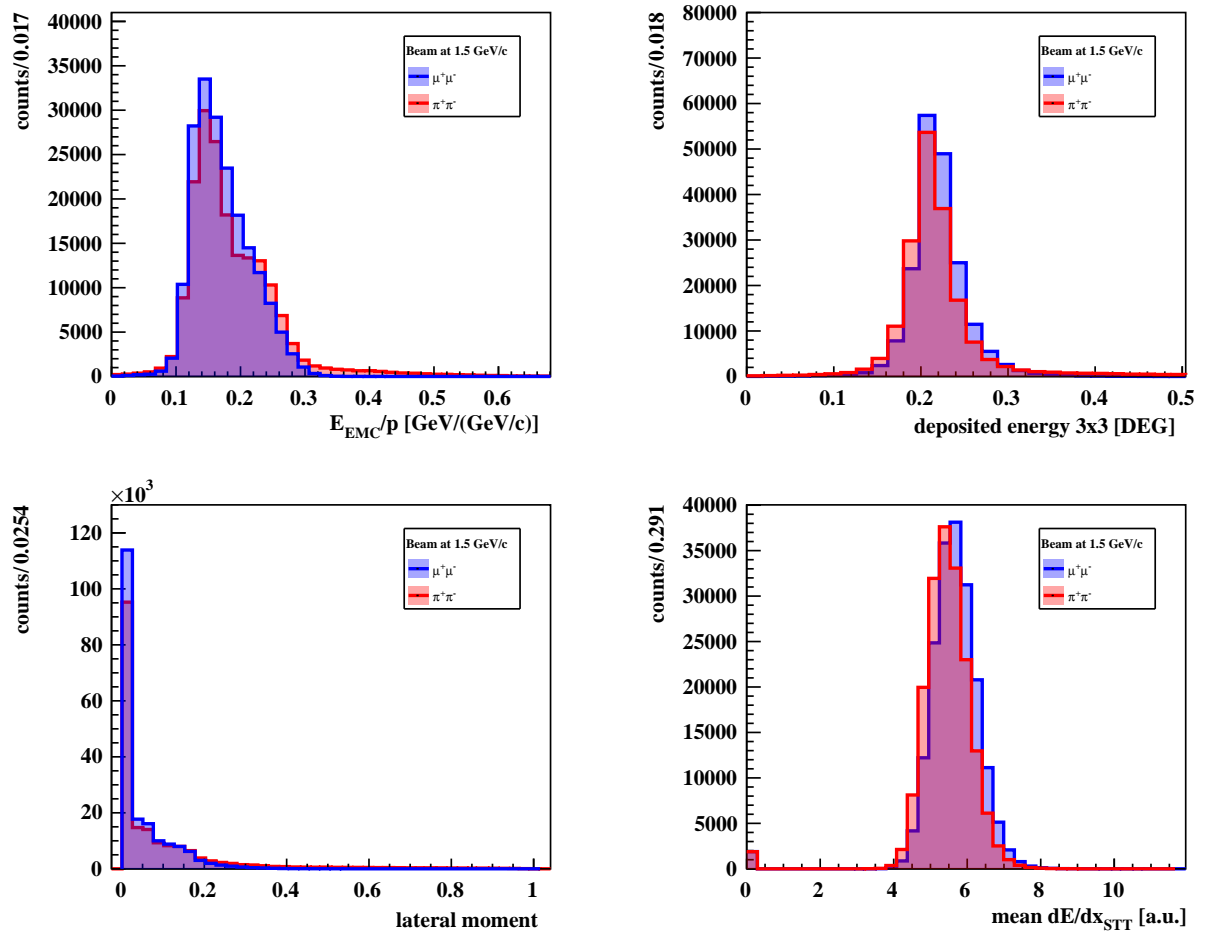


Figure 6.17: Observables from the EMC and the STT at $p_{beam} = 1.5$ GeV/c, which show very similar distributions and therefore are rather weak variables for the MVA in comparison to the variables provided by the Muon System. The signal distributions are shown in blue, while the background distributions are shown in red.

therefore excluded from the set of training variables.

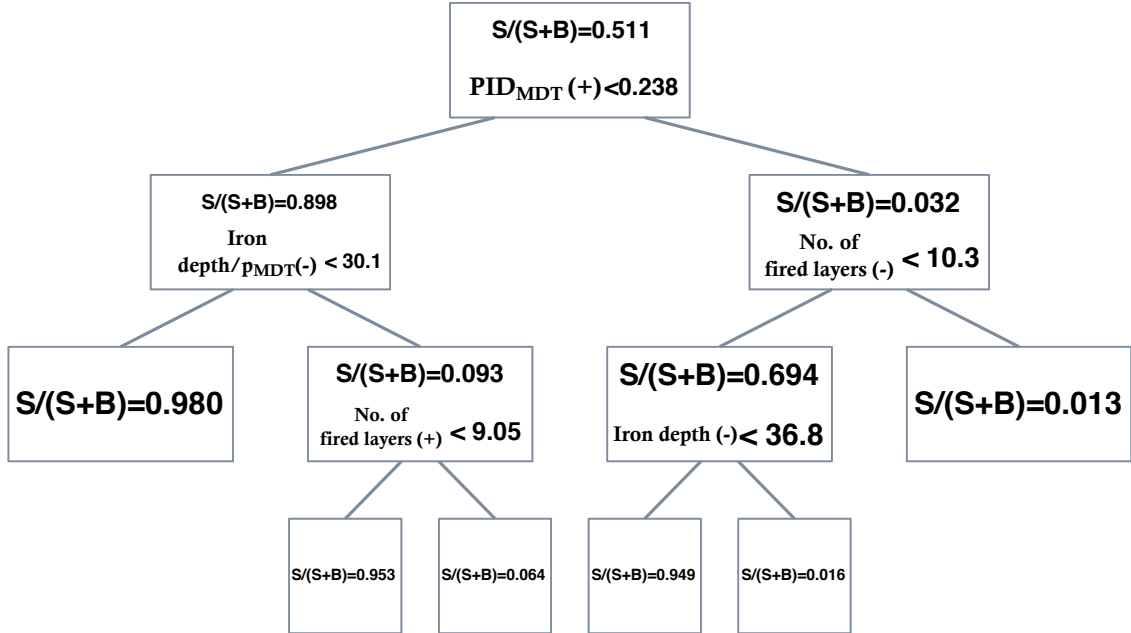


Figure 6.18: Example for a single decision tree of the random forest after optimization of the BDT algorithm. Different variables from the Muon System have been chosen in this case, since they have strong separation power concerning the separation of muons and pions. At each node, the variable is chosen, which achieves the best separation between signal and background. For the determination of the chosen variable, the Gini-Index ($= p(1-p)$) is used, while in this example the achieved purity $S/(S+B)$ of the signal is shown at each node.

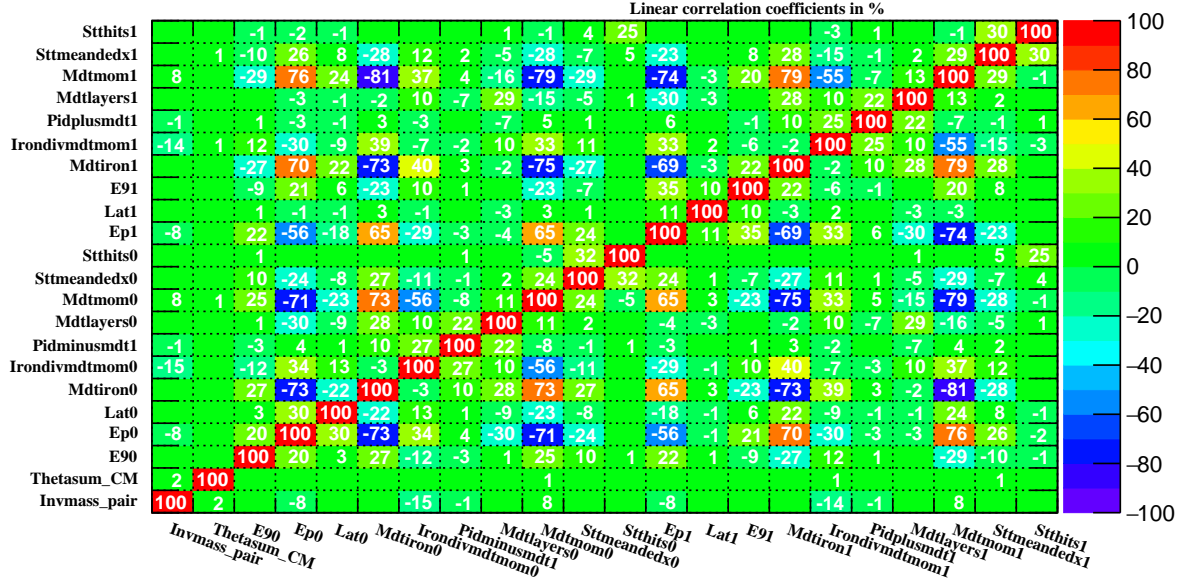
An example for a single tree from the grown and optimized forest of the BDT is illustrated in Figure 6.18. Different variables from the Muon System have been chosen as e.g. the identification probability P_{MDT} or the number of fired detection layers in the Muon System, each of them achieving the best possible separation between signal and background at the individual node.

The linear correlation matrices for the input variables of the signal $\bar{p}p \rightarrow \mu^+\mu^-$ and the background $\bar{p}p \rightarrow \pi^+\pi^-$ sample are shown in Fig. 6.19. These input samples were generated for the purpose of the MVA training and contain each $\sim 10^6$ events. This set of chosen variables does not show strong linear (anti-)correlations ($> 90\%$) between the variables. It is obvious that each variable is fully correlated to itself (diagonal entries have always 100%). The scale on the right shows the linear correlation in %. Green entries indicate no or a very small linear correlation between the two corresponding variables, which is the case for most of the variables.

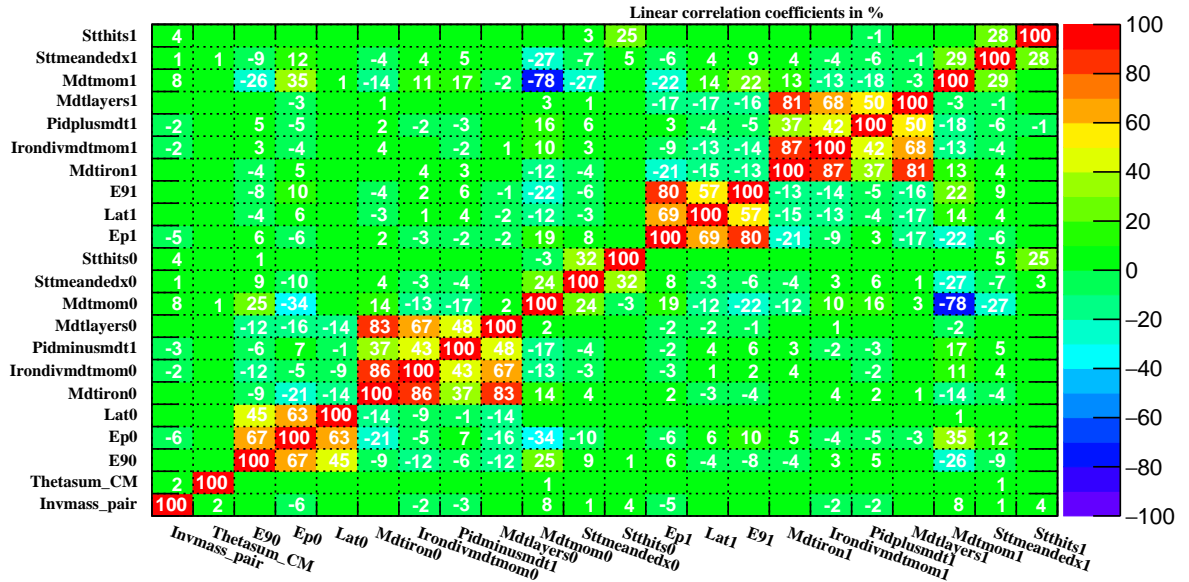
Figure 6.20 shows the slightly overlapping BDT (BDTG) response distributions of the test

Table 6.5: Ranking of the input variables for MVA after the training step at $p_{beam} = 1.5$ GeV/ c . Also listed are the spectator variables, which are not considered by the BDT algorithm but are also saved in the output files of MVA for the final cuts applied after the multivariate classification. The charge of the particle connected to a certain variable is indicated as (+) or (-). This set of input variables was chosen for the MVA training at $p_{beam} = 1.5, 1.7$ and 2.5 GeV/ c .

Rank	Variable	Name	Separation [10^{-1}]
1	PID_{MDT} (+)	Pidplusmdt1	7.41
2	No. of fired layers MS (-)	Mdtlayers0	7.28
3	PID_{MDT} (-)	Pidminusmdt1	7.25
4	iron depth (+) / p_{MDT} (+)	Irondivmdtmom1	7.21
5	iron depth (-) / p_{MDT} (-)	Irondivmdtmom1	7.10
6	No. of fired layers MS (+)	Mdtlayers1	7.10
7	iron depth (-)	Ironthickness0	6.72
8	iron depth (+)	Ironthickness1	6.35
9	$(\theta^+ + \theta^-)_{CM}$	Thetasum_CM	2.52
10	lateral moment (+)	Lat1	0.49
11	deposited energy 3x3 (+)	E91	0.42
12	E_{EMC}/p (+)	Ep1	0.41
13	lateral moment (-)	Lat0	0.36
14	deposited energy 3x3 (-)	E90	0.35
15	E_{EMC}/p (-)	Ep0	0.29
16	dE/dx (STT) (-)	Sttmeandedx0	0.29
17	p_{MDT} (-)	Mdtmom0	0.14
18	p_{MDT} (+)	Mdtmom1	0.14
19	dE/dx (STT) (+)	Sttmeandedx1	0.14
20	M_{inv}	Invmass_pair	0.07
21	No. of hits STT (-)	Stthits0	< 0.01
22	No. of hits STT (+)	Stthits1	< 0.01
	Spectator Variables	Name	
	$(\phi^+ - \phi^-)_{lab}$	Phidiff_lab	-
	$\cos(\theta_{CM})$ (-)	Costheta0_CM	-
	$\cos(\theta_{CM})$ (+)	Costheta1_CM	-

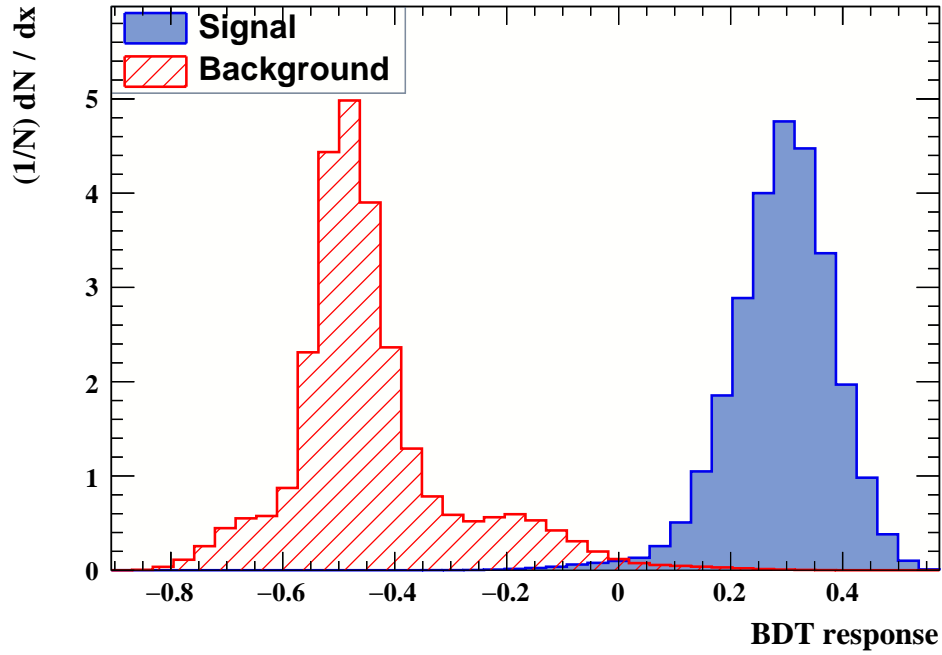


(a)

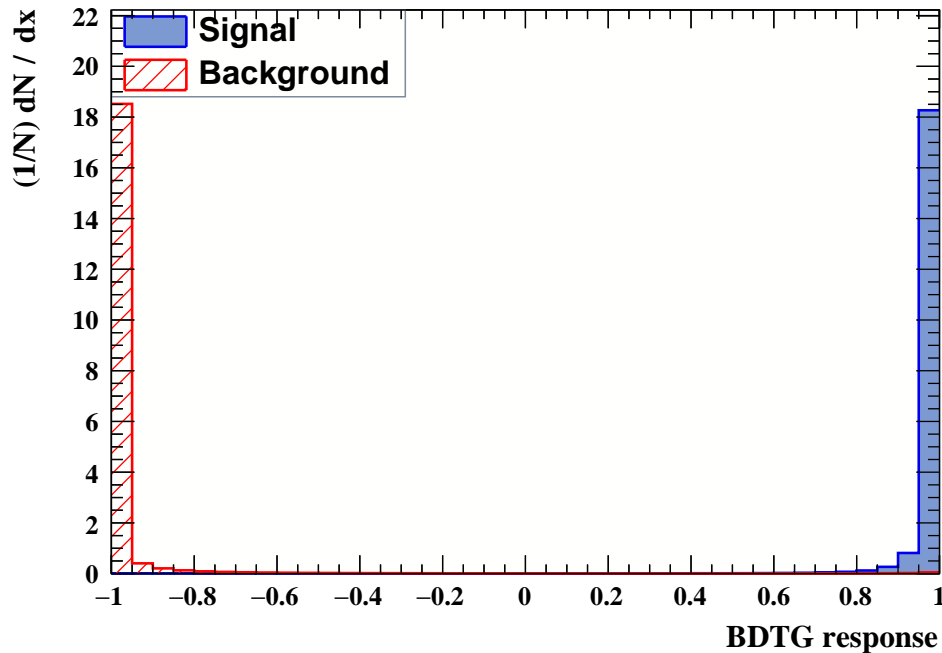


(b)

Figure 6.19: Linear correlation coefficients [%] for the set of input variables used for the MVA at $p_{beam} = 1.5$ GeV/c for the signal (a) and for the background (b). For each input sample, $\sim 10^6$ events have been generated. From strongly correlated variables ($> 90\%$) only one variable was included since the other variable does not carry significant new information.



(a) Training based on BDT algorithm



(b) Training based on BDTG algorithm

Figure 6.20: Normalized response distribution from the BDT for the signal $\bar{p}p \rightarrow \mu^+\mu^-$ (blue) and the background $\bar{p}p \rightarrow \pi^+\pi^-$ (red) for a) the BDT algorithm and b) the BDTG algorithm. The distributions of the response for the signal and the background should be pushed away from each other as far as possible. For the BDTG response, a small fraction of the background events, which have been misclassified, are contained in the signal peak, which is starting around $\text{BDTG} > 0.95$, so that it is also for this method not feasible to remove the full amount of background events.

sample for both signal and background. The cut on the BDT response allows to suppress the background events mostly, however it is not possible to reject it completely in this case. Also for the BDTG this is the case. The optimal cut value on the response (working point) can be chosen based on different parameters of quality as e.g. signal purity, signal significance, etc. In this work, the working point was chosen aiming to keep high signal statistics in each histogram bin for the reconstructed signal events (see section 6.2.4) and at the same time, achieve a sufficient rejection of the events stemming from all kind of possible background sources. Details on the studies of other background channels (e.g. $\bar{p}p \rightarrow \pi^+\pi^-\pi^0$, $\bar{p}p \rightarrow K^+K^-\pi^0$, $\bar{p}p \rightarrow K^+K^-$, etc.) will be given later in Sec. 6.5.

ROC curve

A possibility to directly compare the classification performance of different classification methods is the receiver operating characteristics (ROC) curve. The ROC curve allows to evaluate and compare the performance of different classification algorithms. The ROC curves of this MVA are illustrated for several classification methods in Fig. 6.21 at $p_{beam} = 1.5 \text{ GeV}/c$. The ROC curve shows the dependence of the background rejection ($= 1 - \text{background efficiency}$) on the signal efficiency for different cuts on the classifiers response. An integration over the ROC curve (*area under the curve*) provides a direct performance indicator. The higher the integrated area below a ROC curve, the higher its discrimination performance.

For example, the performance of boosted decision trees (BDT, BDTG) is compared to an artificial neural network (feed-forward multilayer perceptron and two methods of Fisher discriminants. Other methods were tested as well (MLP, k-nearest neighbor, Support Vector Machine, etc.), but could not achieve the very good performance of the Boosted Decision Trees. The curves in Fig. 6.21 are based on data samples for signal and background, which contain $2 \cdot 10^5$ events. The performance of the BDT and the BDTG are very similar. The ROC curves obtained at $p_{beam} = 3.3 \text{ GeV}/c$ confirm the very good performance of the BDT and the BDTG, again being almost identical (see Appendix B). Both methods were used for the full analysis at the different beam momenta, giving results (the uncertainties of the extracted form factors) which are well compatible within their statistical uncertainties and their performance can be seen as identical. In these feasibility studies, the BDT method is chosen for all considered values of beam momentum.

To test whether overtraining happened during the training, a Kolmogorov-Smirnov test is performed. The Kolmogorov-Smirnov test compares the two BDT response distributions, based on the training respectively the test sample (they are obtained from the data sample with $2 \cdot 10^5$ events used for the training, which is split into two statistically independent subsamples of the same size (each contains $1 \cdot 10^5$ events)). It checks whether they differ significantly from each other, which is the case for overtrained classifiers.

Figure 6.22 shows the BDT response for the training and testing data. The output of the Kolmogorov-Smirnov test shows that (almost) no overtraining is present for both methods, since the corresponding distributions match well and high signal (background) probabilities are obtained.

At this point, the trained classifiers are ready for their application on sets of un-known data. All reconstructed and preselected samples for the signal $\bar{p}p \rightarrow \mu^+\mu^-$ and the main background $\bar{p}p \rightarrow \pi^+\pi^-$ process are classified using BDT. The output files (using a tree structure) contain the BDT response together with the events. Also spectator variables are saved in the output tree. Those are variables which are not included into the process of data classification and can be used afterwards for additional cuts on the classified data. As an example, the angular information $\cos(\theta_{CM})$ is a spectator variable.

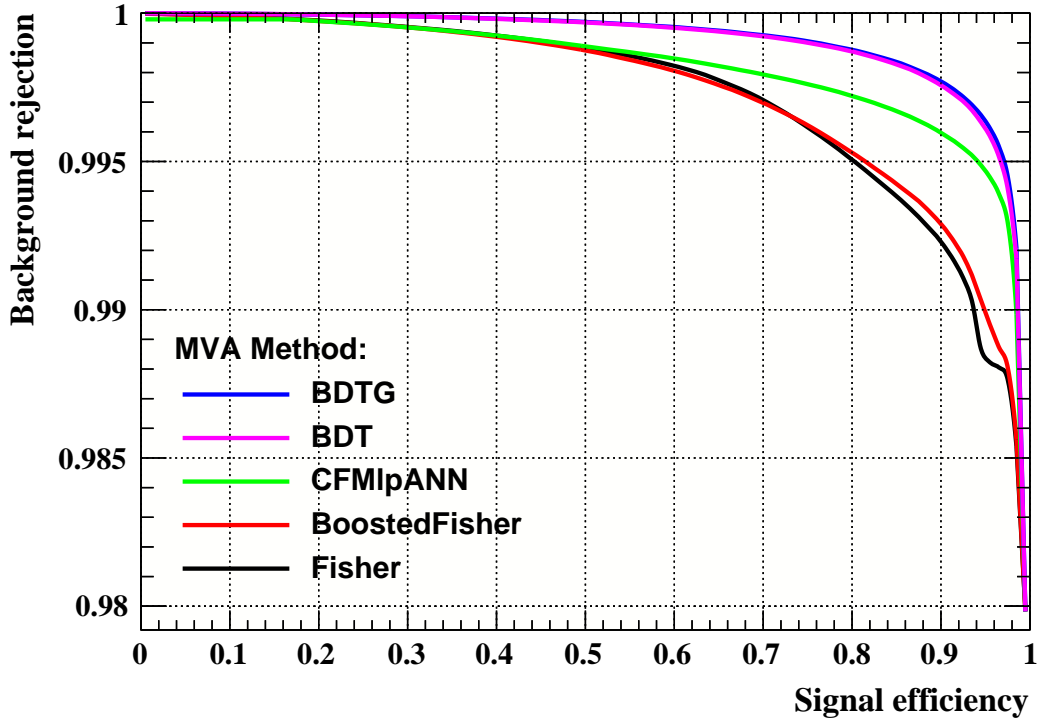


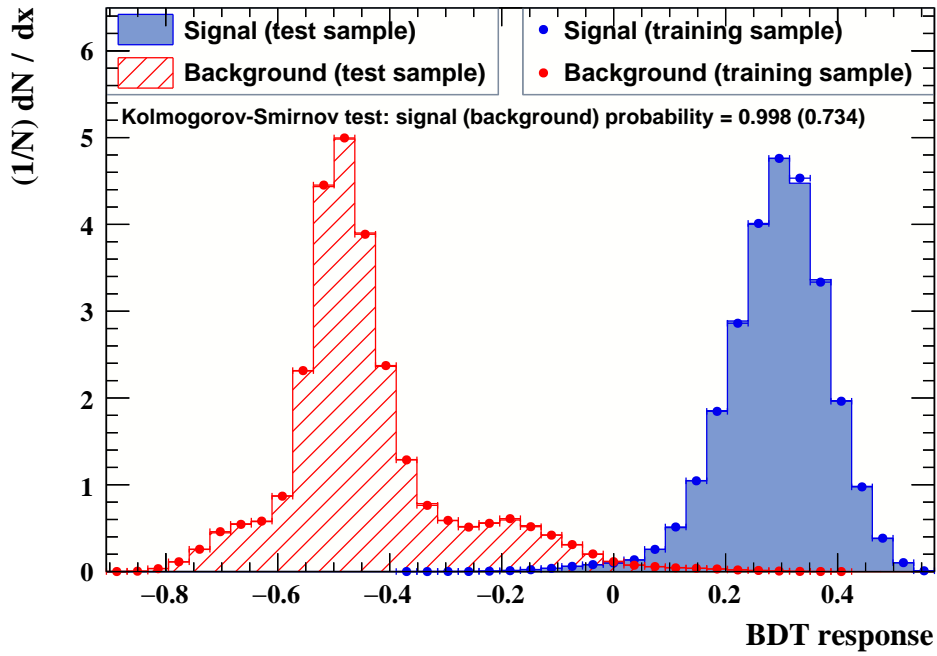
Figure 6.21: Receiver operating characteristics (ROC) for different classification methods, which is used to evaluate the classification performance of each method. The Boosted Decision Trees (BDT, BDTG) show the best performance of all tested methods, with their performance being almost identical. The higher the area under the curve of a certain classification method, the better its performance.

The signal-background separation is done by cutting on the BDT response and a set of additional variables. The cuts on the additional variables are those, which have been applied on the training data before the training and therefore need to be applied on the classified un-known data as well. Different cut values are tested and the corresponding (expected) signal-to-background (S-B) ratio is calculated, what is summarized in Tab. 6.6 together with the corresponding cut configuration used at the individual value of beam momentum.

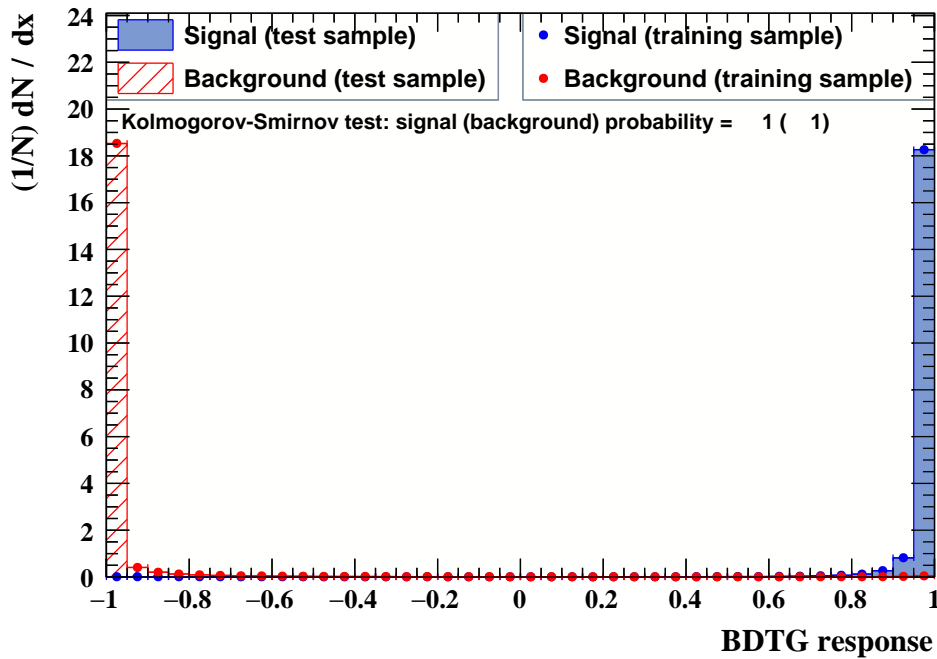
Choice of cuts on the BDT response

In order to choose a possible working point (= optimal cut configuration), different options are investigated which correspond to different cuts on the BDT variable. The goal is to achieve the highest possible precision of the extracted FF's and their ratio R. A possible quantity to search for a working point is provided by the signal significance, which is often used in high energy physics to estimate the probability of a new particle resonance. It is defined as:

$$\text{signal significance} = \frac{S}{\sqrt{S+B}} \quad (6.9)$$



(a)



(b)

Figure 6.22: A Kolmogorov-Smirnov Test is used for overtraining check for a) the BDT algorithm and b) the BDTG algorithm. Overtraining indicates that the classifier is sensitive to statistical fluctuations in the data, which destroys its general operability.

where S (B) stands for the number of signal (background) events after application of the cut criteria. For the case of $S \ll B$, the significance can be written as

$$\text{signal significance} = S/\sqrt{B} \quad (6.10)$$

The maximal value of the signal significance marks the working point in this approach. Nevertheless, this option is not necessarily the solution for all kind of analyses, and the individual goal of the analysis must be defined. The obtained values for the signal significance are shown in Table 6.6. The most powerful signal-background separation is accomplished at 1.5 GeV/ c due to the highest signal statistics and - at the same time - the lowest values of final state particle momenta. Lower muon and pion momenta allow a more effective separation due to the fact, that lower energetic pions can be easier stopped inside the Muon System.

Based on the obtained values, the cut configuration "medium cuts" at $p_{beam} = 1.5$ GeV/ c and $p_{beam} = 1.7$ GeV/ c , as well as at $p_{beam} = 2.5$ GeV/ c , the "tight cuts" and at $p_{beam} = 3.3$ GeV/ c , the "loose cuts" achieve a maximal signal significance (for the definitions of the cut configurations see Tab. 6.6). At this point, one could already choose the final cut configuration based on the maximal signal significance value. However, this will be done after a discussion of the choice of cuts in Sec. 7.1, when the extracted uncertainties of the FF's as well as all relevant rejection factors for all relevant background channels are presented. Based on that collection of information, also the discussion of the working point will be resumed.

The name of the individual cut configuration at a certain value of beam momentum was given in an arbitrary manner. Therefore, cut configurations at different values of beam momentum, which share the same name, are not connected in terms of cut values on the BDT response, total signal efficiency or other parameters.

All possible cut criteria for the μ -selection are listed in Tab. 6.6. At lower beam momenta of 1.5 and 1.7 GeV/ c , the highest pion background rejection factors ϵ_B of the order 10^{-6} - 10^{-5} can be achieved. The analysis of the reconstructed data samples at $p_{beam} = 3.3$ GeV/ c is based on the set of input variables given in Tab. 6.7. Also in this case, the set of input variables was chosen according to their separation power. Weak or highly correlated variables were excluded from the set of input variables. In comparison to lower values of beam momentum, the more powerful variables (mainly from the Muon System) contribute significantly to the signal-background separation at 3.3 GeV/ c and are chosen for the training. The reason for that is the behavior of muon and pion inside the \bar{P} ANDA detector, which is getting more similar for increasing beam momenta. Therefore the smaller set of input variables is sufficient in this case, which is presented in Tab. 6.7.

The background rejection factor ϵ_B is defined as

$$\epsilon_B = \frac{N^{reco}}{N^{MC}} \quad (6.11)$$

Table 6.6: Different cut configurations are tested at beam momenta of 1.5, 1.7, 2.5 and 3.3 GeV/ c . The difference between the configurations is the cut on the BDT response.

1.5 GeV/c									
cut configuration	M_{inv} [GeV/ c^2]	$ \phi^+ - \phi^- _{lab}$ [DEG]	$(\theta^+ + \theta^-)_{CM}$ [DEG]	BDT	ϵ_{tot}	ϵ_B [10^{-6}]	S-B ratio	$\frac{S}{\sqrt{B}}$	
"very loose"]2.1; 2.4[]175.0; 185.0[]179.65; 185.0[> 0.3050	0.351	15.6	1:9	221.0	
"loose"]2.1; 2.4[]175.0; 185.0[]179.65; 185.0[> 0.3140	0.315	12.2	1:8	224.4	
"medium"]2.1; 2.4[]175.0; 185.0[]179.65; 185.0[> 0.3355	0.242	6.9	1:6	229.4	
"tight"]2.1; 2.4[]175.0; 185.0[]179.65; 185.0[> 0.3550	0.180	3.9	1:4	227.4	
"very tight"]2.1; 2.4[]175.0; 185.0[]179.65; 185.0[> 0.3650	0.153	2.8	1:4	223.3	
1.7 GeV/c									
cut configuration	M_{inv} [GeV/ c^2]	$ \phi^+ - \phi^- _{lab}$ [DEG]	$(\theta^+ + \theta^-)_{CM}$ [DEG]	BDT	ϵ_{tot}	ϵ_B [10^{-6}]	S-B ratio	$\frac{S}{\sqrt{B}}$	
"very loose"]2.2; 2.5[]175.0; 185.0[]179.65; 185.0[> 0.290	0.445	33.6	1:18	141.9	
"loose"]2.2; 2.5[]175.0; 185.0[]179.65; 185.0[> 0.300	0.407	26.6	1:16	146.0	
"medium"]2.2; 2.5[]175.0; 185.0[]179.65; 185.0[> 0.335	0.274	11.2	1:10	151.6	
"tight"]2.2; 2.5[]175.0; 185.0[]179.65; 185.0[> 0.348	0.227	7.9	1:8	149.0	
"very tight"]2.2; 2.5[]175.0; 185.0[]179.65; 185.0[> 0.360	0.186	5.6	1:7	144.4	
2.5 GeV/c									
cut configuration	M_{inv} [GeV/ c^2]	$ \phi^+ - \phi^- _{lab}$ [DEG]	$(\theta^+ + \theta^-)_{CM}$ [DEG]	BDT	ϵ_{tot}	ϵ_B [10^{-6}]	S-B ratio	$\frac{S}{\sqrt{B}}$	
"very loose"]2.4; 2.8[]175.0; 185.0[]179.65; 185.0[> 0.172	0.689	183.0	1:67	42.8	
"loose"]2.4; 2.8[]175.0; 185.0[]179.65; 185.0[> 0.234	0.531	59.6	1:28	57.7	
"medium"]2.4; 2.8[]175.0; 185.0[]179.65; 185.0[> 0.260	0.424	31.2	1:19	63.7	
"tight"]2.4; 2.8[]175.0; 185.0[]179.65; 185.0[> 0.280	0.334	17.5	1:13	67.0	
"very tight"]2.4; 2.8[]175.0; 185.0[]179.65; 185.0[> 0.300	0.242	9.2	1:10	63.3	
3.3 GeV/c									
cut configuration	M_{inv} [GeV/ c^2]	$(\phi^+ - \phi^-)_{lab}$ [DEG]	$(\theta^+ + \theta^-)_{CM}$ [DEG]	BDT	ϵ_{tot}	ϵ_B [10^{-6}]	S-B ratio	$\frac{S}{\sqrt{B}}$	
"very loose"]2.6; 3.1[]175.0; 185.0[]179.65; 185.0[> 0.300	0.371	23.3	1:8	49.6	
"loose"]2.6; 3.1[]175.0; 185.0[]179.65; 185.0[> 0.320	0.295	13.0	1:5	53.0	
"medium"]2.6; 3.1[]175.0; 185.0[]179.65; 185.0[> 0.327	0.269	11.6	1:5	51.0	
"tight"]2.6; 3.1[]175.0; 185.0[]179.65; 185.0[> 0.330	0.258	10.6	1:5	51.1	
"very tight"]2.6; 3.1[]175.0; 185.0[]179.65; 185.0[> 0.340	0.222	7.8	1:4	51.3	

where N^{reco} stands for the total number of reconstructed events after application of all cut criteria. The total number of generated Monte-Carlo events for the pion background process is denoted as N^{MC} . While at such low beam momenta, most of the muons traverse the Muon System without being stopped, the pions are mostly stopped within the first absorber layers of the Muon System. The S/B separation becomes more difficult at higher values of beam momentum, where the pions become more energetic and therefore are able to traverse more absorber layers inside the Muon System. Hence, they behave more signal-like and therefore are much

Table 6.7: Chosen variables for the MVA training at $p_{beam} = 3.3$ GeV/ c with ranking of the variables according to their separation power. The particle charge connected to a certain variable is indicated as (+) or (-). A smaller set of input variables is chosen at $p_{beam} = 3.3$ GeV/ c in comparison to the case of $p_{beam} = 1.5, 1.7$ and 2.5 GeV/ c , since only the more powerful variables (mainly from the Muon System) contribute significantly to the signal-background separation, due to the more similar behavior of muon and pion for increasing beam momentum.

Rank	Variable	Name	Separation [10^{-1}]
1	No. of fired layers MS (-)	Mdtlayers0	8.16
2	No. of fired layers MS (+)	Mdtlayers1	7.86
3	iron depth (+)	Ironthickness1	7.74
4	PID_{MDT} (+)	Pidminusmdt1	7.63
5	iron depth (-) / p_{MDT} (-)	Irondivmdtmom0	7.12
6	PID_{MDT} (+)	Pidplusmdt1	6.86
7	iron depth (-)	Ironthickness0	6.45
8	iron depth (+) / p_{MDT} (+)	Irondivmdtmom1	3.79
9	E_{EMC}/p (+)	Ep1	3.26
10	E_{EMC}/p (-)	Ep0	2.48
11	$(\theta^+ + \theta^-)_{CM}$	Thetasum_CM	2.44
12	dE/dx STT (+)	Sttmeandedx1	1.54
13	dE/dx STT (-)	Sttmeandedx0	0.23
and as spectator variables			
	M_{inv}	Invmass_pair	-
	$(\phi^+ - \phi^-)_{lab}$	Phidiff_lab	-
	$\cos(\theta_{CM})$ (-)	Costheta0_CM	-
	$\cos(\theta_{CM})$ (+)	Costheta1_CM	-

more difficult to be distinguished from the signal muons.

The expected signal-to-background (S-B) ratios can be calculated based on the value of total signal efficiency ϵ_{tot} , the corresponding background rejection factor ϵ_B and the number of physically expected signal and background events (the numbers can be found in Tab. 5.1). The obtained values of the expected S-B ratio are presented in Tab. 6.6. For beam momenta of 1.5 GeV/ c (1.7 GeV/ c) it can be seen, that signal-to-background ratios from 1:4 up to 1:9 (1:7 up to 1:18) are expected. At 2.5 GeV/ c , the cross section ratio $\sigma(\bar{p}p \rightarrow \pi^+\pi^-)/\sigma(\bar{p}p \rightarrow \mu^+\mu^-)$ is maximal in comparison to the case of the other considered values of beam momentum, what could be seen in Tab. 5.1 in the previous chapter. Therefore, the expected S/B ratios are much worse with values between 1:10 up to 1:67, depending on the cut configuration. It will be seen in the next subsection, that for $p_{beam} = 3.3$ GeV/ c the reconstruction efficiency of the signal drops strongly for values of $\cos(\theta_{CM}) > 0.4$ so that the corresponding histogram bins of the

signal angular distribution need to be excluded in the analysis. Here, the cut values on the BDT response were chosen to keep enough signal efficiency in the histogram bins for the range of $-0.8 < \cos(\theta_C M) < 0.4$. The corresponding rejection factor is of the order of 10^{-5} - 10^{-4} , depending on the cut configuration. The cross section ratio $\sigma(\bar{p}p \rightarrow \pi^+\pi^-)/\sigma(\bar{p}p \rightarrow \mu^+\mu^-)$ is minimal in comparison to the case of other values of beam momenta. This allows to achieve better expected signal-to-background ratios from 1:4 up to 1:8.

After application of the cut criteria, the reconstructed and μ -selected signal events are filled into histograms which are presented in Figures 6.23 - 6.26. The reconstruction efficiency of the signal (denoted in the following as *signal efficiency*) is calculated using

$$\epsilon_i = N_i^{reco}/N_i^{gen} \quad (6.12)$$

with the corresponding error

$$\Delta\epsilon_i = \sqrt{\epsilon_i \cdot \frac{1 - \epsilon_i}{N_i^{gen}}} \quad (6.13)$$

where ϵ_i is the signal efficiency in the i -th histogram bin, N_i^{reco} is the number of reconstructed and μ -selected signal events and N_i^{gen} is the number of generated MC signal events in the i -th histogram bin. The error $\Delta\epsilon_i$ was derived assuming a Binomial probability distribution, since the efficiency is not close to zero.

A comparison between this study based on multivariate analysis and a more simple study based on simple cuts can be found in the Appendix F. It is shown for the lowest beam momentum, that the application of multivariate analysis methods improves the signal-background separation strongly. The expected signal-background separation is obtained as 1:6 for the MVA, while for simple cuts, a strongly worse ratio of 1:72 is obtained.

6.2.4 Signal efficiency distribution

In the previous subsection, possible cut configurations, the signal significance and the corresponding expected S-B ratios were discussed. In this section, the effect of the cut on the BTD response on the angular distribution of the signal efficiency shall be discussed. Since the signal efficiency - in particular its angular distribution - has a strong influence on the statistical uncertainty of the extracted FF's later, it is important to keep enough signal efficiency over the whole considered range of $|\cos(\theta_{CM})| < 0.8$.

Figures 6.23 - 6.26 show the angular distributions of the reconstruction efficiency of the signal (denoted as signal efficiency ϵ), based on the signal event sample of high statistics after μ -selection as well as the corresponding generated MC signal events at the considered values of beam momentum of $p_{beam} = 1.5, 1.7, 2.5$ and 3.3 GeV/ c . The shape of the angular distributions of ϵ as well as the μ -selected signal counts is mostly determined by the cut value on the BDT response. In the following, the signal efficiency distribution is shown for each beam momentum. The considered cut configurations are discussed. For all considered values of beam momentum, the final cut configurations will be chosen later, when the FF's are extracted in the next chapter.

1) $p_{beam} = 1.5$ GeV/ c

Figure 6.23 shows the angular distributions of the signal reconstruction efficiency, the MC generated signal events and the reconstructed signal events at four different cut configurations. From this figure, it can be seen that the highest total signal statistics is obtained with loose cuts. For more stricter cuts, lower values of the signal reconstruction efficiency in the region around $\cos(\theta_{CM}) \approx 0.0$ as well as at very forward (backward) angles are obtained, which are the regions where the pion differential cross section has high values. The suppression of this large background in these areas result in a loss of signal statistics. Lower values of ϵ lead to larger error bars later in the efficiency corrected signal distribution at those intervals of $\cos(\theta_{CM})$. Therefore, loose cuts should be preferred over stricter cuts.

2) $p_{beam} = 1.7$ GeV/ c

Figure 6.24 shows the angular distribution of the signal statistics (MC and μ -selected counts) together with the obtained angular distribution of the signal efficiency. Also in this case, signal efficiency is lost while choosing stricter cuts, which can be seen by comparing the distributions shown in 6.24 (a)-(d). This is the case especially at the regions of $\cos(\theta_{CM})$ around 0.0 and at the outer borders, where the pion differential cross section for the $\bar{p}p \rightarrow \pi^+\pi^-$ process has high values (see Fig. 5.5 in the previous chapter). Therefore, the cut applied on the BDT response leads to a much stronger loss of signal statistics in this region in comparison to the regions, where the pion differential cross section has lower values.

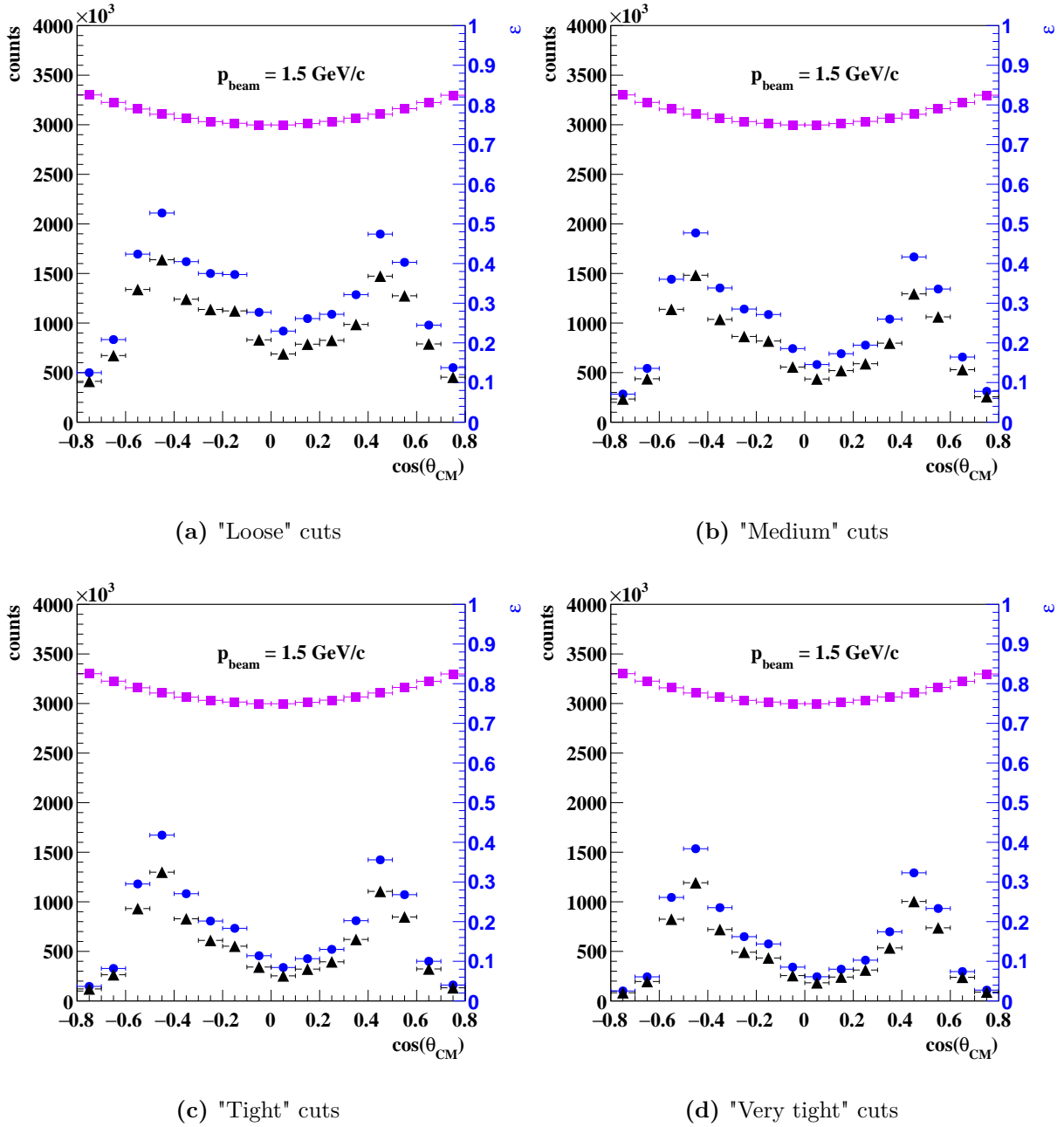


Figure 6.23: Angular distributions of the signal reconstruction efficiency (ϵ) (blue dots), the Monte-Carlo generated signal (magenta squares) and the reconstructed signal (black up triangles) at $p_{\text{beam}} = 1.5 \text{ GeV}/c$ obtained with the cut configurations (a) "Loose" cuts, (b) "Medium" cuts", (c) "Tight" cuts and (d) "Very tight" cuts applied on the reconstructed, preselected signal sample with high statistics. Stricter cut configurations lead to smaller values of the signal efficiency around $\cos(\theta_{CM}) \approx 0.0$ and at the outer borders of $\cos(\theta_{CM})$. Loose cuts should be preferred in this case, to avoid large error bars later when the angular distribution of the signal is corrected with the signal efficiency. This will have a direct influence on the uncertainty of the extracted FF's.

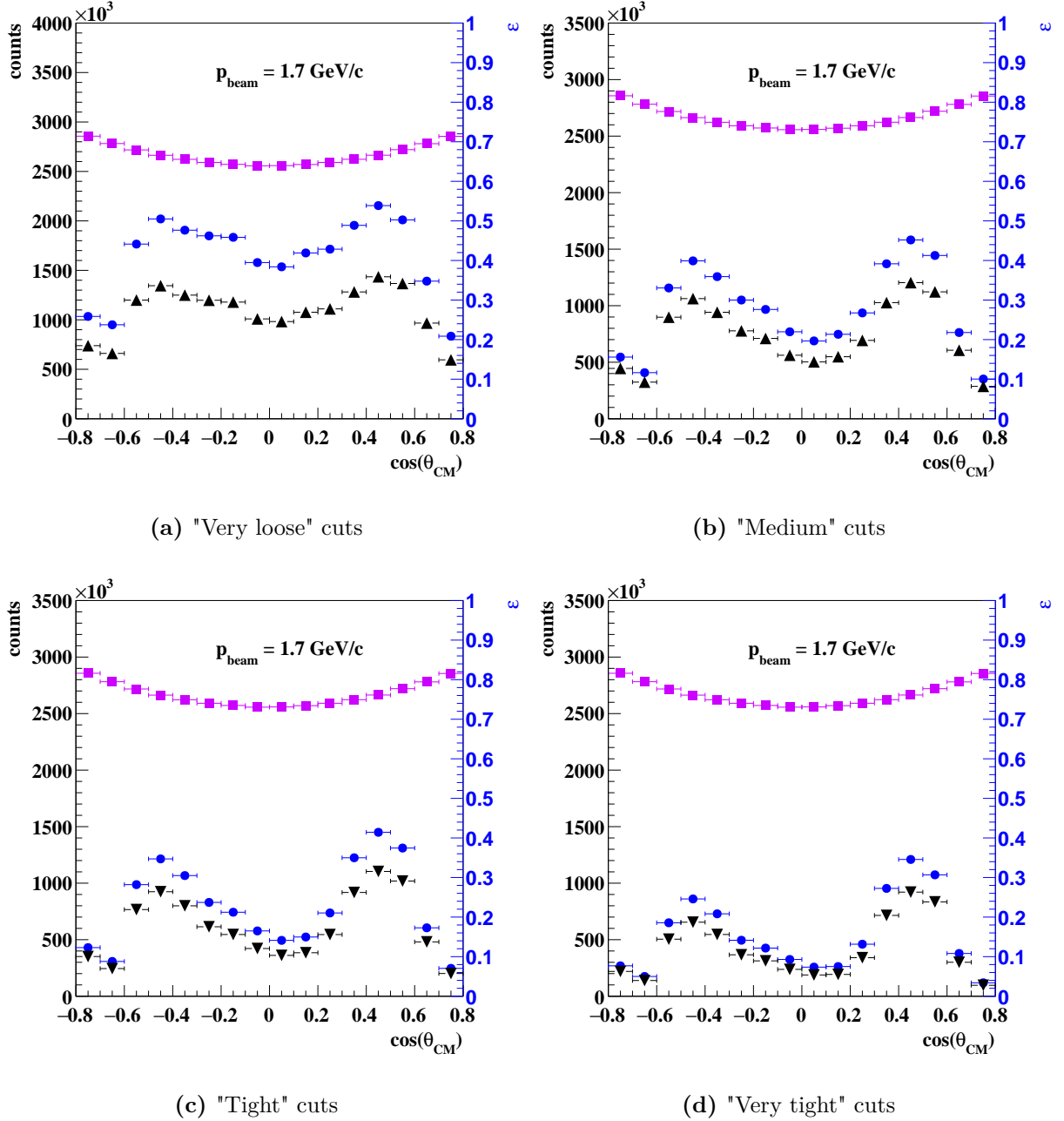


Figure 6.24: Angular distributions of the signal reconstruction efficiency (ϵ) (blue dots), the Monte-Carlo generated signal (magenta squares) and the reconstructed signal (black up triangles) at $p_{beam} = 1.7$ GeV/c (a) "Very loose" cuts, (b) "Medium cuts", (c) "Tight cuts" and (d) "Very tight" cuts, applied on the reconstructed, preselected signal sample with high statistics. To avoid large uncertainties of the extracted values of FF's later, also in the case of $p_{beam} = 1.7$ GeV/c, it can be concluded that loose cuts should be preferred over stricter cuts. The working point will be determined later, when the extracted FF values are presented.

3) $p_{beam} = 2.5 \text{ GeV}/c$

At $p_{beam} = 2.5 \text{ GeV}/c$, the signal efficiency distribution drops in the area of $0.3 < \cos(\theta_{CM}) < 0.7$, where the μ/π separation becomes more challenging due to the increasing values of the pion differential cross section. This behavior can be seen in Fig. 6.25.

4) $p_{beam} = 3.3 \text{ GeV}/c$

At the highest considered beam momentum of $3.3 \text{ GeV}/c$, most of the signal statistics is lost for the region $\cos(\theta_{CM}) > 0.4$, what can be seen in Fig. 6.26. The reason for this are strongly increasing values of the pion differential cross section in this range of $\cos(\theta_{CM})$. None of the cut configurations allows to keep enough signal efficiency in the histogram bins connected to the range of $\cos(\theta_{CM}) > 0.4$, so that they will be excluded in the further analysis, which will be presented in Sec. 7.1, when the extraction of $|G_E|$, $|G_M|$ and R together with their errors is performed.

After applying the μ -selection on the signal samples as well as the background sample, the calculation of the expected signal-to-background ratios shows typical values between 1:4 and 1:9 for the lowest value of beam momentum. A background subtraction can be applied to remove the pion contamination from the contaminated signal data. A possible way to measure and reconstruct the required pion contamination was proposed in Sec. 5.1. In this feasibility study, the effect of the background subtraction on the statistical uncertainty of the extracted FF values must be included. Therefore the angular distribution of the pion contamination is required and must be obtained in a different way in comparison to the experimental strategy, due to the fact, that it is not possible to simulate background data samples with the number of expected events within a reasonable time period. As an example, the simulation of the expected amount of pion events of 2.65×10^{11} events at $p_{beam} = 1.5 \text{ GeV}/c$ would require a pure computing time of approximately 2 years, while 10^8 events require a pure computing time of approximately 17 hours.

In this work, the angular distribution of the expected pion contamination is obtained with a dedicated method, which will be described and discussed in detail in the following section.

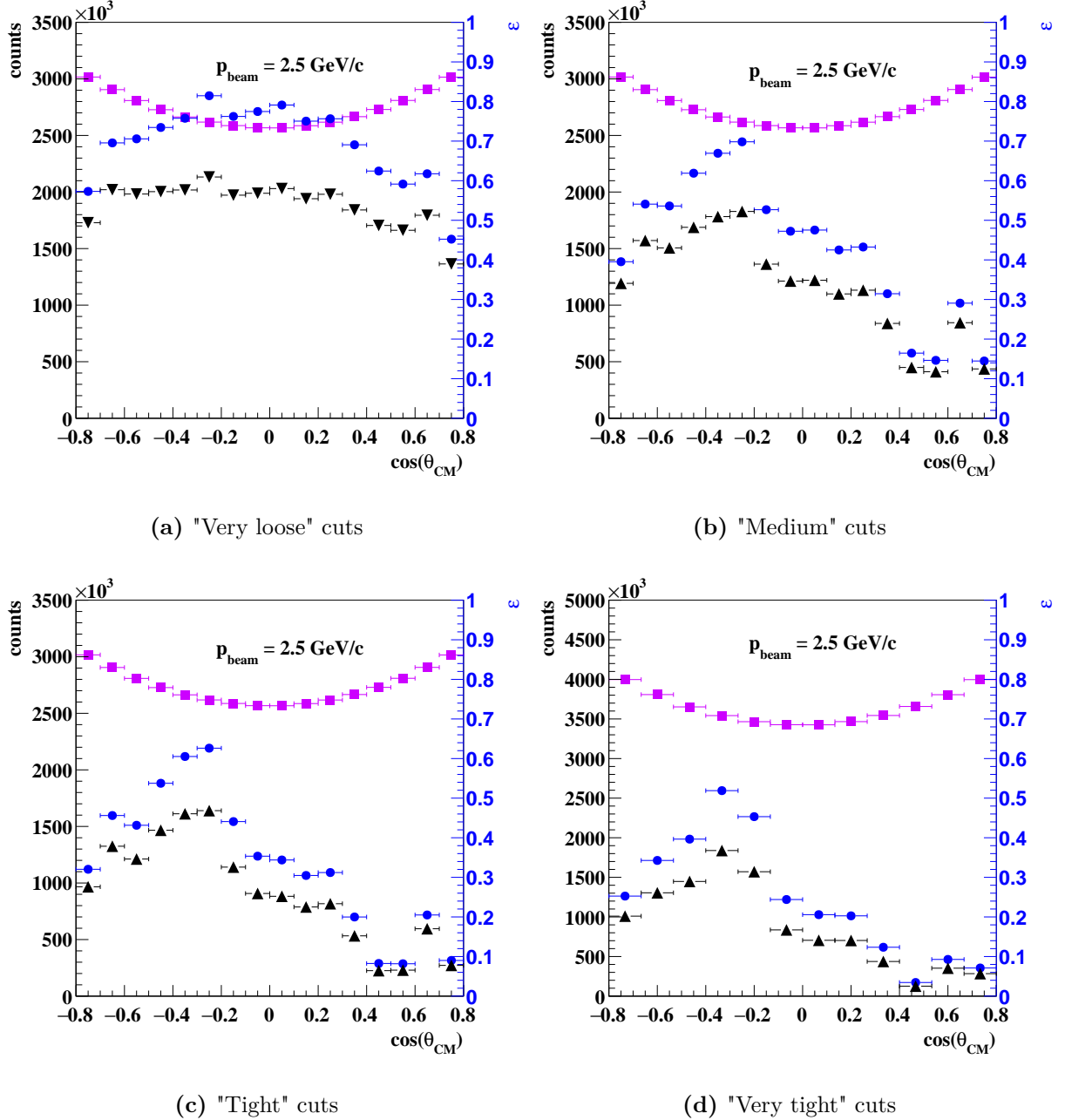


Figure 6.25: Angular distributions of the signal reconstruction efficiency (ϵ) (blue dots), the Monte-Carlo generated signal (magenta squares) and the reconstructed signal (black up triangles) from the signal sample of high statistics at $p_{\text{beam}} = 2.5 \text{ GeV}/c$ (a) "Very loose" cuts, (b) "Medium cuts", (c) "Tight cuts" and (d) "Very tight" cuts. "Very loose" cuts provide the keep the highest signal statistics in all histogram bins, but are connected to very low expected S-B ratios (1:67). Therefore, the "medium" or "tight" cuts should be preferred over "very loose" cuts.

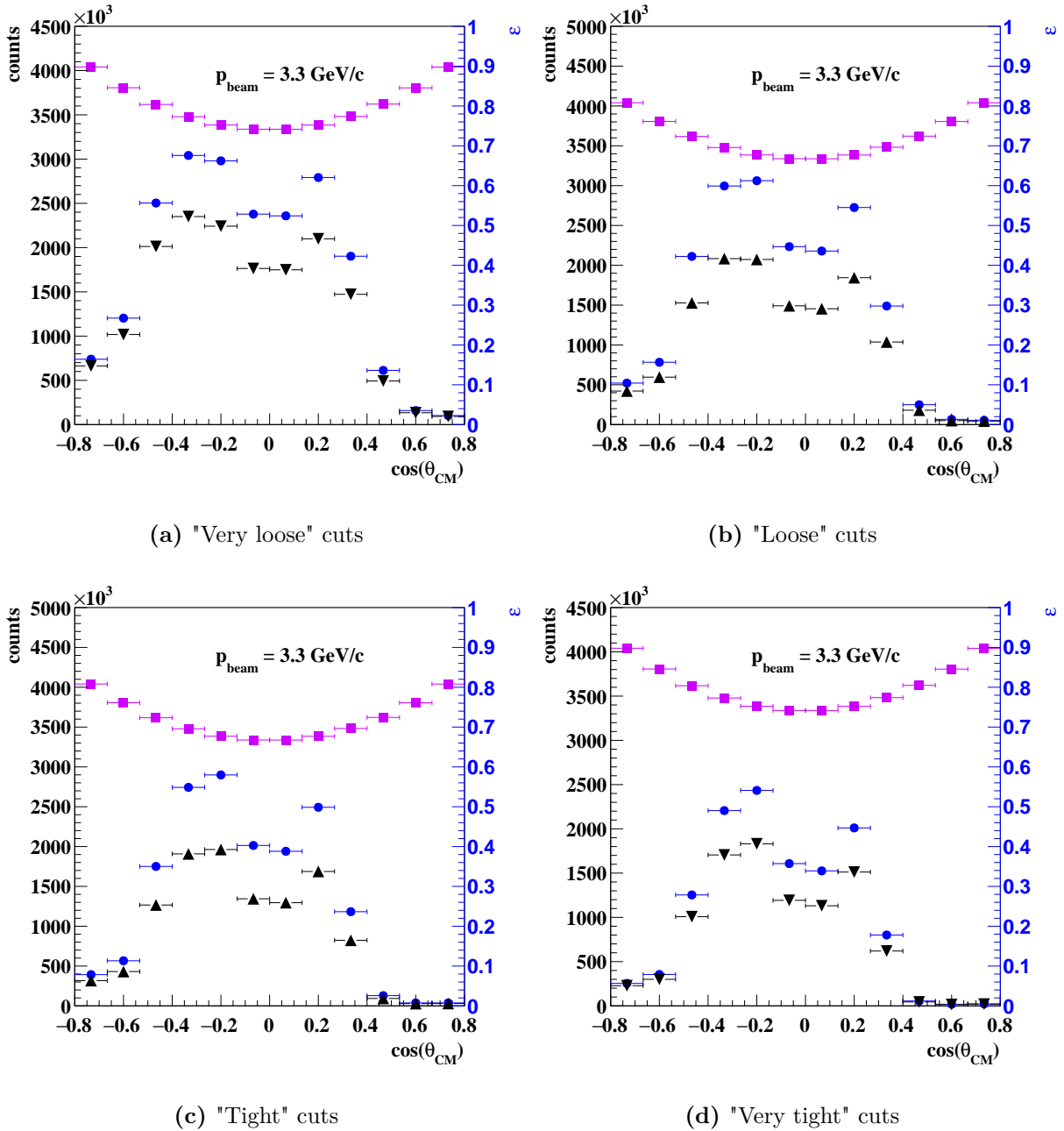


Figure 6.26: Angular distributions of the signal reconstruction efficiency (ϵ) (blue dots), the Monte-Carlo generated signal (magenta squares) and the reconstructed signal (black up triangles) from the signal sample of high statistics at $p_{\text{beam}} = 3.3 \text{ GeV}/c$ (a) "Very loose" cuts, (b) "Loose cuts", (c) "Tight cuts" and (d) "Very tight" cuts.

6.3 Background contamination from $\bar{p}p \rightarrow \pi^+\pi^-$

As it was shown in the previous section, a high pion contamination, including muons from pion decay, will be expected in the μ -selected data. In order to remove this contamination, a background subtraction will be applied in the analysis of the experimental data, which introduces statistical fluctuations from the background contamination in the histograms of the reconstructed, μ -selected signal events. The influence of such statistical background fluctuations on the precision of the extracted FF values needs to be included in this feasibility study. In the future experiment, the measured reconstructed pion contamination and the pion contamination hidden inside the reconstructed μ -selected signal data, will not possess identical statistical fluctuations due to the different analyses used to obtain them. Therefore, two statistically independent angular distributions of the pion contamination are required for the performance of the background subtraction in this study.

In this feasibility study, a background suppression factor of the order of $10^{-5} - 10^{-6}$ is typically achieved (see Tab. 6.6). The physically expected number of background events from $\bar{p}p \rightarrow \pi^+\pi^-$ is of the order of $10^9 - 10^{11}$ (exact numbers are listed in 5.1) assuming a time-integrated luminosity of 2 fb^{-1} at $\bar{\text{P}}\text{ANDA}$ Phase-3. From that, the expected numbers of pion background events after μ -selection (*pion contamination*), denoted as $N_{exp,cuts}(\bar{p}p \rightarrow \pi^+\pi^-)$, were calculated and are summarized in Tab. 6.8.

Table 6.8: Expected counts in the pion contamination $N_{exp,cuts}(\bar{p}p \rightarrow \pi^+\pi^-)$ at the considered values of beam momenta at $\bar{\text{P}}\text{ANDA}$ Phase-3. A time-integrated luminosity of 2 fb^{-1} is assumed. Also shown are the expected numbers for the signal after μ -selection $N_{exp,cuts}(\bar{p}p \rightarrow \mu^+\mu^-)$ for comparison, based on the final cut configuration at each considered value of beam momentum. The final cut configurations will be chosen in Chapter 7.

p_{beam} [GeV/c]	Cut criterium	$N_{exp,cuts}(\bar{p}p \rightarrow \pi^+\pi^-)$	$N_{exp,cuts}(\bar{p}p \rightarrow \mu^+\mu^-)$
1.5	loose	3,229,081	402,857
1.7	medium	2,250,924	227,468
2.5	tight	790,890	59,515
3.3	loose	76,780	14,671

6.3.1 Construction of the angular distribution

It is aimed to obtain the angular distribution of the pion contamination, which contains both the expected statistics and possesses a more realistic shape. In this method, the μ -selection is applied to the reconstructed background sample for the $\bar{p}p \rightarrow \pi^+\pi^-$ process and the obtained angular distribution acts as the *source histogram*. This source histogram typically contains a few thousand entries. The shape of the pion distribution after μ -selection is extracted by adapting

a fit function to the source histogram. As a fit function, a polynomial of the form

$$f(x) = \sum_{n=0}^{n_{max}} a_n x^n, \quad (6.14)$$

is used, where the number of orders n were varied in order to achieve an optimal value of reduced χ^2 close to 1. For beam momenta of 1.5 GeV/ c and 1.7 GeV/ c , a fit function of the order of $n_{max} = 8$ was chosen, since the value of reduced χ^2 did not improve significantly for higher orders $n > 8$. At the two values of higher beam momenta, 2.5 GeV/ c and 3.3 GeV/ c , a fit function with $n = 9$ achieved an optimal performance. This function, which is denoted as f_1 , serves as an input for a random number generator (TRandom3 of the ROOT package), which is used to fill a new histogram (*target histogram*). The target histogram is filled until a number of entries is reached which corresponds to the individual expected statistics. This procedure is repeated to fill a second target histogram, based on a different set of seeds for the random number generation.

The obtained angular distribution in the target histogram does not only contain the expected statistics, but also possesses a more realistic shape. A shortcoming of this method is that in the case of very strict cut configurations, the source histogram has poor statistics and a shape is not visible. An example of the fit function f_1 is shown in Fig. 6.27 (a) for the case of

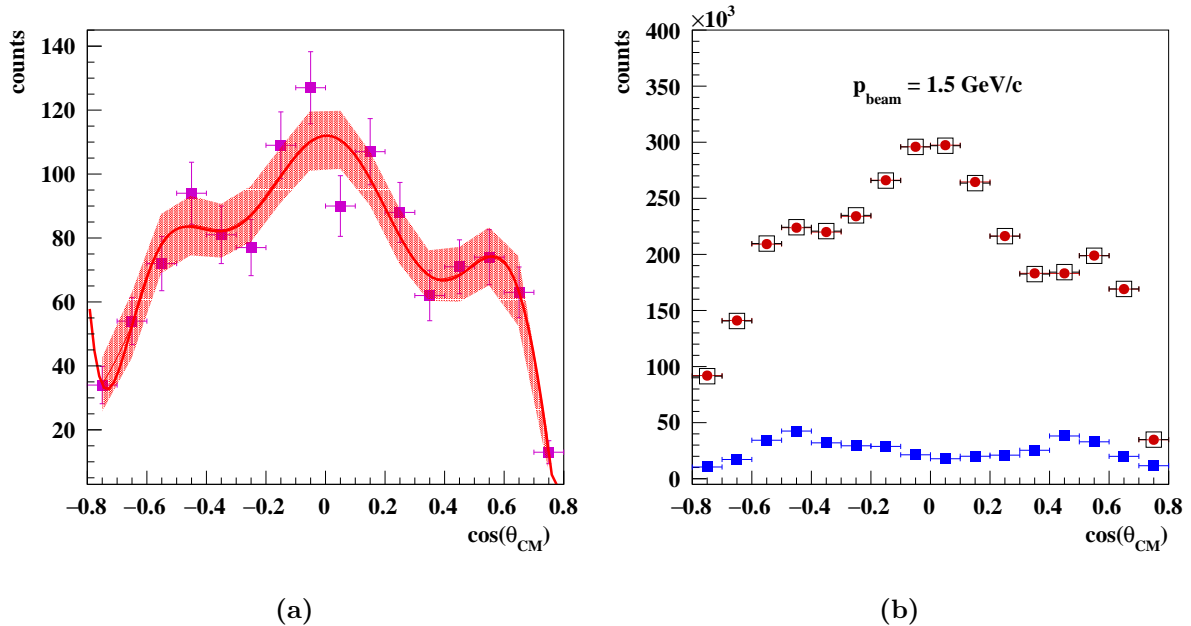


Figure 6.27: (a) Source histogram with adapted fit function f_1 with the $\pm 1\sigma$ error band of the adapted fit function. A reduced χ^2 for the fit of $\chi^2/ndf = 1.59$ was obtained. The function f_1 is used for the generation of the two statistically independent target histograms. (b) The first (black open squares) and second (red dots) target histogram, containing the pion contamination distribution. Also shown is the signal distribution after μ -selection (blue squares).

$p_{beam} = 1.5$ GeV/ c after applying "loose" cuts together with the source histogram. Figure 6.27

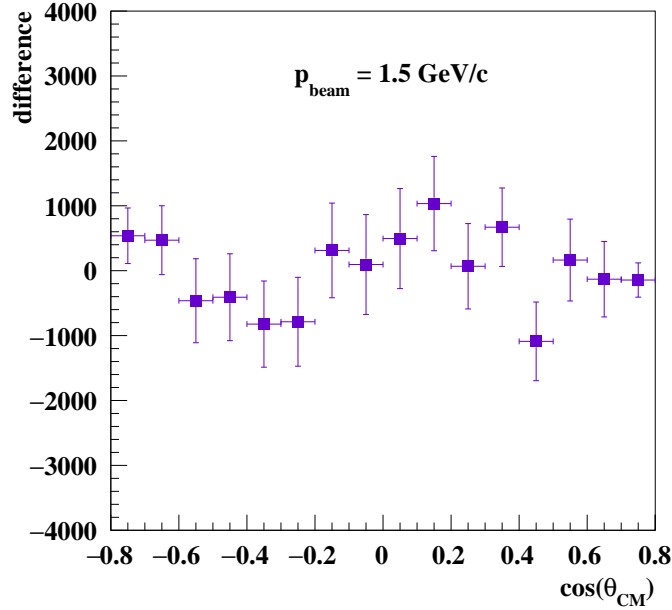


Figure 6.28: Difference of the histograms of the two statistically independent pion contamination distributions, which are shown in Figure 6.27 (b). The difference is due to the statistical fluctuations.

(b) shows the obtained target histogram, which contains both angular distributions of the pion contamination together with the signal distribution after μ -selection. Their statistical fluctuations are not visible in this illustration due to the large number of bin entries, but can be visualized by considering the difference of the two independent pion background distributions, what is shown in Fig. 6.28.

The same strategy is used to generate angular distributions of the pion contamination at higher beam momenta. Further plots of the adapted fit function on the residual background distribution (source histogram) and the corresponding distributions of the pion contamination with realistic shape can be found in the Appendix C.

Fig. 6.29 shows the angular distributions of the signal distribution after μ -selection together with the two independent pion background distributions at the considered values of beam momentum. Here, the distributions at the final chosen cut configurations are already shown. The choice of the cut configuration will be done in Chapter 7.

The influence of the statistical background fluctuations on the results of this feasibility study was studied at $p_{beam} = 1.5 \text{ GeV}/c$ and is presented in the Appendix G. It could be shown in this study, that the background fluctuations dominate the statistical uncertainty of the form factors (which will be extracted in Chapter 7).

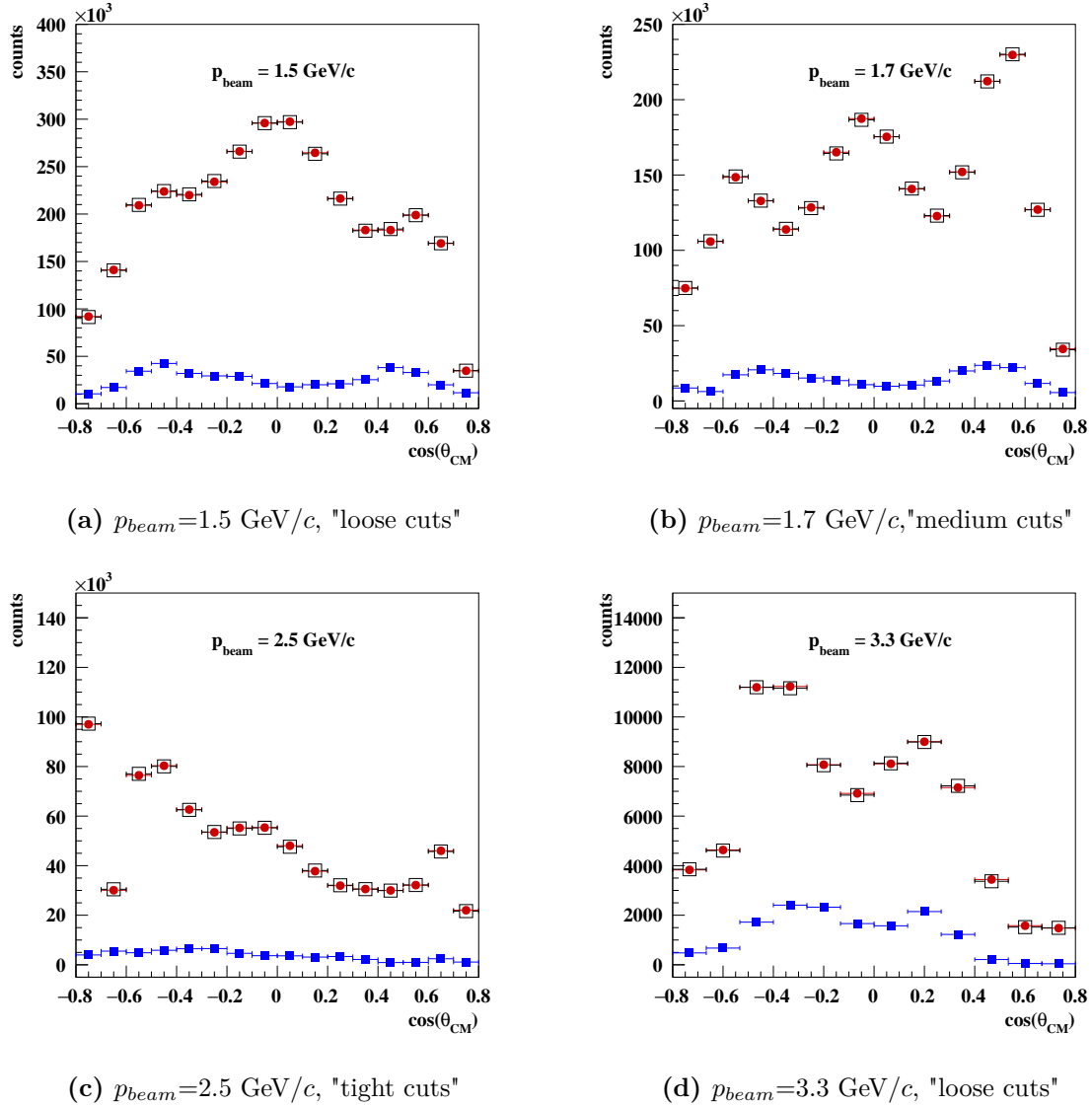


Figure 6.29: Angular distributions of the reconstructed μ -selected signal (based on sample S2) (blue squares) depending on the center-of-mass angle $\cos(\theta_{CM})$. Also shown are the two statistically independent angular distributions of the pion contamination (black open squares, red dots) at the considered values of beam momentum of (a) 1.5 GeV/c, "loose cuts" (b) 1.7 GeV/c, "medium cuts", (c) 2.5 GeV/c, "tight cuts" and (d) 3.3 GeV/c, "loose cuts".

Using the reconstructed signal angular distribution and the two statistically independent pion background distributions, the analysis can be performed in order to obtain the efficiency corrected angular distribution (under the conditions of \bar{P} ANDA Phase-3). The analysis strategy will be summarized in the following section.

6.4 Analysis strategy

The analysis strategy in this feasibility study shall be described on the example of the $p_{beam} = 1.5$ GeV/c and loose cuts, using the angular distribution of the reconstructed, μ -selected signal and the two statistically independent pion background distributions. Figure 6.30 shows the angular distributions used in the analysis. The analysis consists of four steps:

1. The reconstructed, selected data (D) are formed as $D = S2 + B1$
2. Background subtraction: $D - B2$
3. Application of the efficiency correction: $(D-B2)/\epsilon$
4. The efficiency corrected data are fitted with $f_1(x)$ and the proton FF's are extracted simultaneously

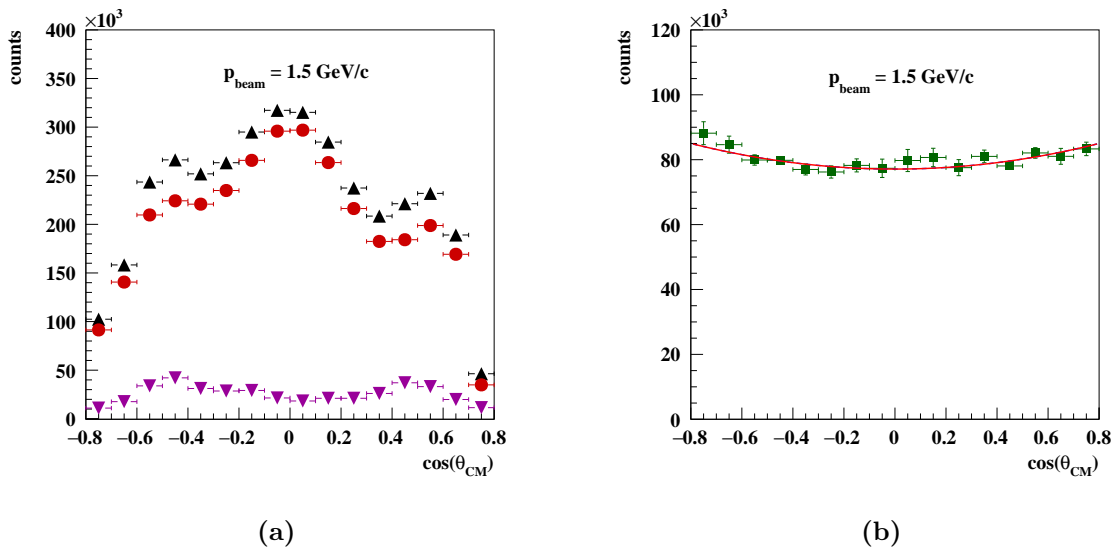


Figure 6.30: (a) Histograms of the selected data (D) (**black triangles up**) containing the selected signal counts (S2) mixed with the expected pion contamination (B1), the statistically independent angular distribution of the pion contamination (B2) (**red dots**) (which will be reconstructed in a separate analysis in the experiment later) used for the background subtraction. Also shown is the obtained angular distribution after background subtraction (**magenta triangles down**) (D-B2). (b) Reconstructed and efficiency corrected signal angular distribution (**green squares**). The fit function $f_1(x)$ (red line) is used to extract $|G_E|$ and $|G_M|$ simultaneously.

Details on the efficiency correction and the used fit functions will be given in the next chapter. In the following, the feasibility for the sufficient suppression of the contribution from other relevant background processes in this work will be shown.

6.5 Suppression of other background channels

Final states including muons from pion decay of $\bar{p}p \rightarrow \pi^+\pi^-$

In the following, the rejection factors for such events are estimated, which undergo a decay of one respectively both final state pions in the $\bar{p}p \rightarrow \pi^+\pi^-$ process. After μ -selection, only such events will survive, which fulfill the cut criteria listed in Tab. 6.6. Especially if the pion decay occurs almost directly after the interaction point, the decay muon has a production angle which is very similar to the original pion vertex production angle. Therefore such events are very likely to be accepted by the μ -selection, since they fulfill the cut criteria.

The development of an analysis for the reconstruction of the final states from $\bar{p}p \rightarrow \pi^+\pi^-$ is an outstanding task and will be performed in the future. The measurement of all final states from this process, including muons from pion decay, is expected to be feasible with high reconstruction efficiency, and at the same time profiting from the very high cross section of the main background reaction. Therefore it is expected that the residual pion contamination can be removed from the data successfully by a background subtraction.

In this study, the achievable rejection factors are estimated at a Confidence Level (CL) of 95% for beam momenta from 1.5 GeV/ c up to 3.3 GeV/ c . For the determination of the rejection factors, the Monte Carlo Particle Number ("PdgCode") was used to select the events of the type ($\mu^+\mu^-$, $\pi^-\mu^+$, $\mu^-\pi^+$) from the residual events in the pion background sample after μ -selection. This number is used to calculate the expectation value of the corresponding Poissonian probability distribution at CL = 95%. From that, the rejection factor can be calculated, using the number of generated events given in Tab. 6.9:

$$\epsilon_{B,c} = \frac{\mu(N_c^{selected} | CL = 95\%)}{N_c^{gen}} \quad (6.15)$$

where μ stands for the expectation value of the Poissonian probability distribution obtained at CL = 95% for the individual channel ($c = \mu^+\mu^-$, $\pi^-\mu^+$, $\mu^-\pi^+$). The number of residual background events after μ -selection is represented by $N^{selected}$. The obtained rejection factors are summarized in Tab. 6.9.

Table 6.9: Reconstruction efficiency for the $\mu^+\mu^-$ final states of the $\bar{p}p \rightarrow \mu^+\mu^-$ signal process and rejection factors for the final states $\mu^+\mu^-$, $\pi^-\mu^+$ and $\mu^-\pi^+$ from pion decay of the $\bar{p}p \rightarrow \pi^+\pi^-$ background process at CL = 95%.

p_{beam} [GeV/ c]	Signal efficiency $\mu^-\mu^+$	Background rejection factor		
		$\mu^-\mu^+$	$\pi^-\mu^+$	$\mu^-\pi^+$
1.5	0.315	$8.9 \cdot 10^{-5}$	$3.1 \cdot 10^{-5}$	$3.0 \cdot 10^{-5}$
1.7	0.274	$4.3 \cdot 10^{-5}$	$2.5 \cdot 10^{-5}$	$4.0 \cdot 10^{-5}$
2.5	0.334	$1.8 \cdot 10^{-4}$	$4.3 \cdot 10^{-5}$	$4.2 \cdot 10^{-5}$
3.3	0.295	$2.0 \cdot 10^{-4}$	$2.8 \cdot 10^{-5}$	$3.1 \cdot 10^{-5}$

Final states containing only one decay muon (μ^+ or μ^-) can be rejected with a factor of approximately 10^{-5} , which corresponds to an expectation of the order of 10^5 events in the real experiment, after application of all chosen cut criteria. Such events will be present in the pion contamination.

In this feasibility study, the pion contamination includes the full amount of expected background events polluting the selected signal events, which includes events from $\pi^-\mu^+$, $\mu^-\pi^+$ and $\mu^-\mu^+$.

Background channel of $\bar{p}p \rightarrow K^+K^-$ and $\bar{p}p \rightarrow K^+K^-\pi^0$

Besides the most challenging background channel of $\bar{p}p \rightarrow \pi^+\pi^-$, kaons from $\bar{p}p \rightarrow K^+K^-$ constitute a strong background source, whose cross section is of the same magnitude as the $\bar{p}p \rightarrow \pi^+\pi^-$ background channel. Therefore it is necessary, to investigate if a sufficient suppression for this channel is possible. The corresponding rejection factor for this channel was estimated in this work in a separate simulation study.

The differential cross section of the $\bar{p}p \rightarrow K^+K^-$ reaction was measured in 1975 by Eisenhandler et al. [134]. Figure 6.31 shows the differential cross section in the $\bar{p}p$ -center-of-mass system for the negative kaon from the $\bar{p}p \rightarrow K^+K^-$ process depending on $\cos(\theta_{CM})$.

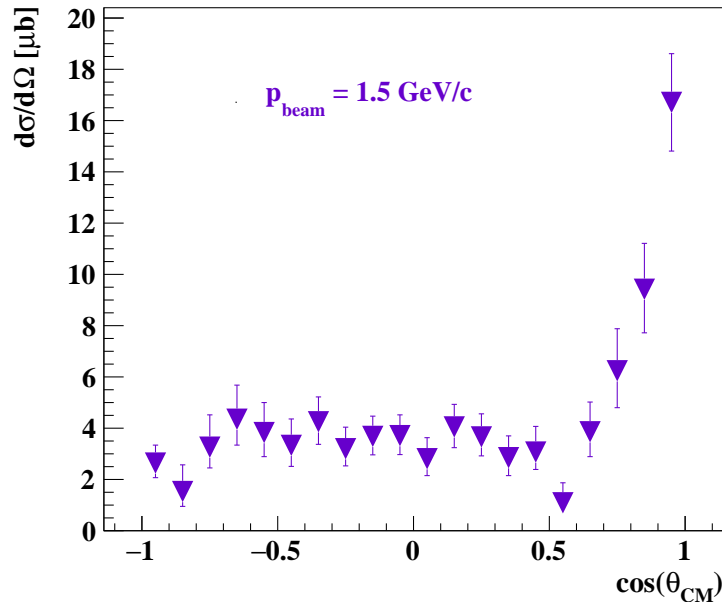


Figure 6.31: Differential cross section for the $\bar{p}p \rightarrow K^+K^-$ process depending on the $\bar{p}p$ -center-of-mass production angle of the K^- from Ref. [134].

For studying the $\bar{p}p \rightarrow K^+K^-$ channel and the estimation of the corresponding rejection factor, the EvtGen generator [142] is used with a phase space PHSP model. This estimation is

done at the lowest value of beam momentum of 1.5 GeV/c, where the highest precision of the FF's was achieved, as well at the highest considered value of beam momentum of 3.3 GeV/c.

At 1.5 GeV/c, the integration of the differential cross section over this angular range leads to a total cross section of 53.38 μb . Assuming a time-integrated luminosity of 2 fb^{-1} (corresponding to the conditions at $\bar{\text{P}}\text{ANDA}$ Phase-3), this corresponds to $1.07 \cdot 10^{11}$ expected kaon events at this value of beam momentum. The total cross section of the $\bar{p}p \rightarrow K^+K^-$ channel decreases with increasing value of beam momentum (see Chapter 2, Sec. 2.1.2).

In total, more than $1.05 \cdot 10^8$ events are generated in the considered $\bar{p}p$ -center-of-mass angular range of $|\cos(\theta_{CM})| < 0.8$. Since the rest masses of the charged kaons are higher by a factor of $m(K^\pm)/m(\mu) \approx 4.7$ in comparison to the muon rest mass, the misidentification probability for kaons is expected to be much smaller than the one for pions. Hence, kinematical cuts are much more powerful for the suppression of this process. Figure 6.32 shows the distributions of the sum of the polar angles of both particle candidates in center-of-mass frame $(\theta^+ + \theta^-)_{CM}$ (left plot) and the invariant mass for the reconstructed and preselected muon pairs (blue) respectively charged kaon pairs (red).

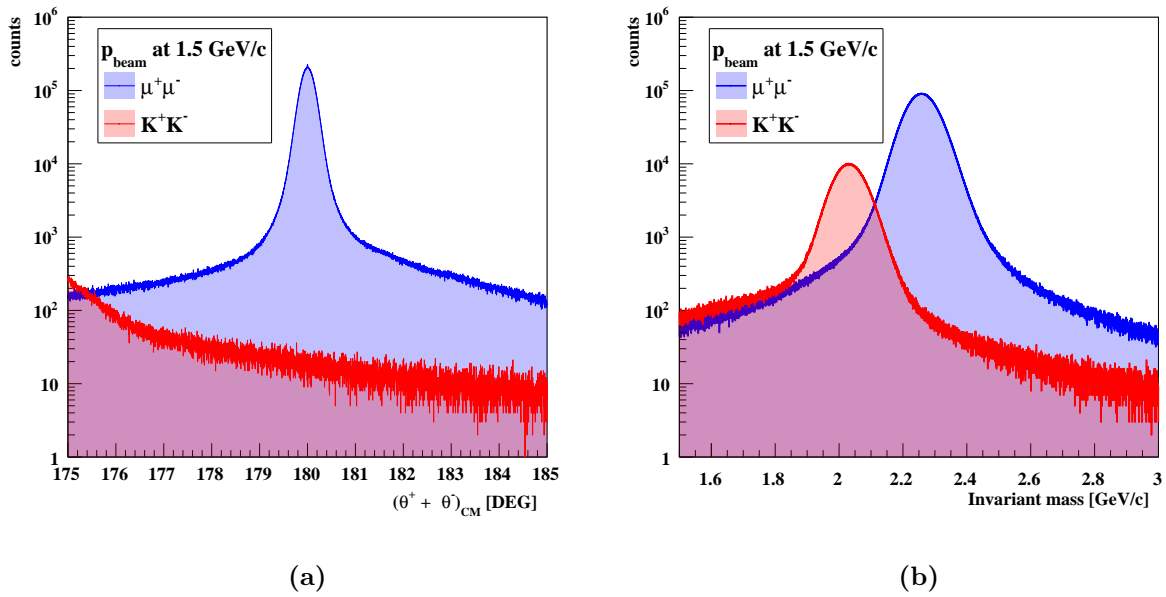


Figure 6.32: (a): Distribution of the reconstructed kinematical variable $(\theta^+ + \theta^-)_{CM}$ after preselection for the muon pairs (blue) and the kaon pairs (red) at $p_{beam} = 1.5$ GeV/c. Due to the assumption of muon mass hypothesis, the peak of the kaon distribution is shifted strongly to smaller angles. Since the particles are produced back-to-back in the $\bar{p}p$ -center-of-mass frame, this variable is peaked around 180° [DEG] for the muon pairs. (b): Distribution of the reconstructed invariant mass M_{inv} of the final state after preselection for the muon pairs (blue) and the kaon pairs (red).

As it was expected, the invariant mass of the charged kaon pairs is shifted strongly to smaller

values of $(\theta^+ + \theta^-)_{CM}$ due to the muon mass hypothesis used for the calculation of the particle energy for the particles' four-momentum. After event classification with the trained Boosted Decision Trees, the reconstructed and preselected K^+K^- events undergo the μ -selection. The final cut configuration is applied on the classified events at the considered values of beam momentum. For the rejection of the K^+K^- events, a suppression factor better than 10^{-8} is achieved with $CL = 95\%$ for loose cuts. This corresponds to a signal pollution $< 1\%$ at a total signal efficiency of 31.5% and therefore the contamination from this channel can be neglected. Also at $p_{beam} = 3.3 \text{ GeV}/c$, a signal pollution $< 1\%$ could be achieved with loose cuts at a total signal efficiency of 29.5%.

The total cross section for the $\bar{p}p \rightarrow K^+K^-\pi^0$ process is one order of magnitude less than the cross section for final states of K^+K^- . At the same time, the probability of misidentification of a kaon as a muon is lower than the probability for misidentification of a pion as a muon. The reason for that is, that the charged kaon has a higher mass and therefore the kinematical constraints are more powerful. Comparing to the channel with K^+K^- final states, the invariant mass of the K^+K^- system is expected to be shifted drastically to smaller values and broadened by the additional π^0 . Therefore a rejection factor better than 10^{-8} is expected (what is achieved for final states of K^+K^-). Hence, the contamination from this channel can be also neglected.

Background channel of $\bar{p}p \rightarrow \pi^+\pi^-\pi^0$

In the considered range of beam momentum in this work, the total cross section values of $\bar{p}p \rightarrow \pi^+\pi^-\pi^0$ are seven orders of magnitude larger than for the signal process. This corresponds to an order of $\sim 10^{12}$ expected background events from the $\bar{p}p \rightarrow \pi^+\pi^-\pi^0$ reaction, assuming a time-integrated luminosity of $\mathcal{L} = 2\text{fb}^{-1}$ (at $\bar{\text{P}}\text{ANDA}$ Phase-3). In order to reach a signal pollution $< 1\%$ from this channel, a rejection factor of the order of 10^{-9} must be achieved.

For the estimation of the rejection factor for this background channel, a sample containing $1.045 \cdot 10^8$ ($1.034 \cdot 10^8$) events were generated at $p_{beam} = 1.5 \text{ GeV}/c$ ($3.3 \text{ GeV}/c$) in the range of $|\cos(\theta_{CM})| < 0.8$. The EvtGen generator is used, which is based on a phase space PHSP model, generating a flat angular distribution depending on $\cos(\theta_{CM})$ in the $\bar{p}p$ center-of-mass system. In case of the lowest value of beam momentum, an even looser cut on the BDT response can be chosen for the cut criteria ($\text{BDT} > 0.277$) than the finally chosen cut criteria for the μ -selection (see Tab. 6.6). Together with the kinematical cuts, already such selection criteria allow to estimate the upper limit of the rejection factor to be better than 10^{-8} . By comparing this cut criteria ($\text{BDT} > 0.277$) with tight cuts from Tab 6.6, one gains an additional rejection factor of the order of 10^{-1} . Therefore, a rejection factor of the order of 10^{-9} is estimated at tight cuts. Also at the highest considered value of beam momentum of $p_{beam} = 3.3 \text{ GeV}/c$, these studies show, that a rejection factor of the order of 10^{-9} will be achieved at $\bar{\text{P}}\text{ANDA}$.

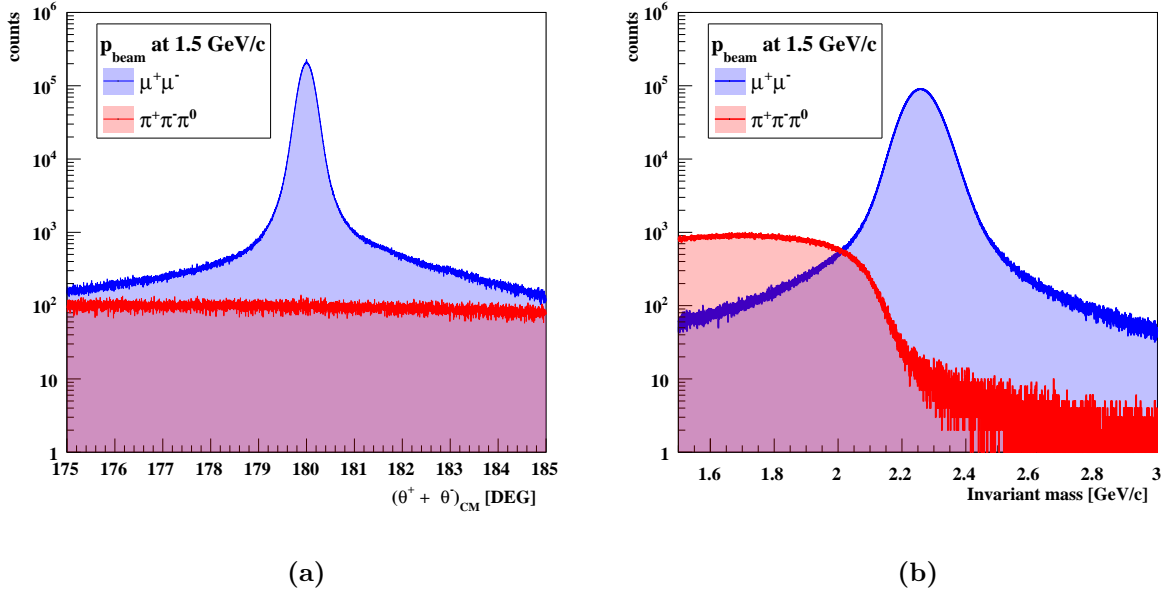


Figure 6.33: (a): Distribution of the reconstructed kinematic variable $(\theta^+ + \theta^-)_{CM}$ after preselection for the muon pairs (blue) and for the final states from $\pi^+\pi^-\pi^0$ (red) at $p_{beam}=1.5$ GeV/c. Due to the three particles in the final states of $\pi^+\pi^-\pi^0$ and the muon mass hypothesis used for the reconstruction of the four momenta, the distributions for signal and background are very different. (b): Distribution of the reconstructed invariant mass M_{inv} of the final state after preselection for the muon pairs (blue) and the charged particle pairs from $\pi^+\pi^-\pi^0$ (red).

Background channel of $\bar{p}p \rightarrow \pi^0\pi^0$

For final states consisting of two neutral pions, the cross section is five orders of magnitude larger than for the signal process. Assuming $\mathcal{L} = 2 \text{ fb}^{-1}$ ($\bar{\text{P}}\text{ANDA}$ Phase-3), a rejection factor of the order of 10^{-7} must be reached to limit the signal pollution to be $< 1\%$. A Monte-Carlo simulation was performed for this background channel at the lowest value of beam momentum, which is based on the EvtGen generator in combination with a phase space PHSP model. In the range of $|\cos(\theta_{CM})| < 0.8$, more than 10^7 events were generated. Already applying very loose cuts allows to estimate the upper limit of the rejection factor to be better than 10^{-7} and therefore one can conclude, that also this background channel is not crucial. Since the total cross section of this channel decreases with increasing beam momentum, a sufficient suppression of final states from this channel is expected at higher values of beam momentum.

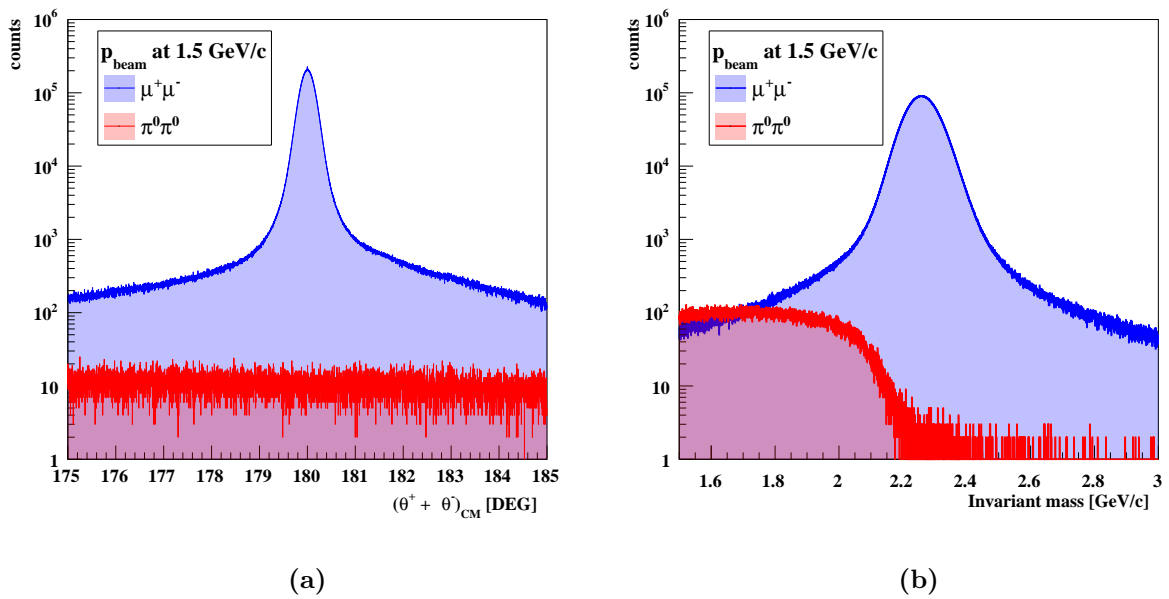


Figure 6.34: (a): Distribution of the reconstructed kinematic variable $(\theta^+ + \theta^-)_{CM}$ after preselection for the muon pairs (blue) and for the final states from $\pi^0\pi^0$ (red) at $p_{beam} = 1.5 \text{ GeV}/c$. Due to the neutral, short-living particles in the final states of $\pi^0\pi^0$ and the muon mass hypothesis used for the reconstruction of the four momenta, the distributions for signal and background are very different to each other. (b): Distribution of the reconstructed invariant mass M_{inv} of the final state after preselection for the muon pairs (blue) and the charged particle pairs from $\pi^0\pi^0$ (red).

Chapter 7

Results of the feasibility studies for $\overline{\text{PANDA}}$ Phase-3

The following chapter describes the extraction of the time-like electromagnetic proton FF's, $|G_E|$ and $|G_M|$, and their ratio $R = |G_E|/|G_M|$ from the reconstruction efficiency corrected angular distribution of the reconstructed and selected pseudo-data. A background subtraction is always included in these studies using the constructed pion contamination distributions, as it was discussed in the previous section. Two different fit functions are used for the extraction of the different physical quantities and their errors. Both of them are based on the differential cross section formula for the signal reaction. At this level of the simulation, systematic uncertainties can already be estimated and included into the calculation of the total uncertainties. Other quantities, which are determined from the selected and efficiency corrected pseudo-data, are the effective FF of the proton and the total signal cross section of $\bar{p}p \rightarrow \mu^+\mu^-$ and their (statistical and total) uncertainties.

7.1 Extraction of $|G_E|$, $|G_M|$ and $R = |G_E|/|G_M|$

7.1.1 Signal reconstruction efficiency correction

After background subtraction, the signal reconstruction efficiency correction is applied to the angular distribution of the selected pseudo-data:

$$N_i^{corr} = \frac{N_{i,fluc}^{reco}}{\epsilon_i} \quad (7.1)$$

where for the i -th histogram bin, N_i^{corr} is the efficiency corrected number of signal counts, $N_{i,fluc}^{reco}$ is the number of reconstructed, selected signal counts after background subtraction and ϵ_i is the signal reconstruction efficiency. The corresponding error is calculated from

$$\Delta N_i^{corr} = \sqrt{\left(\frac{\Delta N_{i,fluc}^{reco}}{\epsilon_i}\right)^2 + \left(\frac{\Delta \epsilon_i \cdot N_{i,fluc}^{reco}}{\epsilon_i^2}\right)^2} \quad (7.2)$$

For the determination of the different quantities, a fit function is used which is based on the differential cross section, given in Eq. 3.23. In this analysis, the fit function is adjusted to

directly extract the requested quantities (R respectively $|G_E|$ and $|G_M|$) together with their statistical uncertainties. The fit is performed by computing the integral of the function in the bin, divided by the bin volume, instead of using the fit function value at the bin center. It is also possible to calculate R from the extracted form factors, what is will be shown in section E. The directly extracted and the calculated values of $R \pm \Delta R$ are the same. The first form of the fit function, denoted as fit function $f_1(x)$, has two fit parameters $P_{0,1}$:

$$f_1(x) = C_1 \cdot W_i \cdot \left[\frac{4M_p^2}{q^2} (1 - \beta_l^2 x^2) P_1 + \left(1 + \frac{4m_\mu^2}{q^2} + \beta_l^2 x^2 \right) P_0 \right], \quad (7.3)$$

The values of $|G_E|$ and $|G_M|$ can be obtained from the fit parameters $P_1 = \mathcal{L} \cdot |G_E|^2$ and $P_0 = \mathcal{L} \cdot |G_M|^2$. Here, \mathcal{L} stands for the time-integrated luminosity, for which $2 fb^{-1}$ is assumed. A direct extraction of the ratio R and its uncertainty can be done with the adjusted fit function, denoted as $f_2(x)$:

$$f_2(x) = C_1 \cdot W_i \cdot L \cdot P_3^2 \cdot \left[\frac{4M_p^2}{q^2} (1 - \beta_l^2 x^2) P_4^2 + \left(1 + \frac{4m_\mu^2}{q^2} + \beta_l^2 x^2 \right) \right] \quad (7.4)$$

with the fit parameters $P_3 = |G_M|$ and $P_4 = R = \frac{|G_E|}{|G_M|}$. C_1 is a constant, which depends on the squared four momentum transfer, q^2 , and contains the rest masses of proton and muon:

$$C_1 = \frac{(\hbar c)^2 \alpha^2 \pi}{2q^2} \sqrt{\frac{q^2 - 4m_\mu^2}{q^2 - 4M_p^2}} \quad (7.5)$$

Here, W_i is the bin width of the i -th histogram bin of the $\cos(\theta_{CM})$ angular distribution.

7.1.2 Efficiency corrected angular distributions

Figure 7.1 shows the resulting signal angular distributions after correction with the signal reconstruction efficiency. The results of the extracted ratio R are summarized in Tab. 7.1. The extracted values of the FF's, $|G_E|$ and $|G_M|$, and their statistical uncertainties can be found in Tab. 7.2.

7.1.3 Choice of cuts

The angular distributions, which are shown in Fig. 7.1, are obtained with the final cut configurations after the full analysis study. The final cut configuration are chosen in order to keep a high value of total signal efficiency (respectively reconstructed signal statistics after μ -selection) in each histogram bin, since the signal efficiency dominates the error of the entries in each histogram bin and therefore influences the statistical uncertainty of the extracted FF's. At the same time, a sufficient suppression of the events from all relevant background channels must be possible, except the contribution of the main background channel $\bar{p}p \rightarrow \pi^+\pi^-$, where the background subtraction will be used to remove the residual amount of background events. It will be seen, that for the final cut configuration the uncertainty of the FF's does not change strongly when a slight variation of the cut on the BDT response is done (what is the case for two neighbor cut configurations given in Tab. 6.6, as e.g. "very loose cuts" and "loose cuts"). In order

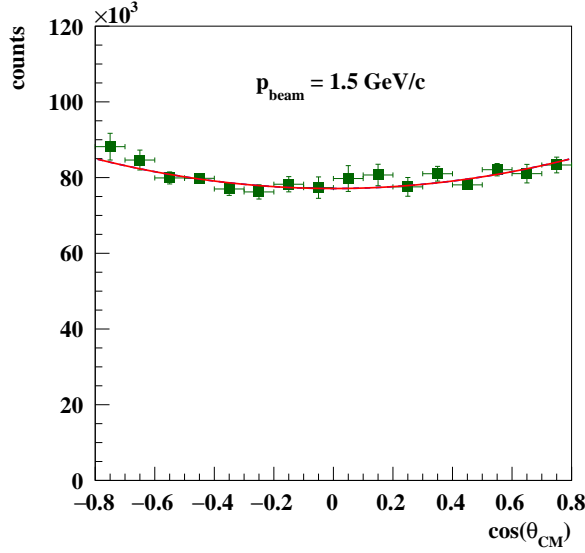
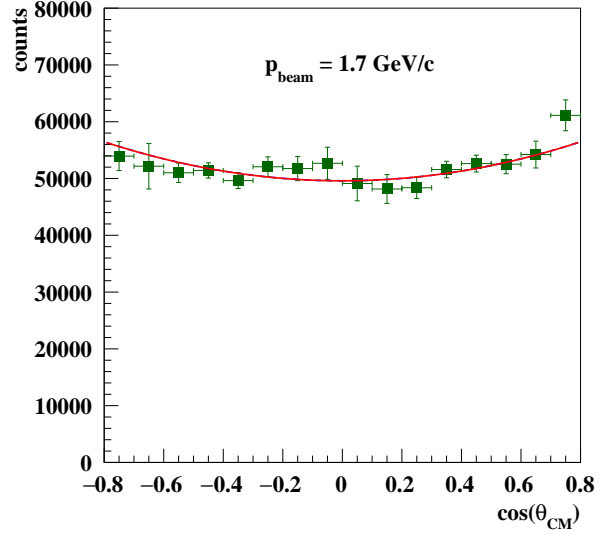
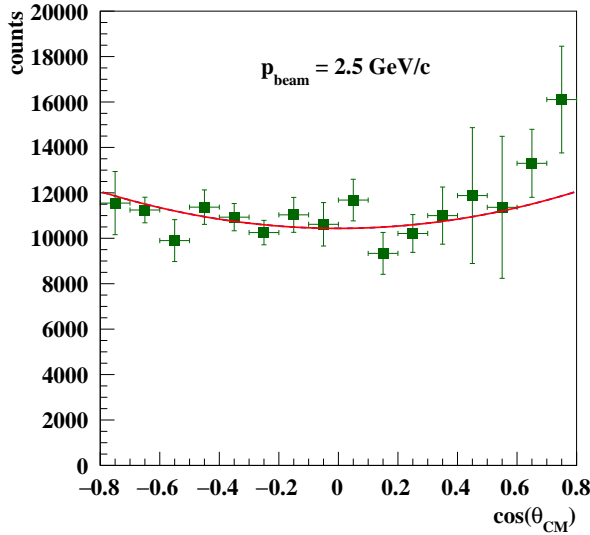
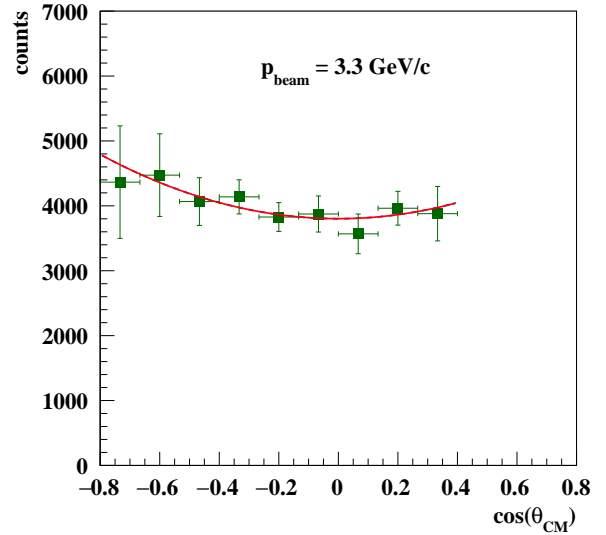
(a) $p_{beam}=1.5$ GeV/c, "loose cuts"(b) $p_{beam}=1.7$ GeV/c, "medium cuts"(c) $p_{beam}=2.5$ GeV/c, "tight cuts"(d) $p_{beam}=3.3$ GeV/c, "loose cuts"

Figure 7.1: Reconstructed and efficiency corrected signal angular distribution (green squares) after full analysis including background subtraction at the considered values of beam momenta. The fit function $f_2(x)$ (red line) is used to extract the ratio R and its uncertainty directly.

Table 7.1: The result $R \pm \Delta R$ corresponds to the fit function $f_2(x)$, where R is one of the free fit parameters and thus can be extracted directly. The studies are based on the assumption of $R = 1$. The obtained results at the final cut configurations are highlighted in bold and italic font.

	$p_{beam} = 1.5 \text{ GeV}/c$				$p_{beam} = 1.7 \text{ GeV}/c$			
	R	ΔR	$\frac{\Delta R}{R}[\%]$	χ^2/ndf	R	ΔR	$\frac{\Delta R}{R}[\%]$	χ^2/ndf
Very loose cuts	0.99	0.05	5	1.01	1.00	0.07	7	0.57
Loose cuts	<i>1.02</i>	<i>0.05</i>	<i>5</i>	<i>0.85</i>	0.96	0.07	7	0.95
Medium cuts	1.02	0.05	5	0.91	<i>0.99</i>	<i>0.07</i>	<i>7</i>	<i>1.12</i>
	$p_{beam} = 2.5 \text{ GeV}/c$				$p_{beam} = 3.3 \text{ GeV}/c$			
	R	ΔR	$\frac{\Delta R}{R}[\%]$	χ^2/ndf	R	ΔR	$\frac{\Delta R}{R}[\%]$	χ^2/ndf
Loose cuts	1.03	0.13	12	1.04	<i>0.99</i>	<i>0.36</i>	<i>37</i>	<i>0.86</i>
Medium cuts	1.08	0.16	16	1.09	0.90	0.39	44	1.12
Tight cuts	<i>1.08</i>	<i>0.16</i>	<i>14</i>	<i>1.13</i>	0.89	0.39	44	0.79

to take into account the systematic uncertainty connected to the choice of cuts, a comparison of the results from such neighbor cut configurations will be done at each value of beam momentum and a systematic uncertainty will be added later to the total uncertainty of the FF's.

7.1.4 Direct extraction of $R \pm \Delta R$

The values of $R \pm \Delta R$ which were extracted with the fit function $f_2(x)$ are summarized in Tab. 7.1. The obtained results are very well compatible with each other (within one sigma) and consistent with the assumption of $R = 1$. The "very tight" cut configuration is not considered, since the total statistics of the background distribution after μ -selection is too low and therefore a shape can not be extracted properly.

The statistical uncertainty at lower values of beam momentum is mostly caused by the statistical fluctuations of the background, which remain in the reconstructed signal data after the subtraction of the pion contamination. When going to higher values of beam momentum, the statistical uncertainty increases strongly due to the decreasing signal statistics.

7.1.5 Simultaneous extraction of $|G_E|$ and $|G_M|$

Tab. 7.2 shows the extracted values of $|G_E|$ and $|G_M|$ with their uncertainties at each considered value of beam momentum ($p_{beam} = 1.5, 1.7, 2.5$ and $3.3 \text{ GeV}/c$). The results are consistent with each other within one sigma. The final cut configurations are highlighted in bold italic font.

The fit results at i) each value of beam momentum and ii) considered cut configuration, are compatible with the assumption of $|G_M|$ (model) within one sigma. The lower precision on $|G_E|$ can be explained by its pre-factor of $4M_p^2/q^2$ in the differential cross section formula which

Table 7.2: The fit function $f_1(x)$ is used for the simultaneous extraction of $|G_E|$ and $|G_M|$ at each considered value of beam momentum ($p_{beam} = 1.5, 1.7, 2.5$ and 3.3 GeV/ c). The chosen cut configurations are highlighted in bold and italic font. The calculated values of the magnetic FF, $|G_M|$ (model), which is based on the FF model for the parameterization of $|G_M|$ from Ref. [54] are shown for comparison.

<i>$p_{beam} = 1.5$ GeV/c</i>						
$ G_M $ (model) = 0.1403	$ G_E $	$\Delta G_E $	$\frac{\Delta G_E }{ G_E }$ [%]	$ G_M $	$\Delta G_M $	$\frac{\Delta G_M }{ G_M }$ [%]
Very loose cuts	0.139	0.005	3.3	0.140	0.002	1.5
Loose cuts	<i>0.142</i>	<i>0.004</i>	<i>3.1</i>	<i>0.139</i>	<i>0.002</i>	<i>1.5</i>
Medium cuts	0.142	0.005	3.4	0.139	0.002	1.6
<i>$p_{beam} = 1.7$ GeV/c</i>						
$ G_M $ (model) = 0.1213	$ G_E $	$\Delta G_E $	$\frac{\Delta G_E }{ G_E }$ [%]	$ G_M $	$\Delta G_M $	$\frac{\Delta G_M }{ G_M }$ [%]
Very loose cuts	0.120	0.006	4.9	0.121	0.003	2.2
Loose cuts	0.118	0.006	5.1	0.1222	0.003	2.1
Medium cuts	<i>0.121</i>	<i>0.006</i>	<i>5.1</i>	<i>0.122</i>	<i>0.003</i>	<i>2.2</i>
<i>$p_{beam} = 2.5$ GeV/c</i>						
$ G_M $ (model) = 0.0703	$ G_E $	$\Delta G_E $	$\frac{\Delta G_E }{ G_E }$ [%]	$ G_M $	$\Delta G_M $	$\frac{\Delta G_M }{ G_M }$ [%]
Loose cuts	0.072	0.006	8.9	0.070	0.002	4.5
Medium cuts	0.075	0.008	10.3	0.075	0.008	3.5
Tight cuts	<i>0.074</i>	<i>0.008</i>	<i>10.2</i>	<i>0.068</i>	<i>0.003</i>	<i>4.4</i>
<i>$p_{beam} = 3.3$ GeV/c</i>						
$ G_M $ (model) = 0.0436	$ G_E $	$\Delta G_E $	$\frac{\Delta G_E }{ G_E }$ [%]	$ G_M $	$\Delta G_M $	$\frac{\Delta G_M }{ G_M }$ [%]
Loose cuts	<i>0.043</i>	<i>0.012</i>	<i>26.9</i>	<i>0.044</i>	<i>0.004</i>	<i>9.6</i>
Medium cuts	0.040	0.014	33.5	0.045	0.005	10.1
Tight cuts	0.042	0.013	30.5	0.044	0.005	10.2

suppresses the corresponding term and leads to a bigger uncertainty. Therefore at higher values of q^2 the cross section is dominated by $|G_M|$.

7.2 Integrated signal cross section and effective form factor of the proton

The integrated cross section of the $\bar{p}p \rightarrow \mu^+\mu^-$ signal process is calculated in this feasibility study at each value of q^2 with

$$\sigma_{int} = N^{corr} / \mathcal{L}, \quad (7.6)$$

where N^{corr} stands for the total signal counts after background subtraction and after efficiency correction with the assumption for the time-integrated luminosity of $\mathcal{L} = 2 \text{ fb}^{-1}$ (PANDA Phase-3). Figure 7.2 shows the obtained values of the integrated cross section at each considered value of beam momentum together with the theoretical curve based on Eq. 3.26 and on the proton FF's parametrization from Ref. [54]. The statistical uncertainties of the obtained results are very small and hidden inside the markers of the data points (orange dots). The corresponding

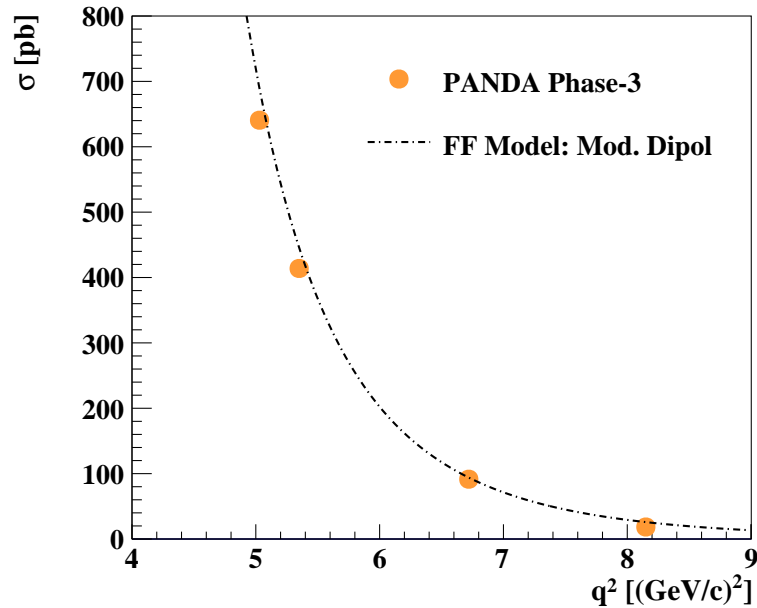


Figure 7.2: Integrated cross section σ (orange dots) for the $\bar{p}p \rightarrow \mu^+\mu^-$ process, depending on q^2 in the range of $\cos(\theta_{CM}) < 0.8$. σ is determined from the reconstructed signal counts after background subtraction, application of the signal reconstruction efficiency and divided by the time-integrated luminosity $\mathcal{L} = 2 \text{ fb}^{-1}$. Also shown is the theoretical curve based on Eq. 3.26.

values of the effective time-like proton FF and their uncertainties are shown in Tab. 7.4.

From the obtained values one can conclude that the integrated cross section of the signal

Table 7.3: Extracted statistical precision of the integrated cross section of the $\bar{p}p \rightarrow \mu^+\mu^-$ signal process together with the calculated value based on Eq. 3.26, Chapter 3, for the considered angular range of $-0.8 < \cos(\theta_{CM}) < 0.8$.

p_{beam} [GeV/c]	q^2 [(GeV/c) ²]	σ (calculation) [pb]	$\sigma \pm \Delta\sigma$ (extracted) (stat.) [pb]	$\Delta\sigma/\sigma$ (extracted) (stat.) [%]
1.5	5.08	640.721	640.637 ± 4.165	0.65
1.7	5.40	414.881	413.865 ± 5.871	1.42
2.5	6.77	89.185	91.484 ± 1.918	2.09
3.3	8.20	24.829	24.911 ± 0.693	2.78

process will be determined with high accuracy at $\overline{\text{PANDA}}$. Especially for the beginning phase of data taking, denoted as $\overline{\text{PANDA}}$ Phase-1, this quantity and the effective proton FF are expected to be measured with good accuracy despite of the reduced luminosity available in this phase. A separate study for this changed experimental conditions were performed and will be presented in Sec. 8.2.

Under the assumption of $R = 1$, the effective FF of the proton can be determined from the integrated cross section in the interval of $|\cos(\theta_{CM})| < \bar{a}$ with $\bar{a} = 0.8$ using

$$|F_p| = \sqrt{\frac{\sigma_{int}(q^2)}{\frac{\pi\alpha^2}{2q^2} \frac{\beta_\ell}{\beta_p} \left[(2 - \beta_\ell^2) + \frac{1}{\tau} \right] \left[2\bar{a} + \frac{2}{3}A_0 \bar{a}^3 \right]}} \quad (7.7)$$

with

$$A_0 = \beta_\ell^2 \frac{1 - \frac{1}{\tau}}{2 - \beta_\ell^2 + \frac{1}{\tau}}$$

and $\tau = q^2/4M_p^2$, $\beta_{\ell,p} = \sqrt{1 - 4M_{\ell,p}^2/q^2}$. Figure 7.3 shows the obtained results together with their corresponding statistical uncertainties. Due to the smallness of the obtained errors, they are not visible. The corresponding values of the effective time-like proton FF and their uncertainties are listed in Tab. 7.4. The extracted relative statistical uncertainty of the effective

Table 7.4: Extracted values and statistical precision of the effective proton FF, $|F_p|$.

p_{beam}	q^2	$ F_p $ (model)	$ F_p \pm \Delta F_p $ (extracted)	$\Delta F_p / F_p $ (extracted)
[GeV/c]	[(GeV/c) ²]		(stat.)	(stat.)
				[%]
1.5	5.08	0.1403	0.1402 ± 0.0005	0.33
1.7	5.40	0.1213	0.1210 ± 0.0009	0.71
2.5	6.77	0.0703	0.0712 ± 0.0007	1.05
3.3	8.20	0.0436	0.0437 ± 0.0006	1.39

FF ranges between 0.33% and 1.39% for beam momenta between 1.5 and 3.3 GeV/c. As a systematic uncertainty, the contribution from the luminosity measurement can be calculated to $\Delta|F_p|/|F_p|$ (syst.) = $\pm 2\%$, assuming a relative uncertainty of the luminosity of 4 % at all values of q^2 .

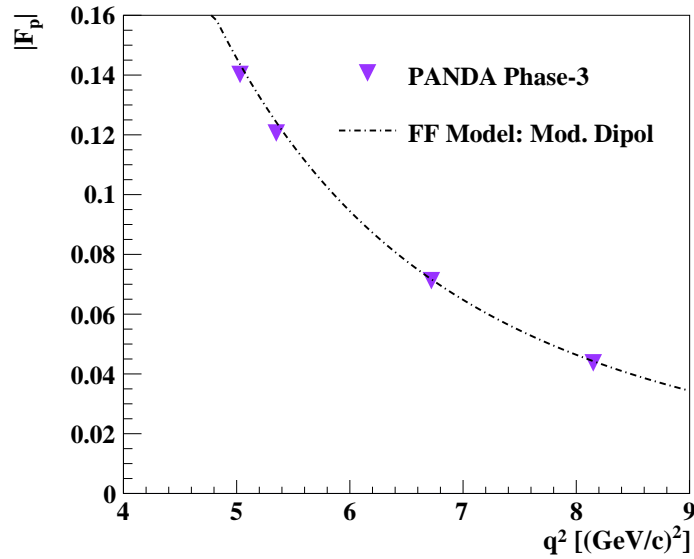


Figure 7.3: Extracted values of the effective time-like proton FF for the $\bar{p}p \rightarrow \mu^+\mu^-$ process at different values of q^2 . The error bars are not visible due to their smallness. Also shown is the FF model from Ref. [54], which is used for the calculation of the expected signal statistics, given in Tab. 5.1.

7.3 Systematic uncertainties

A complete estimation of the systematic uncertainties can only be performed with input data from both the experiment and the MC simulation. Since only MC simulated pseudo-data are currently available, a precise estimation of the systematic uncertainties will only be possible in the future, when FAIR and the $\overline{\text{PANDA}}$ detector exist. However, several sources of systematic uncertainties can already be considered based on the MC study and will be discussed in the following.

Luminosity measurement

$\overline{\text{PANDA}}$ will determine the luminosity \mathcal{L} in processes of elastic $\bar{p}p$ scattering since it is a well-known reference process. \mathcal{L} will be measured with a relative systematic uncertainty from 2.0% up to 5.0%, which depends on the beam momentum, the knowledge of the differential cross section parameters and the $\bar{p}p$ inelastic background contamination [151]. In this estimation, a relative uncertainty of $\Delta\mathcal{L}/\mathcal{L} = 4.0\%$ is assumed at all considered beam momenta. This corresponds to a relative uncertainty of the FF's of 2.0% originating from the luminosity measurement, what can be easily calculated.

Choice of cut configuration

Since the extracted values of the precision on the FF's vary only slightly when the results from two neighbor cut configurations are compared, the contribution from the choice of cuts to the total systematic uncertainty of the FF's is small. For this calculation, the value of R and the

proton FF's obtained with the final cut configuration is compared to the corresponding value, which is obtained with a neighbor cut configuration (which are very loose cuts in the case of 1.5 GeV/c, loose cuts at 1.7 GeV/c, medium cuts at 2.5 GeV/c and medium cuts at 3.3 GeV/c).

Choice of histogram binning

The histogram binning has an influence on the values of the extracted quantities and their uncertainties. For the purpose of comparability to the feasibility studies for the $\bar{p}p \rightarrow e^+e^-$ channel from Ref. [16], the same number of histogram bins (16 bins) was chosen at beam momenta of $p_{beam} = 1.5, 1.7$ and 2.5 GeV/c. At $p_{beam} = 3.3$ GeV/c, wider bins are chosen (12 bins) in comparison to the other beam momenta since the data points show large statistical fluctuations. Therefore, the difference between the results obtained with 12 bins and 16 bins is calculated at 3.3 GeV/c is used for the determination of the systematic error.

Odd contributions to $\cos(\theta_{CM})$

In this work, no radiative corrections are included, since the corresponding calculations for the muon channel do not exist yet. An even angular distribution in $\cos(\theta_{CM})$ is assumed in this work in one-photon exchange approximation.

In Ref. [16] two-photon exchange for the electron channel is discussed (for more details about QED radiative corrections to the first order in α for $\bar{p}p \rightarrow \ell^+\ell^-$ see section 7.8), which introduces odd contributions to the angular distribution [51, 152]. The contribution of the interference term between one- and two-photon-exchange is symmetric under interchange of electron and positron and can be removed from the angular distribution by adding both angular distributions [153]. Furthermore, the contribution of the two-photon exchange to the cross section for the electron channel is expected to be negligible, being less than 1% [154].

7.4 Conclusion

An overview of the statistical and systematic contributions to the relative total uncertainty of the FF's and the ratio R is given in Table 7.5. The considered systematic uncertainties are the choice of histogram binning, the choice of cuts and the luminosity measurement. The total uncertainty is listed for all considered values of beam momentum. The results show, that the total relative uncertainty, $\Delta R/R$, ranges between 5% and 37% for the considered values of q^2 between 5.08 and 8.20 (GeV/c)². The estimated values of the total relative uncertainty $\frac{\Delta|G_M|}{|G_M|}$ lie between 2.5% and 9.9%, as well as for $\frac{\Delta|G_E|}{|G_E|}$ between 3.7% and 27.0%. Figure 7.4 shows the final results of $R \pm \Delta R$ in this work, including all considered statistical and systematic uncertainties. The results show, that $|G_E|$ and $|G_M|$ respectively their ratio R , are expected to be measured with high precision at \bar{P} ANDA during \bar{P} ANDA Phase-3. When going to lower beam momenta, the statistical precision increases due to the increasing cross section of the signal reaction. Therefore, the highest precision of the time-like proton FF's will be obtained at the lowest possible value of $q^2 = 5.1$ (GeV/c)². It can be seen from Fig. 7.4 that the total uncertainties of R at \bar{P} ANDA will be smaller than those of the existing data from BaBar [77] and BESIII [74].

Table 7.5: Statistical and systematic uncertainties, which contribute to the relative total uncertainty of $|G_E|$, $|G_M|$ and R .

	p_{beam} [GeV/c]	q^2 [(GeV/c) ²]	Statistical	Systematic			Total
				Binning	Cuts	Luminosity	
$\frac{\Delta G_E }{ G_E }$ [%]	1.5	5.08	3.1 %	-	0.1 %	2.0 %	3.7 %
	1.7	5.40	5.1 %	-	1.3 %	2.0 %	5.6 %
	2.5	6.77	10.2 %	-	4.2 %	2.0 %	11.2 %
	3.3	8.20	26.9 %	0.9 %	0.9 %	2.0 %	27.0 %
$\frac{\Delta G_M }{ G_M }$ [%]	1.5	5.08	1.5 %	-	< 0.1 %	2.0 %	2.5 %
	1.7	5.40	2.2 %	-	0.5 %	2.0 %	3.0 %
	2.5	6.77	4.4 %	-	0.5 %	2.0 %	4.9 %
	3.3	8.20	9.6 %	< 0.1 %	1.4 %	2.0 %	9.9 %
$\frac{\Delta R}{R}$ [%]	1.5	5.08	5 %	-	0.1 %	-	5 %
	1.7	5.40	7 %	-	2.3 %	-	7 %
	2.5	6.77	14 %	-	4.7 %	-	15 %
	3.3	8.20	37 %	1.0%	3.0 %	-	37 %

Reference [16] presented the feasibility studies for the second channel $\bar{p}p \rightarrow e^+e^-$, which will be used at $\overline{\text{PANDA}}$ to study the proton FF's in the time-like region. As it was already mentioned in Sec. 3.5 in Chapter 3, that it will be possible to achieve a sufficient background suppression of events from $\bar{p}p \rightarrow \pi^+\pi^-$, so that their expected signal pollution is expected to be a few percent and no background subtraction is needed. A very high (total) precision of the FF ratio was obtained in these studies with values up to 1.3% (stat.) and 3.3% (total) at $q^2 = 5.4$ (GeV/c)². In comparison to these results, the muon channel provides a limited precision due to the additional statistical fluctuations in the signal angular distribution, which have been introduced by the necessary background subtraction. Due to the fact, that the muon channel is very challenging due to the strong pion background, the obtained precision of the FF's in these feasibility studies can be seen as a great success and makes the measurement of this channel a very promising contribution to the rich physics program for $\overline{\text{PANDA}}$ Phase-3.

7.5 Test of lepton universality

Assuming that all radiative corrections are well-known, the ratio of the effective form factor obtained with the $\bar{p}p \rightarrow \ell^+\ell^-$ process with $\ell = e, \mu$, can be used to perform a sensitive test of the lepton universality (see 3.5.3). The ratio can be obtained as

$$\mathcal{R}_{e\mu} = \frac{|F_p(\bar{p}p \rightarrow \mu^+\mu^-)|}{|F_p(\bar{p}p \rightarrow e^+e^-)|} \quad (7.8)$$

The estimation of the expected precision of this ratio requires the expected precision of the effective form factor obtained with the $\bar{p}p \rightarrow e^+e^-$ channel. The studies were performed at a

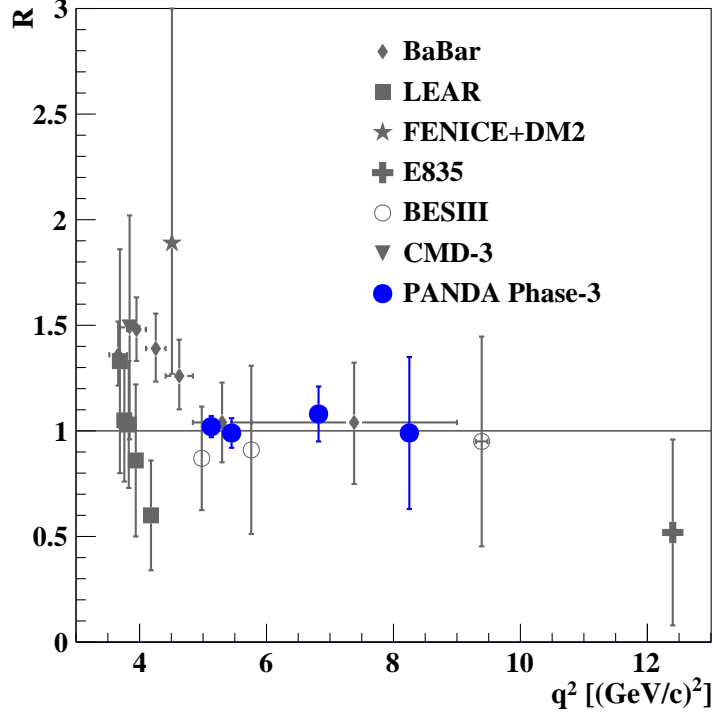


Figure 7.4: Total uncertainties of the ratio $R = |G_E|/|G_M|$ for the $\bar{p}p \rightarrow \mu^+\mu^-$ channel at different values of q^2 (blue dots) obtained under the conditions of \bar{P} ANDA Phase-3. $R = 1$ is assumed in these simulation studies. Also shown are the currently existing data from Ref. [68] (squares), from Ref. [77] (diamonds), from Ref. [99] (star and cross), from Ref. [74] (open circles) and from Ref. [96] (down triangle).

value of $q^2 = 5.4 \text{ (GeV/c)}^2$ ($p_{beam} = 1.7 \text{ GeV/c}$) under the conditions of the \bar{P} ANDA Phase-3 and can be found in Ref. [16]. The determined values of the effective form factor and its uncertainty are not shown in this paper but were kindly provided by the authors. The effective form factor $|F_p(\bar{p}p \rightarrow e^+e^-)|$ is expected as [155]

$$|F_p(\bar{p}p \rightarrow e^+e^-)| = 0.1216 \pm 0.0004 \text{ (stat.)} \pm 0.0024 \text{ (syst.)}. \quad (7.9)$$

From that, the total relative uncertainty is obtained as

$$\Delta|F_p(\bar{p}p \rightarrow e^+e^-)|/|F_p(\bar{p}p \rightarrow e^+e^-)| \sim 2.02\%. \quad (7.10)$$

For the muon channel, the effective proton FF value of

$$|F_p(\bar{p}p \rightarrow \mu^+\mu^-)| = 0.1210 \pm 0.0009 \text{ (stat.)} \pm 0.0024 \text{ (syst.)} \quad (7.11)$$

is used and together with the corresponding value for the electron channel, the uncertainty of the ratio, $\Delta\mathcal{R}_{e\mu}$ can be obtained as

$$\mathcal{R}_{e\mu} = 0.9948 \pm 0.0256, \quad (7.12)$$

which corresponds to a relative total uncertainty of

$$\Delta\mathcal{R}_{e\mu}/\mathcal{R}_{e\mu} \sim 2.92\%. \quad (7.13)$$

An even better precision would be expected for the lowest value of $q^2 = 5.1 \text{ (GeV}/c)^2$ ($p_{beam} = 1.5 \text{ GeV}/c$), since the signal cross section has higher values.

From these values, it can be concluded, that $\overline{\text{PANDA}}$ will be able to perform a test of a possible violation of the lepton universality ($e\text{-}\mu$) with high precision, assuming that the QED radiative corrections are precisely known for both channels, what needs to be calculated in the future.

7.6 Analysis without EMC detector observables

In order to investigate the importance of using the EMC variables, the study was repeated based on the same strategy as described in the previous sections. The lowest possible beam momentum at $p_{beam}=1.5$ GeV/ c is considered, since it allows to extract the FF's with the lowest possible total uncertainty.

For the studies, the same data samples were used as in the previous studies. The training of the BDT algorithm was based on the following input variables:

- Path length inside iron absorber of the MS: *iron depth*.
- Number of fired detection layers of the MS: *MS Number of fired layers*.
- Iron depth divided by initial momentum at layer zero of the MS, denoted as *Iron depth*/ p_{MDT} .
- Initial momentum of the charged particle track at zero bi-layer of the MS: p_{MDT} .
- *Identification probability* for being a muon based on MS observables: $PID_{MDT}(\mu)$.
- Mean energy loss per unit of length inside the STT, (dE/dx) (STT)
- Number of hits inside STT, *STT Hits*
- Invariant mass of the final state particles: M_{inv} .
- Sum of the polar production angles of both reconstructed tracks in center of mass system: $(\theta^+ + \theta^-)_{CM}$.

The "loose" cut configuration at $p_{beam} = 1.5$ GeV/ c , which is given in Tab. 6.6, was changed in terms of the cut on BDT response to match the signal efficiency as it was achieved in the analysis including variables from the EMC (31.5%). Another difference to the previous analysis is the reduced set of input variables for the training of the BDT, since no variables provided by the EMC are used. At the same time, a total rejection factor for the final states from $\bar{p}p \rightarrow \pi^+\pi^-$ of $1.5 \cdot 10^{-5}$ is achieved, leading to an expected signal-to-background ratio of 1:10. A comparison to the previous analysis shows, that if variables from the EMC are included, the expected signal-to-background ratio is slightly improved to 1:8. The small effect on the extraction precision of the FF's is visible when the results of R , $|G_E|$ and $|G_M|$ (given in Tab. 7.6) are compared: by excluding the variables from the EMC, the relative statistical uncertainty of the ratio R slightly deteriorates from 5% to 6%. The reduced χ^2 obtained by fitting the distributions shown in Fig. 8.4 is $\chi^2/ndf = 0.85$ in the first case, and in the second case it is $\chi^2/ndf = 0.96$. The extracted value of the relative statistical uncertainty of $|G_E|$ increases from 3.2% to 3.7%, while for $|G_M|$ it increases from 1.6% to 2.1%. From these results one can conclude, that the EMC variables contribute only little to the successful signal/background separation, as it was expected, but help to improve the extracted precision of R , $|G_E|$ and $|G_M|$.

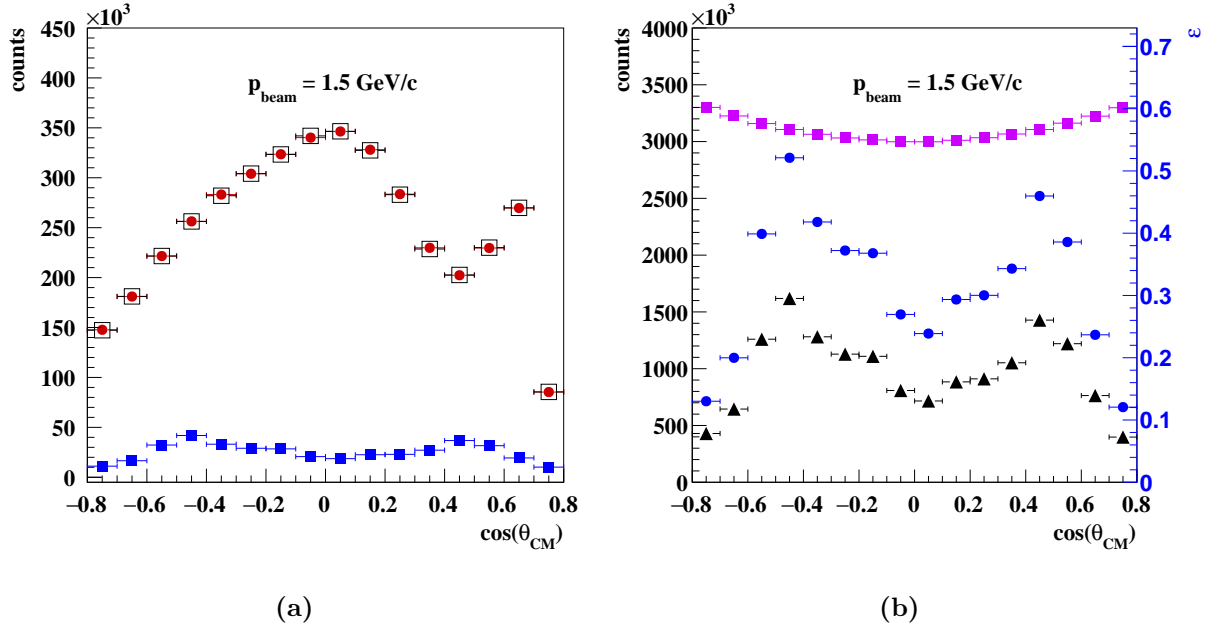


Figure 7.5: Simulation and analysis without any variables from the EMC at $\mathcal{L} = 2 \text{ fb}^{-1}$ ($\bar{\text{PANDA}}$ Phase-3). Left plot: Reconstructed, μ -selected angular distributions of the signal (squares) and of the expected pion contamination (dots and open squares) used for the analysis. Right plot: Angular distributions of the MC generated μ^- (squares), the reconstructed, μ -selected signal (S1) (up triangles) and the corresponding signal reconstruction efficiency (dots).

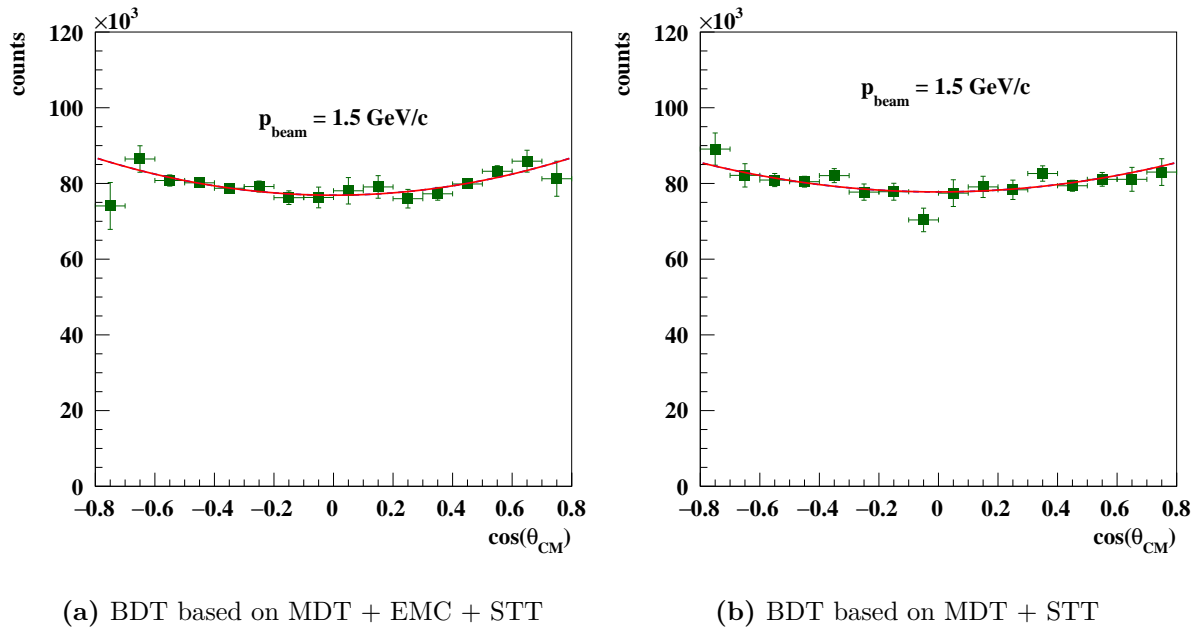


Figure 7.6: Comparison between the reconstructed, signal efficiency corrected angular distributions at $p_{\text{beam}} = 1.5 \text{ GeV}/c$ (for $\bar{\text{PANDA}}$ Phase-3, $\mathcal{L} = 2 \text{ fb}^{-1}$). Loose cuts were used for the μ -selection, including variables from EMC (left) respectively excluding variables from the EMC (right) for the training of the Boosted Decision Trees (BDT).

Table 7.6: Comparison between the extracted values of $R \pm \Delta R$ based on the full analysis with and without variables from EMC. The result $R \pm \Delta R$ was obtained with the fit function $f_2(x)$.

with EMC variables			without EMC variables		
R	ΔR	$\frac{\Delta R}{R} [\%]$	R	ΔR	$\frac{\Delta R}{R} [\%]$
1.00	0.05	5	1.02	0.06	6
$ G_E $	$\Delta G_E $	$\frac{\Delta G_E }{ G_E } [\%]$	$ G_E $	$\Delta G_E $	$\frac{\Delta G_E }{ G_E } [\%]$
0.141	0.004	3.2	0.143	0.005	3.7
$ G_M $	$\Delta G_M $	$\frac{\Delta G_M }{ G_M } [\%]$	$ G_M $	$\Delta G_M $	$\frac{\Delta G_M }{ G_M } [\%]$
0.140	0.002	1.6	0.139	0.003	2.1

7.7 Influence of the angular distribution shape of the pion contamination

The influence of the shape the pion contamination shall be investigated in the following. For this purpose, the full analysis and the extraction of the FF's is repeated, using angular distributions of the pion contamination, which contain the expected statistics, but possess a different shape. A comparison with the results obtained in the previous analysis is done afterwards in order to study the influence of the different shape.

In order to construct new distributions with different shape, the following strategy was used:

1. Starting point is the μ -selection, as it is presented in Tab. 6.6
2. A second, statistically independent data sample for $\bar{p}p \rightarrow \pi^+\pi^-$ is generated (10^8 events), reconstructed and preselected
3. The μ -selection is applied to both preselected background data samples, however the cut on the BDT response is adjusted in such a way as to obtain the expected number of background events shown in Tab. 6.8
4. The two obtained distributions possess the expected statistics for the pion background distribution, but have an unrealistic shape

This strategy is denoted as method II (MII), and only serves the purpose to construct pion contamination of a different shape. The strategy used in this feasibility study, which is described in Sec. 6.3, is denoted as method I (MI) only in this section.

Table 7.7 summarizes the cut configurations used for method II. In Fig. 7.7, both pion contamination distributions are shown, which are used to study the influence of the pion contamination shape on the results of this feasibility study at the lowest beam momentum. The corresponding angular distributions of the pion contamination with unrealistic shape are shown in Fig. 7.8 (red dots, black open squares). Also shown are the angular distributions of the signal counts after

Table 7.7: Overview of the different cut configurations used in method II, which are applied on two statistically independent pion data samples after reconstruction. The cuts on M_{inv} , $(|\phi^+ - \phi^-|)_{lab}$ and $(\theta^+ + \theta^-)_{CM}$ are the same as in the μ -selection. The difference between the cut configuration is the cut on the BDT response, which is adjusted in such a way as to obtain the expected statistics of the pion contamination, $N_{exp,cuts}(\bar{p}p \rightarrow \pi^+\pi^-)$, which can be found in Tab. 6.8.

1.5 GeV/c				
	M_{inv} [GeV/c ²]	$(\phi^+ - \phi^-)_{lab}$ [DEG]	$(\theta^+ + \theta^-)_{CM}$ [DEG]	BDT
"very loose"]2.1; 2.4[]175.0; 185.0[]179.65; 185.0[> -0.5192
"loose"]2.1; 2.4[]175.0; 185.0[]179.65; 185.0[> -0.4846
"medium"]2.1; 2.4[]175.0; 185.0[]179.65; 185.0[> -0.4264
"tight"]2.1; 2.4[]175.0; 185.0[]179.65; 185.0[> -0.3520
"very tight"]2.1; 2.4[]175.0; 185.0[]179.65; 185.0[> -0.2837
1.7 GeV/c				
	M_{inv} [GeV/c ²]	$(\phi^+ - \phi^-)_{lab}$ [DEG]	$(\theta^+ + \theta^-)_{CM}$ [DEG]	BDT
"very loose"]2.2; 2.5[]175.0; 185.0[]179.65; 185.0[> -0.7616
"loose"]2.2; 2.5[]175.0; 185.0[]179.65; 185.0[> -0.6663
"medium"]2.2; 2.5[]175.0; 185.0[]179.65; 185.0[> -0.4551
"tight"]2.2; 2.5[]175.0; 185.0[]179.65; 185.0[> -0.4255
"very tight"]2.2; 2.5[]175.0; 185.0[]179.65; 185.0[> -0.3839
2.5 GeV/c				
	M_{inv} [GeV/c ²]	$(\phi^+ - \phi^-)_{lab}$ [DEG]	$(\theta^+ + \theta^-)_{CM}$ [DEG]	BDT
"very loose"]2.4; 2.8[]175.0; 185.0[]179.65; 185.0[> -0.7850
"loose"]2.4; 2.8[]175.0; 185.0[]179.65; 185.0[> -0.3609
"medium"]2.4; 2.8[]175.0; 185.0[]179.65; 185.0[> -0.2891
"tight"]2.4; 2.8[]175.0; 185.0[]179.65; 185.0[> -0.2076
"very tight"]2.4; 2.8[]175.0; 185.0[]179.65; 185.0[> -0.1254
3.3 GeV/c				
	M_{inv} [GeV/c ²]	$(\phi^+ - \phi^-)_{lab}$ [DEG]	$(\theta^+ + \theta^-)_{CM}$ [DEG]	BDT
"very loose"]2.6; 3.1[]175.0; 185.0[]179.65; 185.0[> 0.0120
"loose"]2.6; 3.1[]175.0; 185.0[]179.65; 185.0[> 0.0645
"medium"]2.6; 3.1[]175.0; 185.0[]179.65; 185.0[> 0.0750
"tight"]2.6; 3.1[]175.0; 185.0[]179.65; 185.0[> 0.0832
"very tight"]2.6; 3.1[]175.0; 185.0[]179.65; 185.0[> 0.1130

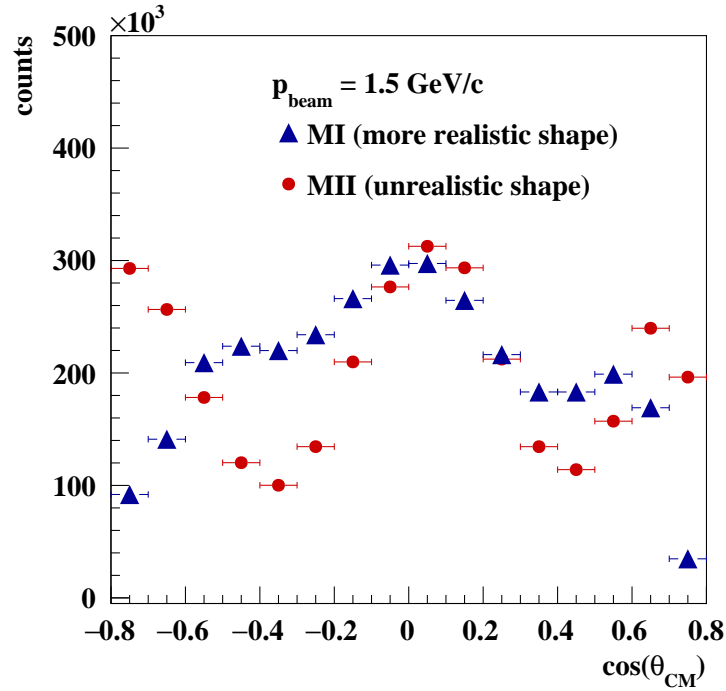


Figure 7.7: Pion contamination distribution at $p_{\text{beam}} = 1.5 \text{ GeV}/c$ used in this feasibility study which is described in section 6.3 (MI, blue triangles up) and has a more realistic shape. In comparison to that, the pion contamination distribution obtained with a modified signal selection (MII, red dots), aiming just to match the number of expected events but with unrealistic shape. Both distributions contain the number of expected events. Repeating the analysis with both pion background distributions allows to test the influence of the distribution shape on the uncertainties of the form factors.

μ -selection (blue squares), corresponding to the final cut configuration at each value of beam momentum. To summarize this method, a new selection is applied on two statistically independent samples after event reconstruction in order to achieve angular distributions of the pion contamination with expected statistics but different shape. The results obtained in the corresponding analysis can be found in the Appendix E. The systematic and total relative uncertainties will be discussed in the following, together with a comparison of both methods.

Systematic and total relative uncertainties

Also in the case of this method, an estimation of systematic uncertainties is performed. The systematic uncertainties originating from the choice of cuts were determined by comparing the extracted value of R respectively the FF's with the corresponding values obtained with a neighbor cut configuration. The results from these two different cut configurations are compared and allow to estimate the corresponding systematic uncertainty. Table 7.8 gives an overview of the relative statistical and systematic uncertainties and the total relative uncertainty of the FF's and R . The study of the systematic uncertainties shows, that at all considered values of

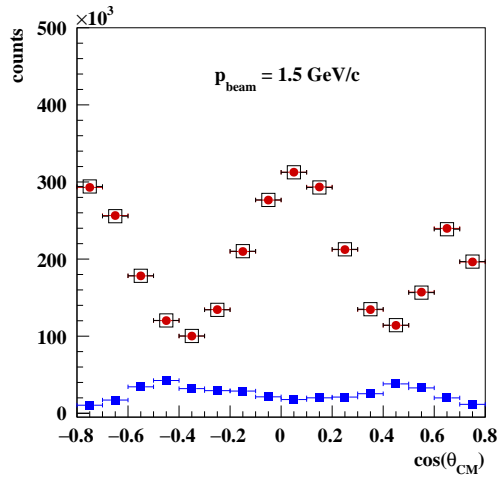
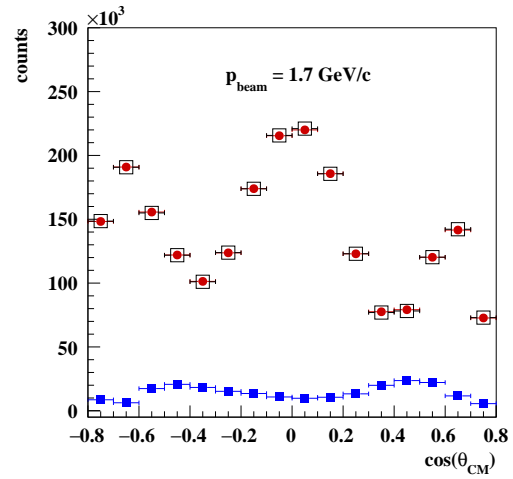
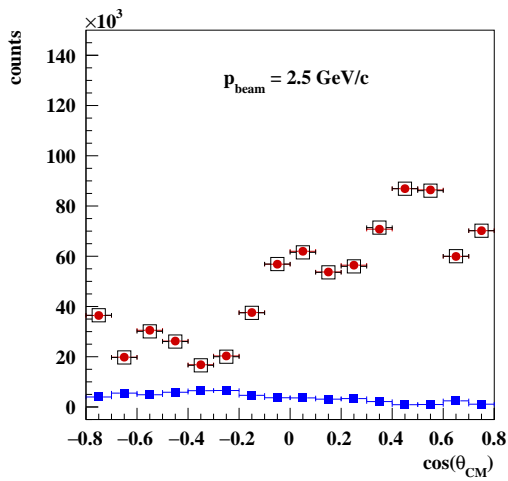
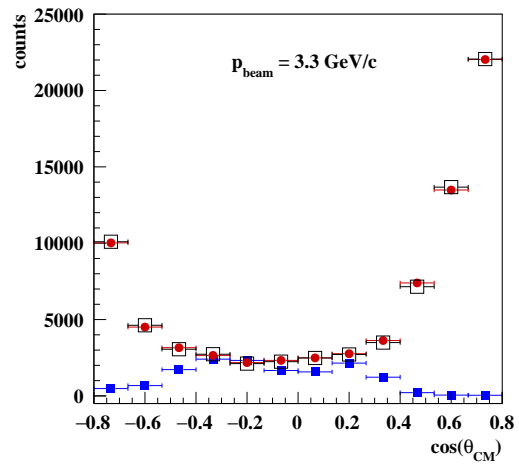
(a) $p_{\text{beam}}=1.5$ GeV/c, "loose cuts"(b) $p_{\text{beam}}=1.7$ GeV/c, "medium cuts"(c) $p_{\text{beam}}=2.5$ GeV/c, "tight cuts"(d) $p_{\text{beam}}=3.3$ GeV/c, "loose cuts"

Figure 7.8: Angular distributions of the reconstructed μ -selected signal counts (blue squares) and pion contamination (red dots, black open squares) obtained with method II as a function of the center-of-mass angle $\cos(\theta_{CM})$. The shape of the distributions of the pion contamination are not realistic in this case. Shown are the cases for (a) 1.5 GeV/c, "loose cuts" (b) 1.7 GeV/c, "medium cuts", (c) 2.5 GeV/c, "tight cuts" and (d) 3.3 GeV/c, "loose cuts".

Table 7.8: Contributions of the relative statistical and systematic uncertainties of $|G_E|$, $|G_M|$ and R to the relative total uncertainty.

	p_{beam} [GeV/c]	q^2 [(GeV/c) ²]	Statistical	systematic			Total
				Binning	Cuts	Luminosity	
$\frac{\Delta G_E }{ G_E }$ [%]	1.5	5.08	3.8 %	-	1.2 %	2.0 %	4.5 %
	1.7	5.40	5.3 %	-	0.2 %	2.0 %	5.7 %
	2.5	6.77	8.8 %	-	4.7 %	2.0 %	10.2 %
	3.3	8.20	19.7 %	0.4%	2.3 %	2.0 %	19.9 %
$\frac{\Delta G_M }{ G_M }$ [%]	1.5	5.08	1.7%	-	0.6 %	2.0 %	2.7 %
	1.7	5.40	2.6%	-	0.1 %	2.0 %	3.3 %
	2.5	6.77	4.8%	-	0.8 %	2.0 %	5.3 %
	3.3	8.20	8.0%	< 0.1%	0.5 %	2.0 %	8.3 %
$\frac{\Delta R}{R}$ [%]	1.5	5.08	5%	-	0.8 %	-	5 %
	1.7	5.40	8%	-	0.3 %	-	8 %
	2.5	6.77	12%	-	5.8 %	-	13 %
	3.3	8.20	28%	0.4%	2.8 %	-	28 %

beam momentum, the largest contribution to the total uncertainty of the ratio R comes from statistical uncertainties. These statistical uncertainties are dominated at lower values of the beam momentum by the statistical fluctuations of the pion contamination, which remain in the signal data after the background subtraction. At higher values of beam momentum, the statistical fluctuations of the signal data increase strongly due to the decreasing signal cross section, which leads to a strong increasement of the statistical uncertainty of R . At lower values of beam momentum, the other sources of systematic uncertainties contribute for most of the cases slightly less to the total uncertainty of the FF's than the statistical uncertainty. Only in the case of $|G_M|$ at 1.5 GeV/c, the luminosity uncertainty has the highest contribution to the total uncertainty. When going to higher values of beam momentum, the contribution of the statistical uncertainties to the total uncertainty increases and clearly dominates the total uncertainty of the FF's at 3.3 GeV/c due to the smaller cross section of the $\bar{p}p \rightarrow \mu^+\mu^-$ process.

Conclusion

Both values of $R \pm \Delta R$, which are obtained with the pion contamination distributions of more realistic (MI) respectively unrealistic (MII) shape, are presented in Fig. 7.9 together with already existing data. At every value of q^2 they are in very good agreement with each other and the assumption $R = 1$. A high precision of the FF's is obtained in both methods. For the purpose of better visualization, the data points are shifted by $\delta q^2 = \pm 0.05$. From these results, it can be concluded that the angular distribution shape of the pion contamination has no significant influence on the results in this work. The extracted values of $|G_E|$ and $|G_M|$ are presented together with their uncertainties in Fig. 7.10. The residual values between the calculated and the extracted values of the time-like FF's are shown in Fig. 7.11 for both MI

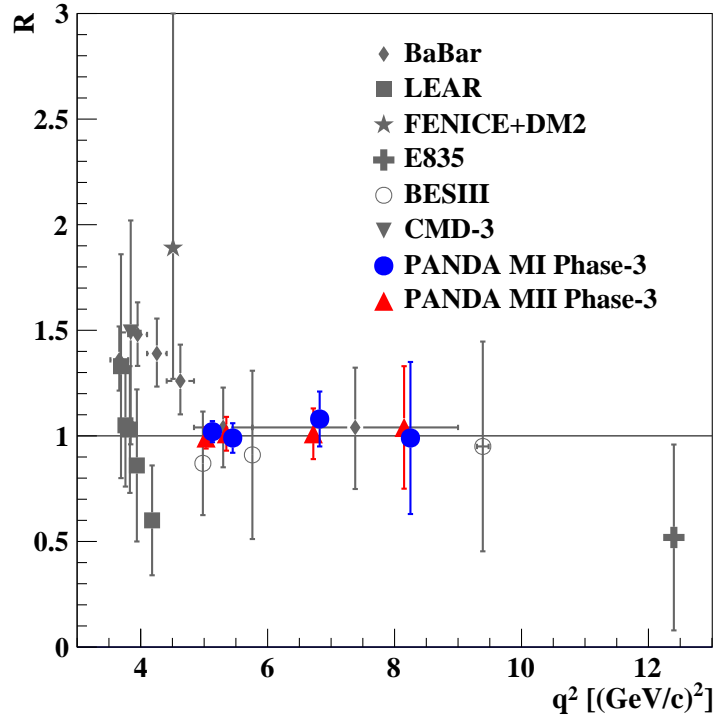


Figure 7.9: Extracted uncertainties of the ratio $R = |G_E|/|G_M|$ for the $\bar{p}p \rightarrow \mu^+\mu^-$ channel at different values of q^2 obtained with pion contamination distribution of more realistic (MI, blue dots) respectively unrealistic shape (MII, red triangles up). $R = 1$ is assumed. For a better visualization, the data points are shifted by $\delta q^2 = \pm 0.05$. Also shown are the currently existing data from Ref. [68] (squares), from Ref. [77] (diamonds), from Ref. [99] (star and cross), from Ref. [74] (open circles) and from Ref. [96] (down triangle).

and MII. They are very well consistent with each other and are also in good agreement with the assumption $R = 1$. In the next section, the influence of processes with final state radiation on the results is studied.

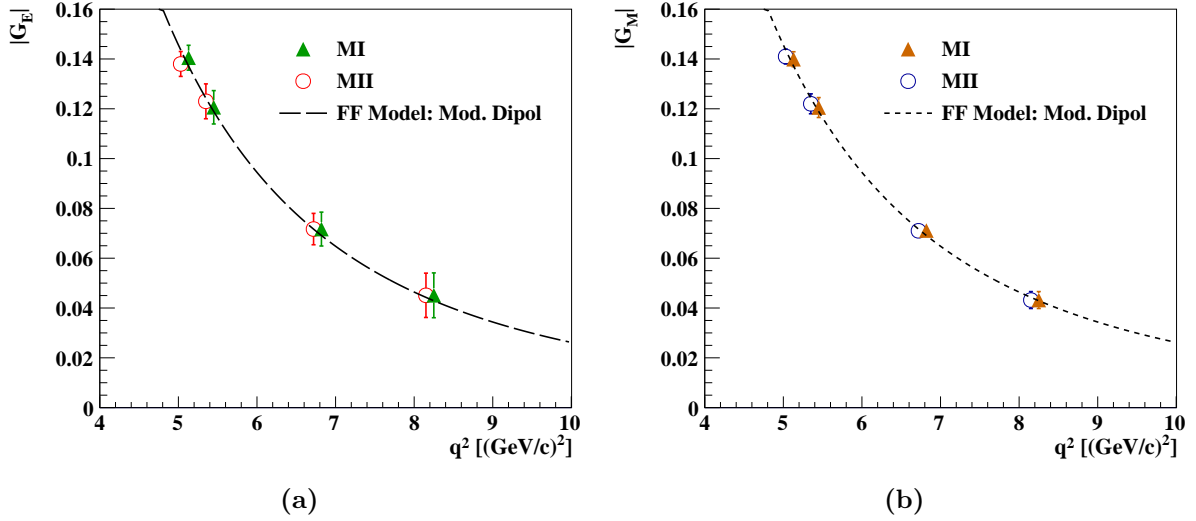


Figure 7.10: Extracted values of $|G_E|$ (a) and $|G_M|$ (b) with their uncertainties, obtained with pion contamination distributions of more realistic (MI, triangles up) respectively unrealistic shape (MII, open circles) depending on q^2 . For a better visualization, the data points are shifted by $\delta q^2 = \pm 0.05$. Also the FF model from [54] is shown (dashed lines), which is used in this feasibility study together with the assumption that $|G_E| = |G_M|$.

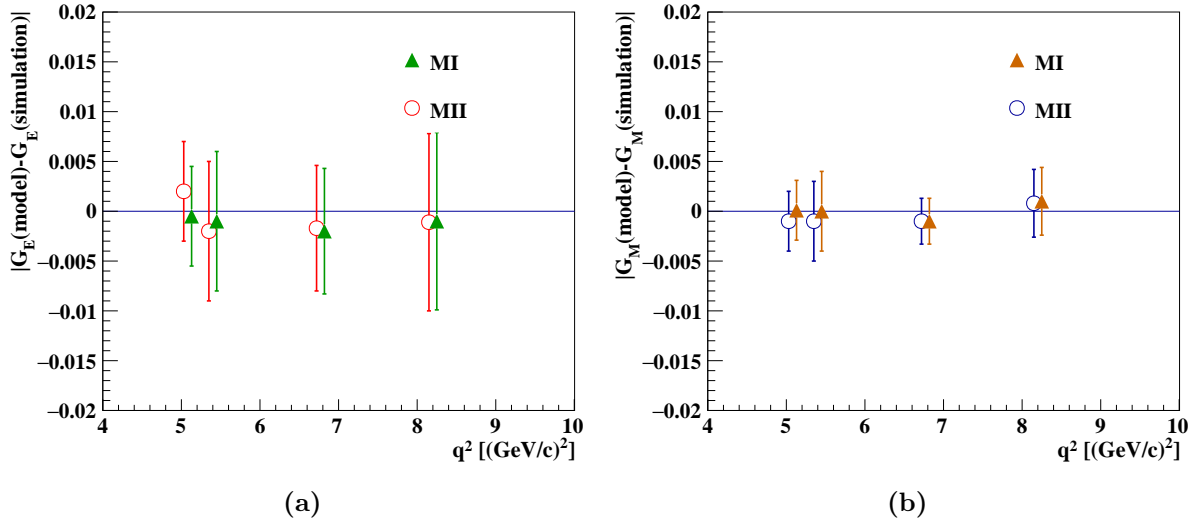


Figure 7.11: Residual values for $|G_E|$ (a) and $|G_M|$ (b) at different q^2 values and corresponding uncertainties. Shown are the results obtained with pion contamination distributions of more realistic (MI, triangles up) respectively unrealistic shape (MII, open circles). For a better visualization, the data points are shifted by $\delta q^2 = \pm 0.05$.

7.8 Radiative corrections to the $\bar{p}p \rightarrow \mu^- \mu^+$ process using PHOTOS

The electromagnetic form factors of the proton in the time-like region, $|G_{E,M}|$ are extracted from the angular distribution of the final state lepton in the $\bar{p}p \rightarrow \ell^- \ell^+$ ($\ell = e, \mu$) process in Born approximation (exchange of a single virtual photon). The differential cross section of this process is a function of $\cos(\theta_{CM})$. In a real experiment, the measured angular distribution is altered from its shape by radiative corrections resulting in a distorted angular distribution. The measured cross section $\left(\frac{d\sigma}{d\Omega}\right)_{exp}$ differs from the Born cross section $\left(\frac{d\sigma}{d\Omega}\right)_B$ [156] as

$$\left(\frac{d\sigma}{d\Omega}\right)_{exp} = \left(\frac{d\sigma}{d\Omega}\right)_B \cdot (1 + \delta), \quad (7.14)$$

where $(1+\delta)$ stands for the radiative correction factor, which must be taken from (highly non-trivial) theoretical calculations.

Figure 7.12 a) shows the Feynman diagram (Born diagram) corresponding to the leading order contribution to the cross section, depending on the electromagnetic coupling constant (α^2), whereas Figure 7.12 b) - j) show the Feynman diagrams contributing to the next-to-leading order (α^3), which are used for the calculation of *radiative corrections*. Radiative corrections can be divided into odd and even contributions with respect to $\cos(\theta_{CM})$. The even contributions do not affect the shape of the angular distribution, but act like a normalization. The odd contributions in next-to-leading order are caused by the interference of the processes with initial and final state real photon emission and also, from the interference of the leading-order process a) with the two photon exchange contribution. They result in a distortion of the angular distribution of the final state lepton. The radiative corrections contain the contributions from

- bremsstrahlung corrections from the processes with real photon emission in the initial state (from the proton (b) and the antiproton (c)) and in the final state (from the antilepton (d) and from the lepton (e)) and their interferences.
- virtual corrections from the interference between the Born process and the processes with emission of one photon at the proton vertex (f), emission of one photon at the lepton vertex (g), the vacuum polarization (h) and the two photon exchange (i) and (j).

Also lepton self-energy corrections (which means photon emission and re-absorption by the same particle) are contributing. Such corrections lead to a renormalization of the coupling constants and masses. In the calculation of the contribution of self-energy corrections to the reaction amplitude, the integration over all photon energies leads to a divergence (ultraviolet divergence). Such ultraviolet divergences are cancelled in the total radiative correction.

Infrared singularities are caused only by bremsstrahlung processes. An infrared singularity occurs, when the energy of the emitted photon goes to zero and the corresponding term diverges. The bremsstrahlung corrections are usually divided into two contributions in order to remove infrared singularities:

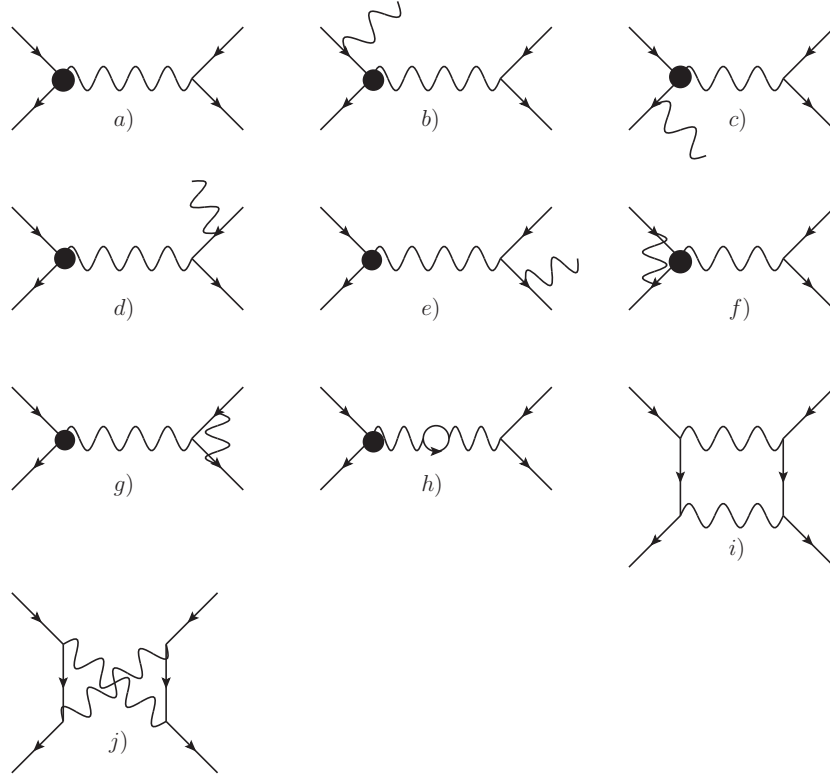


Figure 7.12: Feynman diagrams for the leading order contribution a) and the first-order radiative corrections, which contribute to the cross section of the $\bar{p}p \rightarrow l^- l^+$ ($l = e, \mu$) process [154].

- the soft photon contribution, with photon energies up to an infrared cut-off ¹ (E_γ^{min}), with $E_\gamma^{min} \ll \sqrt{s}$.
- the hard photon contribution, with photon energies larger than E_γ^{min} .

In the calculation of the virtual and soft photon contribution, the emitted photon is assumed to possess a non-zero rest mass, which cancels, when both terms are summed up. The infrared singularities appearing in the soft photon contribution are cancelled order by order by virtual corrections. For details of such calculations see Ref. [156].

A different way to describe radiative corrections is to classify them according to $(\alpha/\pi)^n L^n$, $n = 0, 1, 2, \dots$ with $L = \ln(q^2/\eta^2)$ ($\eta = m_\ell, \lambda_{QCD}, \dots$) [157], instead of considering them order-by-order with respect to α .

Since the calculations of such radiative corrections for the $\bar{p}p \rightarrow \mu^+ \mu^-$ have not been performed yet, they can not be included in this work. However, the influence of final state Bremsstrahlung emission on the reconstruction efficiency of the signal shall be studied in the following. Additionally, the influence on the extracted values of $|G_{E,M}|$ and their uncertainties will be shown.

¹The total radiative corrections are independent on the choice of E_γ^{min} .

This study is based on the same release of the PandaRoot framework as it was used for the previous studies, but this time in combination with the software package PHOTOS, which includes processes with final state radiation into the simulation. Before the study is presented, the PHOTOS software is briefly described.

7.8.1 PHOTOS software package

The PHOTOS software package [158, 159, 160] is a Monte-Carlo algorithm for the implementation of QED photon radiative corrections in particle decays. It can be used to estimate the size of the QED bremsstrahlung in the so-called *leading-logarithmic (LL) approximation* and provides final states with full event topology taking into account energy and momentum conservation. In the LL approximation, only contributions limited to $(\alpha/\pi) L \sim 1$ are considered. PHOTOS generates real photons, which are emitted by the final state particles. The energy and momentum of the parent particle is reduced according to energy and momentum conservation. The generated real photons possess energies above E_{γ}^{min} (hard photons), this value is by default set to $(10^{-7} \times \sqrt{s}/2)$, which is used in this study. The number of generated events remains unchanged by the application of PHOTOS. Radiative corrections due to final state radiation in the signal $\bar{p}p \rightarrow \mu^+\mu^-$ are expected to be small compared to $\bar{p}p \rightarrow e^+e^-$, since they depend on the lepton mass as $\ln(q^2/m_{\ell}^2)$, $\ell = e, \mu$ (for details see Ref. [158, 159, 160]).

Processes of two photon exchange (box diagram) and initial state radiation are contributing very little to the radiative corrections for the $\bar{p}p \rightarrow \ell^-\ell^+$ process and are considered to be negligible in this study. They are not taken into account in PHOTOS. Also the contribution from vacuum polarization is not taken into account in PHOTOS, since it leads to an even contribution with respect to $\cos(\theta_{CM})$ and therefore results in a normalization factor for the undistorted angular distribution corresponding to the Born cross section. PHOTOS is not designed for the correction of experimental data concerning radiative corrections, but allows to study the effects of real photon emission on the signal efficiency.

7.8.2 Simulation studies using PHOTOS in PandaRoot

The Monte-Carlo simulation allows to include the PHOTOS package at the event generation level. If PHOTOS is activated, the final state photon(s) will be emitted together with the final state leptons. This occurs under conservation of momentum and energy of the particle system. Since more than one photon can be emitted, also higher order contributions to the radiative corrections are included in this simulation study.

In the following, the influence of final state radiation processes on the signal angular distribution of the final state muon from $\bar{p}p \rightarrow \mu^+\mu^-$ shall be presented and will be compared to the case of the electron channel $\bar{p}p \rightarrow e^+e^-$.

Influence of final state radiation on the reconstructed angular distribution of the signal

This study was performed at the lowest value of beam momentum of 1.5 GeV/c at \bar{P} ANDA ($q^2 = 5.1 \text{ GeV}^2$). The same simulation and analysis procedure was used as for the previous feasibility study under the conditions of \bar{P} ANDA Phase-3. Also in this study, two independent signal samples were generated: a sample of high statistics used for the determination of the signal reconstruction efficiency, and another, statistically independent sample containing the physically expected number of signal events at $\mathcal{L} = 2 \text{ fb}^{-2}$, as they were given in Tab. 5.1. $R = 1$ was used for the event generation, the FF model from Ref. [54] was assumed for the calculation of the physically expected number of events for the signal $\bar{p}p \rightarrow \mu^- \mu^+$ process.

Figure 7.13 shows the correlation between the $\bar{p}p$ center-of-mass energy of the produced μ^- depending on the corresponding energy of the produced μ^+ on the Monte-Carlo level for the previous analysis (right plot), where PHOTOS is not used and under the same conditions, but when PHOTOS is switched ON (left plot). In the latter case, a tail to lower energies is clearly visible due to the additional final state photons. When PHOTOS is switched off, the available energy is split equally between the muons, so that a sharp peak is visible in Fig. 7.13 (right plot) at $E_{CM}^{\mu^-} = E_{CM}^{\mu^+} = \sqrt{s}/2$. It is possible, that more than one photon is emitted, what is

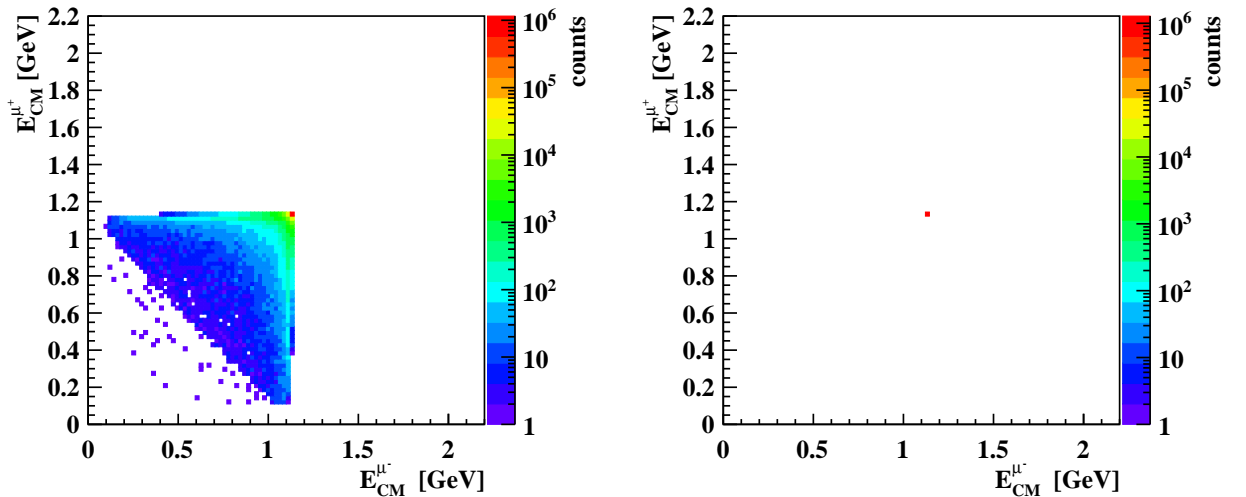


Figure 7.13: Energy of the produced μ^+ versus μ^- at Monte Carlo level in the $\bar{p}p$ center-of-mass system at $p_{beam} = 1.5 \text{ GeV}/c$ for the case that final state photons are emitted and cause a tail to lower energies (left plot) (PHOTOS ON) and for the case that no radiative effects are included (right plot) (PHOTOS OFF).

shown in Figure 7.14 (a), where the number of emitted photons per event is considered. Up to 5 photons are emitted per event (which is a default setting in PHOTOS), which lowers the energy of the corresponding leptons. As a consequence, the invariant mass of the MC generated $\mu^+ \mu^-$ final state particles, $M_{\mu^+ \mu^-}$, shows a tail towards lower energies, what can be seen in Fig. 7.14 (b). If a cut is applied on $M_{\mu^+ \mu^-}$, events are rejected, which do not fulfill the cut criterium, due

to the loss of energy and momentum carried away by the additional final state photon(s). As

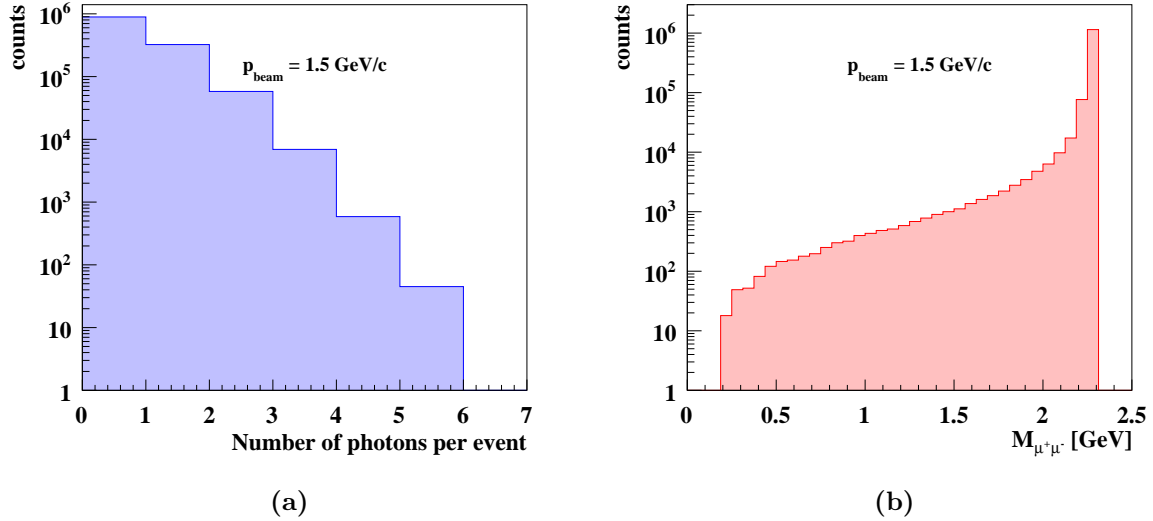


Figure 7.14: Monte-Carlo generation at $p_{beam} = 1.5 \text{ GeV}/c$ for the signal $\bar{p}p \rightarrow \mu^- \mu^+$ process: (a) Number of emitted photons per event. (b) Invariant mass of the generated $\mu^+ \mu^-$ pair in the final state. The tail to lower values of is caused by the loss of energy and momentum which is carried away by the emitted photon(s).

it was mentioned before, the radiative corrections for the muon signal channel due to final state radiation are expected to be much smaller than for the electron channel, since the contribution depends on the lepton mass as $\ln(q^2/m_\ell^2)$. Figure 7.15 shows a comparison of the MC invariant mass of the generated lepton pair in the final state with PHOTOS ON at $p_{beam} = 1.5 \text{ GeV}/c$ for (a) the $\bar{p}p \rightarrow \mu^+ \mu^-$ process and (b) the $\bar{p}p \rightarrow e^+ e^-$ process. Approximately 30.4% of the muon pairs emit at least one real photon. For the electron pairs it is the case in approximately 68.7% of the events.

Different cut values on the MC invariant mass of the final state particles from $\bar{p}p \rightarrow \mu^+ \mu^-$ have been applied and the corresponding angular distributions at Monte-Carlo level and the relative loss of signal statistics are shown in Fig. 7.16. Depending on the cut value, signal statistics is lost homogeneously over the considered range of $|\cos\theta_{CM}| < 0.8$. The shape of the angular distribution is not affected. As an example, using a cut on the invariant mass of $M_{\mu^+ \mu^-} > 2.1 \text{ GeV}$, the loss of signal statistics due to real photon emission in the final state is $\approx 3\%$. This cut value on the invariant mass was used in the previous analysis. It was tested on event samples for $\bar{p}p \rightarrow e^+ e^-$, which have been kindly provided by the authors of Ref. [155, 16], that if electron pairs in the final state are considered and the same cut value on $M_{e^+ e^-} > 2.1 \text{ GeV}$ is used, the loss of signal statistics due to real photon emission in the final state is $\approx 10\%$, as it is expected due to the smaller rest mass of the electron in comparison to the muon.

Equation 7.14 shows, that the experimental measured cross section, which includes radiative corrections, differs from the Born cross section by the factor $(1+\delta)$. This factor can be

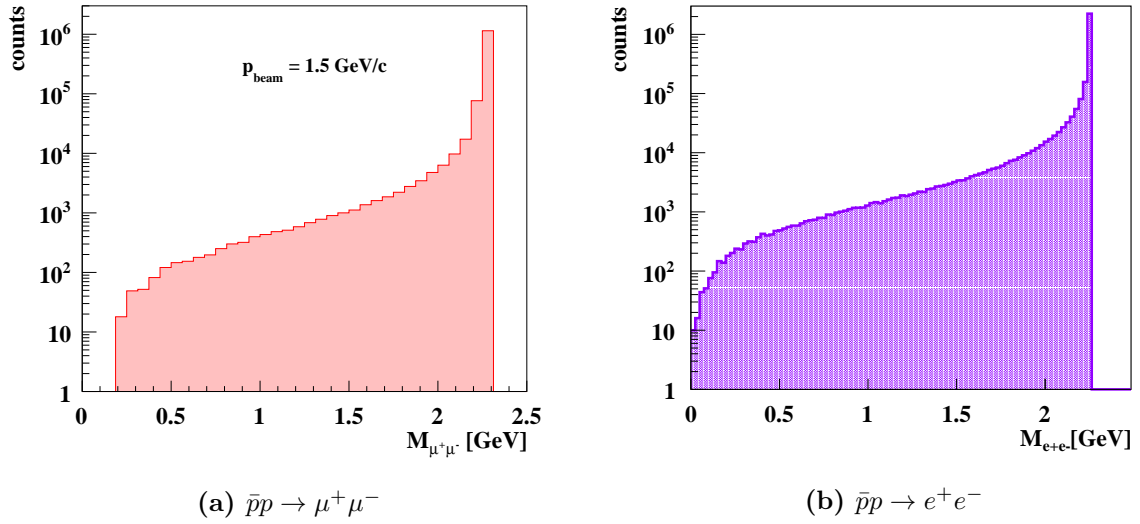


Figure 7.15: Comparison of the MC invariant mass of the generated lepton pair in the final state with PHOTOS ON at $p_{beam} = 1.5 \text{ GeV}/c$ for (a) the $\bar{p}p \rightarrow \mu^+ \mu^-$ process and (b) the $\bar{p}p \rightarrow e^+ e^-$ process. While approximately 30.4% of the muon pairs emit at least one real photon, for the electron pairs it is the case in approximately 68.7% of the events. Please note the different binning used in (b).

obtained by Monte-Carlo simulation, when the radiative corrections are implemented, and will be used for the correction of the measured differential cross section. The extraction of the FF's will be performed on the measured data at \bar{P} ANDA after the correction for radiative corrections has been applied.

In the following, the influence of final state Bremsstrahlung photons on the values of the extracted FF's for the muon channel, will be shown.

Influence of final state radiation on the results

This corresponds to a scenario, where the experimental data are directly used for the analysis without any correction of effects from final state radiation. In order to see the effect of such final state radiation photons on the extracted FF values and their statistical uncertainties, the full analysis is performed again with PHOTOS being switched on during the event generation of the signal samples and following the same procedure as it was used in the previous feasibility study.

Figure 7.17 (b) shows the reconstructed angular distribution of the μ^- after correction with the signal reconstruction efficiency distribution (see Figure 7.17 (a)). The FF's and their ratio R were obtained with the fit function $f_1(x)$ and $f_2(x)$, respectively with a reduced $\chi^2/\text{ndf} = 1.35$.

This study with PHOTOS being switched ON was compared to the case, that PHOTOS is

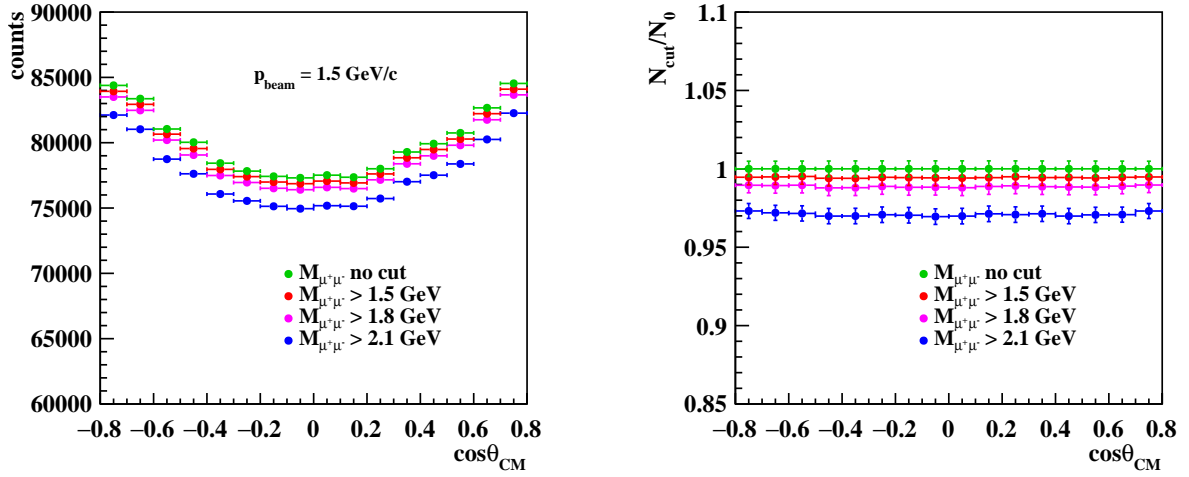


Figure 7.16: Angular distribution of the MC generated μ^- including final state radiation based on PHOTOS for $\bar{p}p \rightarrow \mu^+\mu^-$ for different cuts on the MC invariant mass $M_{\mu^+\mu^-}$ (left plot) and the relative loss of signal statistics due to different cuts (right plot). The cuts lead to a homogeneous loss of signal statistics over the considered range of $|\cos\theta_{CM}| < 0.8$.

switched OFF (as it is the case in the previous analysis). Table 7.9 summarizes the results in both cases. The results for the FF's, R , $|F_p|$ and σ are consistent within one sigma in this analysis. The extracted values of the FF's and their ratio are not significantly changed when the generated muons emit final state radiation, since the shape of the signal angular distribution is not affected. However, the precision gets worse, since the total signal efficiency decreases from 31.5% (when PHOTOS is switched OFF) to 24.2% (when PHOTOS is switched ON) due to the cut on the reconstructed invariant mass of the final state particles. The ratio R has a statistical uncertainty of 6% with PHOTOS ON, which means a deterioration of 1% in comparison to the results obtained while PHOTOS is switched OFF. A detailed study including the calculation of the radiative corrections for the $\bar{p}p \rightarrow \mu^+\mu^-$ channel is needed and will be performed in the future.

In the next chapter, the impact of the reduced setup and luminosity planned for the first data taking phase at $\overline{\text{PANDA}}$ (denoted as $\overline{\text{PANDA}}$ Phase-1) on the extracted uncertainty of the FF's will be investigated. In particular, there is the risk, that the EMC material will not be fully present in the beginning of the $\overline{\text{PANDA}}$ Phase-1.

Table 7.9: Comparison of the relative statistical uncertainty of $|G_E|$, $|G_M|$ and R for PHOTOS ON/OFF. Loose cuts are used for the μ -selection. Also shown are the obtained values and statistical uncertainties for the effective proton FF and the integrated cross section. The results show, that a deterioration of the statistical uncertainty is obtained when PHOTOS is switched ON, due to the loss of signal efficiency.

PHOTOS ON		PHOTOS OFF	
$R \pm \Delta R$	$\Delta R/R$ [%]	$R \pm \Delta R$	$\Delta R/R$ [%]
1.02 ± 0.06 (stat.)	6 (stat.)	1.02 ± 0.05 (stat.)	5 (stat.)
$ G_E \pm \Delta G_E $	$\Delta G_E / G_E $ [%]	$ G_E \pm \Delta G_E $	$\Delta G_E / G_E $ [%]
0.142 ± 0.006 (stat.)	3.9 (stat.)	0.142 ± 0.004 (stat.)	3.1 (stat.)
$ G_M \pm \Delta G_M $	$\Delta G_M / G_M $ [%]	$ G_M \pm \Delta G_M $	$\Delta G_M / G_M $ [%]
0.139 ± 0.003 (stat.)	1.9 (stat.)	0.139 ± 0.002 (stat.)	1.5 (stat.)
$ F_p \pm \Delta F_p $	$\Delta F_p / F_p $ [%]	$ F_p \pm \Delta F_p $	$\Delta F_p / F_p $ [%]
0.1402 ± 0.0005 (stat.)	0.37 (stat.)	0.1402 ± 0.0005 (stat.)	0.33 (stat.)
$\sigma \pm \Delta\sigma$ [pb]	$\Delta\sigma/\sigma$ [%]	$\sigma \pm \Delta\sigma$ [pb]	$\Delta\sigma/\sigma$ [%]
640.39 ± 4.74 (stat.)	0.74 (stat.)	640.64 ± 4.17 (stat.)	0.65 (stat.)

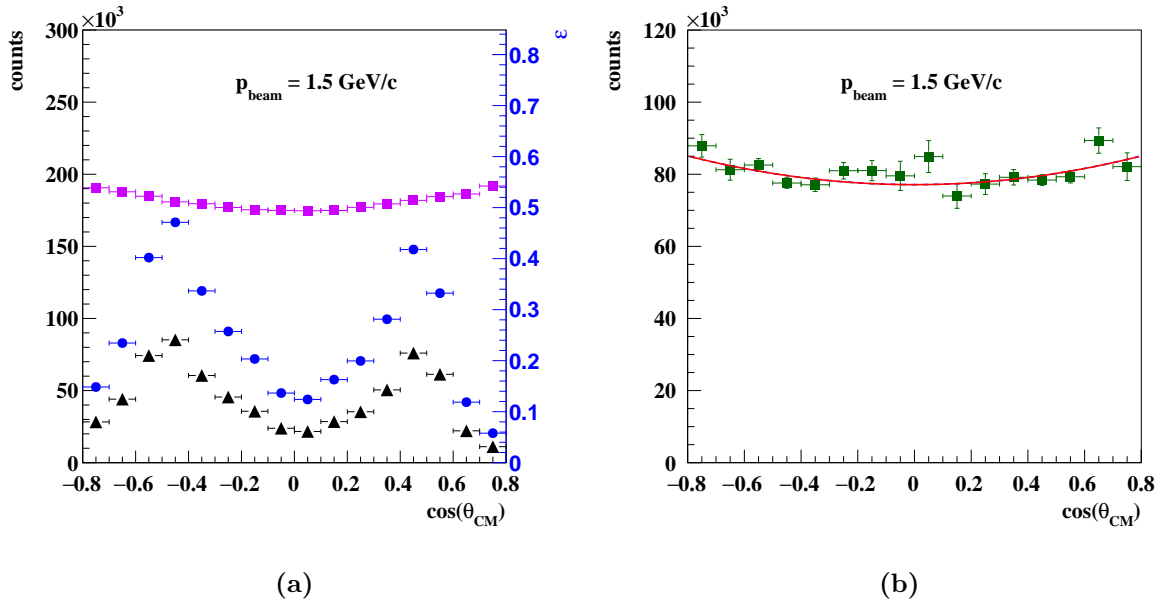


Figure 7.17: Simulation and analysis at $p_{\text{beam}} = 1.5 \text{ GeV}/c$ including final state radiation emission based on the PHOTOS package: (a) Reconstructed angular distributions of the MC signal sample S1 (black triangles up), of the Monte-Carlo generated μ^- (magenta squares) and the distribution of the signal efficiency (blue dots). An integrated signal efficiency of 24.2% is obtained using loose cuts. (b) Angular distribution of the reconstruction efficiency corrected signal counts after background subtraction for negative charges (squares). Also the fit function $f_2(x)$ (red line) is shown, which is used for the direct extraction of $R \pm \Delta R$.

Chapter 8

Feasibility studies for $\overline{\text{PANDA}}$ Phase-1

The first phase of data taking at the future $\overline{\text{PANDA}}$ Experiment is denoted as $\overline{\text{PANDA}}$ *Phase-1*. In this phase, a reduced luminosity will be present due to the absence of the RESR for the antiproton accumulation before injection into HESR. The luminosity during $\overline{\text{PANDA}}$ Phase-1 will be of the order of $10^{31} \text{ cm}^{-2}\text{s}^{-1}$, which corresponds to a reduction by a factor of 20 in comparison to the original design peak luminosity of $\overline{\text{PANDA}}$. Also, several sub-detectors of the $\overline{\text{PANDA}}$ detector (e.g. DISC/Dirc, Forward RICH, ...) will not be present during the $\overline{\text{PANDA}}$ Phase-1. The following simulation studies aim to investigate the possibility to perform the measurement of time-like electromagnetic form factors, $|G_E|$ and $|G_M|$, with the $\bar{p}p \rightarrow \mu^+\mu^-$ reaction during $\overline{\text{PANDA}}$ Phase-1, assuming a time-integrated luminosity of $\mathcal{L} = 0.1 \text{ fb}^{-1}$ and a reduced detector setup. In particular, at the beginning phase of data taking, it is possible, that not the full EMC in the Target Spectrometer will be available. This scenario will be investigated in a second study. Before the feasibility studies for $\overline{\text{PANDA}}$ Phase-1 are presented, a short overview of the reduced $\overline{\text{PANDA}}$ detector setup will be given.

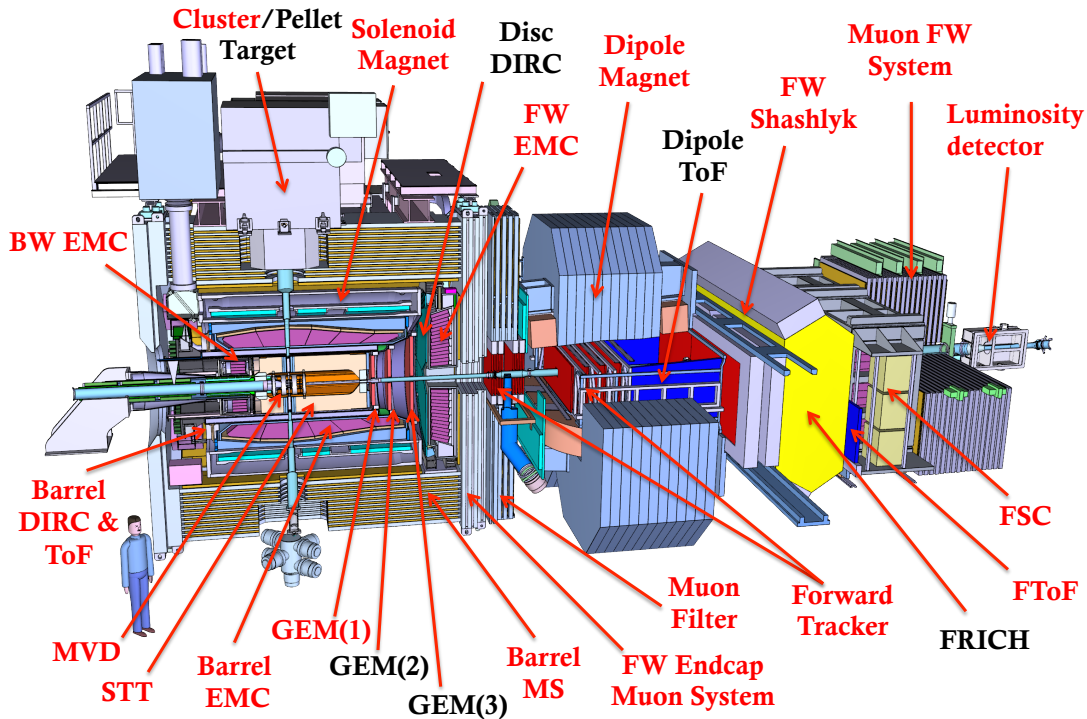


Figure 8.1: The reduced detector setup of the $\bar{\text{PANDA}}$ detector during Phase-1. All available detectors and the Cluster Target are highlighted in red font. The pellet target and several detectors (the second and the third stage of the Gas Electron Multipliers (GEM's), the Detector for Internal Cherenkov Light / Disc (Disc DIRC), the Forward Ring Imaging Cherenkov Detector (FRICH) and the Dipole Time-of-Flight (Dipole ToF) system) will not be present during $\bar{\text{PANDA}}$ Phase-1.

8.1 $\bar{\text{PANDA}}$ detector setup during Phase-1

The reduced detector setup during $\bar{\text{PANDA}}$ Phase-1 is depicted in Figure 8.1. The Pellet Target, all stages of the Gas Electron Multipliers, the Detector for Internal Cherenkov Light / Disc, the Forward Ring Imaging Cherenkov Detector and the Forward Dipole Time-of-Flight will only be present at the second major phase of data taking after Phase-1, denoted as Phase-2, when the full detector setup (still with reduced luminosity) will be available at $\bar{\text{PANDA}}$. The third data taking phase, Phase-3, requires the availability of the RESR. Phase-3 would provide both full detector setup and full luminosity for the measurements at $\bar{\text{PANDA}}$.

8.2 Results of the feasibility study for Phase-1

In the following, the results obtained by two different simulation studies, taking into account the conditions of the $\bar{\text{PANDA}}$ Phase-1, will be presented. The first study is performed following the experimental conditions as it is planned for the Phase-1, when the EMC will be fully present. Since it is possible, that the EMC will not be fully present directly at the beginning of Phase-1,

the second study shall demonstrate the necessity of the EMC detector material and show its influence on the results of this feasibility study. Excluding the EMC detector material in the PandaRoot software influences strongly the statistical precision of R and the FF's, since the EMC material serves as an additional filter for the muons in front of the Muon System. A large fraction of the produced pions and also secondary particles is stopped by the EMC material before entering the MS.

Both studies were performed at the lowest value of beam momentum, $p_{beam} = 1.5 \text{ GeV}/c$, in order to receive the highest possible signal statistics.

8.2.1 Test of lepton universality

As it was done in the studies for the Phase-3 (for details see section 7.5), the ratio of the effective form factor $\mathcal{R}_{e\mu}$, obtained with the $\bar{p}p \rightarrow \ell^+\ell^-$ process with $\ell = e, \mu$, shall be also determined for the conditions which will be present at Phase-1 of $\bar{\text{P}}\text{ANDA}$. Since the cross section rises with decreasing values of beam momentum, the lowest value of $q^2 = 5.1 \text{ (GeV}/c)^2$ shall be considered in the following.

The estimation of the expected precision of this ratio requires the value of the effective form factor, which was obtained in the studies for the electron channel under the conditions of the $\bar{\text{P}}\text{ANDA}$ Phase-1 as $|F_p(\bar{p}p \rightarrow e^+e^-)| = 0.1403 \pm 0.0004$ by Ref. [155]. From that, the total relative uncertainty is obtained as

$$\Delta|F_p(\bar{p}p \rightarrow \mu^+\mu^-)|/|F_p(\bar{p}p \rightarrow e^+e^-)| \sim 2.02\%. \quad (8.1)$$

The ratio $\mathcal{R}_{e\mu}$ can be obtained as

$$\mathcal{R}_{e\mu} = 0.9971 \pm 0.0318, \quad (8.2)$$

which corresponds to a relative total uncertainty of

$$\Delta\mathcal{R}_{e\mu}/\mathcal{R}_{e\mu} \sim 3.2\%. \quad (8.3)$$

It can be concluded that $\bar{\text{P}}\text{ANDA}$ will be able to perform a test of a possible violation of the lepton universality with high precision, assuming that the QED radiative corrections are precisely known.

8.2.2 Study with EMC detector at $\overline{\text{PANDA}}$ Phase-1

The same set of variables and simulation strategy is used for this study, as they were chosen for the $\overline{\text{PANDA}}$ Phase-3 (which were presented in the previous chapters). In the PandaRoot detector setup, only the parts available at Phase-1 are present, including the full EMC detector. Loose cuts have been used in this study at $p_{beam} = 1.5 \text{ GeV}/c$ (details can be found in Tab. 6.6, Chapter 6). The total signal efficiency amounts to 31.5%, a background rejection factor of 1.22×10^{-5} was achieved. The physically expected number of signal events at $\mathcal{L} = 0.1 \text{ fb}^{-1}$ (corresponding to 4 months of pure data taking time) amounts $N(calc)(\overline{pp} \rightarrow \mu^+\mu^-) = 64072$ events. For the main background channel, the expected number of events is higher by a factor of 2×10^5 (since the expectation is $N(calc)(\overline{pp} \rightarrow \pi^+\pi^-) = 1.33 \times 10^{10}$ events). The expected signal-to-background (S-B) ratio is 1 : 8.

Table 8.1: Statistical and systematical contributions to the total relative uncertainty of $|G_E|$, $|G_M|$ and R for $\overline{\text{PANDA}}$ Phase-1 with full EMC detector and reduced detector setup. Loose cuts are used in the μ -selection. The systematic uncertainties are stemming from the chosen cuts (first value) and - in case of $|G_E|$ and $|G_M|$ - the uncertainty of the luminosity (second value). Also shown are the obtained values and uncertainties for the effective proton FF and the integrated cross section together with their systematic uncertainty from the luminosity measurement.

$R \pm \Delta R$	$\Delta R/R$ [%]
1.02 ± 0.21 (stat.)	20.1 (stat.) ± 4.3 (syst.)
<hr/>	
$ G_E \pm \Delta G_E $	$\Delta G_E / G_E $ [%]
0.142 ± 0.020 (stat.)	13.79 (stat.) ± 2.98 (syst.) ± 2.00 (syst.)
<hr/>	
$ G_M \pm \Delta G_M $	$\Delta G_M / G_M $ [%]
0.139 ± 0.009	6.49 (stat.) ± 1.32 (syst.) ± 2.00 (syst.)
<hr/>	
$ F_p \pm \Delta F_p $	$\Delta F_p / F_p $ [%]
0.1397 ± 0.0020 (stat.)	1.46 (stat.) ± 2.0 (syst.)
$\sigma \pm \Delta\sigma$ [pb]	$\Delta\sigma/\sigma$ [%]
636.28 ± 18.61 (stat.)	2.93 (stat.) ± 4.0 (syst.)

The results are summarized in Tab. 8.1. They show, that even with a luminosity of 0.1 fb^{-1} , which is smaller by a factor of 20 in comparison to the $\overline{\text{PANDA}}$ full design luminosity, a meaningful precision can be obtained for the proton FF's, the effective proton FF and the integrated signal cross section in a measurement of $\overline{pp} \rightarrow \mu^-\mu^-$. As a source of systematic error, the luminosity measurement was considered, which leads to the relative total uncertainty for $\Delta|F_p|/|F_p|$ [%] of 2.48%. At the same time, a relative total uncertainty of the integrated cross section of 4.96% is obtained. 20% of relative statistical uncertainty and 21% of relative total uncertainty are expected for the ratio R . The statistical relative uncertainty for $|G_E|$ is expected

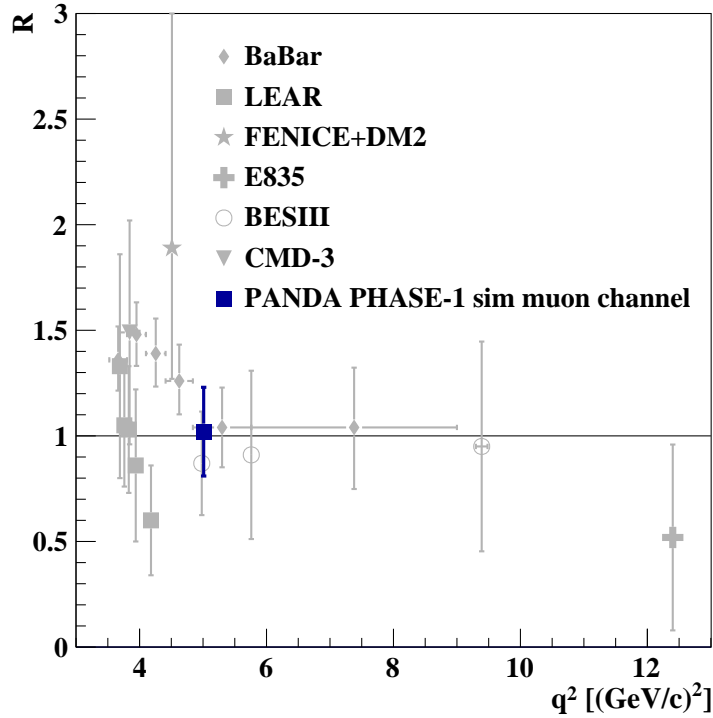


Figure 8.2: Expected uncertainty of the ratio $R = |G_E|/|G_M|$ for the $\bar{p}p \rightarrow \mu^+\mu^-$ channel at $q^2 = 5.1$ GeV/c obtained for the conditions of the $\bar{\text{P}}\text{ANDA}$ Phase-1 (blue square). $R = 1$ is assumed in this study. For a better visualization, the data points are shifted by $\delta q^2 = \pm 0.05$. Also shown are the currently existing data from Ref. [68] (squares), from Ref. [77] (diamonds), from Ref. [99] (star and cross), from Ref. [74] (open circles) and from Ref. [96] (down triangle).

to be measured with 13.8%, and in case of $|G_M|$ with 6.5%. For the total relative uncertainty of $|G_E|$, 14.3% are expected, and in case of $|G_M|$, 6.9% were achieved. At the same time, the effective proton FF is expected to be determined at $\bar{\text{P}}\text{ANDA}$ with a statistical relative uncertainty of 1.46%, the integrated cross section of the signal process with 2.93% at the lowest value of beam momentum. Figure 8.2 shows the result for the FF ratio R obtained with reduced luminosity of 0.1 fb^{-1} and with the reduced detector setup ($\bar{\text{P}}\text{ANDA}$ Phase-1). The comparison to the available world data shows, that the expected precision of R for $\bar{\text{P}}\text{ANDA}$ Phase-1 is comparable to the existing measurements.

Figure 8.3 (a) shows the corresponding angular distributions depending on $\cos(\theta_{CM})$ of the reconstructed physical signal sample (blue squares) and of the pion contamination (red dots and black open squares), which are used for the analysis. The right plot shows the angular distribution of the reconstruction efficiency corrected signal counts after background subtraction for negative charges (green squares) together with the fit function $f_2(x)$ (red line), which is used for the direct extraction of $R \pm \Delta R$ with a value of $\chi^2/\text{ndf} = 0.99$.

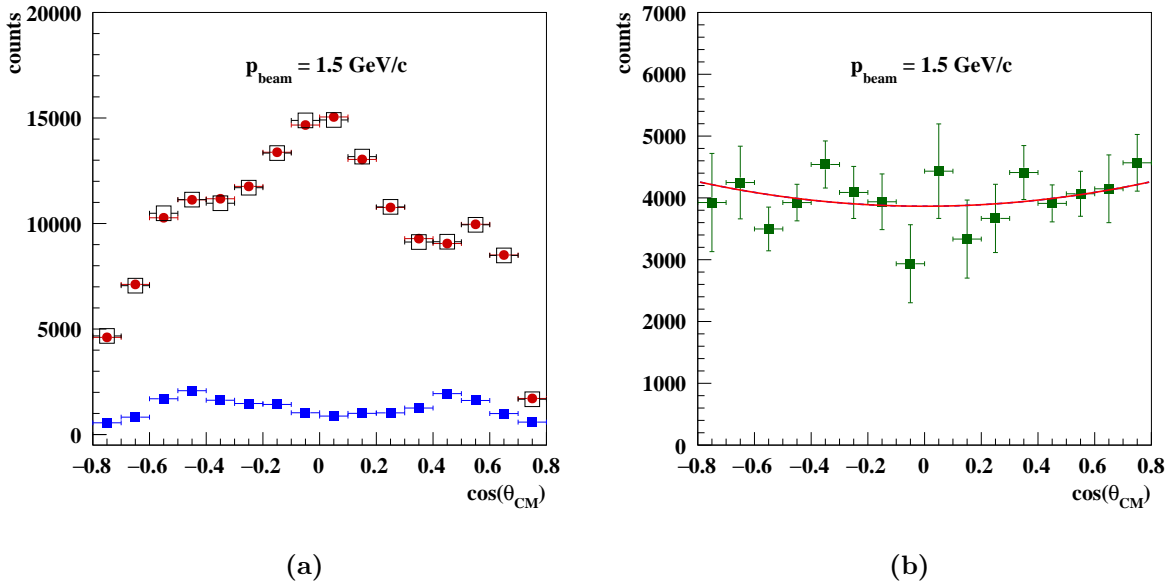


Figure 8.3: Simulation and analysis including the EMC detector at $\mathcal{L} = 0.1 \text{ fb}^{-1}$: (a) Reconstructed angular distributions after μ -selection of the signal sample with realistic statistics (blue squares) and the expected pion contamination (red dots and black open squares) used for further analysis. (b) Angular distribution of the reconstruction efficiency corrected signal counts after background subtraction for negative charges (squares). Also the fit function $f_2(x)$ (red line) is shown, which is used for a direct extraction of $R \pm \Delta R$.

8.2.3 Study without EMC detector at $\overline{\text{PANDA}}$ Phase-1

This simulation study was repeated without EMC detector material in the PandaRoot software. Hence, also all input variables related to the EMC have been removed for the training of the BDT and the following set is used:

- Path length inside iron absorber of the MS
- Number of fired detection layers of the MS
- Iron depth divided by initial momentum at layer zero of the MS
- Initial momentum of the charged particle track at zero bi-layer of the MS
- *Identification probability* for being a muon based on MS observables
- Mean energy loss per unit of length inside the STT
- Number of hits inside STT
- Invariant mass of the final state particles
- Sum of the polar production angles in center of mass system

New event samples were generated for the $\bar{p}p \rightarrow \mu^+\mu^-$ reaction and the $\bar{p}p \rightarrow \mu^+\mu^-$. The high statistics signal sample contains 4.69×10^6 events and is used to obtain the angular distribution of the signal reconstruction efficiency. The physical sample contains the number of physically expected signal events, which is 64,072 events in case of $\mathcal{L} = 0.1 \text{ fb}^{-1}$. The pion background sample contains 10^8 events.

The loose cuts at $p_{beam} = 1.5 \text{ GeV}/c$ (given in Tab. 6.6) are used in this study, with a changed cut on the BDT response ($\text{BDT} > 0.3259$). The new cut on the BDT response is used in order to match the total signal reconstruction efficiency of 31.5%, as it was obtained in the previous analysis using loose cuts.

The left plot in Figure 8.4 shows the corresponding reconstructed angular distributions of the physical signal sample (squares) and of the pion contamination (dots and open squares) used in this analysis. The right plot shows the angular distributions of the MC generated μ^- (squares), the reconstructed, μ^- -selected signal (up triangles) and the corresponding signal reconstruction efficiency (dots) obtained with the signal sample of high statistics.

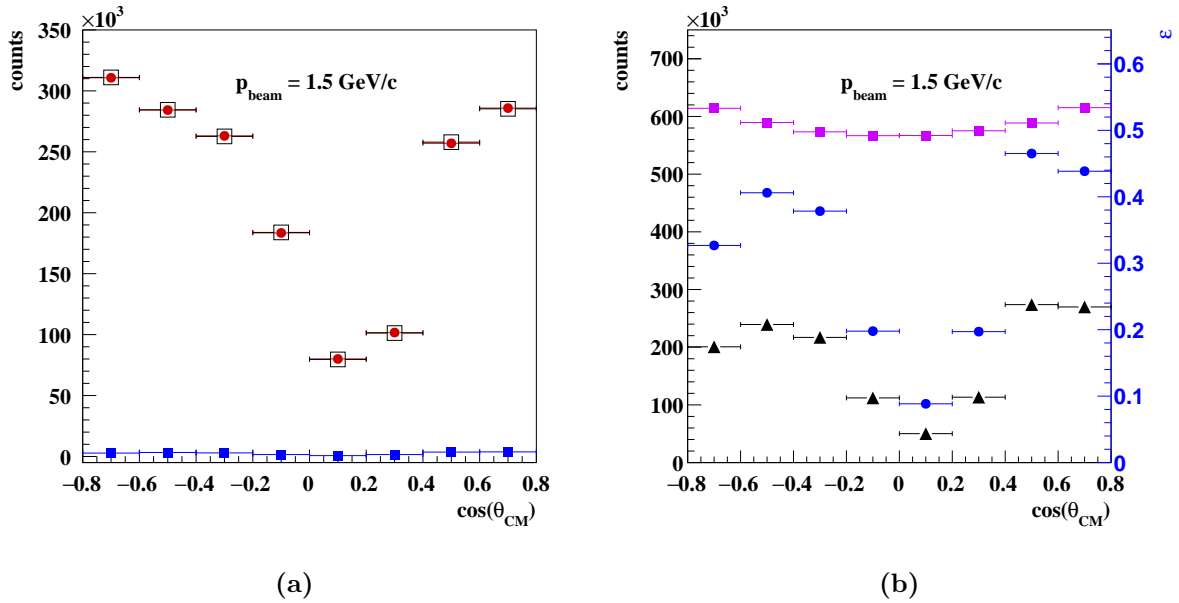


Figure 8.4: Simulation and analysis without EMC detector material at $\mathcal{L} = 0.1 \text{ fb}^{-1}$: (a) Reconstructed angular distributions of the physical signal sample (squares) and pion contamination (dots and open squares) used for the analysis. (b) Angular distributions of the MC generated μ^- (squares), the reconstructed, μ^- -selected signal from the high statistics sample (up triangles) and the corresponding signal reconstruction efficiency (dots).

8.2.4 Comparison with/without EMC detector

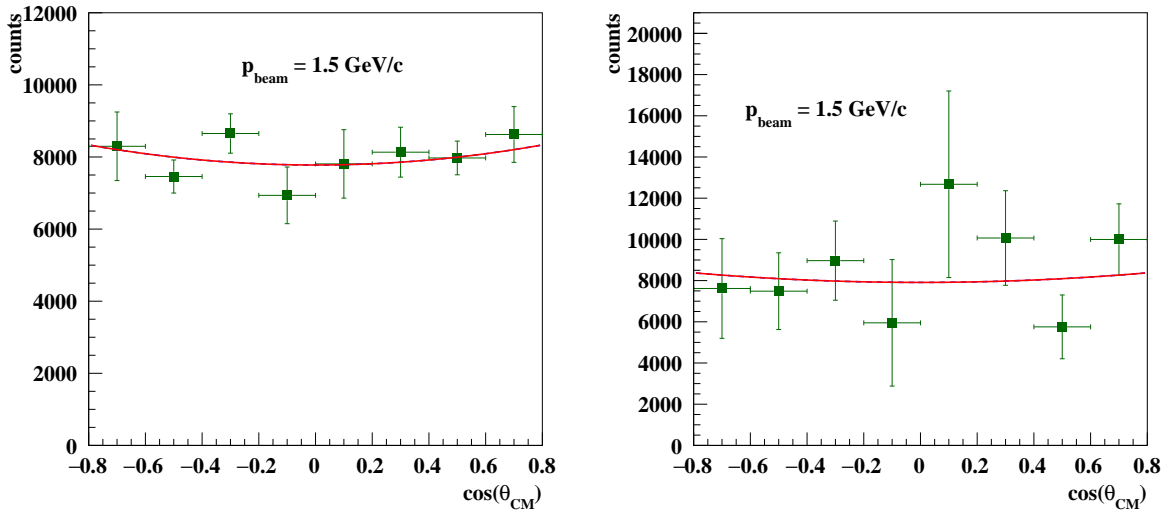
As it is expected, a clear deterioration of the rejection factor for the final states from $\bar{p}p \rightarrow \pi^+\pi^-$ is observed by excluding the EMC in front of the Muon System. The rejection factor is

increased by almost a factor of 10, from $1.2 \cdot 10^{-5}$ up to $1.3 \cdot 10^{-4}$. This leads to a clearly worse value of the expected signal-to-background ratio of 1:88 for the study without EMC material. In the following, 8 histogram bins are used for both cases (with/without EMC) due to the strong statistical fluctuations in the reconstructed and efficiency corrected signal data. A strong deterioration of the extraction precision of the FF's is visible, when the results of R , $|G_E|$ and $|G_M|$ (given in Tab. 8.2) are compared: by excluding the EMC detector material, the statistical relative uncertainty of the ratio R strongly deteriorates from 21% to 60%. The reduced χ^2 obtained by fitting the distributions shown in Fig. 8.5 is $\chi^2/\text{ndf} = 1.07$ in the first case, and in the second case, it is $\chi^2/\text{ndf} = 1.01$. The extracted value of the statistical relative uncertainty of $|G_E|$ increases from 13.8% to 40.2%, and for $|G_M|$ from 7.2% to 19.9%. From these results

Table 8.2: Comparison between the extracted values of $R \pm \Delta R$, and the FF's based on the full analysis with / respectively without EMC detector. The result of $R \pm \Delta R$ corresponds to the fit function $f_2(x)$. The shown uncertainties are of statistical nature.

with EMC material			without EMC material		
R	ΔR	$\frac{\Delta R}{R} [\%]$	R	ΔR	$\frac{\Delta R}{R} [\%]$
1.07	0.22	21	1.09	0.65	60
$ G_E $	$\Delta G_E $	$\frac{\Delta G_E }{ G_E } [\%]$	$ G_E $	$\Delta G_E $	$\frac{\Delta G_E }{ G_E } [\%]$
0.146	0.020	13.8	0.149	0.060	40.2
$ G_M $	$\Delta G_M $	$\frac{\Delta G_M }{ G_M } [\%]$	$ G_M $	$\Delta G_M $	$\frac{\Delta G_M }{ G_M } [\%]$
0.137	0.010	7.2	0.137	0.027	19.9

it becomes clear, that the EMC detector material is essential for an additional μ/π separation before the particles reach the Muon System. A successful signal/background separation requires the detector material of the EMC, and if it was not available, a similar material as a replacement for the missing EMC parts would be required in front of the Muon System.



(a) Study with EMC detector material

(b) Study without EMC detector material

Figure 8.5: Comparison between the reconstructed, signal efficiency corrected angular distributions at $p_{beam} = 1.5 \text{ GeV}/c$ at $\mathcal{L} = 0.1 \text{ fb}^{-1}$ (a) including variables from EMC and (b) a scenario, where no EMC is present in the detector model at all. The larger error bars and stronger fluctuations of the data points (right figure) are due to the missing EMC material. When present, the EMC material acts as an additional muon filtering element in front of the Muon System.

Chapter 9

Conclusions and Outlook

The possibility to measure the time-like electromagnetic proton FF's in annihilation processes of $\bar{p}p \rightarrow \mu^+\mu^-$ at the future \bar{P} ANDA experiment was investigated in this work. In contrast to the $\bar{p}p \rightarrow e^+e^-$ process, which will be also used at \bar{P} ANDA for the extraction of time-like FF's, this channel has the advantage, that radiative corrections due to final state radiations are expected to be very small, due to the high rest mass of the muon in comparison to the electron mass. Measuring both channels allows to test the radiative corrections. It will be the first time, that final state muon pairs are used to extract the time-like FF's of the proton. Furthermore, the measurement of both electron and muon channel at \bar{P} ANDA will allow for a sensitive test of lepton universality based on the determination of the effective FF of the proton with both channels.

The feasibility studies for the measurement of time-like electromagnetic proton FF's with the $\bar{p}p \rightarrow \mu^+\mu^-$ process at the future \bar{P} ANDA Experiment are based on Monte-Carlo simulation and full reconstruction for the signal and all relevant background channels. The most challenging background process is $\bar{p}p \rightarrow \pi^+\pi^-$ due to the fact, that the rest mass of μ and π are very similar which complicates the signal-background separation drastically.

The Monte Carlo simulation utilizes detailed detector geometries and materials together with (in most of the cases) realistic detector response, tracking performance and particle identification. In particular, the geometries and digitization of the Muon System, which constitutes the most important detector system in this feasibility study, are in a preliminary stage. Currently, prototype measurements are in progress which will be the starting point of further improvements concerning the PandaRoot software Muon System implementation. Also the PID algorithm, which is based on simple cuts on observables from the Muon System detector, can be improved allowing an even more efficient μ/π separation in the future.

The advanced event classification, which is used in this work, is based on a multivariate analysis and allows to optimize the signal-background separation. Methods of boosted decision trees improve the classification performance so that expected signal-to-background ratios up to 1:4 could be achieved at the lowest value of beam momentum at \bar{P} ANDA, which is $p_{beam} = 1.5$

GeV/c. For the studies dedicated to the $\bar{\text{P}}\text{ANDA}$ Phase-3, the calculation of the expected signal (background) counts is based on a time-integrated luminosity of $\mathcal{L} = 2 \text{ fb}^{-1}$ corresponding to the original $\bar{\text{P}}\text{ANDA}$ design luminosity at a pure data taking period of 4 months with 100% efficiency.

The expected pion contamination in the μ -selected data originates from $\bar{p}p \rightarrow \pi^+\pi^-$ and contains also muons from pion decay $\pi \rightarrow \mu\nu$. A background subtraction will be applied in the analysis of the future experimental data, which removes the full residual pion contamination from the μ -selected data, also including secondary muons from pion decay and will allow to achieve a high signal purity.

The effect of the background subtraction on the precision of the extracted values of FF was included in this feasibility study. In order to obtain angular distributions of the expected pion contamination, a method was developed to obtain distributions with the expected statistics. The influence of the angular shape on the extracted results was studied. It can be concluded, that the shape of the pion contamination distribution has no significant influence on the results in this work.

It could be shown, that a sufficient rejection of other relevant background channels as e.g. $\bar{p}p \rightarrow \pi^+\pi^-\pi^0$, $\bar{p}p \rightarrow K^+K^-$, $\bar{p}p \rightarrow K^+K^-\pi^0$ or $\bar{p}p \rightarrow \pi^0\pi^0$ will be possible with the μ -selection.

The final results were obtained under the conditions of $\bar{\text{P}}\text{ANDA}$ Phase-3, taking into account a time-integrated luminosity of $\mathcal{L} = 2 \text{ fb}^{-1}$ corresponding to the original $\bar{\text{P}}\text{ANDA}$ design peak luminosity of $2 \times 10^{32} \text{ cm}^{-2} \text{ s}^{-1}$ and using the full $\bar{\text{P}}\text{ANDA}$ detector setup. The results are summarized in Tab. H.1. Also the corresponding values of signal efficiency and the background rejection factors for the considered values of beam momentum are listed. It could be shown, that the measurement of time-like electromagnetic proton FF's at the future $\bar{\text{P}}\text{ANDA}$ Experiment will be possible with a small relative statistical uncertainty on the extracted value of the FF ratio R between 5% and 37% at $\bar{\text{P}}\text{ANDA}$ Phase-3. The individual extraction of $|G_E|$ and $|G_M|$ is expected to be possible with small relative statistical uncertainties in the range of 3.2%–23.9% for $|G_E|$, and in the range of 1.6%–9.8% for $|G_M|$.

A discussion of possible systematic error sources was performed and their contribution to the relative total uncertainties of the FF's and R was calculated. While at lower beam momenta, the statistical and systematic error sources contribute more or less equally to the total relative uncertainty of the FF's, for higher beam momenta the relative total uncertainty is dominated by the statistical fluctuations of the $\bar{p}p \rightarrow \mu^+\mu^-$ signal process, due to the decreasing signal cross section with increasing beam momentum.

Radiative corrections in the signal $\bar{p}p \rightarrow \mu^+\mu^-$ are expected to be small compared to $\bar{p}p \rightarrow e^+e^-$. The largest contribution to the radiative corrections is expected to come from final state radiation. The influence of final state radiation on the extracted values of FF's and their uncertainties

was studied using the PHOTOS software package for the conditions of $\overline{\text{PANDA}}$ Phase-3. The results of this study show, that final state radiation has a small influence on the extracted FF values and their uncertainties. The detailed calculation of the full radiative corrections for the signal channel must be performed in the future.

A dedicated feasibility study was performed for the beginning phase of the $\overline{\text{PANDA}}$ Experiment ($\overline{\text{PANDA}}$ Phase-1), taking into account the reduced luminosity (here assumed as $0.1 \times 10^{32} \text{cm}^{-2} \text{s}^{-2}$, which corresponds to $\mathcal{L} = 0.1 \text{fb}^{-1}$) and using the reduced $\overline{\text{PANDA}}$ detector start setup at Phase-1. Since the variables used in this study are not stemming from the missing sub-detectors in $\overline{\text{PANDA}}$ Phase-1, the most critical point is the reduced signal statistics which leads to larger statistical uncertainties of the extracted FF values in comparison to the results obtained at $\mathcal{L} = 2 \text{fb}^{-1}$. Relative total uncertainties of R of 21%, for $|G_E|$ of 14.3% and for $|G_M|$ of 6.9% are achieved. The effective proton FF was obtained with a relative statistical uncertainty of 1.46%, as well as the integrated signal cross section with 2.93%. Despite the lower signal statistics during Phase-1, these quantities are expected to be measured with meaningful precision.

Since it is possible, that the EMC will not be fully present at the beginning of Phase-1, the importance of the EMC detector material was studied by comparing the scenario with / without the EMC. The relative uncertainty of R increases from 21% up to 60%, due to the missing EMC material in front of the Muon System. Also the extracted uncertainties of the FF's change drastically from 13.8% to 40.2% for $|G_E|$ and from 7.2% to 19.9% for $|G_M|$. The results show, that the presence of the EMC detector material is essential for the μ/π separation and therefore for the measurement of the proton FF from $\bar{p}p \rightarrow \mu^+\mu^-$ with a meaningful precision.

The feasibility studies, which have been presented in this work, show that the individual extraction of the time-like electromagnetic proton FF's, $|G_E|$ and $|G_M|$ will be possible with high precision at $\overline{\text{PANDA}}$ based on the $\bar{p}p \rightarrow \mu^+\mu^-$ signal process. This measurement using muons in the final state will be unique. Under the condition, that the radiative corrections and all systematic uncertainties are well-known for both the $\bar{p}p \rightarrow \mu^+\mu^-$ and also the $\bar{p}p \rightarrow e^+e^-$ channel, the comparison of the effective FF obtained with both channels could serve as a test of the lepton universality. Using the obtained values of the effective FF for both signal channels, the ratio $\mathcal{R}_{e\mu} = \frac{|F_p(\bar{p}p \rightarrow \mu^+\mu^-)|}{|F_p(\bar{p}p \rightarrow e^+e^-)|}$ could be determined as $\Delta\mathcal{R}_{e\mu}/\mathcal{R}_{e\mu} \sim 3.2\%$ (at $\overline{\text{PANDA}}$ Phase-1) at the antiproton beam momentum of 1.5 GeV/c and $\Delta\mathcal{R}_{e\mu}/\mathcal{R}_{e\mu} \sim 2.9\%$ (at $\overline{\text{PANDA}}$ Phase-3) at the antiproton beam momentum of 1.7 GeV/c. From these numbers, it can be concluded that $\overline{\text{PANDA}}$ will provide a sensitive test of a possible violation of the lepton universality between e and μ .

Appendix A

Multivariate Classification Methods

For the search of the best performing classifier in this work, several methods of multivariate data classification are compared. The Root-implemented software package TMVA provides different kinds of classification algorithms and software for their evaluation and application on the individual classification problem.

Besides Boosted Decision Trees (BDT), which are chosen in this work due to their very good performance, Artificial Neural Networks show a quite similar performance. In contrast to the BDT, the ANN has a long evaluating time, which increases when larger training samples are chosen. As the BDT, they are robust against overtraining. Furthermore, methods of linear discriminant analysis (Fisher) have been tested, but can not achieve the good performance of the BDT and ANN in this work. In the following, the methods are briefly described.

A.1 Fisher discriminants (linear discriminant analysis)

The method of Fisher discriminants [161] uses an event selection, which is performed in a transformed variable space for the input variables. In this variable space, zero linear correlations between the input variables is achieved by distinguishing the mean values of the signal and the background distributions. In the linear discriminant analysis, an axis is determined in the correlated hyperspace of the input variables so that the projection of the signal and background events upon this axis are separated as far as possible from each other, while the events of the same class (either signal or background) are confined in a close vicinity. In case that the mean values of the samples are the same, no discrimination can be achieved, even if the corresponding distribution shapes are different. In this case, this method can not be used.

A.2 Artificial Neural Networks

An Artificial Neural Network (ANN) is a collection of connected nodes (so-called *artificial neurons*) which are inspired from biological neural networks. Each of these neurons is able to process an incoming signal and transmit it to another neuron, which is connected to it. Figure A.1 shows the propagation scheme of an ANN. The neurons are arranged in layers, with an input layer and an output layer. The input layer usually possesses as many neurons, as input variables

are used. In the case of Multilayer Perceptrons (MLP), several hidden layers are located in between the input and output layer, where the user can choose the number of hidden layers. Usually the incoming signal is a real number and the processing at a certain node is based on a function (the so-called *activation function*). A node from a hidden or output layer receives a weighted sum of the output of the previous layer, which is given as input to the activation function, which can be either zero (corresponding to a deactivated neuron), a linear function or a non-linear function (as e.g. a sigmoid function). The weights are adjusted during the training step of the ANN so that an error function (containing both the Monte-Carlo truth information of the signal and background events and the training events together with the weights) is minimized, which allows to achieve an optimal classification performance of the ANN. In this work, the artificial neural networks could not achieve the very good performance of Boosted Decision Trees concerning μ/π separation.

TMVA offers several kinds of artificial neural networks (ANN). All of them are Multilayer Perceptrons (MLP), which are feed-forward networks following the propagation schema in Fig. A.1.

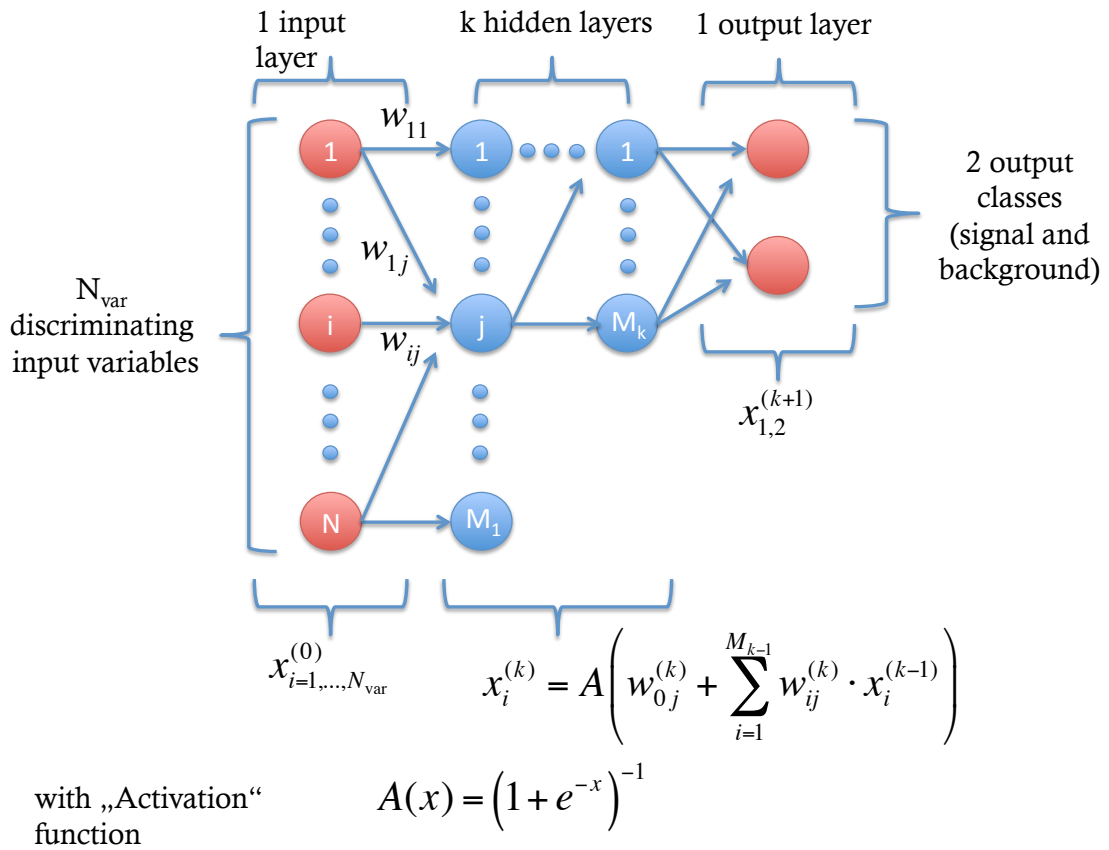
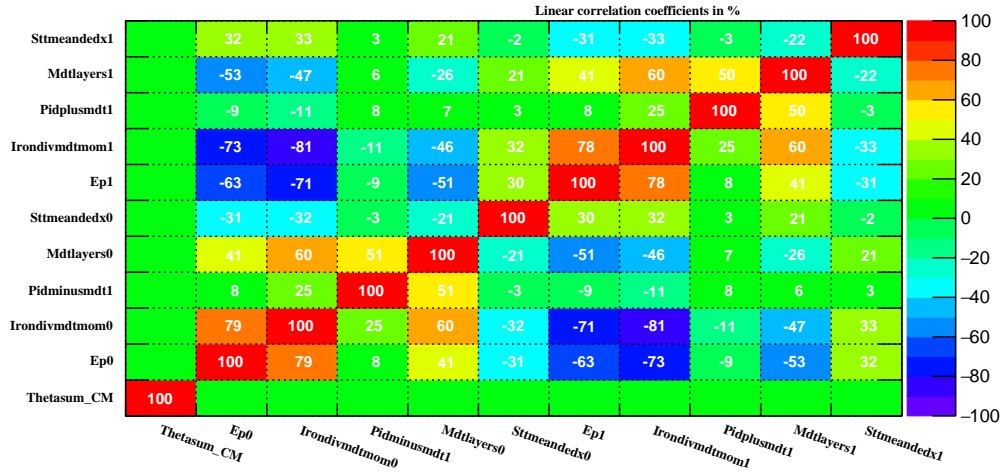


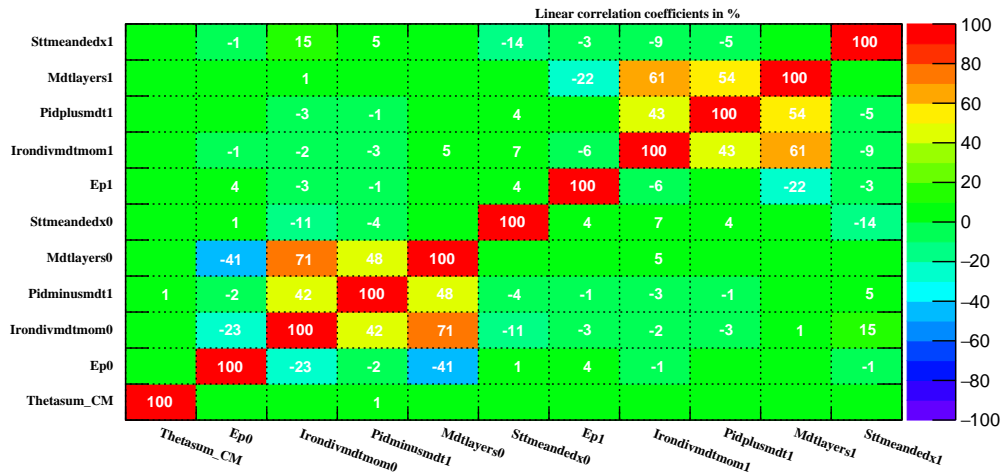
Figure A.1: Working principle of a Multilayer Perceptron, which is a feed-forward network of connected neurons [147]. The neurons are arranged in layers and can be activated with an activation function. The Multilayer Perceptron can be seen as a non-linear mapping from an n-dimensional variable space (n : number of input variables) to a one-dimensional space of output variables in the case of classification problems.

Appendix B

Training of the Boosted Decision Trees at $p_{beam} = 3.3 \text{ GeV}/c$

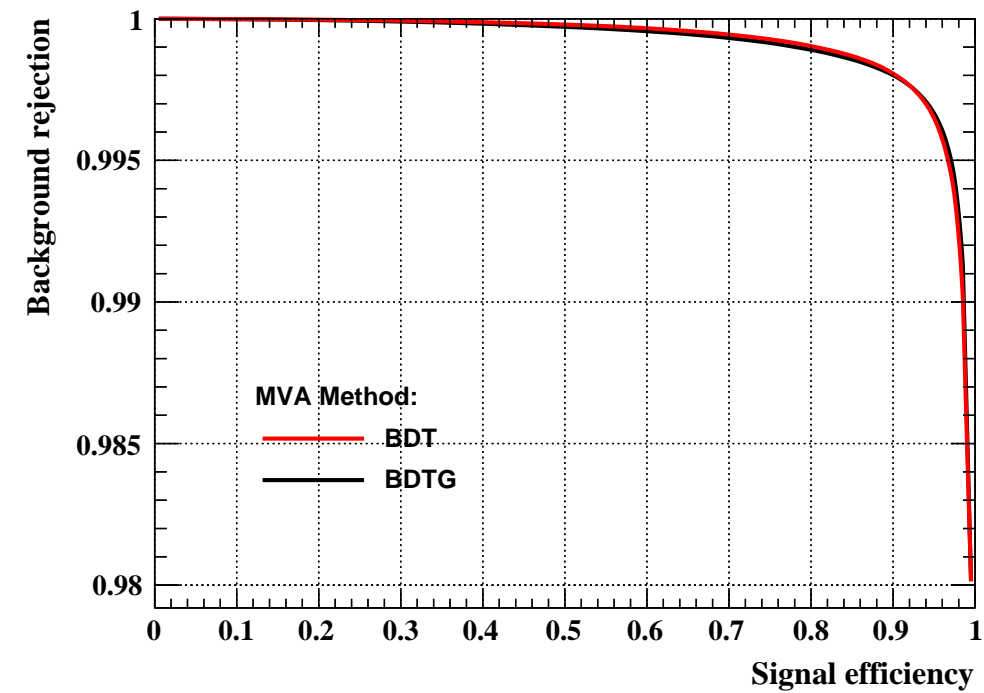


(a)

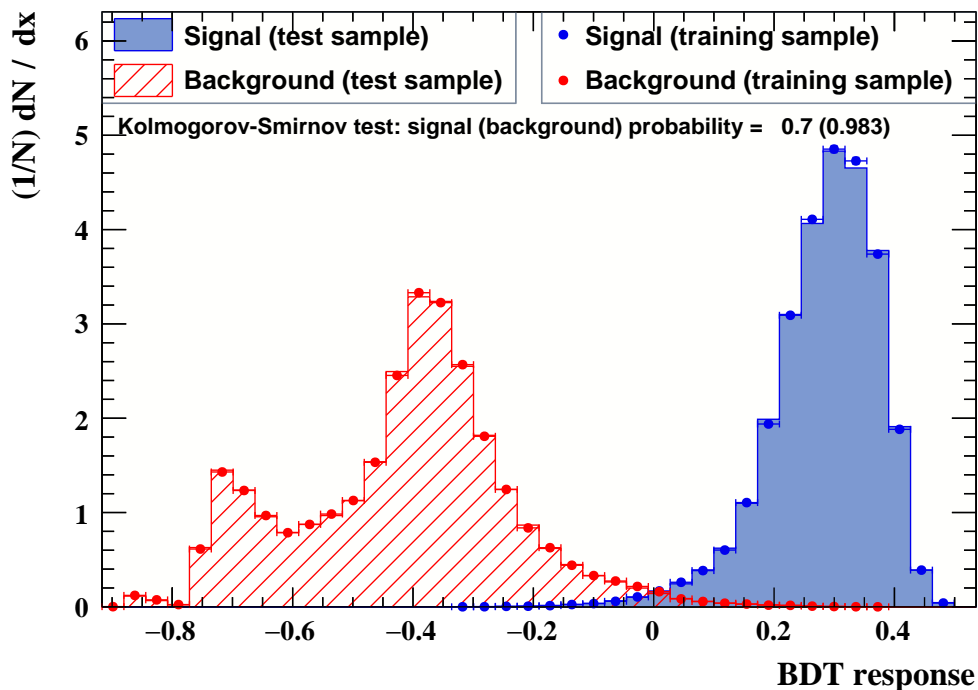


(b)

Figure B.1: Linear correlation coefficients [%] between the input variables for MVA at $p_{beam} = 3.3 \text{ GeV}/c$ for the signal (a) and the background (b). The input variables are not strongly linearly correlated, so that each of the variables provides helpful information for the μ/π separation.



(a)



(b)

Figure B.2: (a) Receiver operating characteristics for Boosted Decision Trees (BDT, BDTG), which show a very similar performance at $p_{beam} = 3.3 \text{ GeV}/c$. (b) A Kolmogorov-Smirnov Test is used for overtraining check for the BDT algorithm. The evaluation of this test can be seen at the high values of signal (background) probability (p-value), which indicates that no overtraining has occurred during the training of the BDT.

Appendix C

Shape extraction of the residual pion distribution after μ -selection

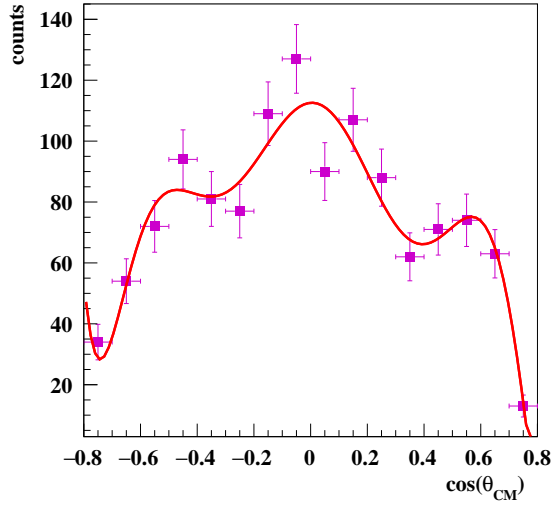
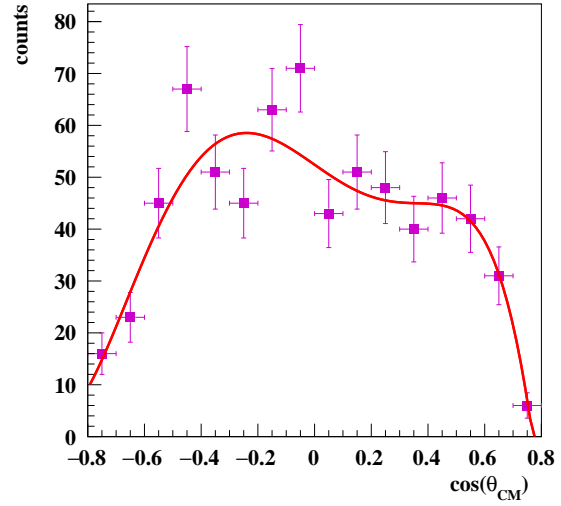
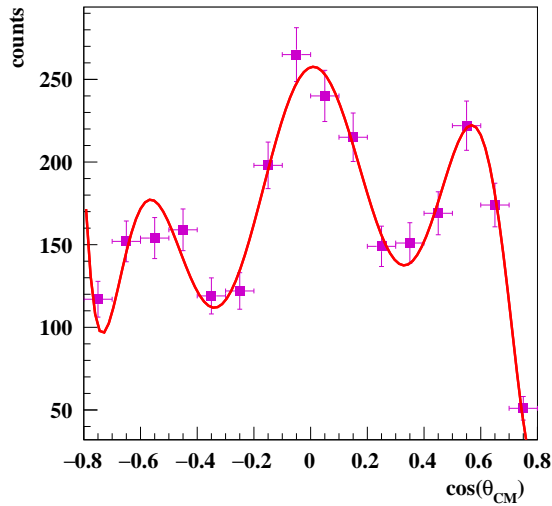
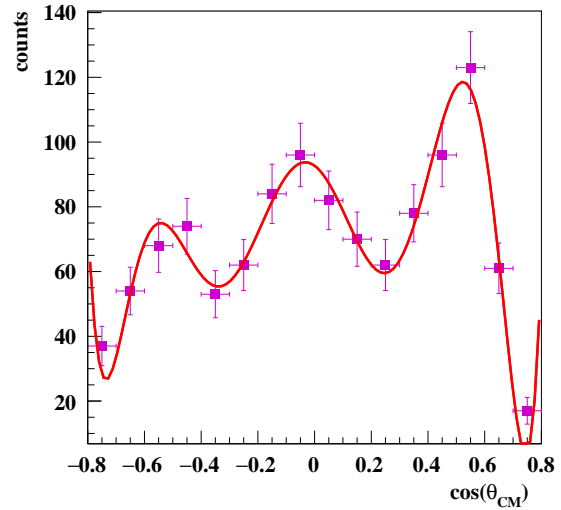
(a) $p_{beam}=1.5$ GeV/ c , "loose cuts"(b) $p_{beam}=1.5$ GeV/ c , "medium cuts"(c) $p_{beam}=1.7$ GeV/ c , "very loose cuts"(d) $p_{beam}=1.7$ GeV/ c , "loose cuts"

Figure C.1: Residual pion background distribution after μ -selection, which is used for a shape extraction with a fit function (red line). For the fit, polynomials of the 7-th order or higher have been used. The obtained curves are used to generate realistic pion contamination distributions for the background subtraction in the analysis.

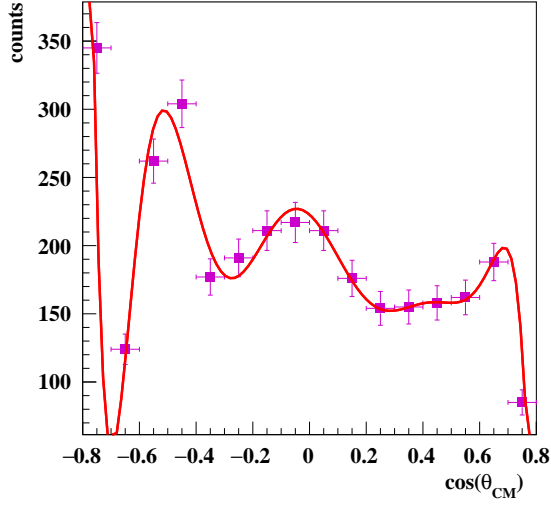
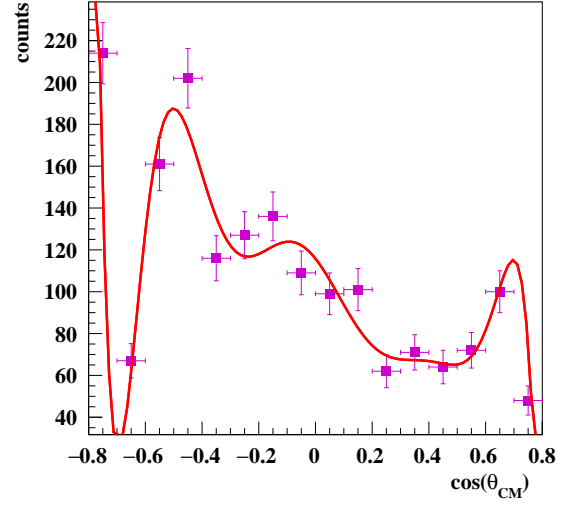
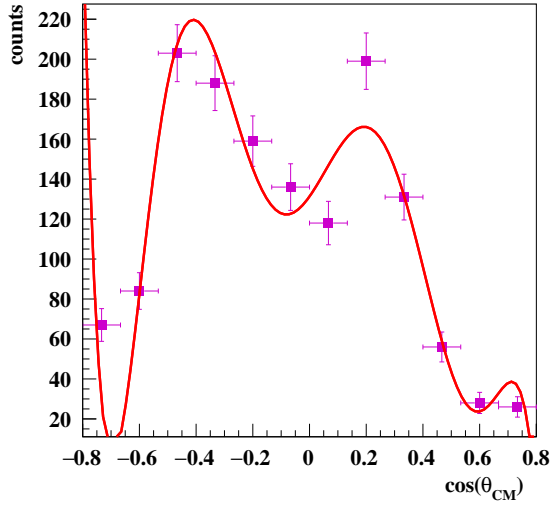
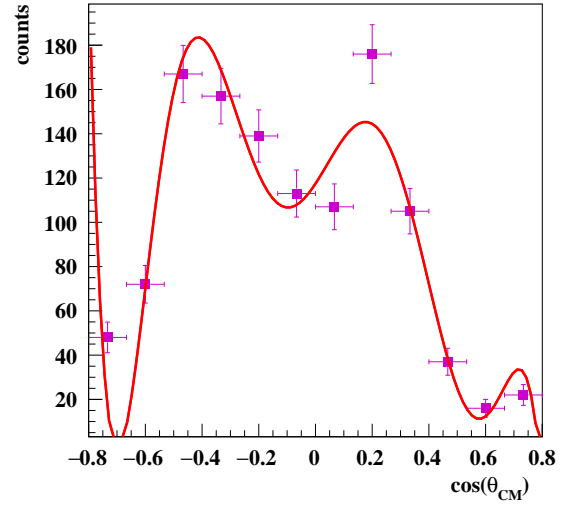
(a) $p_{beam}=2.5$ GeV/ c , "medium cuts"(b) $p_{beam}=2.5$ GeV/ c , "tight cuts"(c) $p_{beam}=3.3$ GeV/ c , "loose cuts"(d) $p_{beam}=3.3$ GeV/ c , "medium cuts"

Figure C.2: Residual pion background distribution after μ -selection, which is used for a shape extraction with a fit function (red line). For the fit, polynomials of the 7-th order or higher have been used. The obtained curves are used to generate realistic pion contamination distributions for the background subtraction in the analysis.

Appendix D

Angular distributions of μ -selected signal counts and pion contamination

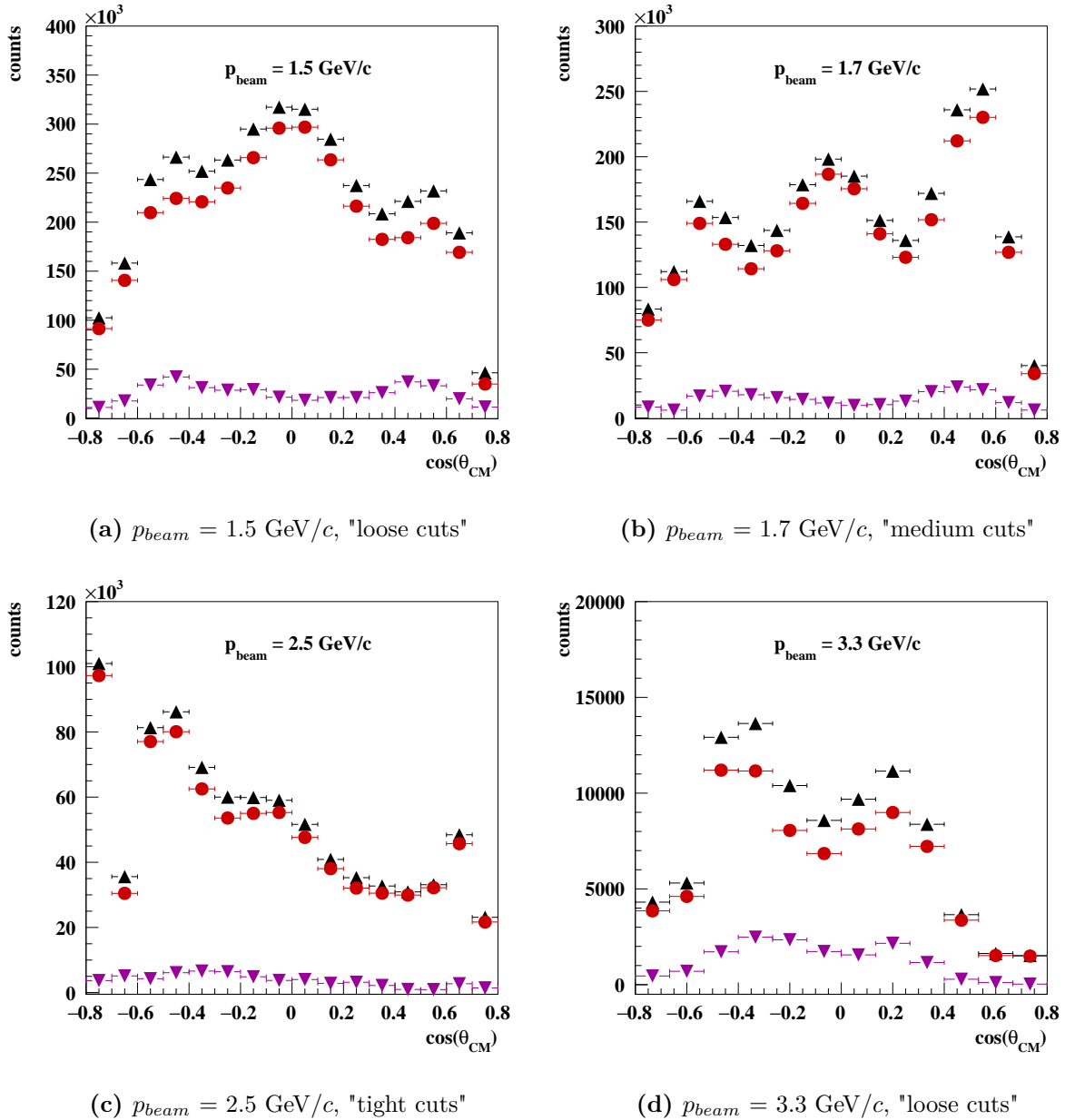


Figure D.1: Angular distributions of the selected data (black triangles up), which consist of the μ -selected signal data from $\bar{p}p \rightarrow \mu^+\mu^-$ plus the expected pion contamination. Also shown are the distributions of the statistically independent pion contamination (red dots), which will be measured and reconstructed in the experiment later. Selected signal data after the background subtraction are shown as well (magenta triangles down), which contain the statistical fluctuations of the pion contamination.

Appendix E

Influence of the shape of the pion contamination distribution

Figure E.1 illustrates the angular dependence of the reconstructed selected and efficiency corrected signal counts after background subtraction at the considered beam momenta of 1.5, 1.7, 2.5 and 3.3 GeV/ c . The fit function $f_2(x)$ is shown as well (red line), which is used for the direct extraction of R and its uncertainty. The fit is performed by computing the integral of the function in the bin, divided by the bin volume, instead of using the fit function value at the bin center.

Fit function $f_2(x)$ is used to fit the efficiency corrected signal distributions after background subtraction. The obtained values of R and their corresponding uncertainties at the considered beam momenta are summarized in Tab. E.1. The results at all considered cut configurations are compatible within one sigma and very well consistent with the assumption of $R = 1$. The statistical uncertainty at lower values of beam momentum is mostly caused by the statistical fluctuations of the background, which remain in the reconstructed signal data after the subtraction of the pion contamination. When going to higher values of beam momentum, the statistical uncertainty increases strongly due to the decreasing signal statistics.

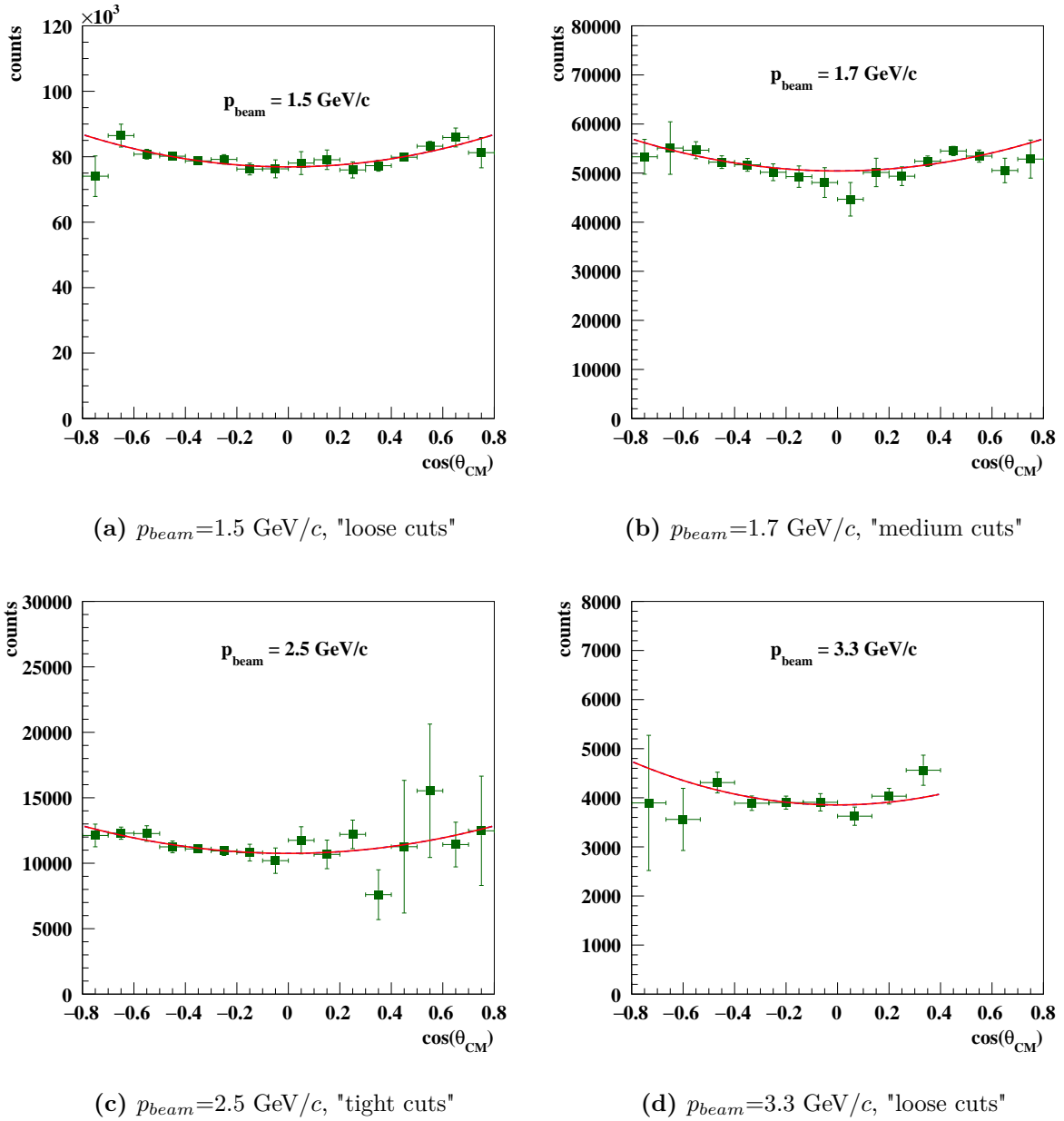


Figure E.1: Reconstructed and efficiency corrected signal angular distribution after background subtraction (green squares). The fit function $f_2(x)$ (red line) is shown, which is used to extract the values of $R \pm \Delta R$ directly. (a): 1.5 GeV/c "loose cuts", (b): 1.7 GeV/c "medium cuts", (c): 2.5 GeV/c "tight cuts" and (d): 3.3 GeV/c "loose cuts".

Table E.1: The result $R \pm \Delta R$ is obtained with the fit function $f_2(x)$, where R is a free fit parameter and thus can be extracted directly. The event generator uses always $R = 1$ as an input for the generation of the signal events. The results, which are obtained with the final cut configurations, are highlighted in bold italic font.

	$p_{beam} = 1.5 \text{ GeV}/c$				$p_{beam} = 1.7 \text{ GeV}/c$			
	R	ΔR	$\frac{\Delta R}{R}[\%]$	χ^2/ndf	R	ΔR	$\frac{\Delta R}{R}[\%]$	χ^2/ndf
Very loose cuts	1.00	0.05	5	0.96	1.01	0.08	8	1.48
Loose cuts	0.99	0.05	5	0.75	1.05	0.08	8	1.64
Medium cuts	0.99	0.06	6	0.67	1.01	0.08	8	1.80
Tight cuts	0.98	0.06	6	0.62	1.01	0.08	8	1.80
Very tight cuts	0.99	0.07	7	0.76	1.00	0.09	9	1.80
	$p_{beam} = 2.5 \text{ GeV}/c$				$p_{beam} = 3.3 \text{ GeV}/c$			
	R	ΔR	$\frac{\Delta R}{R}[\%]$	χ^2/ndf	R	ΔR	$\frac{\Delta R}{R}[\%]$	χ^2/ndf
Very loose cuts	0.94	0.18	19	0.78	0.84	0.30	35	0.80
Loose cuts	0.97	0.14	15	0.44	1.04	0.29	28	1.21
Medium cuts	1.08	0.13	12	0.29	1.02	0.31	31	0.98
Tight cuts	1.01	0.12	12	0.58	0.96	0.32	33	0.72
Very tight cuts	1.10	0.13	11	0.52	1.13	0.35	31	0.76

Simultaneous extraction of $|G_E|$ and $|G_M|$ and their uncertainties

The simultaneous extraction of the FF's was done by fitting the same distributions with the fit function $f_1(x)$. The form factor ratio $R = 1$ is assumed for the event generation together with the parameterization for $|G_M|$ given in Eq. 3.57 from Ref. [54].

The results are shown in Tab. E.2 for $p_{beam} = 1.5, 1.7, 2.5$ GeV/ c and $p_{beam} = 3.3$ GeV/ c .

Table E.2: For the simultaneous extraction of $|G_E|$ and $|G_M|$ with their statistical uncertainties, the fit function $f_1(x)$ is used at each considered value of beam momentum ($p_{beam} = 1.5, 1.7, 2.5$ and 3.3 GeV/ c). The final cut configuration is highlighted in italic bold font.

<i>$p_{beam} = 1.5$ GeV/c</i>						
$ G_M $ (model) = 0.1403	$ G_E $	$\Delta G_E $	$\frac{\Delta G_E }{ G_E }$ [%]	$ G_M $	$\Delta G_M $	$\frac{\Delta G_M }{ G_M }$ [%]
Very loose cuts	0.140	0.005	3.6	0.140	0.002	1.7
Loose cuts	<i>0.138</i>	<i>0.005</i>	<i>3.8</i>	<i>0.141</i>	<i>0.002</i>	<i>1.7</i>
Medium cuts	0.140	0.005	3.9	0.140	0.003	1.9
Tight cuts	0.138	0.006	4.4	0.142	0.003	2.0
Very tight cuts	0.140	0.006	4.6	0.141	0.003	2.1
<i>$p_{beam} = 1.7$ GeV/c</i>						
$ G_M $ (model) = 0.1213	$ G_E $	$\Delta G_E $	$\frac{\Delta G_E }{ G_E }$ [%]	$ G_M $	$\Delta G_M $	$\frac{\Delta G_M }{ G_M }$ [%]
Very loose cuts	0.122	0.007	5.3	0.121	0.003	2.6
Loose cuts	0.125	0.006	5.0	0.119	0.003	2.6
Medium cuts	<i>0.123</i>	<i>0.007</i>	<i>5.7</i>	<i>0.122</i>	<i>0.004</i>	<i>2.9</i>
Tight cuts	0.123	0.007	5.8	0.122	0.003	2.6
Very tight cuts	0.123	0.008	6.2	0.123	0.003	2.7
<i>$p_{beam} = 2.5$ GeV/c</i>						
$ G_M $ (model) = 0.0703	$ G_E $	$\Delta G_E $	$\frac{\Delta G_E }{ G_E }$ [%]	$ G_M $	$\Delta G_M $	$\frac{\Delta G_M }{ G_M }$ [%]
Very loose cuts	0.068	0.010	14.8	0.073	0.004	4.8
Loose cuts	0.069	0.008	11.1	0.072	0.003	3.8
Medium cuts	0.075	0.006	8.5	0.067	0.003	3.8
Tight cuts	<i>0.072</i>	<i>0.006</i>	<i>8.8</i>	<i>0.071</i>	<i>0.002</i>	<i>4.8</i>
Very tight cuts	0.076	0.006	8.0	0.069	0.002	3.5
<i>$p_{beam} = 3.3$ GeV/c</i>						
$ G_M $ (model) = 0.0436	$ G_E $	$\Delta G_E $	$\frac{\Delta G_E }{ G_E }$ [%]	$ G_M $	$\Delta G_M $	$\frac{\Delta G_M }{ G_M }$ [%]
Very loose cuts	0.038	0.011	28.1	0.046	0.003	7.1
Loose cuts	<i>0.045</i>	<i>0.009</i>	<i>19.7</i>	<i>0.043</i>	<i>0.003</i>	<i>8.0</i>
Medium cuts	0.044	0.010	22.0	0.043	0.004	8.5
Tight cuts	0.043	0.010	24.1	0.044	0.004	8.4
Very tight cuts	0.048	0.010	20.8	0.042	0.004	10.1

Calculation of $R \pm \Delta R$ from the FF's

An alternative way to obtain the ratio R and its uncertainty, is the calculation from the extracted values for $|G_E|$ and $|G_M|$, using the free fit parameters $P_{0,1}$ of the fit function $f_1(x)$:

$$R_{calc} = \sqrt{\frac{P_1}{P_0}} \quad (\text{E.1})$$

Since the fit parameters are correlated, the calculation needs to include also their covariance $cov(P_0, P_1)$. The error on R can be calculated from

$$\Delta R = \sqrt{\Delta P_0^2 \cdot \left(\frac{\partial R}{\partial P_0}\right)^2 + \Delta P_1^2 \cdot \left(\frac{\partial R}{\partial P_1}\right)^2 + 2 \cdot \left(\frac{\partial R}{\partial P_0}\right) \left(\frac{\partial R}{\partial P_1}\right) \cdot cov(P_0, P_1)} \quad (\text{E.2})$$

As an example, several calculated values of $R_{calc} \pm \Delta R_{calc}$ at different beam momenta are listed in Tab. E.3 and compared to the values $R_{direct} \pm \Delta R_{direct}$. The values of R_{direct} which were directly extracted using $f_2(x)$. As it is expected, the values of $R \pm \Delta R$ obtained with both methods, agree with each other.

Table E.3: Comparison of the results $R \pm \Delta R$ for the example of very loose and medium cuts at 1.5 and 1.7 GeV/c: the values $R_{direct} \pm \Delta R_{direct}$ are directly extracted with the fit function $f_2(x)$, where R is a free fit parameter. $R_{calc} \pm \Delta R_{calc}$ represents the results obtained with fit function $f_1(x)$, where the ratio is evaluated from the (correlated) fit parameters, P_0 and P_1 .

	$p_{beam} = 1.5 \text{ GeV}/c$				$p_{beam} = 1.7 \text{ GeV}/c$			
R (assumption) = 1	R_{direct}	ΔR_{direct}	R_{calc}	ΔR_{calc}	R_{direct}	ΔR_{direct}	R_{calc}	ΔR_{calc}
Very loose cuts	1.00	0.05	1.00	0.05	1.01	0.08	1.01	0.08
Medium cuts	0.99	0.06	0.99	0.06	1.01	0.08	1.01	0.08

Integrated signal cross section and effective proton form factor

The integrated cross section of the $\bar{p}p \rightarrow \mu^+ \mu^-$ signal process is calculated in this feasibility study at each value of q^2 with

$$\sigma_{int} = N^{corr} / \mathcal{L}, \quad (\text{E.3})$$

where N^{corr} stands for the total signal counts after background subtraction and after efficiency correction with the assumption for the time-integrated luminosity of $\mathcal{L} = 2 \text{ fb}^{-1}$. Table E.4 summarizes the obtained values of the integrated cross section σ and its uncertainties. It can be seen, that for σ a high precision up to 0.65% is obtained when going to lower values of q^2 , due to the increasing signal statistics. In the following, the effective FF of the proton is determined from the integrated cross section based on Eq. 7.7. The time-integrated luminosity is assumed to be $\mathcal{L} = 2 \text{ fb}^{-1}$. At all values of beam momenta, the integration is performed in the range of $|\cos(\theta_{CM})| < 0.8$. Table E.5 gives an overview over the obtained values of the effective time-like proton FF and the corresponding values of the relative uncertainty. The obtained values of high precision on the effective FF range between 0.33% and 1.39% for the beam momenta between 1.5 and 3.3 GeV/c.

Table E.4: Extracted results and relative statistical uncertainty of the integrated cross section for the $\bar{p}p \rightarrow \mu^+\mu^-$ signal process together with the calculated value based on Eq. 3.26, Chapter 3, for the considered angular range of $-0.8 < \cos(\theta_{CM}) < 0.8$.

p_{beam} [GeV/c]	q^2 [(GeV/c) ²]	σ (calculation) [pb]	$\sigma \pm \Delta\sigma$ (extracted) [pb]	$\Delta\sigma/\sigma$ (extracted) [%]
1.5	5.08	640.721	640.637 ± 4.165	0.65
1.7	5.40	414.881	410.825 ± 6.389	1.56
2.5	6.77	89.185	91.484 ± 1.918	2.10
3.3	8.20	24.829	24.911 ± 0.693	2.78

Table E.5: Extracted relative statistical uncertainty on the effective proton FF, $|F_p|$.

p_{beam} [GeV/c]	q^2 [(GeV/c) ²]	$ F_p $ (model)	$ F_p \pm \Delta F_p $ (extracted)	$\Delta F_p / F_p $ (extracted) [%]
1.5	5.08	0.1403	0.1402 ± 0.0005	0.33
1.7	5.40	0.1213	0.1206 ± 0.0010	0.78
2.5	6.77	0.0703	0.0712 ± 0.0007	0.98
3.3	8.20	0.0436	0.0437 ± 0.0006	1.39

Appendix F

Comparison between multivariate data analysis and simple cuts

The improvement of the signal-background separation by using a multivariate data analysis (MVA) in comparison to simple cuts shall be demonstrated on an example at $p_{beam} = 1.5 \text{ GeV}/c$ under the conditions of the $\bar{\text{P}}\text{ANDA}$ Phase-3 (assuming $\mathcal{L} = 2 \text{ fb}^{-1}$). For the MVA, Boosted Decision Trees (BDT) are used for the data classification. As a consequence, the obtained results with MVA show much better precision than those obtained with simple cuts.

In this example, the set of input variables at $p_{beam} = 1.5 \text{ GeV}/c$ is used for both analyses. The set of input variables used for the MVA are given in Tab. 6.6 in Chapter 6. The same total signal reconstruction efficiency of $\epsilon = 24.6\%$ is obtained in both analyses, with a difference which is negligible ($< 0.01\%$). Table F.1 shows the selection criteria for both analyses. In case of simple cuts, only a subset of powerful variables have been used for the selection (from the set of variables used for the training of BDT, see Tab. 6.5), since no further improvement is achieved by using more variables in that case.

As it can be seen in Tab. F.2, a clear improvement in the signal-background separation is achieved, by using the MVA instead of simple cuts: while in the simple cuts analysis, the physically expected signal-to-background ratio is $1 : 72$ and a background suppression factor of $8.58 \cdot 10^{-5}$ is achieved, for the analysis based on BDT, the background suppression factor is $7.16 \cdot 10^{-6}$ which corresponds to a physically expected signal-to-background ratio of $1 : 6$.

Figure F.1 shows the MC angular distributions of μ^- (violet squares), the reconstructed signal distribution after full analysis (black triangles up) and the corresponding signal reconstruction efficiency (blue dots) as a function of $\cos(\theta_{CM})$ for the analysis using simple cuts (Fig. F.1 (a)) respectively MVA (Fig. F.1 (b)). In case of the simple cuts analysis, the signal efficiency drops quickly for increasing values of $|\cos(\theta_{CM})|$. The fast drop of reconstructed events starts around $|\cos(\theta_{CM})| \gtrsim 0.2$ with increasing values of $|\cos(\theta_{CM})|$, mostly due to the cuts on the iron depth and the PID_{MDT} identification probability being muon for both tracks inside the Muon System.

Table F.1: Comparison between the two different analysis methods (**simple cuts** and a multivariate data analysis (**MVA**)).

SIMPLE CUTS						
M_{inv} [GeV/c ²]	$(\phi^+ - \phi^-)_{lab}$ [DEG]	$(\theta^+ + \theta^-)_{CM}$ [DEG]	Iron depth [cm]	PID_{MDT}	E/p (EMC)	No. of fired layers (MS)
]2.1; 2.4[]175.0; 185.0[]179.65; 185.0[42.0	> 0.9	< 0.223	> 12
MVA						
M_{inv} [GeV/c ²]	$(\phi^+ - \phi^-)_{lab}$ [DEG]	$(\theta^+ + \theta^-)_{CM}$ [DEG]			BDT	
]2.1; 2.4[]175.0; 185.0[]179.65; 185.0[-	-	0.3344	

Table F.2: Comparison between the two different analysis methods (**SIMPLE CUTS** and **MVA**). Application of multivariate analysis (here Boosted Decision Trees) clearly improves the background rejection factor physically expected signal-to-background ratio after full analysis.

SIMPLE CUTS		
ϵ	ϵ_B [10 ⁻⁵]	S-B ratio
0.246	8.59	1:72
MVA		
ϵ	ϵ_B [10 ⁻⁶]	S-B ratio
0.246	7.16	1:6

Also contributing are the cuts on the deposited energy E/p (EMC) from the electromagnetic calorimeter. Figure F.1 (b) shows a decreasing signal efficiency in the range between $|\cos(\theta_{CM})| \lesssim 0.4$ caused by the cut on the BDT response.

Figure F.2 shows the efficiency corrected angular distributions of the signal, with the analysis of simple cuts (a) and the MVA (b). It is clear, that MVA shows a strongly better performance than the simple cuts. In particular the simple cuts lead to strongly increasing size of the error bars in histogram bins for $|\cos(\theta_{CM})| > 0.4$ due to the drastically dropping reconstruction efficiency of the signal. A statistical precision for the form factor ratio R of $\sim 86\%$ was obtained for simple cuts, while for the MVA a high precision of $\sim 5\%$ is obtained. Therefore, MVA is used in this work.

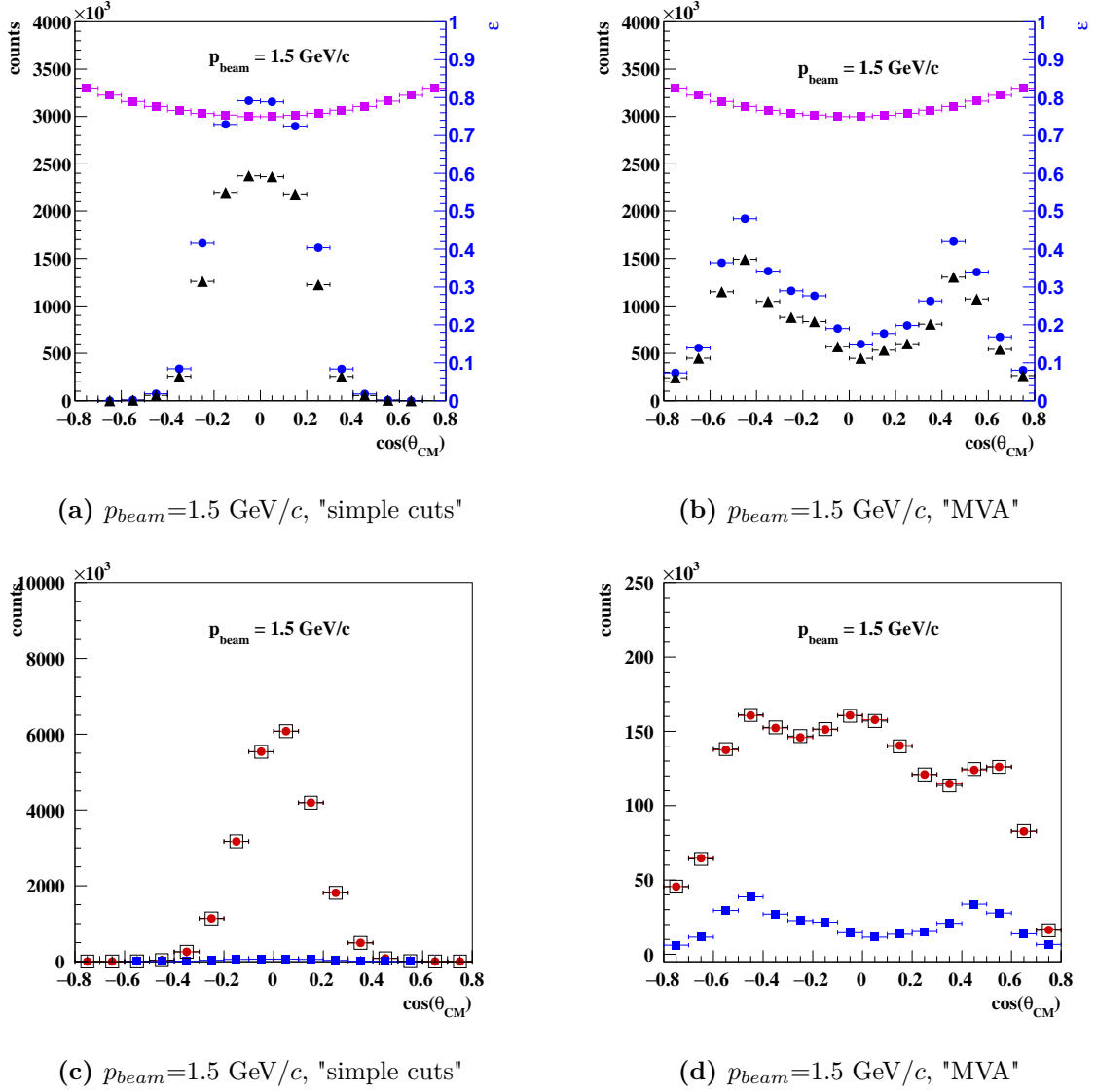


Figure F.1: Comparison between analysis based on simple cuts and MVA at total signal efficiency $\epsilon = 24.6\%$. The angular distribution of the signal reconstruction efficiency (blue dots), the reconstructed signal counts after cuts (black triangles up) and the MC generated signal counts (violet squares) of the negatively charged muon are depicted for (a) simple cuts and (b) MVA. The figures below show the two statistically independent angular distributions of the pion contamination (black open squares and red dots) and of the signal counts (blue squares). A clearly better signal statistics is achieved over a larger range of $\cos(\theta_{CM})$ by using MVA.

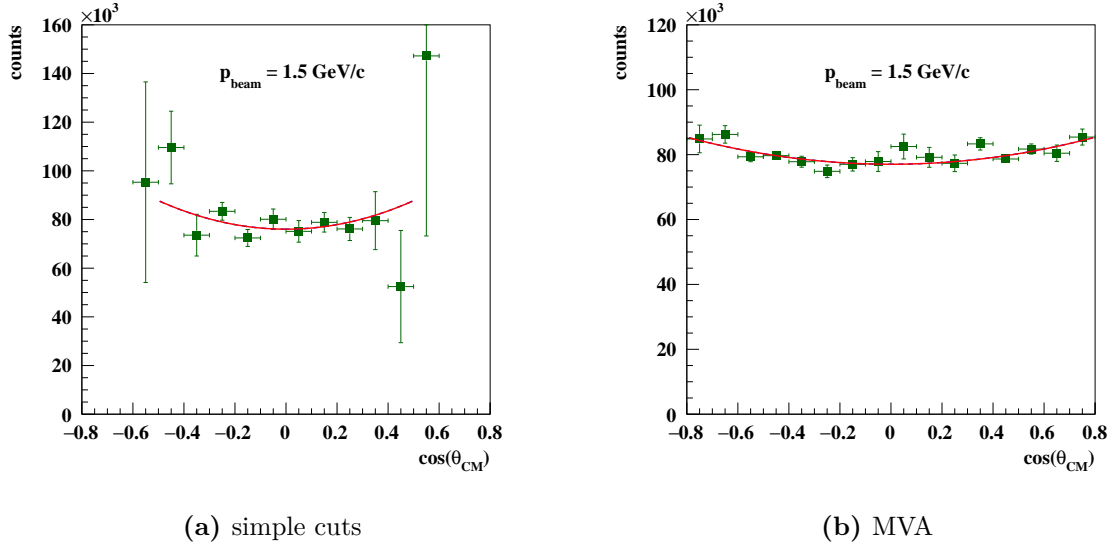


Figure F.2: Angular distribution of the reconstructed and efficiency corrected signal counts after background subtraction for an analysis based on (a) simple cuts and (b) multivariate analysis (Boosted Decision Trees). The angular range, which is suitable for fitting the distribution, is clearly larger for MVA in contrast to simple cuts. The statistical precision of the form factor ratio R is $\sim 86\%$ for simple cuts, while for the MVA a high precision of $\sim 5\%$ is obtained.

Appendix G

Influence of the background fluctuations

In section 6.3, the construction of the pion background subtraction was presented. The influence of the background subtraction on the results was studied and will be presented in the following. For this purpose, the analysis, presented in Chapter 6 and with the results of these feasibility studies presented in Chapter 7, shall be repeated without background subtraction for $p_{beam} = 1.5 \text{ GeV}/c$. Figure G.1 shows the angular distribution of the reconstructed and efficiency

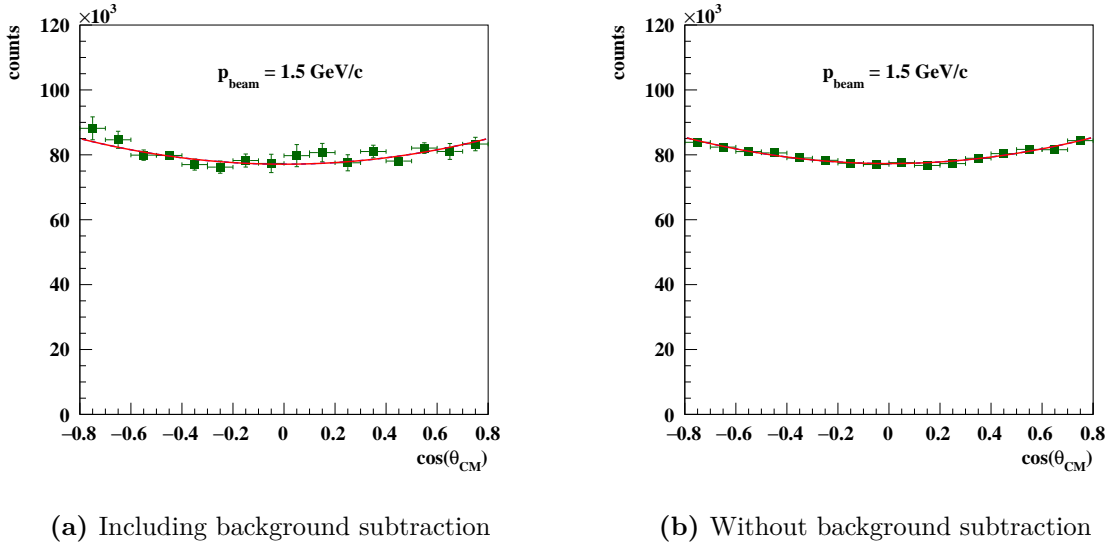


Figure G.1: Angular distribution of the reconstructed and efficiency corrected signal counts obtained at $p_{beam} = 1.5 \text{ GeV}/c$ including background fluctuations (as presented in Chapter 7, Fig. 7.1) (a) and repeated without introducing background fluctuations (b).

corrected signal counts after background subtraction for Multivariate Data Analysis (BDT) at $p_{beam} = 1.5 \text{ GeV}/c$ including background fluctuations (a) and without background fluctuations (b). From these distributions, the form factors and their ratio are extracted and summarized in Tab. G.1. The results show, that the background fluctuations have a significant influence on the

statistical precision of the form factors. For instance, the ratio R was obtained with a statistical precision of 1% when no background fluctuations are introduced to the analysis. In comparison to that, the introduction of such fluctuations lead to a clear deterioration from 1% to 5%. From that, it can be concluded, that it is necessary to include the background subtraction in these feasibility studies.

Table G.1: Comparison of the relative statistical uncertainty of $|G_E|$, $|G_M|$ and R obtained with the analysis described in Chapter 6 (right column) and repeated excluding the background fluctuations (left column).

without background fluctuations		with background fluctuations	
$R \pm \Delta R$	$\Delta R/R$ [%]	$R \pm \Delta R$	$\Delta R/R$ [%]
1.02 ± 0.01 (stat.)	1 (stat.)	1.02 ± 0.05 (stat.)	5 (stat.)

$ G_E \pm \Delta G_E $	$\Delta G_E / G_E $ [%]	$ G_E \pm \Delta G_E $	$\Delta G_E / G_E $ [%]
0.142 ± 0.001 (stat.)	0.7 (stat.)	0.142 ± 0.004 (stat.)	3.1 (stat.)
$ G_M \pm \Delta G_M $	$\Delta G_M / G_M $ [%]	$ G_M \pm \Delta G_M $	$\Delta G_M / G_M $ [%]
0.139 ± 0.001 (stat.)	0.4 (stat.)	0.139 ± 0.002 (stat.)	1.5 (stat.)

Appendix H

Summary tables of the results of
these feasibility studies for $\overline{\text{PANDA}}$
Phase-1 and Phase-3

H. Summary tables of the results of these feasibility studies for $\overline{\text{PANDA}}$ Phase-1 and Phase-3

220

Table H.1: Final results for the $\overline{\text{PANDA}}$ Phase-3: Statistical and systematic contributions to the relative total uncertainty of $|G_E|$, $|G_M|$, $R = |G_E|/|G_M|$, the effective FF $|F_p|$ and the integrated cross section for the signal $\bar{p}p \rightarrow \mu^+\mu^-$ at four different values of beam momenta ($p_{beam} = 1.5, 1.7, 2.5$ and 3.3 GeV/c). An angular interval of $|\cos(\theta_{CM})| < 0.8$ is considered. A time-integrated luminosity of $\mathcal{L} = 2 \text{ fb}^{-1}$ was assumed for the conditions of $\overline{\text{PANDA}}$ Phase-3, which corresponds to a measurement at the $\overline{\text{PANDA}}$ original design luminosity of $2 \times 10^{32} \text{ cm}^{-2} \text{ s}^{-1}$ at pure data taking time of approximately 4 months and full detector setup. Systematic error sources are the luminosity measurement, the choice of cuts and - only at $p_{beam} = 3.3$ GeV/c - the number of histogram bins.

$p_{beam} = 1.5 \text{ GeV}/c$ ($q^2 = 5.08 [(GeV/c)^2]$)			Relative uncertainty					
ϵ_S	ϵ_B	S-B ratio		$\frac{\Delta G_E }{ G_E }$	$\frac{\Delta G_M }{ G_M }$	$\frac{\Delta R}{R}$	$\frac{\Delta F_p }{ F_p }$	$\frac{\Delta\sigma}{\sigma}$
0.315	12.2×10^{-6}	1:8	Statistical	3.1 %	1.5 %	5 %	0.33 %	0.65 %
			Total	3.7 %	2.5 %	5 %	2.03 %	4.05 %
$p_{beam} = 1.7 \text{ GeV}/c$ ($q^2 = 5.40 [(GeV/c)^2]$)			Relative uncertainty					
ϵ_S	ϵ_B	S-B ratio		$\frac{\Delta G_E }{ G_E }$	$\frac{\Delta G_M }{ G_M }$	$\frac{\Delta R}{R}$	$\frac{\Delta F_p }{ F_p }$	$\frac{\Delta\sigma}{\sigma}$
0.274	11.2×10^{-6}	1:10	Statistical	5.1 %	2.2 %	7 %	0.71 %	1.42 %
			Total	5.6 %	3.0 %	7 %	2.12 %	4.24 %
$p_{beam} = 2.5 \text{ GeV}/c$ ($q^2 = 6.77 [(GeV/c)^2]$)			Relative uncertainty					
ϵ_S	ϵ_B	S-B ratio		$\frac{\Delta G_E }{ G_E }$	$\frac{\Delta G_M }{ G_M }$	$\frac{\Delta R}{R}$	$\frac{\Delta F_p }{ F_p }$	$\frac{\Delta\sigma}{\sigma}$
0.334	17.5×10^{-6}	1:13	Statistical	10.2 %	4.4 %	14 %	1.05 %	2.09 %
			Total	11.2 %	4.9 %	15 %	2.26 %	4.51 %
$p_{beam} = 3.3 \text{ GeV}/c$ ($q^2 = 8.20 [(GeV/c)^2]$)			Relative uncertainty					
ϵ_S	ϵ_B	S-B ratio		$\frac{\Delta G_E }{ G_E }$	$\frac{\Delta G_M }{ G_M }$	$\frac{\Delta R}{R}$	$\frac{\Delta F_p }{ F_p }$	$\frac{\Delta\sigma}{\sigma}$
0.295	13.0×10^{-6}	1:5	Statistical	26.9 %	9.6 %	37 %	1.39 %	2.78 %
			Total	27.0 %	9.9 %	37 %	2.44 %	4.87 %

Table H.2: Final results for the $\overline{\text{PANDA}}$ Phase-1: Statistical and systematic contributions to the relative total uncertainty of $|G_E|$, $|G_M|$, $R=|G_E|/|G_M|$, the effective FF $|F_p|$ and the integrated cross section for the signal $\bar{p}p \rightarrow \mu^+\mu^-$ at the lowest value of beam momentum at $\overline{\text{PANDA}}$ ($p_{beam} = 1.5$ GeV/c). An angular interval of $|\cos(\theta_{CM})| < 0.8$ is considered. In this feasibility study a time-integrated luminosity of $\mathcal{L} = 0.1 \text{ fb}^{-1}$ was assumed, which corresponds to a measurement at the $\overline{\text{PANDA}}$ Phase-1 with a luminosity of $1 \times 10^{31} \text{ cm}^{-2} \text{ s}^{-1}$ at pure data taking time of approximately 4 months. Systematic error sources are the luminosity measurement and the choice of cuts.

$p_{beam} = 1.5 \text{ GeV}/c$ ($q^2 = 5.08 [(GeV/c)^2]$)			Relative uncertainty					
ϵ_S	ϵ_B	S-B ratio		$\frac{\Delta G_E }{ G_E }$	$\frac{\Delta G_M }{ G_M }$	$\frac{\Delta R}{R}$	$\frac{\Delta F_p }{ F_p }$	$\frac{\Delta\sigma}{\sigma}$
0.315	12.2×10^{-6}	1:8	Statistical	13.8 %	6.5 %	20 %	1.46 %	2.93 %
			Total	14.2 %	6.9 %	20 %	2.48 %	4.96 %

Bibliography

- [1] C. F. Perdrisat et al. *Prog. Part. Nucl. Phys.*, (59):694–764, 2007.
- [2] R. Hofstadter, H.R. Fechter, and J.A. McIntyre. *Phys. Rev.*, (92):978, 1953.
- [3] R. Hofstadter and R. W. McAllister. *Phys. Rev.*, 98(217), 1955.
- [4] M. N. Rosenbluth. *Phys. Rev.*, 79:615, 1950.
- [5] M. K. Jones et al. *Phys. Rev. Lett.*, (84):1398, 2000.
- [6] O. Gayou et al. *Phys. Rev. Lett.*, (88):092301, 2002.
- [7] V. Punjabi et al. *Phys. Rev.*, C(71):055202, 2005.
- [8] B.S. Henderson et al. *Phys. Rev. Lett.*, (118):092501, 2017.
- [9] R. Pohl et al. *Nature*, 466:213, 07 2010.
- [10] Paul Scherrer Institut (PSI). <https://www.psi.ch/muse/motivation>.
- [11] A. Bianconi and E. Tomasi-Gustafsson. *Phys. Rev. Lett.*, 114:232301, Jun 2015.
- [12] A. Bianconi and E. Tomasi-Gustafsson. *Phys. Rev. C*, 93:035201, Mar 2016.
- [13] M. Lutz et al. *PANDA Physics Performance Report*. arXiv:0903.3905v1 [hep-ex], 2009.
- [14] S. L. Olsen. *Front. Phys.*, 10:101401, 2015.
- [15] B. P. Singh et al. *Eur. Phys. J. A*, 51(8):107, Aug 2015.
- [16] W. Erni B. Singh et al. *Eur. Phys. J. A*, A(52):325, 2016.
- [17] BaBar Collaboration. <http://www.slac.stanford.edu/BFROOT/>.
- [18] BELLE collaboration. <http://belle.kek.jp/>.
- [19] BESIII collaboration. <http://bes3.ihep.ac.cn/index.htm>.
- [20] C. B. Dover, T. Gutsche, M. Maruyama, and A. Faessler. *Prog. Part. Nucl. Phys.*, 29:87, 1992.
- [21] M. Tanabashi et al. *Phys. Rev. D* 98, D(98):030001, 2018.

- [22] C. Patrignani et al. *Particle Data Group*, <http://pdg.lbl.gov/>, *Chin. Phys.*, C(40), 2017.
- [23] J. E. Enstrom et al. *Particle Data Group Compilation*, LBL 58, 1972.
- [24] HEP. <http://durpdg.dur.ac.uk/HEPDATA/>.
- [25] V. Uzhinsky et al. *Phys. Lett.*, B(705):235, 2011.
- [26] A. Dbeyssi. *Study of the internal structure of the proton with the PANDA experiment at FAIR*. PhD thesis, IPN Orsay, 2013.
- [27] A. Dbeyssi and E. Tomasi-Gustafsson. *Prob. Atomic Sci. Technol.*, N1, 2012.
- [28] Y. M. Bystritskiy Y. Wang and E. Tomasi-Gustafsson. *Phys. Rev.*, C(95), 2017.
- [29] J. Aubert et al. *Phys. Rev. Lett.*, (33):1404, 1974.
- [30] J. Augustin et al. *Phys. Rev. Lett.*, 33(1406), 1974.
- [31] M. Burkardt. *Phys. Rev.*, D(62):071503, 2000.
- [32] S. Boffi and B. Pasquini. *Generalized Parton Distributions and the structure of the nucleon*. arXiv:0711.2625v2 [hep-ph] 28 Jan 2008, 2008.
- [33] A. V. Belitsky and A. V. Radyushkin. *Phys. Rep.*, (418):1, 2005.
- [34] X. Ji et al. *Ann. Rev. Nucl. Part. Sci.*, 54(413), 2004.
- [35] M. Diehl et al. *Phys. Rept.*, (388):41, 2003.
- [36] K. Goeke, M. V. Polyakov, and M. Vanderhaeghen. *Prog. Part. Nucl. Phys.*, 47:401, 2001.
- [37] P. Kroll et al. *Eur. Phys. J.*, A(26):89, 2005.
- [38] C. C. Kuo et al. *Phys. Lett.*, B(621):41, 2005.
- [39] B. Pire, L. Szymanowski, et al. *Phys. Rev.*, D(71):111, 2005.
- [40] B. Pire, L. Szymanowski, et al. *Phys. Lett.*, B(622):83, 2005.
- [41] B. Fröhlich. PhD thesis, Helmholtz-Institut Mainz, October 2017.
- [42] R. Hofstadter. *Rev. Mod. Phys.*, (28):214, 1956.
- [43] O. Stern. *Nature*, 132:103, 1933.
- [44] R. W. McAllister and R. Hofstadter. *Phys. Rev.*, 102:851, 1956.
- [45] E. Clementel and C. Villi. *Nuov. Cim*, 4:1207, 1956.
- [46] R. Hofstadter, F. Bumiller, and M.R. Yearian. *Rev. Mod. Phys.*, 30:482, 1958.
- [47] M. N. Rosenbluth. *Phys. Rev.*, 79:615, 1950.

- [48] L. L. Foldy. *Phys. Rev.*, 87:688, 1952.
- [49] G. Salzman. *Phys. Rev.*, 99:973, 1955.
- [50] S. Pacetti et al. *Phys. Rep.*, 550:1, 2015.
- [51] S. Pacetti, R. Baldini, and E. Tomasi-Gustafsson. *Proton electromagnetic form factors: Basic notions, present achievements and future perspectives. Phys.Rept.*, 550-551:1–103, 2014.
- [52] A. Zichichi, S. M. Berman, N. Cabibbo, et al. *Nuovo Cim.*, 24:170–180, 1962.
- [53] J. van de Wiele. *Internal Note*, 2011.
- [54] E. Tomasi-Gustafsson and M. P. Rekalo. *Phys.Lett.*, B(504):291–295, 2001.
- [55] E. Titchmarsh. *The Theory of Functions*. 1939.
- [56] M. P. Rekalo. *Sov. J. Nucl. Phys.*, (1):760, 1965.
- [57] F. Iachello et al. *Phys. Lett.*, B(43):191, 1973.
- [58] A. J. R. Puckett et al. *Phys. Rev. Lett.*, 104(242301), 2010.
- [59] W. R. Frazer and J. R. Fulco. *Phys. Rev.*, (117):1609, 1960.
- [60] G. J. Gounaris and J. J. Sakurai. *Phys. Rev. Lett.*, (21):244, 1968.
- [61] F. Iachello and Q. Wan. *Phys. Rev.*, C(69):055204, 2004.
- [62] V. A. Matveev, R. M. Muradyan, and A. N. Tavkhelidze. *Lett. Al Nuovo Cim.*, 7(719), 1973.
- [63] S. J. Brodsky and G. R. Farrar. *Phys. Rev. Lett.*, (31):1153, 1973.
- [64] D.V. Shirkov et al. *Phys.Rev. Lett.*, 79:1209, 1997.
- [65] M. Andreotti et al. *Phys.Lett.*, B(559):20, 2003.
- [66] M. Ambrogiani et al. *Phys.Rev. D*, 60(032002), 1999.
- [67] A. Antonelli et al. *Nucl. Phys.*, B(517):3, 1998.
- [68] G. Bardin et al. *Nucl.Phys.*, B411:3–32, 1994.
- [69] T. A. Armstrong et al. *Phys.Rev. Lett.*, 70:1212, 1993.
- [70] B. Delcourt et al. *Phys.Lett. B*, B(86):395, 1979.
- [71] D. Bisello et al. *Nucl.Phys. B*, B(224):379, 1983.
- [72] D. Bisello et al. *Z. Phys. C*, C(48):23, 1990.

- [73] M. Ablikim et al. *Phys.Lett.*, B(630):14.
- [74] M. Ablikim et al. *Phys.Rev.*, D(91), 2015.
- [75] T.K. Pedlar et al. *Phys.Rev. Lett.*, 95(261803), 2005.
- [76] J. P. Lees et al. *Phys. Rev. D*, 88(032011), 2013.
- [77] J.P. Lees et al. *Phys.Rev. D*, 87(092005), 2013.
- [78] L. Andivahis et al. *Phys. Rev.*, D(50), 1994.
- [79] P. E. Bosted et al. *Phys. Rev. Lett.*, (68):3841, 1992.
- [80] A. Akhiezer and M. Rekalov. *Sov. Phys. Dokl.*, (13):572, 1968.
- [81] X. Zhan et al. *Phys. Lett.*, B(705):59–64, 2011.
- [82] R.C. Walker et al. *Phys. Rev.*, D(49):5671, 1994.
- [83] M. E. Christy et al. *Phys. Rev.*, C(70):015206, 2004.
- [84] I. A. Qattan et al. *Phys. Rev. Lett.*, (94):142301, 2005.
- [85] Y.-S. Tsai et al. *Phys. Rev.*, (122):1898, 1961.
- [86] L. W. Mo and Y. S. Tsai. *Rev. Mod. Phys.*, (41):205, 1969.
- [87] L. C. Maximon and J. A. Tjo. *Phys. Rev.*, C(62):054320, 2000.
- [88] J. Guttman et al. *Eur. Phys. J.*, A:47–77, 2011.
- [89] S. Bassompierre et al. *Phys. Lett.*, B(64/68), 1976/1977.
- [90] G. Bardin et al. *Phys. Lett.*, B(255):149, 1991.
- [91] G. Bardin et al. *Phys. Lett.*, B(257):514, 1991.
- [92] A. Denig and G. Salme. arXiv:1210.4689v1 [hep-ex] 17 Oct 2012, 2018.
- [93] M. Castellano et al. *Nuovo Cim.*, 14 A(1), 1973.
- [94] A. Antonelli et al. *Phys. Lett.*, B(313):283, 1993.
- [95] A. Antonelli et al. *Phys. Lett.*, B(334):431, 1994.
- [96] R. R. Akhmetshin et al. arXiv:1507.08013v2 [hep-ex], April 2016.
- [97] J. P. Lees et al. *Phys. Rev.*, D(73):012005, 2006.
- [98] T. A. Armstrong et al. *Phys. Rev.*, D(47):772, 1993.
- [99] R. Baldini, C. Bini, P. Gauzzi, et al. *Eur. Phys. J. C*, C(46):421–428, 2006.

- [100] B. Delcourt et al. *Phys. Lett.*, B(86):395, 1982.
- [101] A. Antonelli et al. *Z. Phys.*, C(48):23, 1990.
- [102] C. Rosner. *Proton time-like electromagnetic form factor measurements at BESIII*. Talk by C. Rosner at the 668. Heraeus Seminar on Baryon Form Factors, 2018.
- [103] J. Boucher et al. *Feasibility studies of the $\bar{p}p \rightarrow \pi^0 e^+ e^-$ electromagnetic channel at PANDA*. PhD thesis, 2011.
- [104] J. Guttmann and M. Vanderhaeghen. *Phys. Lett.*, B(719):136–142, 2013.
- [105] R. Aaij, B. Adeva, M. Adinolfi, et al. *Phys. Rev. Lett.*, 113:151601, 2014.
- [106] C. Bobeth, G. Hiller, and G. Piranishvili. *JHEP*, 12 2007.
- [107] C. Bouchard et al. *Phys. Rev. Lett.*, 111(162002), 2013.
- [108] M. Bordone, Isidori G., and A. Pattori. *Eur. Phys. J.*, C(76):440, 2016.
- [109] FAIR. <https://www.gsi.de/forschungbeschleuniger/fair.htm>.
- [110] G. Clemente et al. *Proceedings of HB2010*. MOPD26, 2010.
- [111] F. Nolden et al. *The Collector Ring of the FAIR Project*. Proceedings of EPAC 2006, 2008.
- [112] R. Maier. *Conf. Proc.*, C110328:2104–2106, 2011.
- [113] R. Maier et al. *Conf. Proc.*, C110904:3432–3434, 09 2011.
- [114] V. Parkhomchuk et al. *Proceedings of EPAC 2004*, 2004.
- [115] W. Erni, I. Keshelashvili, B. Krusche, et al. *Technical Design Report for the PANDA Internal Targets: The Cluster-Jet Target and Developments for the Pellet Target*. Technical report, 2014.
- [116] W. Erni, I. Keshelashvili, B. Krusche, et al. *Technical Design Report for the PANDA Solenoid and Dipole Spectrometer Magnets*. Technical report, 2009.
- [117] W. Erni, I. Keshelashvili, B. Krusche, et al. *Technical Design Report for the PANDA Micro Vertex Detector*. Technical report, 2012. arXiv:physics.ins-det/1207.6581.
- [118] W. Erni, I. Keshelashvili, B. Krusche, et al. *Technical Design Report for the PANDA Straw Tube Tracker*. *Eur. Phys. J.*, A(49), 2009.
- [119] PANDA Collaboration. <http://www-panda.gsi.de>, May 2018.
- [120] M. J. Berger and S. M. Seltzer. Technical report, NASA-SP-3012, 1964.

- [121] W. Erni, I. Keshelashvili, B. Krusche, et al. *Technical Design Report for the PANDA electromagnetic calorimeter*. arXiv:physics.ins-det/0810.1216, 2008.
- [122] W. Erni, I. Keshelashvili, B. Krusche, et al. *Technical Design Report for the PANDA Forward Spectrometer Calorimeter*. Technical report, 2016.
- [123] W. Erni et al. *Technical Design Report for the PANDA Barrel DIRC Detector*. Technical report, 2005. arXiv:1710.00684 [physics.ins-det].
- [124] I. Adam et al. *Nucl. Instr. Meth.*, A(538):281, 2005. BaBar DIRC.
- [125] W. Erni, I. Keshelashvili, B. Krusche, et al. *Technical Design Report for the PANDA Muon System*. Technical report, 2012.
- [126] V. Abramov. *Nucl. Instrum. Meth.*, A(419):660–666, 1998.
- [127] T. Zhao et al. *IEEE Trans. Nucl. Sci.*, 2002.
- [128] V. M. Abazov et al. *Nucl.Instrum.Meth.*, A(552):372 – 398, 2005.
- [129] P. Abbon et al. *Nucl.Instrum.Meth.*, A(557):455–518, 2007.
- [130] G. D. Alexeev et al. *Nucl. Instrum. Meth.*, A(462):494–505, 2001.
- [131] S. Spataro et al. *J. Phys.: Conf. Series*, 396:9, 2012.
- [132] M. Zambrana et al. Technical report, HIM Mainz, 2014.
- [133] *TOSCA 9.0 Reference Manual*, 2003.
- [134] E. Eisenhandler, W.R. Gibson, et al. *Nucl.Phys.*, B(96):109, 1975.
- [135] J. Van de Wiele and S. Ong. *Eur. Phys. J.*, A46:291–298, 2010.
- [136] *J. Phys. Conf. Ser.* volume 396, 2012.
- [137] CERN ROOT. <https://root.cern.ch/root/html/TROOT.html>.
- [138] R. Brun et al. *ROOT software package*, 1987.
- [139] S. Agostinelli et al. *Nucl. Instrum. Meth.*, A(506), 2003.
- [140] I. Hrivnacova. *J. Phys. Conf. Ser.*, 396, 2012.
- [141] T. Sjostrand et al. *Comput. Phys. Commun.*, 178, 2008.
- [142] A. Ryd et al. *EvtGen: A Monte Carlo Generator for B-Physics*, 2005.
- [143] A. Eide et al. *Nucl.Phys.*, B(60):173–220, 1973.
- [144] T. Buran et al. *Nucl.Phys.*, B(116):51, 1976.

- [145] T.A. Armstrong et al. *Nucl. Phys.*, B284:643, 1987.
- [146] C. White, R. Appel, D. S. Barton, et al. *Phys. Rev.*, D(49):58–78, 1994.
- [147] A. Hoecker et al. *TMVA User Guide*. arXiv:physics/0703039, October 2013.
- [148] A. Hoecker et al. <http://tmva.sourceforge.net/>, 09 2013.
- [149] Y. Freund and R. E. Schapire. *Journal of Computer and System Science*, 55:119, 1997.
- [150] L. Breiman, J. Friedman, R. Olsen, and C. Stone. *Classification and Regression Trees*. Wadsworth, 1984.
- [151] W. Erni et al. *Technical Report for the PANDA Luminosity Monitor*. Technical Report.
- [152] J. Guttmann, N. Kivel, and M. Vanderhaeghen. *Phys. Rev.*, D(83):094021, 2011.
- [153] G.I. Gakh and E. Tomasi-Gustafsson. *Nucl.Phys.*, A(761):120–131, 2005.
- [154] J. van de Wiele and S. Ong. *Eur. Phys. J. A (2013) 49: 18*, A(49):18, 2013.
- [155] A. Dbeyssi, D. Khaneft, et al. *Release Note*, 2018.
- [156] J. V. de Wiele and S. Ong. *Eur. Phys. J.*, A(49):18, 2013.
- [157] E. A. Kuraev, Yu. M. Bystritskiy, A. Ahmadov, and E. Tomasi-Gustafsson. *Phys. Rev. C*, 89:065207, Jun 2014.
- [158] E. Barberio et al. *Comput. Phys. Commun.*, (79):291, 1994.
- [159] P. Golonka and Z. Was. *Eur. Phys. J.*, C(45):97, 2006.
- [160] N. Davidson, T. Predzinski, and Z. Was. *PHOTOS Interface in C++*. arXiv:1011.0937v2 [hep-ph] 28 Apr 2015, 2015.
- [161] R. A. Fisher. *Annals Eugenics*, 7:179, 1936.

List of Figures

- 2.1 Total (black data points) and elastic (blue data points) cross section of the $\bar{p}p$ -interaction. Shown are the data points from the Particle Data Group (2017) [22] together with parametrizations from Ref. [25]. 7
- 2.2 Production cross sections of different hadronic states in the $\bar{p}p$ annihilation process depending on the antiproton momentum in the laboratory frame from Ref. [20, 24, 27]. Parameterizations are from Ref. [27]. Hadronic final states, in particular $\pi^+\pi^-$, are of special interest in this work, since they constitute a strong hadronic background in the measurement of time-like electromagnetic form factors of the proton using electromagnetic processes $\bar{p}p \rightarrow \ell^+\ell^-$ ($\ell = e, \mu$). 9
- 2.3 The mass spectrum of charmonium and charmonium-like resonances [14], including the recently discovered XYZ states. The nature of the XYZ states is currently unknown. They are possible candidates for tetra-quarks, penta-quarks, hybrid-states or molecule-like states. \bar{P} ANDA will perform precise measurements of widths with an accuracy of $\sim 10\%$ and masses up to 100 keV in the region below and above the open charm threshold [13] in the $\bar{p}p$ center-of-mass range between 2.2 and 5.5 GeV using $\bar{p}p$ annihilations. 10
- 2.4 (a): Deeply virtual Compton scattering can be described by the handbag diagram, which uses a factorization of the process amplitude into a hard upper part, which can be treated by perturbative QCD and QED and a soft lower part, which can be described by Generalized Parton Distributions (GPD's). (b): Generalized Distribution Amplitudes (GDA's) can be studied in the inverted wide angle Compton scattering process $\bar{p}p \rightarrow \gamma\gamma$ [13]. 14
- 2.5 The process of $\bar{p}p \rightarrow e^+e^-\gamma$ can be factorized into a hard upper part, where the virtual photon has a large value of q^2 and a soft lower part, where the transition between the proton and the (virtual) photon can be described by a TDA. 14
- 2.6 Tree-level contribution to the reaction amplitude of the $\bar{p}p \rightarrow \ell^+\ell^-$ process ($\ell = e, \mu$). \bar{P} ANDA will be able to investigate time-like electromagnetic form factors through this reaction over a wide kinematical range of q^2 15
- 3.1 Original results from the paper of R. Hofstadter in 1956 [42]: "The square of the FF plotted against q^2 . q^2 is given in units of $10^{26}cm^{-2}$. The solid line is calculated for the exponential model with rms radii = 0.80×10^{-13} cm." 18

3.2	Feynman diagram of the lowest order contribution to the reaction amplitude of the elastic electron proton scattering process.	19
3.3	Lowest order contributing diagram to the reaction amplitude of the antiproton-proton annihilation into final states of $\ell^+\ell^-$	22
3.6	Integrated cross-section of the reaction $\bar{p}p \rightarrow \ell^+\ell^-$ (in Born approximation) as a function of the $\bar{p}p$ center-of-mass energy squared, s . It was integrated over the full angular range for the produced final states e^+e^- (black dashed line), $\mu^+\mu^-$ (red solid line) and $\tau^+\tau^-$ (blue solid line). The cross section curves of the $\bar{p}p \rightarrow e^+e^-$ and $\bar{p}p \rightarrow \mu^+\mu^-$ processes coincide within the solid line.	24
3.7	Feynman diagrams for the $\bar{p}p \rightarrow e^+e^-\pi^0$ process with the production of an e^+e^- pair from the antiproton (left) respectively from the proton (right).	27
3.8	Lowest order diagram in pQCD for the photon-proton interaction vertex in electron-proton scattering.	30
3.9	The effective form factor of the proton in the time-like region, $ F_p $, as a function of q^2 determined for different form factor parametrizations. Shown are the curves based on the VMD model (violet plain line), which shows structures at the meson poles in the unphysical region, the pQCD inspired model (blue dashdotted line) and the modified dipole parameterization based on Eq. 3.57 (black dashed line). The last one is used in these feasibility studies. Also shown are experimental data, that were taken under the assumption that $ G_E = G_M $ at E835 [65, 66], FENICE [67], PS170 [68], E760 [69], DM1 [70], DM2 [71, 72], BES [73], BESIII [74], CLEO [75] and BABAR [76, 77].	31
3.10	The SL electric (left) and magnetic (right) FF of the proton depending on Q^2 [GeV/c^2], being normalized to the dipole function $G_d(Q^2)$ (see Ref. [1] and references therein). The data shown were obtained with the Rosenbluth method.	33
3.11	Available experimental data on the proton FF's ratio $R = \mu_p G_E/G_M$ obtained with the Rosenbluth [82, 78, 83, 84] (red data points) and polarization method [5, 6, 7, 58, 81] (blue data points) at different values of Q^2 . The data obtained with both methods show clearly a different trend.	34
3.12	Available data on the proton FF's ratio $R = G_E / G_M $ depending on q^2 , from Ref. [77] (diamonds), from Ref. [68] (squares), from Ref. [99] (massive cross) and (star), from Ref. [74] (dots) and from Ref. [96] (down triangle). The data taken at BABAR and LEAR show clearly different trends.	37
3.13	The effective time-like FF of the proton, $ F_p $, at different values of q^2 , determined by using cross sections of reactions of $e^+e^- \rightarrow \bar{p}p$ respectively $\bar{p}p \rightarrow e^+e^-$. The data were taken under the assumption that $ G_E = G_M $ at E835 [65, 66], FENICE [67], PS170 [68], E760 [69], DM1 [70], DM2 [71, 72], BES [73], BESIII [74], CLEO [75] and BABAR [76, 77]. Also shown is the parameterization based on Eq. 3.57 (black dashed line), which is used in this feasibility study.	38

3.14	Expected precisions of the determination of the proton form factor ratio from the feasibility studies for $\bar{\text{P}}\text{ANDA}$ obtained by method I (red circles) and method II (blue up triangles) for the $\bar{p}p \rightarrow e^+e^-$ process at different values of q^2 [16]. The existing world data on the time-like ratio $R = G_E / G_M $ are also shown, from Ref. [68] (triangles down), from Ref. [77] (up triangles), from Ref. [99] (diamond) and (square), from Ref. [96] (star) and from Ref. [74] (massive crosses). The expected precision of R at PANDA is much better than the currently available data, in particular when going to lower values of q^2 , where the cross section for the signal process increases.	39
4.1	Facility for Antiproton and Ion Research	46
4.2	The High Energy Storage Ring (HESR).	49
4.3	Time dependence of the luminosity during an operation cycle $L(t)$ at HESR including the RESR [115]. The red line corresponds to a fixed target density and therefore decreases during the time measurement (Target ON).	51
4.4	Full experimental setup of the $\bar{\text{P}}\text{ANDA}$ Experiment. The detector consists of two major parts, providing almost full 4π coverage: the Target Spectrometer and the Forward Spectrometer, which will be both equipped with sub-detectors ensuring high tracking capabilities, precise particle identification and electromagnetic calorimetry at high event rates.	53
4.5	The Electromagnetic Calorimeter (EMC) inside the Target Spectrometer, consisting of the Barrel EMC, the Backward End-cap EMC and the Forward End-cap EMC. In the Forward Spectrometer, the <i>Shashlyk</i> -type Forward EMC will be located for electromagnetic calorimetry [121]. A challenging task in this work is an efficient μ/π separation, which is done mostly with variables provided by the Muon System. Variables from the EMC improve the μ/π separation and are also used for the data classification.	58
4.6	PANDA	64
4.7	Cross section of a typical Barrel module of the $\bar{\text{P}}\text{ANDA}$ Muon System [125]. A sandwich structure of alternating absorber (Fe plates) and regular detector layers (Mini-Drift Tubes arranged in layers) is used for the detection of muons. The path length of a charged particle track inside the sandwich structure serves as one of the most powerful variables for μ/π separation, which is challenging due to the similar rest mass of muon and pion. The innermost detection layer ("zero" bi-layer) consists of two MDT layers with a common strip board in between and provides a precise starting point coordinate of each particle track.	66
4.8	PANDA	67
4.9	Angular coverage of the Muon System subsystems in the $\bar{p}p$ center-of-mass frame for low center-of-mass energies $s = 5.08, 6.77$ and 8.20 GeV^2 , which are relevant for this work.	68
4.10	PANDA	69

5.3	Procedure of the standard simulation and analysis chain in PandaRoot.	80
5.4	Layout of the Mini Drift Tubes (MDT's) of the $\bar{\text{P}}\text{ANDA}$ Muon System as it is seen by the PandaRoot software.	81
5.6	Angular distributions of data and model calculations for the π^- angular distribution from the main background reaction $\bar{p}p \rightarrow \pi^+\pi^-$ as a function of $\cos(\theta_{CM})$ [16] at the following values of beam momentum: p_{beam} at 1.7 GeV/c (green triangles and dash-triple dotted line) from Ref. [134], 5 GeV/c [143] (blue full squares and dash-dotted line) and 6.21 GeV/c [144] (black full circles and solid line). For $p_{beam} = 3$ GeV/c (red dotted line) and $p_{beam} = 10$ GeV/c (magenta dashed line) the results of the event generator are given additionally.	86
6.3	Spatial production vertices of the μ^- from the decay process $\pi^- \rightarrow \mu^- \bar{\nu}_\mu$ from Geant4 in (left) the x-y plane and (right) the x-z plane (lab frame) at $p_{beam} = 1.5$ GeV/c. The antiproton beam points along the the z-axis, the x-y plane is oriented perpendicular to the beam direction, where the y-axis is oriented antiparallel to the hydrogen injection from above by the Cluster-Jet target. The x-z plane shows a cross section view through the $\bar{\text{P}}\text{ANDA}$ detector. Most of the pion decays occur close to the origin of the $\pi^- \pi^+$ production.	94
6.4	Spatial production vertices of the μ^- from the decay process $\pi^- \rightarrow \mu^- \bar{\nu}_\mu$ from Geant4 at $p_{beam} = 3.3$ GeV/c in (left) the x-y plane and (right) the x-z plane (lab frame). The antiproton beam points along the the z-axis, the x-y plane is oriented perpendicular to the beam direction, where the y-axis is oriented antiparallel to the hydrogen injection from above by the Cluster-Jet target. The x-z plane shows a cross section view through the $\bar{\text{P}}\text{ANDA}$ detector.	95
6.6	The left column shows the distribution of the reconstructed kinematic variable $(\theta^+ + \theta^-)_{CM}$ after preselection for the signal (blue) and the background (red). The plots are based on the preselected samples of the high statistics for the signal and the main background at (a) $p_{beam} = 1.5$ GeV/c and (c) $p_{beam} = 1.7$ GeV/c. The right column shows the distribution of the reconstructed invariant mass M_{inv} of the final state after preselection for the signal (blue) and the background events (red) at (b) $p_{beam} = 1.5$ GeV/c and (d) $p_{beam} = 1.7$ GeV/c.	97
6.7	The left column shows the distribution of the reconstructed kinematic variable $(\theta^+ + \theta^-)_{CM}$ after preselection for the signal (blue) and the background (red). The plots are based on the preselected samples of the high statistics for the signal and the main background at (a) $p_{beam} = 2.5$ GeV/c and (c) $p_{beam} = 3.3$ GeV/c. The right column shows the distribution of the reconstructed invariant mass M_{inv} of the final state after preselection for the signal (blue) and the background events (red) at (b) $p_{beam} = 2.5$ GeV/c and (d) $p_{beam} = 3.3$ GeV/c.	98
6.8	Momentum dependence of the polar production angle in lab frame, θ_{lab} (reconstructed at vertex) [DEG], for reconstructed and preselected negatively charged particles from (left) $\bar{p}p \rightarrow \mu^+ \mu^-$ and from (right) $\bar{p}p \rightarrow \pi^+ \pi^-$	99

- 6.9 Angular dependence of the number of fired detection layers in laboratory frame for negatively charged particles from the signal (left column) and the background (right column) after reconstruction and preselection at (a) $p_{beam} = 1.5 \text{ GeV}/c$ and (b) $p_{beam} = 3.3 \text{ GeV}/c$. The different behavior of muons and pions in the Muon System is the key ingredient for an efficient μ/π separation. From these differences in the detector response from muon and pion, one can deduct, that the number of fired detection layers is a variable of strong separation power. . . . 100
- 6.10 Dependence of the iron depth inside the iron absorber on the initial momentum at the zero bi-layer from the Muon System, for negatively charged particles for the reconstructed and preselected signal (left column) and the background (right column) at $p_{beam} = 1.5 \text{ GeV}/c$ (a) and $p_{beam} = 3.3 \text{ GeV}/c$ (b). This variable has a strong separation power and is used, in combination with p_{MDT} , for the determination of the PID probability from the Muon System. 101
- 6.11 Mean energy loss per unit of length in the STT depending on the reconstructed momentum at vertex for negatively charged particles for the reconstructed and preselected signal (left column) and the background (right column) at $p_{beam} = 1.5 \text{ GeV}/c$ (a) and $p_{beam} = 3.3 \text{ GeV}/c$ (b). 103
- 6.12 Deposited energy inside the EMC divided by reconstructed momentum at vertex versus reconstructed momentum at vertex ($p_{vertex} \equiv p \text{ [GeV}/c]$). The detector response for negatively charged particles after reconstruction and preselection are shown at (a) $p_{beam} = 1.5 \text{ GeV}/c$ and (b) $p_{beam} = 3.3 \text{ GeV}/c$. The left column (right column) shows the reconstructed and preselected signal (background). Since this detector response is very similar for muons and pions, it is obvious, that this variable has a much lower separation power than variables from the Muon System. 104
- 6.13 The PID probability for being a muon, PID_{MDT} , is calculated based on simple cuts on variables from the Muon System for μ^- (left) and μ^+ (right). The iron depth and the initial particle momentum measured at the zero bi-layer of the Muon System are used for the determination of the PID probability. $PID_{MDT}(\mu^-|\mu^-)$ is the probability to identify a μ^- correctly, while $PID_{MDT}(\pi^-|\mu^-)$ is the probability misidentify a π^- as μ^- 105
- 6.14 Basic working principle of the data classification with MVA. The working flow consists of two major steps: The training phase, where the training, testing and evaluation of the classifiers are performed, followed by the application phase (= analysis of the unknown data sample). 108

- 6.15 Typical structure of a decision tree [147]. The uppermost node are the root nodes, from which the tree is developed during the training phase. The most powerful variable is chosen to achieve the best signal-background separation at this node. A cut is applied on this variable which splits the data sample into two sub-samples. The growing process of the tree stops as soon as a certain criterium is fulfilled. The leaf nodes define the end of the tree and are labeled as "S" (Signal) or "B" (Background) depending on the majority of the events ending up in the individual node. 109
- 6.16 Kinematical variables and Muon System observables at $p_{beam} = 1.5 \text{ GeV}/c$, after event reconstruction and preselection, which are used for the MVA. Shown are the distributions of the invariant mass (upper left plot) and the sum of the polar production angles of both tracks in the $\bar{p}p$ center-of-mass system (upper right plot). The iron depth and the number of fired layers for negatively charged particles show different patterns, which makes them very useful for the μ/π separation. The signal distributions are shown in blue, while the background distributions are shown in red. 115
- 6.17 Observables from the EMC and the STT at $p_{beam} = 1.5 \text{ GeV}/c$, which show very similar distributions and therefore are rather weak variables for the MVA in comparison to the variables provided by the Muon System. The signal distributions are shown in blue, while the background distributions are shown in red. 116
- 6.18 Example for a single decision tree of the random forest after optimization of the BDT algorithm. Different variables from the Muon System have been chosen in this case, since they have strong separation power concerning the separation of muons and pions. At each node, the variable is chosen, which achieves the best separation between signal and background. For the determination of the chosen variable, the Gini-Index ($= p(1-p)$) is used, while in this example the achieved purity $S/(S+B)$ of the signal is shown at each node. 117
- 6.19 Linear correlation coefficients [%] for the set of input variables used for the MVA at $p_{beam} = 1.5 \text{ GeV}/c$ for the signal (a) and for the background (b). For each input sample, $\sim 10^6$ events have been generated. From strongly correlated variables ($> 90\%$) only one variable was included since the other variable does not carry significant new information. 119
- 6.20 Normalized response distribution from the BDT for the signal $\bar{p}p \rightarrow \mu^+\mu^-$ (blue) and the background $\bar{p}p \rightarrow \pi^+\pi^-$ (red) for a) the BDT algorithm and b) the BDTG algorithm. The distributions of the response for the signal and the background should be pushed away from each other as far as possible. For the BDTG response, a small fraction of the background events, which have been misclassified, are contained in the signal peak, which is starting around BDTG > 0.95 , so that it is also for this method not feasible to remove the full amount of background events. 120

- 6.21 Receiver operating characteristics (ROC) for different classification methods, which is used to evaluate the classification performance of each method. The Boosted Decision Trees (BDT, BDTG) show the best performance of all tested methods, with their performance being almost identical. The higher the area under the curve of a certain classification method, the better its performance. 123
- 6.22 A Kolmogorov-Smirnov Test is used for overtraining check for a) the BDT algorithm and b) the BDTG algorithm. Overtraining indicates that the classifier is sensitive to statistical fluctuations in the data, which destroys its general operationality. 124
- 6.23 Angular distributions of the signal reconstruction efficiency (ϵ) (blue dots), the Monte-Carlo generated signal (magenta squares) and the reconstructed signal (black up triangles) at $p_{beam} = 1.5 \text{ GeV}/c$ obtained with the cut configurations (a) "Loose" cuts, (b) "Medium cuts", (c) "Tight cuts" and (d) "Very tight" cuts applied on the reconstructed, preselected signal sample with high statistics. Stricter cut configurations lead to smaller values of the signal efficiency around $\cos(\theta_{CM}) \approx 0.0$ and at the outer borders of $\cos(\theta_{CM})$. Loose cuts should be preferred in this case, to avoid large error bars later when the angular distribution of the signal is corrected with the signal efficiency. This will have a direct influence on the uncertainty of the extracted FF's. 130
- 6.24 Angular distributions of the signal reconstruction efficiency (ϵ) (blue dots), the Monte-Carlo generated signal (magenta squares) and the reconstructed signal (black up triangles) at $p_{beam} = 1.7 \text{ GeV}/c$ (a) "Very loose" cuts, (b) "Medium cuts", (c) "Tight cuts" and (d) "Very tight" cuts, applied on the reconstructed, preselected signal sample with high statistics. To avoid large uncertainties of the extracted values of FF's later, also in the case of $p_{beam} = 1.7 \text{ GeV}/c$, it can be concluded that loose cuts should be preferred over stricter cuts. The working point will be determined later, when the extracted FF values are presented. . . . 131
- 6.25 Angular distributions of the signal reconstruction efficiency (ϵ) (blue dots), the Monte-Carlo generated signal (magenta squares) and the reconstructed signal (black up triangles) from the signal sample of high statistics at $p_{beam} = 2.5 \text{ GeV}/c$ (a) "Very loose" cuts, (b) "Medium cuts", (c) "Tight cuts" and (d) "Very tight" cuts. "Very loose" cuts provide the keep the highest signal statistics in all histogram bins, but are connected to very low expected S-B ratios (1:67). Therefore, the "medium" or "tight" cuts should be preferred over "very loose" cuts. 133
- 6.26 Angular distributions of the signal reconstruction efficiency (ϵ) (blue dots), the Monte-Carlo generated signal (magenta squares) and the reconstructed signal (black up triangles) from the signal sample of high statistics at $p_{beam} = 3.3 \text{ GeV}/c$ (a) "Very loose" cuts, (b) "Loose cuts", (c) "Tight cuts" and (d) "Very tight" cuts. 134

- 6.27 (a) Source histogram with adapted fit function f_1 with the $\pm 1\sigma$ error band of the adapted fit function. A reduced χ^2 for the fit of $\chi^2/ndf = 1.59$ was obtained. The function f_1 is used for the generation of the two statistically independent target histograms. (b) The first (black open squares) and second (red dots) target histogram, containing the pion contamination distribution. Also shown is the signal distribution after μ -selection (blue squares). 136
- 6.28 Difference of the histograms of the two statistically independent pion contamination distributions, which are shown in Figure 6.27 (b). The difference is due to the statistical fluctuations. 137
- 6.29 Angular distributions of the reconstructed μ -selected signal (based on sample S2) (blue squares) depending on the center-of-mass angle $\cos(\theta_{CM})$. Also shown are the two statistically independent angular distributions of the pion contamination (black open squares, red dots) at the considered values of beam momentum of (a) 1.5 GeV/c, "loose cuts" (b) 1.7 GeV/c, "medium cuts", (c) 2.5 GeV/c, "tight cuts" and (d) 3.3 GeV/c, "loose cuts". 138
- 6.30 (a) Histograms of the selected data (D) (**black triangles up**) containing the selected signal counts (S2) mixed with the expected pion contamination (B1), the statistically independent angular distribution of the pion contamination (B2) (**red dots**) (which will be reconstructed in a separate analysis in the experiment later) used for the background subtraction. Also shown is the obtained angular distribution after background subtraction (**magenta triangles down**) (D-B2). (b) Reconstructed and efficiency corrected signal angular distribution (**green squares**). The fit function $f_1(x)$ (red line) is used to extract $|G_E|$ and $|G_M|$ simultaneously. 139
- 6.31 Differential cross section for the $\bar{p}p \rightarrow K^+K^-$ process depending on the $\bar{p}p$ -center-of-mass production angle of the K^- from Ref. [134]. 141
- 6.32 (a): Distribution of the reconstructed kinematical variable $(\theta^+ + \theta^-)_{CM}$ after preselection for the muon pairs (blue) and the kaon pairs (red) at $p_{beam} = 1.5$ GeV/c. Due to the assumption of muon mass hypothesis, the peak of the kaon distribution is shifted strongly to smaller angles. Since the particles are produced back-to-back in the $\bar{p}p$ -center-of-mass frame, this variable is peaked around 180° [DEG] for the muon pairs. (b): Distribution of the reconstructed invariant mass M_{inv} of the final state after preselection for the muon pairs (blue) and the kaon pairs (red). 142
- 6.33 (a): Distribution of the reconstructed kinematic variable $(\theta^+ + \theta^-)_{CM}$ after preselection for the muon pairs (blue) and for the final states from $\pi^+\pi^-\pi^0$ (red) at $p_{beam} = 1.5$ GeV/c. Due to the three particles in the final states of $\pi^+\pi^-\pi^0$ and the muon mass hypothesis used for the reconstruction of the four momenta, the distributions for signal and background are very different. (b): Distribution of the reconstructed invariant mass M_{inv} of the final state after preselection for the muon pairs (blue) and the charged particle pairs from $\pi^+\pi^-\pi^0$ (red). 144

- 6.34 (a): Distribution of the reconstructed kinematic variable $(\theta^+ + \theta^-)_{CM}$ after preselection for the muon pairs (blue) and for the final states from $\pi^0\pi^0$ (red) at $p_{beam} = 1.5 \text{ GeV}/c$. Due to the neutral, short-living particles in the final states of $\pi^0\pi^0$ and the muon mass hypothesis used for the reconstruction of the four momenta, the distributions for signal and background are very different to each other. (b): Distribution of the reconstructed invariant mass M_{inv} of the final state after preselection for the muon pairs (blue) and the charged particle pairs from $\pi^0\pi^0$ (red). 145
- 7.1 Reconstructed and efficiency corrected signal angular distribution (green squares) after full analysis including background subtraction at the considered values of beam momenta. The fit function $f_2(x)$ (red line) is used to extract the ratio R and its uncertainty directly. 149
- 7.2 Integrated cross section σ (orange dots) for the $\bar{p}p \rightarrow \mu^+\mu^-$ process, depending on q^2 in the range of $\cos(\theta_{CM}) < 0.8$. σ is determined from the reconstructed signal counts after background subtraction, application of the signal reconstruction efficiency and divided by the time-integrated luminosity $\mathcal{L} = 2 \text{ fb}^{-1}$. Also shown is the theoretical curve based on Eq. 3.26. 152
- 7.3 Extracted values of the effective time-like proton FF for the $\bar{p}p \rightarrow \mu^+\mu^-$ process at different values of q^2 . The error bars are not visible due to their smallness. Also shown is the FF model from Ref. [54], which is used for the calculation of the expected signal statistics, given in Tab. 5.1. 154
- 7.4 Total uncertainties of the ratio $R = |G_E|/|G_M|$ for the $\bar{p}p \rightarrow \mu^+\mu^-$ channel at different values of q^2 (blue dots) obtained under the conditions of $\bar{\text{P}}\text{ANDA}$ Phase-3. $R = 1$ is assumed in these simulation studies. Also shown are the currently existing data from Ref. [68] (squares), from Ref. [77] (diamonds), from Ref. [99] (star and cross), from Ref. [74] (open circles) and from Ref. [96] (down triangle). 157
- 7.5 Simulation and analysis without any variables from the EMC at $\mathcal{L} = 2 \text{ fb}^{-1}$ ($\bar{\text{P}}\text{ANDA}$ Phase-3). Left plot: Reconstructed, μ -selected angular distributions of the signal (squares) and of the expected pion contamination (dots and open squares) used for the analysis. Right plot: Angular distributions of the MC generated μ^- (squares), the reconstructed, μ -selected signal (S1) (up triangles) and the corresponding signal reconstruction efficiency (dots). 160
- 7.6 Comparison between the reconstructed, signal efficiency corrected angular distributions at $p_{beam} = 1.5 \text{ GeV}/c$ (for $\bar{\text{P}}\text{ANDA}$ Phase-3, $\mathcal{L} = 2 \text{ fb}^{-1}$). Loose cuts were used for the μ -selection, including variables from EMC (left) respectively excluding variables from the EMC (right) for the training of the Boosted Decision Trees (BDT). 160

- 7.7 Pion contamination distribution at $p_{beam} = 1.5 \text{ GeV}/c$ used in this feasibility study which is described in section 6.3 (MI, blue triangles up) and has a more realistic shape. In comparison to that, the pion contamination distribution obtained with a modified signal selection (MII, red dots), aiming just to match the number of expected events but with unrealistic shape. Both distributions contain the number of expected events. Repeating the analysis with both pion background distributions allows to test the influence of the distribution shape on the uncertainties of the form factors. 163
- 7.8 Angular distributions of the reconstructed μ -selected signal counts (blue squares) and pion contamination (red dots, black open squares) obtained with method II as a function of the center-of-mass angle $\cos(\theta_{CM})$. The shape of the distributions of the pion contamination are not realistic in this case. Shown are the cases for (a) $1.5 \text{ GeV}/c$, "loose cuts" (b) $1.7 \text{ GeV}/c$, "medium cuts", (c) $2.5 \text{ GeV}/c$, "tight cuts" and (d) $3.3 \text{ GeV}/c$, "loose cuts". 164
- 7.9 Extracted uncertainties of the ratio $R = |G_E|/|G_M|$ for the $\bar{p}p \rightarrow \mu^+\mu^-$ channel at different values of q^2 obtained with pion contamination distribution of more realistic (MI, blue dots) respectively unrealistic shape (MII, red triangles up). $R = 1$ is assumed. For a better visualization, the data points are shifted by $\delta q^2 = \pm 0.05$. Also shown are the currently existing data from Ref. [68] (squares), from Ref. [77] (diamonds), from Ref. [99] (star and cross), from Ref. [74] (open circles) and from Ref. [96] (down triangle). 166
- 7.10 Extracted values of $|G_E|$ (a) and $|G_M|$ (b) with their uncertainties, obtained with pion contamination distributions of more realistic (MI, triangles up) respectively unrealistic shape (MII, open circles) depending on q^2 . For a better visualization, the data points are shifted by $\delta q^2 = \pm 0.05$. Also the FF model from [54] is shown (dashed lines), which is used in this feasibility study together with the assumption that $|G_E| = |G_M|$ 167
- 7.11 Residual values for $|G_E|$ (a) and $|G_M|$ (b) at different q^2 values and corresponding uncertainties. Shown are the results obtained with pion contamination distributions of more realistic (MI, triangles up) respectively unrealistic shape (MII, open circles). For a better visualization, the data points are shifted by $\delta q^2 = \pm 0.05$. . . 167
- 7.13 Energy of the produced μ^+ versus μ^- at Monte Carlo level in the $\bar{p}p$ center-of-mass system at $p_{beam} = 1.5 \text{ GeV}/c$ for the case that final state photons are emitted and cause a tail to lower energies (left plot) (PHOTOS ON) and for the case that no radiative effects are included (right plot) (PHOTOS OFF). 171
- 7.14 Monte-Carlo generation at $p_{beam} = 1.5 \text{ GeV}/c$ for the signal $\bar{p}p \rightarrow \mu^-\mu^+$ process: (a) Number of emitted photons per event. (b) Invariant mass of the generated $\mu^+\mu^-$ pair in the final state. The tail to lower values of is caused by the loss of energy and momentum which is carried away by the emitted photon(s). 172

- 7.15 Comparison of the MC invariant mass of the generated lepton pair in the final state with PHOTOS ON at $p_{beam} = 1.5 \text{ GeV}/c$ for (a) the $\bar{p}p \rightarrow \mu^+\mu^-$ process and (b) the $\bar{p}p \rightarrow e^+e^-$ process. While approximately 30.4% of the muon pairs emit at least one real photon, for the electron pairs it is the case in approximately 68.7% of the events. Please note the different binning used in (b). 173
- 7.16 Angular distribution of the MC generated μ^- including final state radiation based on PHOTOS for $\bar{p}p \rightarrow \mu^+\mu^-$ for different cuts on the MC invariant mass $M_{\mu^+\mu^-}$ (left plot) and the relative loss of signal statistics due to different cuts (right plot). The cuts lead to a homogeneous loss of signal statistics over the considered range of $|\cos\theta_{CM}| < 0.8$ 174
- 7.17 Simulation and analysis at $p_{beam} = 1.5 \text{ GeV}/c$ including final state radiation emission based on the PHOTOS package: (a) Reconstructed angular distributions of the MC signal sample S1 (black triangles up), of the Monte-Carlo generated μ^- (magenta squares) and the distribution of the signal efficiency (blue dots). An integrated signal efficiency of 24.2% is obtained using loose cuts. (b) Angular distribution of the reconstruction efficiency corrected signal counts after background subtraction for negative charges (squares). Also the fit function $f_2(x)$ (red line) is shown, which is used for the direct extraction of $R \pm \Delta R$ 175
- 8.2 Expected uncertainty of the ratio $R = |G_E|/|G_M|$ for the $\bar{p}p \rightarrow \mu^+\mu^-$ channel at $q^2 = 5.1 \text{ GeV}/c$ obtained for the conditions of the PANDA Phase-1 (blue square). $R = 1$ is assumed in this study. For a better visualization, the data points are shifted by $\delta q^2 = \pm 0.05$. Also shown are the currently existing data from Ref. [68] (squares), from Ref. [77] (diamonds), from Ref. [99] (star and cross), from Ref. [74] (open circles) and from Ref. [96] (down triangle). 181
- 8.3 Simulation and analysis including the EMC detector at $\mathcal{L} = 0.1 \text{ fb}^{-1}$: (a) Reconstructed angular distributions after μ -selection of the signal sample with realistic statistics (blue squares) and the expected pion contamination (red dots and black open squares) used for further analysis. (b) Angular distribution of the reconstruction efficiency corrected signal counts after background subtraction for negative charges (squares). Also the fit function $f_2(x)$ (red line) is shown, which is used for a direct extraction of $R \pm \Delta R$ 182
- 8.4 Simulation and analysis without EMC detector material at $\mathcal{L} = 0.1 \text{ fb}^{-1}$: (a) Reconstructed angular distributions of the physical signal sample (squares) and pion contamination (dots and open squares) used for the analysis. (b) Angular distributions of the MC generated μ^- (squares), the reconstructed, μ -selected signal from the high statistics sample (up triangles) and the corresponding signal reconstruction efficiency (dots). 183

- 8.5 Comparison between the reconstructed, signal efficiency corrected angular distributions at $p_{beam} = 1.5 \text{ GeV}/c$ at $\mathcal{L} = 0.1 \text{ fb}^{-1}$ (a) including variables from EMC and (b) a scenario, where no EMC is present in the detector model at all. The larger error bars and stronger fluctuations of the data points (right figure) are due to the missing EMC material. When present, the EMC material acts as an additional muon filtering element in front of the Muon System. 185
- A.1 Working principle of a Multilayer Perceptron, which is a feed-forward network of connected neurons [147]. The neurons are arranged in layers and can be activated with an activation function. The Multilayer Perceptron can be seen as a non-linear mapping from an n-dimensional variable space (n : number of input variables) to a one-dimensional space of output variables in the case of classification problems. 193
- B.1 Linear correlation coefficients [%] between the input variables for MVA at $p_{beam} = 3.3 \text{ GeV}/c$ for the signal (a) and the background (b). The input variables are not strongly linearly correlated, so that each of the variables provides helpful information for the μ/π separation. 196
- B.2 (a) Receiver operating characteristics for Boosted Decision Trees (BDT, BDTG), which show a very similar performance at $p_{beam} = 3.3 \text{ GeV}/c$. (b) A Kolmogorov-Smirnov Test is used for overtraining check for the BDT algorithm. The evaluation of this test can be seen at the high values of signal (background) probability (p-value), which indicates that no overtraining has occurred during the training of the BDT. 197
- C.1 Residual pion background distribution after μ -selection, which is used for a shape extraction with a fit function (red line). For the fit, polynomials of the 7-th order or higher have been used. The obtained curves are used to generate realistic pion contamination distributions for the background subtraction in the analysis. . . . 200
- C.2 Residual pion background distribution after μ -selection, which is used for a shape extraction with a fit function (red line). For the fit, polynomials of the 7-th order or higher have been used. The obtained curves are used to generate realistic pion contamination distributions for the background subtraction in the analysis. . . . 201
- D.1 Angular distributions of the selected data (black triangles up), which consist of the μ -selected signal data from $\bar{p}p \rightarrow \mu^+\mu^-$ plus the expected pion contamination. Also shown are the distributions of the statistically independent pion contamination (red dots), which will be measured and reconstructed in the experiment later. Selected signal data after the background subtraction are shown as well (magenta triangles down), which contain the statistical fluctuations of the pion contamination. 204

- E.1 Reconstructed and efficiency corrected signal angular distribution after background subtraction (green squares). The fit function $f_2(\mathbf{x})$ (red line) is shown, which is used to extract the values of $R \pm \Delta R$ directly. (a): 1.5 GeV/ c "loose cuts", (b): 1.7 GeV/ c "medium cuts", (c): 2.5 GeV/ c "tight cuts" and (d): 3.3 GeV/ c "loose cuts". 206
- F.1 Comparison between analysis based on simple cuts and MVA at total signal efficiency $\epsilon = 24.6\%$. The angular distribution of the signal reconstruction efficiency (blue dots), the reconstructed signal counts after cuts (black triangles up) and the MC generated signal counts (violet squares) of the negatively charged muon are depicted for (a) simple cuts and (b) MVA. The figures below show the two statistically independent angular distributions of the pion contamination (black open squares and red dots) and of the signal counts (blue squares). A clearly better signal statistics is achieved over a larger range of $\cos(\theta_{CM})$ by using MVA. 214
- F.2 Angular distribution of the reconstructed and efficiency corrected signal counts after background subtraction for an analysis based on (a) simple cuts and (b) multivariate analysis (Boosted Decision Trees). The angular range, which suitable for fitting the distribution, is clearly larger for MVA in contrast to simple cuts. The statistical precision of the form factor ratio R is $\sim 86\%$ for simple cuts, while for the MVA a high precision of $\sim 5\%$ is obtained. 215
- G.1 Angular distribution of the reconstructed and efficiency corrected signal counts obtained at $p_{beam} = 1.5$ GeV/ c including background fluctuations (as presented in Chapter 7, Fig. 7.1) (a) and repeated without introducing background fluctuations (b). 217

List of Tables

2.1	Quantum numbers of the $\bar{p}p$ system and its individual components: electric charge Q , strong isospin I and its 3rd component I_3 , total angular momentum J , parity P , spin s and baryon number B [20, 21].	6
2.2	Coefficients used in the parameterization from Ref. [27] for several inelastic channels of antiproton-proton annihilation into charged di-pion and di-kaon pairs. . .	8
2.3	Coefficients used in the parameterization from Ref. [27] for several inelastic channels of antiproton-proton annihilation with light mesons in the final state.	8
3.1	Overview of experimental results from $\bar{p}p$ annihilation experiments for extraction of the time-like nucleon FF's [92].	35
3.2	Overview of experimental results from e^+e^- annihilation experiments for extraction of the time-like nucleon FF's [92].	36
4.1	Operation modes of the High Energy Storage Ring (HESR) for the Modularized Start Version in the beginning phase of FAIR and the original design version, with high resolution and high luminosity mode [13].	48
4.2	Overview of the \bar{P} ANDA target solutions, Cluster-Jet and Pellet Target, and their properties [115]. The Pellet target will be only available at a later stage of the experiment.	50
4.3	Main properties of PWO-II.	59
4.4	The instrumentation of the Muon System at \bar{P} ANDA [125].	67
5.1	Number of physically expected events N_{int} and integrated cross-sections σ_{int} for an angular range, which is limited to $ \cos(\theta_{CM}) < 0.8$. For the calculations, a time-integrated luminosity of $\mathcal{L} = 2 \text{ fb}^{-1}$ was assumed, corresponding to the conditions of \bar{P} ANDA Phase-3. For $ G_M $, the parameterization from Ref. [54], which is given in Eq. 3.57, is used together with the assumption that $ G_E = G_M $	76
5.2	Number of generated Monte-Carlo events (N_{gen}) for each value of the considered beam momenta. The reconstruction efficiency of the signal is determined with samples of high statistics ($N_{gen}^{(1)}$). For the data analysis, real data samples with the expected signal statistics are generated ($N_{gen}^{(2)}$), each containing the expected number of signal events under the assumption of a time-integrated luminosity of $\mathcal{L} = 2 \text{ fb}^{-1}$ (corresponding to \bar{P} ANDA Phase-3).	84

6.1	Composition of the reconstructed and preselected background event sample for the $\bar{p}p \rightarrow \pi^+\pi^-$ process. The preselection of the reconstructed data requires one positively (+) and one negatively (-) charged track per event. In total 7.27×10^6 events from the generated background sample were accepted by the preselection at $p_{beam} = 1.5 \text{ GeV}/c$. 10^8 events were originally generated.	91
6.2	Composition of the reconstructed event sample for $\bar{p}p \rightarrow \pi^+\pi^-$ after preselection. In total 7.82×10^6 events from the generated sample (1×10^8 events were originally generated for the $\bar{p}p \rightarrow \pi^+\pi^-$ process) were accepted by the preselection at $p_{beam} = 1.7 \text{ GeV}/c$. The preselection of the reconstructed data requires one positively (+) and one negatively (-) charged track per event. Different particle species can be found in the preselected data, the percentage and absolute numbers are given.	92
6.3	Percentage of MC events without/with pion decay (one respectively both of the final state pions) in 10^8 generated events at the considered values of beam momentum.	93
6.4	Used configuration options for BDT classification. The purity of a node (p) is defined as the ratio of the signal events to all events in the node.	112
6.5	Ranking of the input variables for MVA after the training step at $p_{beam} = 1.5 \text{ GeV}/c$. Also listed are the spectator variables, which are not considered by the BDT algorithm but are also saved in the output files of MVA for the final cuts applied after the multivariate classification. The charge of the particle connected to a certain variable is indicated as (+) or (-). This set of input variables was chosen for the MVA training at $p_{beam} = 1.5, 1.7$ and $2.5 \text{ GeV}/c$	118
6.6	Different cut configurations are tested at beam momenta of 1.5, 1.7, 2.5 and 3.3 GeV/c . The difference between the configurations is the cut on the BDT response.	126
6.7	Chosen variables for the MVA training at $p_{beam} = 3.3 \text{ GeV}/c$ with ranking of the variables according to their separation power. The particle charge connected to a certain variable is indicated as (+) or (-). A smaller set of input variables is chosen at $p_{beam} = 3.3 \text{ GeV}/c$ in comparison to the case of $p_{beam} = 1.5, 1.7$ and $2.5 \text{ GeV}/c$, since only the more powerful variables (mainly from the Muon System) contribute significantly to the signal-background separation, due to the more similar behavior of muon and pion for increasing beam momentum.	127
6.8	Expected counts in the pion contamination $N_{exp,cuts}(\bar{p}p \rightarrow \pi^+\pi^-)$ at the considered values of beam momenta at $\bar{\text{PANDA}}$ Phase-3. A time-integrated luminosity of 2 fb^{-1} is assumed. Also shown are the expected numbers for the signal after μ -selection $N_{exp,cuts}(\bar{p}p \rightarrow \mu^+\mu^-)$ for comparison, based on the final cut configuration at each considered value of beam momentum. The final cut configurations will be chosen in Chapter 7.	135
6.9	Reconstruction efficiency for the $\mu^+\mu^-$ final states of the $\bar{p}p \rightarrow \mu^+\mu^-$ signal process and rejection factors for the final states $\mu^+\mu^-$, $\pi^-\mu^+$ and $\mu^-\pi^+$ from pion decay of the $\bar{p}p \rightarrow \pi^+\pi^-$ background process at $\text{CL} = 95\%$	140

- 7.1 The result $R \pm \Delta R$ corresponds to the fit function $f_2(x)$, where R is one of the free fit parameters and thus can be extracted directly. The studies are based on the assumption of $R = 1$. The obtained results at the final cut configurations are highlighted in bold and italic font. 150
- 7.2 The fit function $f_1(x)$ is used for the simultaneous extraction of $|G_E|$ and $|G_M|$ at each considered value of beam momentum ($p_{beam} = 1.5, 1.7, 2.5$ and 3.3 GeV/ c). The chosen cut configurations are highlighted in bold and italic font. The calculated values of the magnetic FF, $|G_M|$ (model), which is based on the FF model for the parameterization of $|G_M|$ from Ref. [54] are shown for comparison. 151
- 7.3 Extracted statistical precision of the integrated cross section of the $\bar{p}p \rightarrow \mu^+\mu^-$ signal process together with the calculated value based on Eq. 3.26, Chapter 3, for the considered angular range of $-0.8 < \cos(\theta_{CM}) < 0.8$ 152
- 7.4 Extracted values and statistical precision of the effective proton FF, $|F_p|$ 153
- 7.5 Statistical and systematic uncertainties, which contribute to the relative total uncertainty of $|G_E|$, $|G_M|$ and R 156
- 7.6 Comparison between the extracted values of $R \pm \Delta R$ based on the full analysis with and without variables from EMC. The result $R \pm \Delta R$ was obtained with the fit function $f_2(x)$ 161
- 7.7 Overview of the different cut configurations used in method II, which are applied on two statistically independent pion data samples after reconstruction. The cuts on M_{inv} , $(|\phi^+ - \phi^-|)_{lab}$ and $(\theta^+ + \theta^-)_{CM}$ are the same as in the μ -selection. The difference between the cut configuration is the cut on the BDT response, which is adjusted in such a way as to obtain the expected statistics of the pion contamination, $N_{exp,cuts}(\bar{p}p \rightarrow \pi^+\pi^-)$, which can be found in Tab. 6.8. 162
- 7.8 Contributions of the relative statistical and systematic uncertainties of $|G_E|$, $|G_M|$ and R to the relative total uncertainty. 165
- 7.9 Comparison of the relative statistical uncertainty of $|G_E|$, $|G_M|$ and R for PHOTOS ON/OFF. Loose cuts are used for the μ -selection. Also shown are the obtained values and statistical uncertainties for the effective proton FF and the integrated cross section. The results show, that a deterioration of the statistical uncertainty is obtained when PHOTOS is switched ON, due to the loss of signal efficiency. 175
- 8.1 Statistical and systematic contributions to the total relative uncertainty of $|G_E|$, $|G_M|$ and R for \bar{P} ANDA Phase-1 with full EMC detector and reduced detector setup. Loose cuts are used in the μ -selection. The systematic uncertainties are stemming from the chosen cuts (first value) and - in case of $|G_E|$ and $|G_M|$ - the uncertainty of the luminosity (second value). Also shown are the obtained values and uncertainties for the effective proton FF and the integrated cross section together with their systematic uncertainty from the luminosity measurement. 180

8.2	Comparison between the extracted values of $R \pm \Delta R$, and the FF's based on the full analysis with / respectively without EMC detector. The result of $R \pm \Delta R$ corresponds to the fit function $f_2(x)$. The shown uncertainties are of statistical nature.	184
E.1	The result $R \pm \Delta R$ is obtained with the fit function $f_2(x)$, where R is a free fit parameter and thus can be extracted directly. The event generator uses always $R = 1$ as an input for the generation of the signal events. The results, which are obtained with the final cut configurations, are highlighted in bold italic font.	207
E.2	For the simultaneous extraction of $ G_E $ and $ G_M $ with their statistical uncertainties, the fit function $f_1(x)$ is used at each considered value of beam momentum ($p_{beam} = 1.5, 1.7, 2.5$ and 3.3 GeV/ c). The final cut configuration is highlighted in italic bold font.	208
E.3	Comparison of the results $R \pm \Delta R$ for the example of very loose and medium cuts at 1.5 and 1.7 GeV/ c : the values $R_{direct} \pm \Delta R_{direct}$ are directly extracted with the fit function $f_2(x)$, where R is a free fit parameter. $R_{calc} \pm \Delta R_{calc}$ represents the results obtained with fit function $f_1(x)$, where the ratio is evaluated from the (correlated) fit parameters, P_0 and P_1	209
E.4	Extracted results and relative statistical uncertainty of the integrated cross section for the $\bar{p}p \rightarrow \mu^+\mu^-$ signal process together with the calculated value based on Eq. 3.26, Chapter 3, for the considered angular range of $-0.8 < \cos(\theta_{CM}) < 0.8$	210
E.5	Extracted relative statistical uncertainty on the effective proton FF, $ F_p $	210
F.1	Comparison between the two different analysis methods (simple cuts and a multivariate data analysis (MVA)).	212
F.2	Comparison between the two different analysis methods (SIMPLE CUTS and MVA). Application of multivariate analysis (here Boosted Decision Trees) clearly improves the background rejection factor physically expected signal-to-background ratio after full analysis.	212
G.1	Comparison of the relative statistical uncertainty of $ G_E $, $ G_M $ and R obtained with the analysis described in Chapter 6 (right column) and repeated excluding the background fluctuations (left column).	218

- H.1 Final results for the $\overline{\text{PANDA}}$ Phase-3:** Statistical and systematic contributions to the relative total uncertainty of $|G_E|$, $|G_M|$, $R = |G_E|/|G_M|$, the effective FF $|F_p|$ and the integrated cross section for the signal $\bar{p}p \rightarrow \mu^+\mu^-$ at four different values of beam momenta ($p_{beam} = 1.5, 1.7, 2.5$ and 3.3 GeV/ c). An angular interval of $|\cos(\theta_{CM})| < 0.8$ is considered. A time-integrated luminosity of $\mathcal{L} = 2 \text{ fb}^{-1}$ was assumed for the conditions of $\overline{\text{PANDA}}$ Phase-3, which corresponds to a measurement at the $\overline{\text{PANDA}}$ original design luminosity of $2 \times 10^{32} \text{ cm}^{-2} \text{ s}^{-1}$ at pure data taking time of approximately 4 months and full detector setup. Systematic error sources are the luminosity measurement, the choice of cuts and - only at $p_{beam} = 3.3$ GeV/ c - the number of histogram bins. 220
- H.2 Final results for the $\overline{\text{PANDA}}$ Phase-1:** Statistical and systematic contributions to the relative total uncertainty of $|G_E|$, $|G_M|$, $R=|G_E|/|G_M|$, the effective FF $|F_p|$ and the integrated cross section for the signal $\bar{p}p \rightarrow \mu^+\mu^-$ at the lowest value of beam momentum at $\overline{\text{PANDA}}$ ($p_{beam} = 1.5$ GeV/ c). An angular interval of $|\cos(\theta_{CM})| < 0.8$ is considered. In this feasibility study a time-integrated luminosity of $\mathcal{L} = 0.1 \text{ fb}^{-1}$ was assumed, which corresponds to a measurement at the $\overline{\text{PANDA}}$ Phase-1 with a luminosity of $1 \times 10^{31} \text{ cm}^{-2} \text{ s}^{-1}$ at pure data taking time of approximately 4 months. Systematic error sources are the luminosity measurement and the choice of cuts. 220

